Godunov-type schemes for hydrodynamic and magnetohydrodynamic modeling

Jeaniffer Vides Higueros

UNIVERSITÉ DE NICE-SOPHIA ANTIPOLIS - UFR Sciences

École Doctorale en Sciences Fondamentales et Appliquées

THÈSE

pour obtenir le titre de

Docteur en Sciences

de l'UNIVERSITÉ de Nice-Sophia Antipolis

Spécialité : Mathématiques Appliquées

présentée et soutenue par

Jeaniffer VIDES HIGUEROS

Schémas de type Godunov pour la modélisation hydrodynamique et magnétohydrodynamique

Godunov-type schemes for hydrodynamic and magnetohydrodynamic modeling

Thèse dirigée par Boniface NKONGA & Hervé GUILLARD

soutenue le 21 octobre 2014

Jury :

M. Édouard AUDIT	Chercheur, CEA Saclay/MdlS	Co-enc. de thèse
M. Dinshaw BALSARA	Conc. Assoc. Professor, Univ. of Notre Dame	Rapporteur
M. Alain DERVIEUX	Directeur de Recherche, Inria Sophia Antipolis	Président
M. Bruno DESPRÉS	Professeur, Univ. Paris VI, UPMC	Rapporteur
M. Hervé GUILLARD	Directeur de Recherche, Inria Sophia Antipolis	Codir. de thèse
M. Pierre-Henri MAIRE	Directeur de Recherche, CEA-CESTA	Examinateur
M. Boniface NKONGA	Professeur, Univ. de Nice-Sophia Antipolis	Dir. de thèse

To my loving parents

Acknowledgements

These three years of thesis were for me an incredible experience from a scientific and a personal point of view. First and foremost, I offer my sincerest gratitude to Boniface Nkonga, for giving me the opportunity to experience the thrill of doing research and for sharing his passion for numerical methods and challenges with me. His great efforts to explain things clearly were always greatly appreciated. I would also like to thank Édouard Audit for his enthusiasm, encouragement and guidance; his most valuable lesson was to appreciate the physics behind the research. I thank Hervé Guillard for his support and assistance during CEMRACS. I would also like to thank all of my other co-authors, namely Christophe Berthon, Benjamin Braconnier, Serge Van Criekingen and Mikolaj Szydlarski.

I express my gratitude to Dinshaw Balsara and Bruno Després for accepting to be the reviewers of my manuscript and for the time they devoted to reading and commenting on it. I also thank Alain Dervieux and Pierre-Henri Maire for accepting to be part of the jury. I thank my team at Inria and Maison de la Simulation for making the working environment a special one; I want to particularly thank Alex, Feng, Florence, Giorgio, Michel, Pierre, Ralitsa, Samuel and Sophie.

My heartfelt thanks goes to Maria Laura, who always makes sure I feel her confidence and encouragement; I thank her for all those hours she kept me company and for all those amazing trips and experiences we had together. I also want to thank my lovely sister, who gave me plenty of support these years and also joy when she gave birth to Karina Sofia, of whom I am blessed to be her godmother; she always makes me feel part of my niece's life and I sincerely appreciate this. I thank her husband Mario, my grandmother, my close aunts and cousins, my uncles and other members of my family who cheered for me and made it feel it was possible, and my friends Adrián, Alexa, Ammy, Karen, Lester, Luis (Wichon), Marco and Mirna. I especially thank God for giving me the strength and resources to complete my thesis.

This thesis is dedicated to my parents. I have felt their love, moral and emotional support throughout this important stage in my life, and, despite the geographical distance, they have always been nearby and watching my back. I cannot repay them for all they have given or all they have loved me but dedicating this thesis to them is a start. None of this could have happened without them.

Contents

Introduction

The objective of this thesis work concerns the study, design and numerical implementation of finite volume approximations belonging to a particular class of methods known as Godunov-type methods [65, 74], which are based on the reconstruct-evolve-average (REA) algorithm (see, for instance, [90]), for hyperbolic conservation laws. In the context of the standard finite volume approach, the conservative form of the governing equations is especially important when dealing with problems admitting discontinuities, e.g., shocks and contact discontinuities, in the solution. Non-conservative formulations lead not only to incorrect estimates of wave speeds, but also to inconsistency of the numerical approximation with the weak form [76], whereas convergent conservative approximations are known to be always consistent with the weak formulation [88] as Rankine-Hugoniot relations are satisfied.

It has been pointed out, since the early fifties [116, 144], that artificial viscosity is unavoidable when designing stable and convergent approximations for hyperbolic systems, and in this setting, we mention the pioneering work of Godunov [65], who formulated a conservative scheme that employs the solutions of classic initial-value problems known as Riemann problems [37] at cell interfaces to approximate the local numerical flux. Indeed, numerical dissipation is the effect of fine unresolved scales on the coarse resolved ones (refer to the variational multiscale framework, e.g., [77]), and interface Riemann problems are ways to describe the evolution of these fine scales for given coarse scale data. It was Godunov who proposed the general approach of the REA algorithm as a means to solve the Euler equations of gas dynamics [65, 90] and thus show that even for nonlinear systems, the Riemann problem solution for general piecewise constant initial data consists of a finite set of waves propagating with finite velocities. His contribution then became the bedrock upon which many authors based their work, addressing the method's weaknesses, e.g., the cost related to computing exact solutions for nonlinear Riemann problems, and arguing that it might be sufficient and computationally less expensive to construct approximations of these problems, as suggested by Roe [117] and Harten et. al. [74], among others; the latter are credited with defining and coining the term *Godunov-type* for a certain class of projection-evolution schemes that use an approximation to the Riemann problem, in the finite volume context.

Given that these schemes have wide applicability as they are able to accurately reproduce much of the relevant physics, combined with the fact that numerical simulation is becoming increasingly important and employed in numerous fields for research and development, it is not surprising to find that an enormous amount of Godunov-type

schemes have been constructed over the recent years. Despite their inherent weaknesses noted by several authors such as Quirk (who duly cataloged, diagnosed and proposed how to overcome some of the perceived shortcomings in [114, 115]) and the subtle flaws that sometimes might become apparent whilst performing a simulation, Godunov-type solvers are known to be nonetheless robust and produce high fidelity simulations; generally speaking, their advantages tend to overshadow the potential disadvantages. Moreover, given the vast amount of approximate Riemann solvers available in the literature (which some consider has evolved into a growing industry [115]) and their underlying simplicity, Godunov-type finite volume methods are likely to be chosen as tools to simulate real problems in various contexts, e.g., fluid dynamics, see [2, 3, 15, 23, 26, 50, 51, 54, 60, 64, 65, 89, 90, 92, 117, 129, 131, 145], and magnetohydrodynamics, see [9, 10, 12, 45, 58, 61, 66, 72, 80, 97, 101, 107, 112, 124, 142, 141], naming a few.

Our objective is then to contribute to the undoubted success of numerically simulating real-world problems by means of Godunov-type solvers. Prominently interesting physical events occur during everyday life in a wide range of scenarios, and after managing to describe the associated phenomena in the language of mathematical equations as theoretical models, numerical simulation becomes a major tool in their study. In point of fact, scientific computing is not meant to replace theory nor experimentation, but rather work alongside them; however, there are several fundamental problems that can only be addressed with code since laboratory experimentation is not always possible, as is usual in astrophysics. This branch of astronomy is fairly broad and its research on the nature of heavenly bodies, such as stars or planets, is constantly verified by numerical simulation. Surprisingly, some of the theoretical properties or aspects that are simple enough to comprehend are in fact quite difficult to adapt to numerical systems, e.g., stationary solutions. In stellar physics, among others, many gravitational flows reach steady or quasi-steady states characterized by a balance between gravitational forces and distinct forces, such as pressure gradients, and in view of numerical simulations, the proper treatment of source terms that allows to preserve discrete equilibrium states presents a challenge (see, for instance, [55, 71, 82, 91]).

Typically, diverse observations of the extraordinary heavenly objects and their emissions facilitate a better understanding of the universe. An interesting line of research is that of nuclear fusion reactions occurring naturally and powering active stars, e.g., the Sun, which is a main-sequence star [34] and therefore generates thermal energy in its dense core region by nuclear fusion of hydrogen nuclei into helium. In general terms, nuclear fusion is the process in which two or more atomic nuclei collide at considerable high speed and fuse or join together to form a new type of atomic nucleus, releasing or absorbing energy, as matter is not conserved during the process. With this knowledge, the ambition to develop controlled thermonuclear fusion on Earth for the production of energy led to the development of the tokamak and other interesting confinement devices. In particular, the tokamak is a type of machine that uses magnetic fields to confine plasma in the shape of a doughnut-shaped torus and is the basis of the current, international ITER project [1]. Indeed, to induce large-scale thermonuclear fusion reactions, extremely high temperatures and densities are needed: since plasma consists of freely

moving electrons and ions, it can be shaped into the form of a torus by employing a combination of different types of magnetic fields (given the plasma's inherent property of electrical conductivity) and thus heat it to high temperatures so that numerous reactions (the most promising seeming to be of deuterium-tritium type) can take place and ideally, be sustained. Due to the growing need of alternative energy sources and the potential found in fusion to produce power in the nearby future, tokamak research is being extensively performed, with numerical modeling and simulation playing key roles.

In the field of plasma physics, the magnetohydrodynamic (MHD) model is used to treat plasma as a single conducting fluid and describe different phenomena at the macroscopic level, i.e., we do not consider what the electrons and ions are doing separately, but as a whole. The need of obtaining physical and stable solutions to these equations, which can be written in hyperbolic conservation form, has led to the development of several schemes that attempt to closely approximate aspects of real plasma behavior, such as Alfvén waves, MHD equilibria, and field line freezing [42]. Actually, the conservative formulation of the magnetohydrodynamic equations allows the use of Godunov-type schemes for their solution, all requiring to satisfy and preserve the divergence constraint of the magnetic field numerically. In consequence, a suite of strategies in Godunov-type MHD codes and a number algorithms that can be combined with shock-capturing Godunov-type base schemes have been developed, see [12, 45, 61, 97, 107, 112, 130], some of which require the use of multidimensional solvers for the adequate estimation of staggered electric fields [52].

Many plasma physics problems, not only in the context of magnetic confinement fusion, but also in the field of astrophysics (for instance, problems characterized by a central gravitational field, e.g., thin accretion disks [93, 94] or the evolution of protoplanetary nebula leading to the formation of planets around a young star [78]), occur in a spatial domain that can be represented by a torus. From a mathematical point of view, even if space and time scales are not exactly the same, these problems can be described by systems of equations having a common structure such that similar (to some extent) numerical methods can be applied to obtain their approximate solutions. In particular, the choice of an adequate approximation strategy depends heavily on the geometry and on the existence of an intense force field governing the physics of the problem, e.g., gravitational force for astrophysical problems and Lorentz force in tokamak devices. In this context, the numerical methods need to take into account all geometrical effects arising from the presence of the magnetic or gravitational fields and any strong anisotropy existing in the flows.

Contribution and Organization of this Manuscript

After briefly introducing all necessary background theory on hyperbolic systems of conservation laws, including the Euler and ideal magnetohydrodynamic equations, the focus of Chapter 1 shifts towards the main theoretical and numerical aspects frequently found in the Godunov-type scheme framework, such as the Riemann problem and MUSCL reconstruction, which are fundamental concepts to this thesis and thus, worth mentioning. The rest of the thesis is organized as follows.

In Chapter 2, we report on our study aimed at deriving a simple method to numerically approximate the solution of the two-dimensional Riemann problem for hyperbolic systems of conservation laws, using the literal extension of the well-known HLL formalism as its basis. Essentially, any strategy attempting to extend the three-state HLL Riemann solver to multiple space dimensions will by some means involve a piecewise constant approximation of the complex 2D interaction of waves, and the derived numerical scheme is not the exception. In order to determine closed form expressions for the involved fluxes, we rely on the equivalence between the consistency condition and the use of Rankine-Hugoniot conditions that hold across the outermost planar waves emerging from the Riemann problem's initial discontinuities. The proposed scheme is then carefully designed to simplify its eventual numerical implementation and its advantages are attested. We also present several numerical results that display its robustness and stability.

Next, in Chapter 3, we aim to show the importance of maintaining the divergence constraint of the magnetic field numerically when performing numerical simulations of the MHD equations. We investigate in particular the hyperbolic divergence cleaning technique applied to the ideal MHD equations on a collocated grid and compare it to the constrained transport technique that uses a staggered grid to maintain the property. Additionally, for the latter, we demonstrate the applicability of the two-dimensional HLL Riemann solver to obtain the electric fields at corners and zone edges in two and three dimensions, respectively. The methods are implemented in the same software and several numerical tests are presented, where the robustness and accuracy of the different schemes can be directly compared.

Chapter 4 deals with the derivation of a relaxation scheme for astrophysical flows governed by the Euler equations with gravity source terms derived from a potential, the evolution of which is described by a Poisson equation. The corresponding scheme, in which the pressure is a supplementary variable and the Poisson equation is transformed into a hyperbolic equation with a penalty parameter, is obtained in the limit as the introduced parameter tends to zero. The proposed Riemann solver provides better robustness compared to other approaches available in the same software and is capable of preserving gravitational equilibria when required. Several numerical tests and results are presented, as well.

Finally, Chapter 5 reviews the design of a finite volume approximation for hyperbolic systems of conservation laws in curvilinear coordinates, as numerous problems posses obvious geometric symmetries in coordinate systems for Euclidean space in which the associated coordinate are not all straight lines. As a matter of fact, several of these problems are related to plasma physics and are encountered not only in the astrophysical but also in the magnetic confinement fusion setting, a research area of growing importance. The approach relies on constructing the approximation without utilizing any preliminary projection when dealing with vector equations, such as those that describe the momentum of an element in multidimensions, and is later illustrated in cylindrical coordinates for toroidal geometries. Numerical experiments in a three-dimensional rectangular torus are then carefully examined.

List of Publications

From this work, two articles have been published or accepted for publication in international peer-reviewed journals:

- J. Vides, B. Braconnier, E. Audit, C. Berthon, and B. Nkonga. A Godunov-type solver for the numerical approximation of gravitational flows. *Communications in Computational Physics*, 15(1):46–75, 2014.

- J. Vides, B. Nkonga, and E. Audit. A simple two-dimensional extension of the HLL Riemann solver for hyperbolic systems of conservation laws. *Journal of Computational Physics*, forthcoming 2014.

In addition, the following peer-reviewed conference proceedings have been published or accepted for publication:

- J. Vides, E. Audit, H. Guillard, and B. Nkonga. Divergence-free MHD simulations with the HERACLES code. In *ESAIM: Proc.*, volume 43, pages 180–194, 2013.

- J. Vides, E. Audit, and B. Nkonga. A relaxation scheme for inviscid flows under gravitational influence. In *ESAIM Proc. of the SMAI 2013 Congress, Seignosse, France*, forthcoming 2014.

- J. Vides, S. Van Criekingen, M. Szydlarski, and E. Audit. A Godunov-type solver for gravitational flows: Towards a time-implicit version in the HERACLES code. In *8th International Conference of Numerical Modeling of Space Plasma Flows (ASTRONUM 2013)*, volume 488, pages 279–284, 2014.

- S. Van Criekingen, E. Audit, J. Vides, and B. Braconnier. Time-implicit hydrodyanmics for Euler flows. In *ESAIM Proc. of the SMAI 2013 Congress, Seignosse, France*, forthcoming 2014.

An Inria research report has been written:

- J. Vides, B. Nkonga, and E. Audit. A simple two-dimensional extension of the HLL Riemann solver for gas dynamics. INRIA Research Report No. 8540, 2014.

Introduction

L'objectif de ce travail de thèse est l'étude, la construction et la mise en œuvre numérique d'approximations volumes finis appartenant à une classe particulière de méthodes dites de type Godunov [65, 74], fondées sur l'algorithme REA («reconstruct-evolve-average», voir par exemple [90]), pour les lois de conservation hyperboliques. Dans le contexte de l'approche des volumes finis, la forme conservative des équations est particulièrement importante lorsqu'il s'agit de problèmes présentant des discontinuités, comme par exemple des ondes de choc ou des discontinuités de contact, dans la solution. Les formulations non conservatives conduisent non seulement à des estimations erronées des vitesses d'onde, mais aussi à l'inconsistance de l'approximation numérique de la formulation faible [76], alors que les approximations conservatives convergentes sont connues pour être toujours en accord avec la formulation faible [88] puisque des relations de Rankine-Hugoniot sont satisfaites.

Il a été souligné, depuis le début des années cinquante [116, 144], que la viscosité artificielle est inévitable lors de la construction d'approximations stables et convergentes pour les systèmes hyperboliques, et dans ce cadre, nous parlons ici du travail pionnier de Godunov [65], qui a formulé un schéma conservatif qui utilise les solutions du problème de Riemann (un problème de Cauchy classique [37]) aux interfaces pour rapprocher le flux numérique local. En effet, la dissipation numérique prend en compte l'effet des échelles fines non résolues sur les grandes échelles résolues (voir les méthodes variationnelles multi-échelles, par exemple [77]). Les problèmes de Riemann aux interfaces permettent de décrire l'évolution de ces fines échelles pour les données grossières. Godunov a proposé l'approche générale de l'algorithme REA comme un moyen de résoudre les équations d'Euler de la dynamique des gaz [65, 90] et a ainsi montré que, même pour les systèmes non linéaires, la solution du problème de Riemann se compose d'un ensemble fini d'ondes qui se propagent à vitesse finie. Sa contribution est devenu la référence sur laquelle de nombreux auteurs ont développé des recherches répondant aux points faibles de la méthode initiales, par exemple les coûts liés au calcul numérique des solutions exactes pour des problèmes de Riemann non linéaires. Certains affirment qu'il pourrait être suffisant et moins coûteux de construire des approximations «consistantes» du problème de Riemann, comme suggéré par Roe [117] et Harten et. al. [74], entre autres. Ces derniers sont connus pour avoir défini le terme «schémas de type Godunov» pour une certaine classe de schémas projection/évolution qui utilisent une approximation du

problème de Riemann.

Étant donné que ces schémas ont une large applicabilité parce qu'ils reproduisent avec précision une grande partie de la physique, combiné avec le fait que la simulation numérique est de plus en plus importante et utilisé dans de nombreux domaines de recherche et de développement, il n'est donc pas surprenant que plusieurs versions des schémas de type Godunov aient été construits au cours des dernières années. Malgré leurs faiblesses inhérentes mentionnées par plusieurs auteurs comme Quirk (qui a énuméré et proposé comment surmonter certaines des lacunes constatées en [114, 115]) et malgré les défauts numériques qui parfois devient apparent en temps très long, les solveurs de type Godunov sont néanmoins connus pour être robustes et produisent des simulations de haute fidélité ; de manière générale, leurs avantages ont tendance à éclipser les inconvénients potentiels. En outre, étant donné la grande quantité de solveurs de Riemann approchés disponibles dans la littérature (en forte croissance dans l'industrie [115]) et leur simplicité sous-jacente, les méthodes volume finis de type Godunov sont très souvent utilisés pour les simulations de problèmes réels, dans des contextes variés comme la dynamique des fluides, [2, 3, 15, 23, 26, 50, 51, 54, 60, 64, 65, 89, 90, 92, 117, 129, 131, 145], la magnétohydrodynamique, [9, 10, 12, 45, 58, 61, 66, 72, 80, 97, 101, 107, 112, 124, 142, 141], parmi tant d'autres.

Notre objectif est donc de contribuer à la promotion des simulations numériques de problèmes du monde réel avec des solveurs de type Godunov. Des phénomènes physiques intéressants se produisent pendant la vie quotidienne avec une large gamme de scénarios, après avoir décrit les phénomènes comme des modèles mathématiques, la simulation numérique devient un outil essentiel. En effet, le calcul scientifique n'a pas pour objectif de remplacer la modélisation ni l'expérimentation, mais plutôt de travailler en synergie. Cependant, il y a plusieurs problèmes fondamentaux qui ne peuvent pas être considérés que par les outils de simulation numérique, en effet puisque l'expérimentation en laboratoire n'est pas toujours possible, voire impossible, comme en astrophysique. Cette branche de l'astronomie est assez large et sa recherche sur la nature des corps célestes, comme les étoiles ou les planètes, est constamment vérifiée par la simulation numérique. De manière surprenante, certaines des propriétés théoriques et des comportements intuitivement simples sont en fait très difficiles à reproduire par des outils numériques, par exemple, des solutions stationnaires. En physique stellaire, parmi d'autres, de nombreux écoulements gravitationnels atteignent états stables ou quasi-stables caractérisés par un équilibre entre les forces gravitationnelles et d'autres forces (comme des gradients de pression). Dans le contexte de simulations numériques, le traitement adéquat des termes sources qui permet de préserver des états discrets d'équilibre reste un défi (voir par exemple [55, 71, 82, 91]).

En règle générale, diverses observations des objets célestes et leurs émissions contribuent à une meilleure compréhension de l'univers. Un domaine de recherche intéressant est celui des réactions de fusion nucléaire qui se produisent naturellement dans les étoiles actives (comme par exemple le Soleil [34]) et qui génèrent de l'énergie thermique

par fusion nucléaire des noyaux d'hydrogène en hélium. Plus généralement, la fusion nucléaire est le processus par lequel deux ou plusieurs noyaux atomiques entrent en collision à grande vitesse et fusionnent pour former un nouveau type de noyau atomique, libérant ou absorbant de l'énergie (la matière n'est pas conservée au cours du processus). Fort de cette connaissance, l'ambition de développer la fusion thermonucléaire contrôlée sur Terre pour la production d'énergie a conduit à l'élaboration du tokamak tout comme d'autres dispositifs de confinement intéressants. Le tokamak est un type de machine qui utilise des champs magnétiques pour confiner un plasma en forme de tore et qui est à base du projet international ITER [1] en cours. En effet, pour induire des réactions de fusion thermonucléaire à grande échelle, il est nécessaire d'avoir des températures et des densités extrêmement élevées. Comme les plasmas sont constitués d'électrons et d'ions qui se déplacent librement, ils peuvent être confinés en utilisant une combinaison de différents types de champs magnétiques (étant donné la propriété inhérente de la conductivité électrique des plasmas). Le confinement porte le plasma à températures suffisamment élevées qui rendent possible des réactions persistantes de fusion en cascade. En raison de la nécessité croissante de sources d'énergie alternatives et le potentiel en production d'énergie que représente la fusion par confinement magnétique, la recherche sur les tokamaks est en plein essor. Dans ce contexte la modélisation numérique et la simulation jouent un rôle de premier plan.

Dans le domaine de la physique des plasmas, le modèle magnétohydrodynamique (MHD) est utilisé pour traiter le plasma comme un seul fluide conducteur et décrit les phénomènes à l'échelle macroscopique, c'est à dire, que nous ne considérons pas les électrons et les ions séparément, mais comme un ensemble. Le besoin d'obtenir des solutions physiques et stables à ces équations hyperboliques, qui peuvent être écrites sous forme conservative, a conduit à l'élaboration de plusieurs schémas qui reproduisent avec une certaine fiabilité la dynamique de plasmas réels (ondes d'Alfvén, équilibres MHD, et lignes de champ magnétique «gelées»[42]). La formulation conservative des équations MHD permet l'utilisation de schémas de type Godunov pour leur résolution, tout en préservant la contrainte de divergence nulle sur le champ magnétique numérique. En conséquence, une série de stratégies pour assurer la contrainte de divergence nulle, combinées avec des schémas de type Godunov, ont été développées, [12, 45, 61, 97, 107, 112, 130]. Certains nécessitent des solveurs multidimensionnelles pour l'estimation adéquate de champs électriques décalés [52].

De nombreux problèmes de la physique des plasmas, non seulement dans le contexte de la fusion par confinement magnétique, mais aussi dans le domaine de l'astrophysique (comme les problèmes caractérisés par un champ de gravitation central, par exemple, les disques d'accrétion [93, 94], ou l'évolution de la nébuleuse protoplanétaire conduisant à la formation de planètes autour d'une jeune étoile [78]), se produisent dans un domaine spatial qui peut être représenté par un tore. D'un point de vue mathématique, même si les échelles spatiales et temporelles ne sont pas exactement les mêmes, ces problèmes peuvent être décrits par des systèmes d'équations ayant une structure commune et des

méthodes numériques similaires peuvent souvent être appliquées pour obtenir leurs so-
lutions approchées. En particulier, le choix d'une stratégie d'approximation adéquate
dépend fortement de la géométrie et de l'existence d'un champ de force intense régissant
la physique du problème. Dans ce contexte, les méthodes numériques doivent prendre
en compte tous les effets géométriques résultants de la présence de champs magnétiques
ou gravitationnelles mais aussi une forte anisotropie existant dans les écoulements.

Résumé

L'étude des phénomènes physiques divers a fait l'objet de nombreux travaux de recherche qui ont pour objectif de les reproduire numériquement. Après avoir décrit ces phénomènes comme des modèles mathématiques, la simulation numérique devient un outil essentiel et notre but est de contribuer à l'avancement des simulations de problèmes du monde réel avec des solveurs de type Godunov. Après une brève présentation de la théorie de base nécessaire des systèmes de lois de conservation, y compris les équations d'Euler et de la magnétohydrodynamique idéale, le chapitre se consacre au rappel des principaux aspects théoriques et numériques trouvés dans le cadre des schémas de type Godunov, comme le problème de Riemann et la reconstruction MUSCL qui sont des concepts fondamentaux de cette thèse.

Nous considérons dans un premier temps, un système hyperbolique de lois de conservation en deux dimensions, de la forme

$$\partial_t \boldsymbol{w} + \partial_x \boldsymbol{f}(\boldsymbol{w}) + \partial_y \boldsymbol{g}(\boldsymbol{w}) = 0,$$

et nous nous intéressons à l'approximation numérique de la solution du problème de Riemann bidimensionnel pour ce système à travers l'extension du formalisme HLL éprouvé en monodimensionnel. Le solveur numérique est alors constitué d'ondes planes séparant des états constants. Essentiellement, la généralisation multidimensionnelle des trois états 1D du solveur HLL conduit, inévitablement, à la construction d'un profil approché de propagation constitué d'états constants et représentatif de la complexité des interactions d'ondes associées au problème de Riemann multidimensionnel où la condition initiale est

$$\boldsymbol{w}(x,y,0) = \sum_{\substack{i=1,\ldots,N_x \\ j=1,\ldots,N_y}} \mathbf{w}_{i,j}^n \, \chi_{i,j}(x,y) \quad \text{with} \quad \chi_{i,j}(x,y) = \begin{cases} 1 & \text{si } (x,y) \in \mathcal{C}_{i,j}, \\ 0 & \text{si } (x,y) \notin \mathcal{C}_{i,j}. \end{cases}$$

Nous montrons d'abord comment l'état intermédiaire peut être obtenu par une intégration spatio-temporelle sur un modèle d'ondes spécifique. Ensuite, nous proposons d'utiliser la consistance avec la formulation intégrale à travers les relations de Rankine-Hugoniot afin d'obtenir des expressions du flux numérique assez simples à mettre en

œuvre. Ces relations de sauts s'écrivent sous la forme

$$[\![n_x f^{[\theta]} + n_y g^{[\theta]}]\!] = \sigma [\![w^{[\theta]}]\!], \quad \theta = 1, \ldots, \vartheta,$$

et conduisent à formuler les flux comme solution d'un système linéaire, en général sur-déterminé, dont le rang est égal au nombre d'inconnus. La méthode des moindres carrés permet de construire une solution qui défini la formulation approchée du problème de Riemann et des différents flux numériques

$$\widetilde{\boldsymbol{\phi}}_{x,i+\frac{1}{2},j+\frac{1}{2}}^{hll2D} = \widetilde{\boldsymbol{\phi}}_x^{hll2D}(\mathbf{w}_{i+1,j+1}^n, \mathbf{w}_{i,j+1}^n, \mathbf{w}_{i,j}^n, \mathbf{w}_{i+1,j}^n) = \sum_{(\mu\nu) \in \mathcal{L}_{i+\frac{1}{2},j+\frac{1}{2}}} \beta_{y,\mu\nu} \, \boldsymbol{f}_{\mu\nu}.$$

Les schémas numériques obtenus s'avèrent assez simples à mettre en œuvre, même pour des maillages non structurées. Nous présentons également quelques résultats numériques qui exposent la robustesse, l'isotropie et la stabilité des solveurs multidimensionnels sur des cas d'école de la littérature.

Ensuite, dans le chapitre 3, nous montrons l'importance de préserver numériquement la contrainte de divergence nulle du champ magnétique lors de l'exécution des simulations numériques de la MHD idéale. Au fil des ans, la simulation numérique de ces équations a joué un rôle important dans la recherche en physique des plasmas et la nécessité de trouver des solutions physiques et stables a conduit à l'élaboration de plusieurs schémas numériques, tout en préservant la contrainte de divergence nulle $\nabla \cdot \boldsymbol{B} = 0$. Pour des solutions lisses, cette contrainte est garantie par l'équation d'évolution du champ magnétique de manière que

$$\partial_t(\nabla \cdot \boldsymbol{B}) = 0.$$

Idéalement, lors de la réalisation de simulations numériques, nous voulons que cette équation particulière reste nulle à tout moment. Tel est le cas en une dimension, où la contrainte devient $\partial_x B_x = 0$ et l'équation d'évolution pour B_x est réduite à $\partial_t B_x(\cdot, t) = 0$ pour tout temps $t > 0$. Cependant, pour les écoulements multidimensionnels, Brackbill and Barnes [24] ont montré que des erreurs de discrétisation numériques ont un impact sur l'évolution dans le temps de la façon suivante:

$$\partial_t(\nabla \cdot \boldsymbol{B}) = 0 + \mathcal{O}\left((\Delta x)^m, (\Delta t)^n\right).$$

En conséquence, une série de stratégies pour assurer $\nabla \cdot \boldsymbol{B} = 0$ numériquement, combinées avec des schémas de type Godunov, ont été développées, [12, 45, 61, 97, 107, 112, 130]. Nous étudions la technique de «hyperbolic divergence cleaning» appliquée aux équations discrétisées sur une grille colocalisée et nous la comparons à la technique du transport contraint qui utilise une grille décalée pour maintenir cette propriété. En particulier, pour le premier, nous considérons la formulation GLM-MHD suggérée par Dedner et al. [45] où la contrainte de divergence et l'équation d'évolution du champ magnétique sont

remplacées par

$$\partial_t \boldsymbol{B} + \nabla \cdot (\boldsymbol{B} \otimes \boldsymbol{u} - \boldsymbol{u} \otimes \boldsymbol{B}) + \nabla \psi = 0, \tag{0.2}$$

$$\mathrm{D}(\psi) + \nabla \cdot \boldsymbol{B} = 0. \tag{0.3}$$

Pour la technique du transport contraint, le solveur Riemann 2D peut facilement être utilisé pour estimer le champ électrique aux coins du maillage :

$$E_{z,i+\frac{1}{2},j+\frac{1}{2}} = E_z^{hll2D}(\mathbf{w}_{i+1,j+1}, \mathbf{w}_{i,j+1}, \mathbf{w}_{i,j}, \mathbf{w}_{i+1,j}). \tag{0.4}$$

Les méthodes sont implémentées et des tests numériques sont présentés. Il est ainsi possible de comparer directement la robustesse et la précision des méthodes.

Le chapitre 4 concerne un problème important en astrophysique numérique. Certains écoulements gravitationnels en astrophysique sont modélisés par équations d'Euler avec des termes sources de gravité dérivant d'un potentiel dont l'évolution est décrite par une équation de Poisson (Euler-Poisson). Le modèle associé est décrit par le système d'équations aux dérivées partielles (EDP) suivant :

$$\begin{cases} \partial_t (\rho) + \nabla \cdot (\rho \boldsymbol{u}) = 0, \\ \partial_t (\rho \boldsymbol{u}) + \nabla \cdot (\rho \boldsymbol{u} \otimes \boldsymbol{u}) + \nabla p = -\rho \nabla \Phi, \\ \partial_t (\rho e) + \nabla \cdot ((\rho e + p) \boldsymbol{u}) = -\rho \boldsymbol{u} \cdot \nabla \Phi, \\ \Delta \Phi = 4\pi G \rho, \end{cases}$$

où $\rho > 0$ est la densité, $\mathbf{u} \in \mathbb{R}^d$ la vitesse, e l'énergie totale spécifique et ϕ le potentiel gravitationnel. La pression p est reliée aux variables précédentes par une équation d'état de la forme $p = p(\rho, \epsilon)$ avec $\epsilon = e - |\mathbf{u}|^2/2$ l'énergie interne spécifique. La constante gravitationnelle G est égale à $G = 6.67 \times 10^{-11} m^3 kg^{-1} s^{-2}$.

Ces écoulements développent des états d'équilibre autogravitationnels qu'il est nécessaire de préserver dans la formulation numérique. Dans le contexte de l'approche volumes finis, nous présentons ici un solveur de Riemann construit à partir d'un modèle de relaxation dans lequel la pression est une variable complémentaire [23, 83] et l'équation de Poisson est transformée en une équation hyperbolique avec un paramètre de pénalisation c_h. Le schéma est obtenu à la limite quand ce paramètre de pénalisation tend vers zéro [140] et devient

$$\mathbf{w}_i^{n+1} = \mathbf{w}_i^n - \frac{\Delta t}{\Delta x} \left(\boldsymbol{\phi}_{x,i+\frac{1}{2}}^l - \boldsymbol{\phi}_{x,i-\frac{1}{2}}^r \right),$$

où

$$\begin{aligned} \boldsymbol{\phi}_{x,i+\frac{1}{2}}^l &= \boldsymbol{\phi}_{x,i+\frac{1}{2}}^l (\rho_i^n, u_i^n, (\rho e)_i^n, \Phi_i^n, \rho_{i+1}^n, u_{i+1}^n, (\rho e)_{i+1}^n, \Phi_{i+1}^n) \\ &= \mathbf{f}_l \left(\boldsymbol{w}_\delta(\mathbf{w}_i^n), \boldsymbol{w}_\delta(\mathbf{w}_{i+1}^n) \right), \end{aligned}$$

$$\boldsymbol{\phi}^r_{x,i+\frac{1}{2}} = \boldsymbol{\phi}^r_{x,i+\frac{1}{2}}(\rho^n_i,\, u^n_i,\, (\rho e)^n_i,\, \Phi^n_i,\ \rho^n_{i+1},\, u^n_{i+1},\, (\rho e)^n_{i+1},\, \Phi^n_{i+1})$$
$$= \mathbf{f}_r\left(\boldsymbol{w}_\delta(\mathbf{w}^n_i), \boldsymbol{w}_\delta(\mathbf{w}^n_{i+1})\right),$$

avec $\boldsymbol{w}_\delta(\mathbf{w}^n_i) = (\mathbf{w}_\delta)^n_i$ défini selon l'équilibre de relaxation. Cette stratégie, mise en œuvre dans la plate-forme de calcul HERACLES [66], permet de préserver certains équilibres autogravitationnels et offre plus de robustesse numérique par rapport aux précédentes approches disponibles dans la plate-forme, comme celui des pas fractionnaires

$$\partial_t \boldsymbol{w} + \nabla \cdot \boldsymbol{\mathcal{F}}(\boldsymbol{w}) = 0,$$
$$\partial_t \boldsymbol{w} \qquad\qquad = -\boldsymbol{\mathcal{B}}(\boldsymbol{w})\nabla\Phi.$$

Enfin, le dernier chapitre s'attaque à la dérivation des méthodes volumes finis en coordonnées cylindriques pour les lois de conservation hyperboliques. De nombreux problèmes de physique des plasmas se produisent dans un domaine spatial pouvant être représenté par un tore

$$\hat{\Omega}^{\mathcal{T}}_{3d} = \bigcup_{\phi=0}^{2\pi} \hat{\Omega}_{2d}(\phi).$$

On pense aux problèmes d'astrophysique caractérisés par un champ de gravitation central : évolution de la nébuleuse protoplanétaire conduisant à la formation des planètes autour d'une jeune étoile [78]. Un autre exemple, d'une grande actualité concerne l'étude des plasmas magnétisés dans les futurs réacteurs de fusion.

Sur le plan mathématique, bien que les échelles d'espace et de temps soient évidemment très différentes, ces deux types de problèmes peuvent être décrits par des systèmes d'équation ayant une structure commune. De ce fait les problèmes d'approximation numériques sont largement communs à ces deux ensembles d'applications. En particulier la géométrie toroïdale et l'existence d'un champ de force intense pilotant l'essentiel de la physique va gouverner le choix des stratégies d'approximation. Celles-ci devront tenir compte des effets géométriques dus à ces champs de forces (magnétique ou gravitationnel) et des très fortes anisotropies des écoulements qui en découlent. En fait, nous avons étudié la bonne approximation de ces termes géométriques afin que toutes les propriétés de conservation du système soient conservées :

$$\frac{r_i}{|\hat{\Omega}_{i,j,k}|}\int_{\hat{\Omega}_{i,j,k}} \tilde{T}^{\phi\phi}(\boldsymbol{\xi})\,d\boldsymbol{\xi} = \tfrac{1}{2}(\tilde{T}^{\phi\phi}_{i,j+1/2,k} + \tilde{T}^{\phi\phi}_{i,j-1/2,k}) + c(\Delta\phi)(\tilde{T}^{\phi r}_{i,j+1/2,k} + \tilde{T}^{\phi r}_{i,j-1/2,k})$$
$$\frac{r_i}{|\hat{\Omega}_{i,j,k}|}\int_{\hat{\Omega}_{i,j,k}} \tilde{T}^{\phi r}(\boldsymbol{\xi})\,d\boldsymbol{\xi} = \tfrac{1}{2}(\tilde{T}^{\phi r}_{i,j+1/2,k} + \tilde{T}^{\phi r}_{i,j-1/2,k}) - c(\Delta\phi)(\tilde{T}^{\phi\phi}_{i,j+1/2,k} + \tilde{T}^{\phi\phi}_{i,j-1/2,k}),$$

où $c(x) = 1/x - \sin x/(2 - 2\cos x)$. La méthode a été appliquée pour simuler un écoulement hydrodynamique stable dans un tore rectangulaire tridimensionnel.

Riemann Problems and Godunov-Type Schemes

The purpose of this chapter is twofold: first, it aims to present the background and theoretical framework for numerical approximation techniques of the Euler and magnetohydrodynamic (MHD) equations in the context of Godunov-type methods, and second, it helps to standardize the notation and terminology that will be used consistently throughout this manuscript.

We begin our study by introducing the subject of systems of conservation laws, which is widely known and included here for completeness. Consider a system of ϑ conservation laws in d spatial dimensions

$$\partial_t \boldsymbol{w} + \nabla \cdot \boldsymbol{\mathcal{F}}(\boldsymbol{w}) = 0, \quad \text{in } \Omega_d \times (0,T), \tag{1.1a}$$

with $\boldsymbol{w} = (w^{[1]}, \ldots, w^{[\vartheta]})^T$ the state vector of conservative variables and $\boldsymbol{\mathcal{F}} = (\boldsymbol{f}_1, \ldots, \boldsymbol{f}_d)$ the flux tensor. The unknown $\boldsymbol{w} : \Omega_d \subset \mathbb{R}^d \times [0,T) \to \mathcal{V}$ is a function from space $\boldsymbol{x} \in \Omega_d$ and time t to the system's state space $\mathcal{V}$, and each flux in the ith spatial dimension is defined as $\boldsymbol{f}_i : \mathcal{V} \to \mathbb{R}^\vartheta$, for $i = 1, \ldots, d$. The numerical solution of such system, complemented with initial conditions of the form

$$\boldsymbol{w} = \boldsymbol{w}_0, \quad \text{on } \Omega_d \times \{t = 0\}, \tag{1.1b}$$

is of considerable interest for modeling diverse physical phenomena, such as in gas dynamics and plasma physics. For simplicity of presentation, we momentarily restrict ourselves to the case where $d = 1$ and denote the flux $\boldsymbol{f}_1$ by $\boldsymbol{f}$ such that

$$\begin{cases} \partial_t \boldsymbol{w} + \partial_x \boldsymbol{f}(\boldsymbol{w}) = 0, & \text{in } \Omega_1 \times (0,T), \\ \boldsymbol{w} = \boldsymbol{w}_0, & \text{on } \Omega_1 \times \{t = 0\}. \end{cases} \tag{1.2a} \\ \tag{1.2b}$$

Generally speaking, conservation laws are a class of homogenous hyperbolic equations, which in turn are a class of evolution equations (since partial differential equations can be viewed as evolution equations on an infinite-dimensional state space). System (1.2a) is said to be *hyperbolic* if the Jacobian matrix $\nabla_{\boldsymbol{w}} \boldsymbol{f}$ has real eigenvalues λ_θ and

each corresponding eigenvector $\mathbf{r}_\theta$ is linearly independent, for $\theta \in \{1, \dots, \vartheta\}$, and it is *strictly hyperbolic* if these eigenvalues are also distinct, i.e.,

$$\lambda_1(\boldsymbol{w}) < \dots < \lambda_\vartheta(\boldsymbol{w}). \tag{1.3}$$

Physically, eigenvalues represent speeds of wave propagation and also define characteristic fields, which are either *linearly degenerate* or *genuinely nonlinear* (see [23, 90, 129]). The former implies that

$$\nabla \lambda_\theta(\boldsymbol{w}) \cdot \mathbf{r}_\theta = 0 \quad \text{for all } \boldsymbol{w}, \tag{1.4}$$

where $\nabla \lambda_\theta$ is the gradient vector of λ_θ, namely, $\nabla \lambda_\theta = (\partial_{w^{[1]}} \lambda_\theta, \dots, \partial_{w^{[\vartheta]}} \lambda_\theta)^T$. In addition, a λ_θ-characteristic field is *genuinely nonlinear* if the following relation holds:

$$\nabla \lambda_\theta(\boldsymbol{w}) \cdot \mathbf{r}_\theta \neq 0 \quad \text{for all } \boldsymbol{w}. \tag{1.5}$$

1.1   Scalar Conservation Laws

System (1.2a) describes the conservation of the ϑ components associated with the state vector $\boldsymbol{w}$. Setting $\vartheta = 1$, we recover

$$\partial_t w + \partial_x f(w) = 0, \tag{1.6}$$

i.e., a first-order partial differential equation where w is the conserved quantity and $f(w)$ the flux. The term *conservation law*, which has hitherto been employed, can now be justified by integrating (1.6) over an interval $[x_a, x_b]$ that is fixed in time, to get

$$\frac{d}{dt} \int_{x_a}^{x_b} w(x,t) \, dx = f(w(x_a, t)) - f(w(x_b, t)), \tag{1.7}$$

or, in other words, the quantity $\int_{x_a}^{x_b} w(x,t) \, dx$ changes only due to fluxes at points x_a and x_b. It is then clear that this integral conservation law arises from physical principles, whereas the differential form (1.6) is derived from (1.7) under smoothness assumptions.

However, the method of characteristics shows that we cannot always expect a smooth solution of (1.6) for all times $t > 0$, even if the initial data (see [64, 90]) is smooth. For instance, let us consider Burgers' equation equipped with initial data

$$\begin{cases} \partial_t w + \partial_x (\frac{1}{2} w^2) = 0, \\ w(x, 0) = w_0(x), \end{cases} \tag{1.8}$$

and the curves $x(t)$, $w(x(t), t)$ that solve

$$\begin{cases} \dfrac{dx}{dt} = w(x, t), & x(y, 0) = x_0, \tag{1.9a} \\[2mm] \dfrac{dw}{dt} = 0, & w(y, 0) = w_0(y), \tag{1.9b} \end{cases}$$

where $x_0 \in \mathbb{R}$ is a base point. The integral curves $t \to x(x_0, t) = x_0 + w_0(x_0) t$ satisfying equation (1.9a) are called characteristics, along which the PDE becomes an ordinary

differential equation (ODE). It is well-known that for times $t > 0$, problem (1.9) may not have a unique solution as characteristics cross (see [53]). We note that this solution is implicit since x_0 depends on (x, t) and we write

$$w(x, t) = w_0(x - w_0(x_0) t). \tag{1.10}$$

1.1.1 Breakdown of Smooth Solutions

Focusing on the intersection of characteristics, we have mentioned that a smooth solution of (1.6) can break down at a finite time regardless of the initial data's nature, and thus, it is necessary to introduce (with the help of the theory of distributions) the concept of weak solutions that account for possible discontinuities.

Definition 1.1.1. *A function $w : \mathbb{R} \times \mathbb{R}^+ \to \mathbb{R}$ is a weak solution to the Cauchy Problem*

$$\begin{cases} \partial_t w + \partial_x f(w) = 0, \\ w(x, 0) = w_0(x), \end{cases} \tag{1.11}$$

if it holds

$$\int_{\mathbb{R}^+} \int_{\mathbb{R}} (w \, \partial_t \varphi + f(w) \, \partial_x \varphi) \, dx \, dt + \int_{\mathbb{R}} w_0(x) \, \varphi(x, 0) \, dx = 0. \tag{1.12}$$

for every $\mathcal{C}^1(\mathbb{R} \times \mathbb{R}^+)$ function φ with compact support.

The solutions of (1.11) are not necessarily unique, since it is possible to construct infinitely many weak solutions from particular initial data. It is therefore necessary to introduce some admissibility conditions and we start with the *entropy condition* that is motivated by the second principle of thermodynamics, hence its name. This principle basically tells us that non-smooth flows of gas dynamics are irreversible.

Definition 1.1.2. *A $\mathcal{C}^1$ function $\eta : \mathbb{R} \to \mathbb{R}$ is an entropy for (1.6) if it is convex and there exists a $\mathcal{C}^1$ function $q : \mathbb{R} \to \mathbb{R}$ such that*

$$\eta'(w) \, f'(w) = q'(w), \tag{1.13}$$

for every $w \in \mathbb{R}$. The function q is called an entropy flux for η and the pair (η, q) is said to be an entropy-entropy flux pair for (1.6).

Definition 1.1.3. *A weak solution w is called entropy satisfying if*

$$\int_{\mathbb{R}^+} \int_{\mathbb{R}} (\eta(w) \, \partial_t \varphi + q(w) \, \partial_x \varphi) \, dx \, dt \leq - \int_{\mathbb{R}} \eta(w_0(x)) \, \varphi(x, 0) \, dx \tag{1.14}$$

for every $\mathcal{C}^1$ function $\varphi \geq 0$ with compact support in $\mathbb{R} \times \mathbb{R}^+$ and for every entropy-entropy flux pair (η, q).

Therefore, the weak entropy inequality helps us choose the physically relevant one among all of the weak solutions. Now, we consider a function w with a jump of the form

$$w(x, t) = \begin{cases} w_l & \text{if } x < st, \\ w_r & \text{if } x > st, \end{cases} \tag{1.15}$$

being s the slope of a discontinuity in the (t, x) plane. The function w in (1.15) is then a solution of (1.6) if and only if

$$s(w_r - w_l) = f(w_r) - f(w_l). \tag{1.16}$$

This condition is known as the *Rankine-Hugoniot condition* and characterizes the discontinuities that may appear in the weak solutions to (1.6).

1.1.2 Scalar Riemann Problem in One Dimension

A one-dimensional *Riemann problem* for scalar conservation laws is a Cauchy problem (1.11) with initial data

$$w_0(x) = w_l \mathcal{H}(x) + w_r \mathcal{H}(-x), \tag{1.17}$$

where $\mathcal{H}(x)$ is the classical Heavisde function; we then seek for unique, admissible solutions of (1.11,1.17). For a uniformly convex flux function f, these solutions may be of two kinds: *rarefaction waves* and *shock waves* (see Figure 1.1).

- If $w_l < w_r$, the solution has a rarefaction wave and $w(x, t)$ is defined as

$$w(x,t) = \begin{cases} w_l & \text{if } x < f'(w_l) t, \\ (f')^{-1}(\frac{x}{t}) & \text{if } f'(w_l) t < x < f'(w_r) t, \\ w_r & \text{if } x > f'(w_r) t. \end{cases} \tag{1.18}$$

- If $w_r < w_l$, the solution contains a shock curve of speed s, which can be found by means of the Rankine-Hugoniot condition (1.16), and $w(x, t)$ is given by (1.15).

1.1.3 Vanishing Viscosity

Before proceeding with the governing equations that are considered in this manuscript, we wish to present a way to justify the conditions discussed in Section 1.1.1. In reality, the conservation law (1.6) describes an idealized process obtained in the limit $\varepsilon = 0$ of the viscous equation

$$\partial_t w + \partial_x f(w) = \varepsilon \partial_x^2 w, \tag{1.19}$$

which is parabolic according to the standard PDE classification. The term in the right-hand side of the above equation corresponds to viscosity or diffusion and ε is normally a small parameter. Thus, having $\varepsilon > 0$, it can be proved that (1.19) has a unique solution for any initial data and for all times $t > 0$: away from a shock, the second derivative term is bounded and the viscosity is negligible; near a shock, the derivatives of w start to blow up and the right-hand side term of equation (1.19) becomes important (see, for instance, [92]). It is clear that by modeling shock waves as sharp discontinuities and by setting $\varepsilon = 0$, we are then in need of additional conditions, i.e., those of Section 1.1.1.

1.2 Systems of Conservation Laws: Governing Equations

In the context of systems of conservation laws (1.1), we are particularly interested in relations that govern the motions of compressible, inviscid fluids and in those that model the dynamics of perfectly conducting, inviscid plasma, i.e., our main interest lies on the Euler and ideal magnetohydrodynamic (MHD) equations, respectively.

1.2.1 Euler Equations

Due to their known importance in applications, we first consider the Euler equations for inviscid compressible gas flows, given by the following system of nonlinear hyperbolic partial differential equations:

$$\begin{cases} \partial_t(\rho) \quad + \nabla \cdot (\rho \boldsymbol{u}) \qquad\qquad = 0, \\ \partial_t(\rho \boldsymbol{u}) + \nabla \cdot (\rho \boldsymbol{u} \otimes \boldsymbol{u}) + \nabla p = 0, \\ \partial_t(\rho e) \quad + \nabla \cdot ((\rho e + p)\boldsymbol{u}) \quad = 0, \end{cases} \tag{1.20}$$

where $\rho > 0$ is the density, $\boldsymbol{u} \in \mathbb{R}^d$ the velocity, and $e = \epsilon + |\boldsymbol{u}|^2/2$ the specific total energy. In order to close system (1.20), we introduce an equation of state of the form

$$p = p(\rho, \epsilon), \tag{1.21}$$

to relate the thermodynamic pressure p with both density ρ and specific internal energy (denoted ϵ). Unless stated otherwise, the ideal equation of state

$$p = (\gamma - 1)\rho\epsilon, \tag{1.22}$$

is assumed. The adiabatic index $\gamma = c_p/c_v$ is the ratio of heat capacity at constant pressure and volume, respectively, and its common value of 1.4 corresponds to the heat capacity ratio of terrestrial air.

Let us note that system (1.20) can be easily be put in compact form (1.1a), by casting the pressure gradient as a divergence, i.e., $\nabla p = \nabla \cdot (p\mathbf{I})$ with $\mathbf{I}$ the identity matrix. For the moment, let u_i denote the components of the velocity $\boldsymbol{u}$ and x_i those of the space vector $\boldsymbol{x}$. Employing Einstein notation where a repeated index i appearing in a term implies summation of that term over $i = 1, \ldots, 3$ $(d = 3)$, we are able to rewrite the Euler equations (1.20) as

$$\begin{cases} \partial_t(\rho) \quad + \partial_{x_j}(\rho u_j) \qquad\qquad = 0, \\ \partial_t(\rho u_i) + \partial_{x_j}(\rho u_i u_j) + \partial_{x_i} p = 0, \\ \partial_t(\rho e) \quad + \partial_{x_j}((\rho e + p)u_j) \quad = 0, \end{cases} \tag{1.23}$$

which in compact form becomes

$$\partial_t(\boldsymbol{w}) + \partial_{x_i} \boldsymbol{f}_i(\boldsymbol{w}) = 0, \tag{1.24}$$

with

$$\boldsymbol{w} = \begin{pmatrix} \rho \\ \rho u_1 \\ \rho u_2 \\ \rho u_3 \\ \rho e \end{pmatrix}, \quad \boldsymbol{f}_i(\boldsymbol{w}) = \begin{pmatrix} \rho u_i \\ \rho u_i u_1 + p\,\delta_{i1} \\ \rho u_i u_2 + p\,\delta_{i2} \\ \rho u_i u_3 + p\,\delta_{i3} \\ (\rho e + p)u_i \end{pmatrix}, \quad i = 1, 2, 3, \tag{1.25}$$

where δ_{ij} is the Kronecker delta. In quasilinear form, system (1.24) is

$$\partial_t(\boldsymbol{w}) + \boldsymbol{A}_i(\boldsymbol{w})\, \partial_{x_i} \boldsymbol{w} = 0, \tag{1.26}$$

being $\boldsymbol{A}_i(\boldsymbol{w}) = \partial_{\boldsymbol{w}} \boldsymbol{f}_i(\boldsymbol{w})$ the Jacobian matrix of the ith flux vector, from which we expect to analyze its eigenstructure to determine the hyperbolic property of system (1.24).

Definition 1.2.1. *System* (1.24) *is called hyperbolic if any combination of the form* $\boldsymbol{A} = \sum_{i}^{d} \alpha_i \boldsymbol{A}_i$, *where* $\boldsymbol{A}_i(\boldsymbol{w}) = \partial_{\boldsymbol{w}} \boldsymbol{f}_i(\boldsymbol{w})$ *and* $\boldsymbol{\alpha} = (\alpha_1, \dots, \alpha_d) \in \mathbb{R}^d \setminus \{0\}$, *is diagonalizable with* ϑ *real eigenvalues. Additionally, if these* ϑ *eigenvalues are distinct, system* (1.24) *is called strictly hyperbolic.*

1.2.1.1   Properties and Characteristic Structure

Here, we study a few basic properties of the three-dimensional, time-dependent Euler equations and we begin by looking at the matrix $\boldsymbol{A}_1(\boldsymbol{w})$, its eigenvalues and the associated right eigenvectors. Thus, the Jacobian matrix of the flux $\boldsymbol{f}_1(\boldsymbol{w})$ is given by

$$\boldsymbol{A}_1(\boldsymbol{w}) = \begin{pmatrix} 0 & 1 & 0 & 0 & 0 \\ \hat{\gamma}H - u_1^2 - c^2 & (3-\gamma)u_1 & -\hat{\gamma}u_2 & -\hat{\gamma}u_3 & \hat{\gamma} \\ -u_1 u_2 & u_2 & u_1 & 0 & 0 \\ -u_1 u_3 & u_3 & 0 & u_1 & 0 \\ \frac{1}{2}u_1[(\gamma-3)H - c^2] & H - \hat{\gamma}u_1^2 & -\hat{\gamma}u_1 u_2 & -\hat{\gamma}u_1 u_3 & \gamma u_1 \end{pmatrix}, \qquad (1.27)$$

with $\hat{\gamma} = \gamma - 1$, and expressed in terms of the total specific enthalpy

$$H = \tfrac{1}{\rho}(\rho e + p) = \tfrac{1}{2}|\boldsymbol{u}|^2 + \tfrac{1}{\gamma-1} c^2, \qquad (1.28)$$

and the speed of sound c satisfying $c^2 = \partial_\rho p(\rho, \epsilon) + \frac{1}{\rho^2} p(\rho, \epsilon) \partial_\epsilon p(\rho, \epsilon) > 0$. A direct computation yields the eigenvalues of the above matrix (1.27), i.e.,

$$\lambda_- = u_1 - c, \quad \lambda_u^1 = \lambda_u^2 = \lambda_u^3 = u_1, \quad \lambda_+ = u_1 + c, \qquad (1.29)$$

with the matrix of corresponding right eigenvectors defined as

$$\boldsymbol{K}_1(\boldsymbol{w}) = \begin{pmatrix} 1 & 1 & 0 & 0 & 1 \\ u_1 - c & u_1 & 0 & 0 & u_1 + c \\ u_2 & u_2 & 1 & 0 & u_2 \\ u_3 & u_3 & 0 & 1 & u_3 \\ H - u_1 c & \frac{1}{2}|\boldsymbol{u}|^2 & u_2 & u_3 & H + u_1 c \end{pmatrix}. \qquad (1.30)$$

Similar expressions can be found for $\boldsymbol{A}_2(\boldsymbol{w})$ and $\boldsymbol{A}_3(\boldsymbol{w})$ noting that the Euler equations are symmetric to cyclic permutation of the indices. Moreover, they satisfy the important property of rotational invariance stated in the following proposition:

Proposition 1.2.2. *The three-dimensional Euler equations are rotationally invariant, i.e., they satisfy the property*

$$\cos \phi^y \cos \phi^z \, \boldsymbol{f}_1(\boldsymbol{w}) + \cos \phi^y \sin \phi^z \, \boldsymbol{f}_2(\boldsymbol{w}) + \sin \phi^y \boldsymbol{f}_3(\boldsymbol{w}) = \boldsymbol{O}^{-1} \boldsymbol{f}_1(\boldsymbol{O}\boldsymbol{w}) \qquad (1.31)$$

for all angles ϕ^y and ϕ^z and state vectors $\boldsymbol{w}$; $\boldsymbol{O} \equiv \boldsymbol{O}(\phi^y, \phi^z)$ is the rotation matrix

$$\boldsymbol{O} = \begin{pmatrix} 1 & 0 & 0 & 0 & 0 \\ 0 & \cos\phi^y \cos\phi^z & \cos\phi^y \sin\phi^z & \sin\phi^y & 0 \\ 0 & -\sin\phi^z & \cos\phi^z & 0 & 0 \\ 0 & -\sin\phi^y \cos\phi^z & -\sin\phi^y \sin\phi^z & \cos\phi^y & 0 \\ 0 & 0 & 0 & 0 & 1 \end{pmatrix}, \tag{1.32}$$

which is the product of two rotation matrices, namely $\boldsymbol{O}(\phi^y, \phi^z) = \boldsymbol{O}_y(\phi^y)\boldsymbol{O}_z(\phi^z)$, where

$$\boldsymbol{O}_y = \begin{pmatrix} 1 & 0 & 0 & 0 & 0 \\ 0 & \cos\phi^y & 0 & \sin\phi^y & 0 \\ 0 & 0 & 1 & 0 & 0 \\ 0 & -\sin\phi^y & 0 & \cos\phi^y & 0 \\ 0 & 0 & 0 & 0 & 1 \end{pmatrix}, \quad \boldsymbol{O}_z = \begin{pmatrix} 1 & 0 & 0 & 0 & 0 \\ 0 & \cos\phi^z & \sin\phi^z & 0 & 0 \\ 0 & -\sin\phi^z & \cos\phi^z & 0 & 0 \\ 0 & 0 & 0 & 1 & 0 \\ 0 & 0 & 0 & 0 & 1 \end{pmatrix}.$$

Additional details about this property and related ones can be found in [21]. Now, we wish to briefly comment on the structure of the Riemann problem solution for system (1.20), which can be described as a set (with cardinality ϑ) of the three elementary waves depicted in Figure 1.1, i.e., rarefactions, shock waves and contact discontinuities. The latter, sometimes called *entropy waves* since they carry a jump in the entropy, are linearly degenerate characteristics (1.4). The exact solution of the Riemann problem for the Euler equations typically consists of one contact discontinuity and $d-1$ shear waves (associated to the multiplicity of the eigenvalue λ_u), and two nonlinear waves corresponding to the first and ϑth characteristic fields. The type of these genuinely nonlinear waves, also referred to as *acoustic waves*, is determined given the nature of the initial left and right states (for which we refer, for instance, to Section 1.1.2).

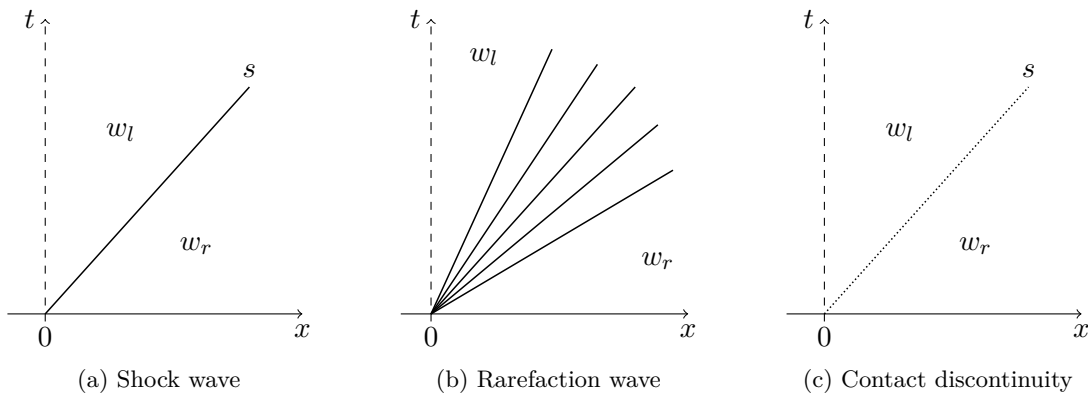(a) Shock wave   (b) Rarefaction wave   (c) Contact discontinuity

FIGURE 1.1. Elementary wave solutions of the Riemann problem for the (nonlinear hyperbolic) system of Euler equations.

The structure of the *similarity* solution (a term introduced later in Section 1.3.1) is roughly the same in three dimensions as in the one- or two-dimensional cases. The pressure p and normal velocity component u_i are both constant across the middle wave; from inspection of (1.30), one is able to deduce the following: across the contact discontinuity, the density has a jump, and across each shear wave, the respective tangential particle velocity changes discontinuously. With regard to the genuinely nonlinear characteristics, both tangential velocity components remain constant across the corresponding waves, irrespective of their type.

Basically, finding the solution of the Riemann problem for the three-dimensional Euler equations is straightforward if one knows that of the one-dimensional case and properly models the behavior of the "additional" velocity variables. Godunov is credited with developing the first exact Riemann solver in [65], for which several improvements were later proposed by Chorin [35] and Van Leer [137], among others; another interesting and efficient Riemann solver for perfect gases is that of Gottlieb and Groth [67]. More recent solvers include those of Schleicher [121] and Saurel et al. [120], for example. Approximate Riemann solvers (see Section 1.3.1) have also been proposed and several interesting works include those of Harten et al. [74], Roe [117, 118], Einfeldt [50], Chalons and Coulombel [29], Xing and Shu [149] naming few since the list is vast. Regardless of whether an exact solution or an approximated one is proposed, the associated scheme should be constructed with the purpose of numerically solving or simulating real-world phenomena, such as the shock-tube problem [37] or Sedov explosion [123].

1.2.2   Magnetohydrodynamics (MHD) Equations

The governing equations of magnetohydrodynamics are used to model electrically conducting fluid flows in the presence of magnetic fields. Given that numerical simulations of these equations have played a significant role in plasma research over the years, we must understand what these equations are like in a general sense and why they are useful to describe the evolution of plasmas (among other fluids) at a macroscopic level.

1.2.2.1   Derivation of the Ideal MHD Equations

The general field of MHD was initiated by H. Alfvén and consists of the study of electrically conducting fluid dynamics, as the analysis of the word *magnetohydrodynamics* (*magneto*→magnetic field, *hydro*→ liquid, and *dynamics*→movement) suggests. The simplest form of MHD, i.e., ideal MHD, models the plasma as an inviscid perfect conductor and its equations are a set of nonlinear hyperbolic equations in conservation form, given by

$$
\begin{cases}
\partial_t\left(\rho\right) & + \nabla \cdot \left(\rho \boldsymbol{u}\right) & = 0, & \text{(1.33a)} \\
\partial_t\left(\rho \boldsymbol{u}\right) + \nabla \cdot \left(\rho \boldsymbol{u} \otimes \boldsymbol{u}\right) + \nabla(p + \tfrac{1}{2}\boldsymbol{B}\cdot\boldsymbol{B}) - \nabla \cdot \left(\boldsymbol{B} \otimes \boldsymbol{B}\right) & = 0, & \text{(1.33b)} \\
\partial_t\left(\rho e\right) & + \nabla \cdot \left(\left(\rho e + p + \tfrac{1}{2}\boldsymbol{B}\cdot\boldsymbol{B}\right)\boldsymbol{u} - \left(\boldsymbol{u}\cdot\boldsymbol{B}\right)\boldsymbol{B}\right) & = 0, & \text{(1.33c)} \\
\partial_t\left(\boldsymbol{B}\right) & + \nabla \cdot \left(\boldsymbol{B} \otimes \boldsymbol{u} - \boldsymbol{u} \otimes \boldsymbol{B}\right) & = 0, & \text{(1.33d)}
\end{cases}
$$

where ρ and $\boldsymbol{u}$ are the fluid density and velocity as in the Euler equations (Section 1.2.1), and $\boldsymbol{B} = (B_x, B_y, B_z)$ is a new variable representing the magnetic field. Moreover, this

magnetic field satisfies the constraint

$$\nabla \cdot \boldsymbol{B} = 0, \tag{1.34}$$

a property that will be thoroughly discussed in Chapter 3. The total energy density ρe and the thermal pressure p are related through the ideal gas law

$$p = (\gamma - 1)\left(\rho e - \tfrac{1}{2}\rho\,\boldsymbol{u}\cdot\boldsymbol{u} - \tfrac{1}{2}\boldsymbol{B}\cdot\boldsymbol{B}\right), \tag{1.35}$$

completing the set of equations. Note that the evolution equation for the magnetic field (1.33d) is conveniently written in divergence form and it comes from Faraday's law:

$$\partial_t \boldsymbol{B} + \nabla \times \boldsymbol{E} = 0, \tag{1.36}$$

with the electric field $\boldsymbol{E}$ given by the ideal Ohm's law

$$\boldsymbol{E} = -\boldsymbol{u} \times \boldsymbol{B}. \tag{1.37}$$

Following this line of thought and for the sake of completeness, let us briefly specify all equations of system (1.33) in a point-by-point manner:

- **Conservation of mass**
  The continuity equation (1.33a) simply states that mass of a plasma is conserved.

- **Conservation of momentum**
  The full momentum equation in differential form is

$$\partial_t(\rho\boldsymbol{u}) + \nabla \cdot (\rho\boldsymbol{u} \otimes \boldsymbol{u} + p\mathbf{I}) = \boldsymbol{J} \times \boldsymbol{B} - \rho g\,\boldsymbol{e}_n, \tag{1.38}$$

  being $\boldsymbol{J}$ the current density and $\rho g\,\boldsymbol{e}_n$ a source term, where g is a constant gravity acceleration in the direction $\boldsymbol{e}_n$. The Lorentz force $\boldsymbol{J} \times \boldsymbol{B}$ exerted by the magnetic field can be expanded by substituting the current density with

$$\boldsymbol{J} = \nabla \times \boldsymbol{B}, \tag{1.39}$$

  i.e., Ampere's Law under the assumption of ideal magnetohydrodynamics, to obtain the semi-conservative relation

$$\partial_t(\rho\boldsymbol{u}) + \nabla \cdot (\rho\boldsymbol{u} \otimes \boldsymbol{u} + (p + \tfrac{1}{2}\boldsymbol{B}\cdot\boldsymbol{B})\mathbf{I} - \boldsymbol{B} \otimes \boldsymbol{B}) = -\boldsymbol{B}(\nabla \cdot \boldsymbol{B}) - \rho g\boldsymbol{e}_n. \tag{1.40}$$

  The above relation without the gravity source term yields (1.33b), having considered the divergence constraint (1.34).

- **Conservation of energy density**
  Temporarily denoting by $(\rho e)^{hd}$ the hydrodynamic energy density of an ideal gas so that $(\rho e)^{hd} = p/(\gamma - 1) + \tfrac{1}{2}\rho|\boldsymbol{u}|^2$, one writes its conservation in the form

$$\partial_t(\rho e)^{hd} + \nabla \cdot (((\rho e)^{hd} + p)\,\boldsymbol{u}) = \boldsymbol{J} \cdot (\boldsymbol{B} \times \boldsymbol{u}). \tag{1.41}$$

For the right-hand side of the above expression, which represents a change in energy due to the presence of $\boldsymbol{B}$, one can utilize once more Ampere's law (1.39) and standard vector identities to obtain

$$\boldsymbol{J} \cdot (\boldsymbol{B} \times \boldsymbol{u}) = (\boldsymbol{B} \cdot \partial_t \boldsymbol{B} - (\boldsymbol{u} \cdot \boldsymbol{B})(\nabla \cdot \boldsymbol{B}) - \nabla \cdot ((\boldsymbol{B} \cdot \boldsymbol{B}) \boldsymbol{u}) - (\boldsymbol{u} \cdot \boldsymbol{B}) \boldsymbol{B}). \qquad (1.42)$$

Now, defining the total energy density of the plasma by $\mathcal{E} = \rho e = (\rho e)^{hd} + \frac{1}{2}|\boldsymbol{B}|^2$, the conservation of this term can be written as

$$\partial_t (\rho e) + \nabla \cdot ((\rho e + p + \tfrac{1}{2}\boldsymbol{B} \cdot \boldsymbol{B}) \boldsymbol{u} - (\boldsymbol{u} \cdot \boldsymbol{B}) \boldsymbol{B}) = -(\boldsymbol{u} \cdot \boldsymbol{B})(\nabla \cdot \boldsymbol{B}), \qquad (1.43)$$

and with gravity source terms as

$$\partial_t (\rho e) + \nabla \cdot ((\rho e + p + \tfrac{1}{2}\boldsymbol{B} \cdot \boldsymbol{B}) \boldsymbol{u} - (\boldsymbol{u} \cdot \boldsymbol{B}) \boldsymbol{B}) = -(\boldsymbol{u} \cdot \boldsymbol{B})(\nabla \cdot \boldsymbol{B}) - \rho g(\boldsymbol{u} \cdot \boldsymbol{e}_n). \qquad (1.44)$$

■ **Evolution equation for the magnetic field vector**
Faraday's law (1.36) in integral form is

$$\frac{d}{dt} \int_{\mathcal{S}} \boldsymbol{B} \cdot d\boldsymbol{S} = -\oint_{\partial \mathcal{S}} \boldsymbol{E} \cdot d\boldsymbol{l}, \qquad (1.45)$$

where $\mathcal{S}$ is a surface bounded by the closed contour $\partial \mathcal{S}$. By using Stokes' theorem and the fact that $\boldsymbol{E}$ in the comoving frame is zero at infinite conductivity, one gets

$$\partial_t \boldsymbol{B} + \nabla \times (\boldsymbol{B} \times \boldsymbol{u}) = -\boldsymbol{u}(\nabla \cdot \boldsymbol{B}), \qquad (1.46)$$

and by employing equalities $\nabla \times (\boldsymbol{B} \times \boldsymbol{u}) = \nabla \cdot (\boldsymbol{B} \otimes \boldsymbol{u} - \boldsymbol{u} \otimes \boldsymbol{B})$ and $\nabla \cdot \boldsymbol{B} = 0$, one recovers (1.33d).

Summarizing the results found in the previous list, one is able to determine the ideal magnetohydrodynamic equations in semi-conservative form, namely,

$$\begin{cases} \partial_t (\rho) + \nabla \cdot (\rho \boldsymbol{u}) = 0, \\ \partial_t (\rho \boldsymbol{u}) + \nabla \cdot (\rho \boldsymbol{u} \otimes \boldsymbol{u} + (p + \tfrac{1}{2}\boldsymbol{B} \cdot \boldsymbol{B}) \mathbf{I} - \boldsymbol{B} \otimes \boldsymbol{B}) = -\boldsymbol{B}(\nabla \cdot \boldsymbol{B}) - \rho g \boldsymbol{e}_n, \\ \partial_t (\rho e) + \nabla \cdot ((\rho e + p + \tfrac{1}{2}\boldsymbol{B} \cdot \boldsymbol{B}) \boldsymbol{u} - (\boldsymbol{u} \cdot \boldsymbol{B}) \boldsymbol{B}) = -(\boldsymbol{u} \cdot \boldsymbol{B})(\nabla \cdot \boldsymbol{B}) - \rho g(\boldsymbol{u} \cdot \boldsymbol{e}_n), \\ \partial_t (\boldsymbol{B}) + \nabla \cdot (\boldsymbol{B} \otimes \boldsymbol{u} - \boldsymbol{u} \otimes \boldsymbol{B}) = -\boldsymbol{u}(\nabla \cdot \boldsymbol{B}). \end{cases}$$

In addition, by neglecting gravity in the above system, the resulting set of equations can be written in the following form:

$$\partial_t \begin{pmatrix} \rho \\ \rho \boldsymbol{u} \\ \rho e \\ \boldsymbol{B} \end{pmatrix} + \nabla \cdot \begin{pmatrix} \rho \boldsymbol{u} \\ \rho \boldsymbol{u} \otimes \boldsymbol{u} + \left(p + \tfrac{1}{2}\boldsymbol{B} \cdot \boldsymbol{B}\right) \mathbf{I} - \boldsymbol{B} \otimes \boldsymbol{B} \\ (\rho e + p + \tfrac{1}{2}\boldsymbol{B} \cdot \boldsymbol{B}) \boldsymbol{u} - (\boldsymbol{u} \cdot \boldsymbol{B}) \boldsymbol{B} \\ \boldsymbol{B} \otimes \boldsymbol{u} - \boldsymbol{u} \otimes \boldsymbol{B} \end{pmatrix} = -\begin{pmatrix} 0 \\ \boldsymbol{B} \\ \boldsymbol{u} \cdot \boldsymbol{B} \\ \boldsymbol{u} \end{pmatrix} \nabla \cdot \boldsymbol{B}, \qquad (1.47)$$

which is commonly known as the Godunov-Powell form of the ideal MHD equations [112, Eq.(14)]. Strictly speaking, since $\boldsymbol{B}$ satisfies the divergence-free property (1.34), the Godunov-Powell source terms disappear and one recovers (1.33); in practice, however, this is not always the case (a topic that will be further discussed in Chapter 3).

1.2.2.2 Characteristic Structure of Ideal MHD

The ideal MHD system (1.33) can be written in compact form (1.24) with

$$
\boldsymbol{w} = \begin{pmatrix} \rho \\ \rho u_1 \\ \rho u_2 \\ \rho u_3 \\ B_1 \\ B_2 \\ B_3 \\ \rho e \end{pmatrix}, \quad \boldsymbol{f}_i(\boldsymbol{w}) = \begin{pmatrix} \rho u_i \\ \rho u_i u_1 + P\,\delta_{i1} - B_i B_1 \\ \rho u_i u_2 + P\,\delta_{i2} - B_i B_2 \\ \rho u_i u_3 + P\,\delta_{i3} - B_i B_3 \\ u_i B_1 - B_i u_1 \\ u_i B_2 - B_i u_2 \\ u_i B_3 - B_i u_3 \\ (\rho e + P)u_i - (u_j B_j)B_i \end{pmatrix}, \quad i = 1,2,3, \tag{1.48}
$$

having employed once more Einstein notation and having defined $P = p + \frac{1}{2}\sum_i B_i^2$. In addition, given the vector of primitive variables $\boldsymbol{v} = (\rho, u_1, u_2, u_3, B_1, B_2, B_3, p)^T$, system (1.33) may be rewritten in quasilinear form

$$
\partial_t(\boldsymbol{v}) + \boldsymbol{A}_i(\boldsymbol{v})\,\partial_{x_i}\boldsymbol{v} = 0, \tag{1.49}
$$

with $\boldsymbol{A}_i(\boldsymbol{v}) = \partial_{\boldsymbol{v}}\boldsymbol{f}_i(\boldsymbol{v})$, e.g.,

$$
\boldsymbol{A}_1(\boldsymbol{v}) = \begin{pmatrix} u_1 & \rho & 0 & 0 & 0 & 0 & 0 & 0 \\ 0 & u_1 & 0 & 0 & -\frac{B_1}{\rho} & \frac{B_2}{\rho} & \frac{B_3}{\rho} & \frac{1}{\rho} \\ 0 & 0 & u_1 & 0 & -\frac{B_2}{\rho} & -\frac{B_1}{\rho} & 0 & 0 \\ 0 & 0 & 0 & u_1 & -\frac{B_3}{\rho} & 0 & -\frac{B_1}{\rho} & 0 \\ 0 & 0 & 0 & 0 & 0 & 0 & 0 & 0 \\ 0 & B_2 & -B_1 & 0 & -u_2 & u_1 & 0 & 0 \\ 0 & B_3 & 0 & -B_1 & -u_3 & 0 & u_1 & 0 \\ 0 & \gamma p & 0 & 0 & (\gamma-1)\boldsymbol{u}\cdot\boldsymbol{B} & 0 & 0 & u_1 \end{pmatrix}, \tag{1.50}
$$

which is clearly singular since the fifth row is zero. This leads to a zero eigenvalue that is non-physical and does not bode well numerically [112].

Given that in one-dimension ($d=1$) the evolution equation for B_1 is simply $\partial_t B_1 = 0$, it is common to define another matrix $\boldsymbol{A}'_1(\boldsymbol{v})$ by removing the fifth row and column of $\boldsymbol{A}_i(\boldsymbol{v})$ and thus assuming B_1 constant. The resulting matrix is diagonalizable with seven eigenvalues (see Figure 1.2) corresponding to one entropy wave, two Alfvén waves and four magneto-acoustic (two slow and two fast) waves traveling with speeds

$$
\lambda_4 = u_1, \quad \lambda_{2,6} = u_1 \mp c_a, \quad \lambda_{3,5} = u_1 \mp c_s, \quad \lambda_{1,7} = u_1 \mp c_f, \tag{1.51}
$$

respectively, where

$$
c_a = \frac{|B_1|}{\sqrt{\rho}} \quad \text{and} \quad c_{f,s}^2 = \frac{1}{2}\left(\frac{\gamma p + \boldsymbol{B}\cdot\boldsymbol{B}}{\rho} \pm \sqrt{\left(\frac{\gamma p + \boldsymbol{B}\cdot\boldsymbol{B}}{\rho}\right)^2 - 4\frac{\gamma p B_1^2}{\rho^2}} \right). \tag{1.52}
$$

All eigenvalues (1.51) are real, making the system of magnetohydrodynamic equations a hyperbolic one, and it is evident that

$$\lambda_1 \leq \lambda_2 \leq \lambda_3 \leq \lambda_4 \leq \lambda_5 \leq \lambda_6 \leq \lambda_7, \tag{1.53}$$

are satisfied. Note that these inequalities reveal that some eigenvalues may coincide, i.e., system (1.33) is not strictly hyperbolic, and consequently, the computation of the complete set of eigenvectors is not straightforward (see, for instance, the contribution of Brio and Wu [25] or that of Balsara [8]).
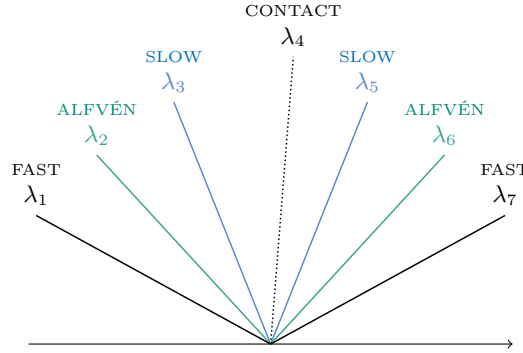

FIGURE 1.2. Structure of the solution of the Riemann problem for the MHD equations with the state variable defined as $\boldsymbol{w} = (\rho, \rho u_1, \rho u_2, \rho u_3, B_2, B_3, \rho e)^T$ and B_1 a constant.

Moreover, as the flux $\boldsymbol{f}_1$ is not convex in $\boldsymbol{w}$, compound waves and overcompressible shocks may be part of the solution to the Riemann problem for the MHD equations [25, 107]; we wish to mention that in Chapter 3, more references and details on numerical schemes for these equations are given. Now, given the complexity that this model presents, the concept of *an approximation to the Riemann problem* needs to be introduced.

1.3   Finite Volume Approximation

Here, we are interested in the numerical approximation of weak solutions to system (1.1). However, for simplicity of presentation, we once again restrict ourselves to the one-dimensional case and consider system (1.2) instead.

We start by discretizing the spatial domain into cells; thus, let us set a uniform numerical mesh with N_x cells $\mathcal{C}_i = (x_{i-1/2}, x_{i+1/2})$ of a determined width Δx, where $x_{i\pm1/2} = x_i \pm \Delta x/2$ (as depicted in Figure 1.3a). Henceforth, subscripts refer to spatial location, with cell centers denoted by integer subscripts $i = 1, \ldots, N_x$ and interfaces denoted by half integers. In a similar way, we discretize the time such that the temporal increment is given by Δt and $t^{n+1} = t^n + \Delta t$, for $n \in \mathbb{N}$.

Regardless of the initial data's nature in $\boldsymbol{w}_0$, a smooth solution to system (1.2) can break down at a finite time $t > 0$, such that it no longer satisfies the differential equations in the classical sense (recall Section 1.1.1). Hence, it is necessary to introduce the associated integral form to account for possible discontinuities. For any rectangle
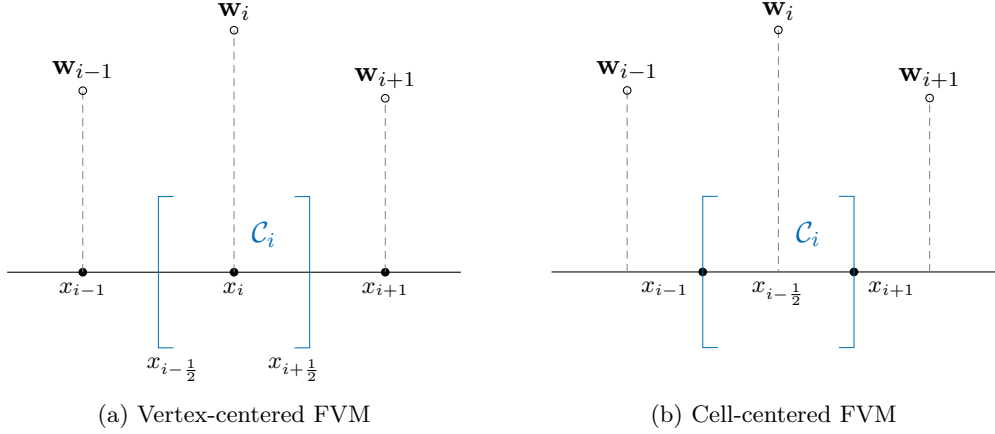
(a) Vertex-centered FVM (b) Cell-centered FVM

FIGURE 1.3. Difference between vertex-centered and cell-centered discretizations in the finite volume context.

$\mathcal{C}_i \times (t^n, t^{n+1})$, the integral of (1.2) over it becomes

$$\int_{\mathcal{C}_i} \boldsymbol{w}(x, t^{n+1})\, dx = \int_{\mathcal{C}_i} \boldsymbol{w}(x, t^n)\, dx + \int_{t^n}^{t^{n+1}} \boldsymbol{f}(\boldsymbol{w}(x_{i-\frac{1}{2}}, t))\, dt - \int_{t^n}^{t^{n+1}} \boldsymbol{f}(\boldsymbol{w}(x_{i+\frac{1}{2}}, t))\, dt, \tag{1.54}$$

which in the context of finite volume (FV) approximations, can then be expressed as

$$\mathbf{w}_i^{n+1} = \mathbf{w}_i^n - \frac{\Delta t}{\Delta x}\left(\boldsymbol{\phi}_{x, i+\frac{1}{2}} - \boldsymbol{\phi}_{x, i-\frac{1}{2}}\right), \tag{1.55}$$

where $\mathbf{w}_i^n$ is a cell-averaged value of $\boldsymbol{w}$ at time level t^n and $\boldsymbol{\phi}_{x, i\pm 1/2}$ are time-averaged numerical fluxes at $x = x_{i\pm 1/2}$, specifically

$$\mathbf{w}_i^n = \frac{1}{\Delta x} \int_{x_{i-\frac{1}{2}}}^{x_{i+\frac{1}{2}}} \boldsymbol{w}(x, t^n)\, dx, \tag{1.56}$$

$$\boldsymbol{\phi}_{x, i\pm\frac{1}{2}} = \frac{1}{\Delta t} \int_{t^n}^{t^{n+1}} \boldsymbol{f}(\boldsymbol{w}(x_{i\pm\frac{1}{2}}, t))\, dt. \tag{1.57}$$

Thus, the finite volume method is based on the integral form of the conservation laws rather than the differential one and relies on the fact that volume integrals containing a divergence term can be converted to surface integrals by applying the divergence theorem. Essentially, one finds average values of a solution $\boldsymbol{w}$ over each cell or *control volume* $\mathcal{C}_i$ and updates them to the next time step by employing the fluxes at the faces of the grid cells as in (1.55). The difficulty lies in finding adequate approximations to the terms $\boldsymbol{\phi}_{x, i\pm 1/2}$, since the exact evaluation of (1.57) is not always possible (or simple) to carry out.

We note that the mathematical formulation (1.55) cannot be considered a numerical scheme unless one specifies how to compute $\boldsymbol{\phi}_{x, i\pm 1/2}$. Since information for hyperbolic

problems propagates with finite speed, a reasonable approximation for $\phi_{x,i+1/2}$ may, for example, depend only on cell averages of $\boldsymbol{w}$ in the close neighborhood of the interface $x_{i+1/2}$, i.e., on $\mathbf{w}_i^n$ and $\mathbf{w}_{i+1}^n$ such that

$$\phi_{x,i+1/2} = \phi(\mathbf{w}_i^n, \mathbf{w}_{i+1}^n), \tag{1.58}$$

where ϕ is called a *numerical flux*. This leads to the three-point finite volume numerical method of the form

$$\mathbf{w}_i^{n+1} = \mathbf{w}_i^n - \frac{\Delta t}{\Delta x}\left(\phi_{x,i+\frac{1}{2}}(\mathbf{w}_i^n, \mathbf{w}_{i+1}^n) - \phi_{x,i-\frac{1}{2}}(\mathbf{w}_{i-1}^n, \mathbf{w}_i^n)\right), \tag{1.59}$$

which is conservative. Indeed, if we sum $\mathbf{w}_i^{n+1}$ (1.55) over any set of cells, we get

$$\sum_{i=I}^{J} \mathbf{w}_i^{n+1} = \sum_{i=I}^{J} \mathbf{w}_i^n - \frac{\Delta t}{\Delta x}\left(\phi_{x,J+\frac{1}{2}} - \phi_{x,I-\frac{1}{2}}\right), \tag{1.60}$$

and the total mass of $\boldsymbol{w}$ over (x_I, x_J) is conserved by the scheme.

Before proceeding with interesting ways to define the numerical flux function ϕ, let us briefly comment on another essential requirement that the FV numerical methods should satisfy: convergence. The numerical solution should converge to the true solution of the differential equation as one refines the grid [90], specifically, as Δt and Δx go to zero. Generally, this requires the method to be consistent with the differential form (approximating it well locally) and stable against small errors (meaning that errors stay bounded). Indeed, the numerical flux (1.58) is consistent if

$$\forall \bar{\boldsymbol{w}} \in \mathcal{V}, \quad \phi(\bar{\boldsymbol{w}}, \bar{\boldsymbol{w}}) = \boldsymbol{f}(\bar{\boldsymbol{w}}); \tag{1.61}$$

typically, some requirement of Lipschitz continuity is also made, namely

$$\exists L \in \mathbb{R}, \quad s.t. \quad |\phi(\mathbf{w}_i^n, \mathbf{w}_{i+1}^n) - \boldsymbol{f}(\bar{\boldsymbol{w}})| \leq L \max(|\mathbf{w}_i^n - \bar{\boldsymbol{w}}|, |\mathbf{w}_{i+1}^n - \bar{\boldsymbol{w}}|). \tag{1.62}$$

Furthermore, a necessary condition that must be satisfied by any FV method if one expects it to be stable and convergent is the *CFL condition* [38], named after Courant, Friedrichs and Lewy.

Definition 1.3.1 (CFL Condition). *A numerical method can be convergent only if its numerical domain of dependence contains the true domain of dependence of the PDE, at least in the limit as $\Delta x, \Delta t \to 0$.*

Moreover, we write down the Lax-Wendroff theorem, named after Peter Lax and Burton Wendroff, which states that if a conservative numerical scheme converges to some solution as the grid is refined, then that solution will be a weak solution of the associated hyperbolic system of conservation laws, see [90] for a detailed proof.

Theorem 1.3.2 (Lax and Wendroff [88]). *Consider a sequence of grids indexed by $j = 1, 2,...$ with mesh parameters $\Delta t^{(j)}$, $\Delta x^{(j)} \to 0$ as $j \to \infty$. Let $\mathrm{w}^{(j)}(x,t)$ denote the numerical approximation computed with a consistent and conservative method on the jth grid. Suppose that $\mathrm{w}^{(j)}$ converges to a function w as $j \to \infty$, i.e.,*

$$\|\mathrm{w}^{(j)} - w\|_p \to 0, \quad as \quad j \to \infty, \tag{1.63}$$

with $\|(\cdot)\|_p$ the usual L^p norm. Then $w(x,t)$ is a weak solution of the conservation law.

1.3.1 Godunov and Godunov-Type Schemes

In his seminal paper [65], Godunov introduced a novel numerical approach (1.55) that forms the basis of numerous interesting schemes. He aimed to express the numerical flux $\boldsymbol{\phi}_{x,i+1/2}$ in terms of neighboring values $\mathbf{w}_i$ and $\mathbf{w}_{i+1}$ by means of the associated Riemann problem (RP). Formally speaking, a Riemann problem for a system of conservation laws centered at $x = x_0$ is simply an initial-value problem

$$\partial_t \boldsymbol{w} + \partial_x \boldsymbol{f}(\boldsymbol{w}) = 0, \quad \boldsymbol{w}(x, t_0) = \begin{cases} \boldsymbol{w}_l & \text{if } x < x_0, \\ \boldsymbol{w}_r & \text{if } x > x_0, \end{cases} \tag{1.64}$$

which has a solution that depends only on the initial left and right states, respectively given by $\boldsymbol{w}_l$ and $\boldsymbol{w}_r$, and on the value $\xi = (x - x_0)/(t - t_0)$, $0 \le t_0 < t$. Thus, we denote an exact solution of (1.64) by $\boldsymbol{w}(\xi; \boldsymbol{w}_l, \boldsymbol{w}_r)$.

(a) Piecewise constant approximation   (b) Piecewise linear approximation
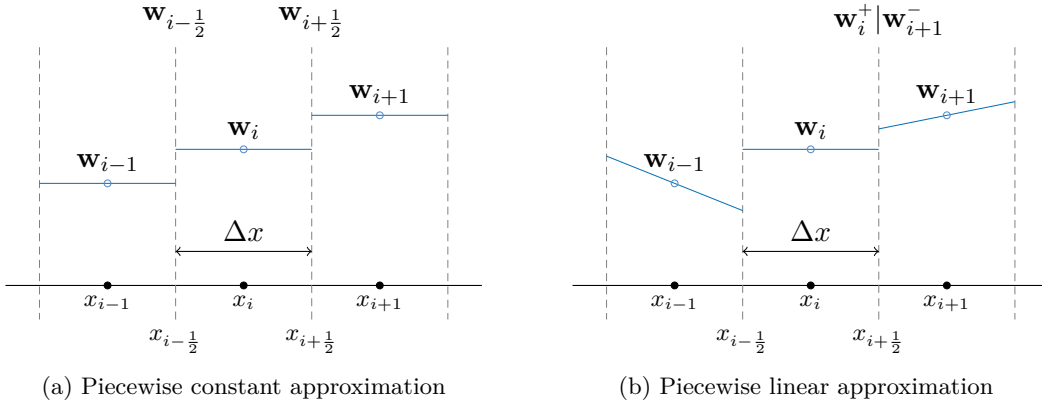
FIGURE 1.4. Piecewise constant and piecewise linear distributions of the conserved quantities over each cell $\mathcal{C}_i$.

Within the finite volume framework, Godunov's first-order method [65] assumes a piecewise constant distribution of the conserved quantities over each cell, see Figure 1.4a, and evolves it in time by solving a one-dimensional Riemann problem in the normal direction at each cell interface. Consequently, the value $\mathbf{w}_i^{n+1}$ is calculated in terms of the exact solutions of local Riemann problems in the following way:

$$\mathbf{w}_i^{n+1} = \frac{1}{\Delta x} \int_{x_{i-\frac{1}{2}}}^{x_i} \boldsymbol{w}_{i-\frac{1}{2}}(\xi) \, dx + \frac{1}{\Delta x} \int_{x_i}^{x_{i+\frac{1}{2}}} \boldsymbol{w}_{i+\frac{1}{2}}(\xi) \, dx, \tag{1.65}$$

where

$$\boldsymbol{w}_{i+\frac{1}{2}}(\xi) \equiv \boldsymbol{w}\left(\xi; \mathbf{w}_i^n, \mathbf{w}_{i+1}^n\right) \quad \text{with} \quad \xi = \frac{x - x_{i+1/2}}{\Delta t}, \tag{1.66}$$

which can also be written in conservative form (1.55) by defining the intercell numerical fluxes as

$$\boldsymbol{\phi}_{x,i-\frac{1}{2}} = \boldsymbol{f}(\boldsymbol{w}(0; \mathbf{w}_{i-1}^n, \mathbf{w}_i^n)) \quad \text{and} \quad \boldsymbol{\phi}_{x,i+\frac{1}{2}} = \boldsymbol{f}(\boldsymbol{w}(0; \mathbf{w}_i^n, \mathbf{w}_{i+1}^n)). \tag{1.67}$$

As was mentioned before, information for hyperbolic problems propagates with finite speed; therefore, we denote by $\lambda_{-,0}(\boldsymbol{w}_l, \boldsymbol{w}_r)$ and $\lambda_{+,0}(\boldsymbol{w}_l, \boldsymbol{w}_r)$ the smallest and largest signal speeds of the waves arising from the Riemann problem (1.64) centered at $x = x_0$. Thus, a necessary condition to prevent the interaction of solutions from local Riemann problems in (1.65) is the CFL condition

$$\Delta t \max_i \left(|\lambda_{-,i+\frac{1}{2}}(\mathbf{w}_i^n, \mathbf{w}_{i+1}^n)|, |\lambda_{+,i+\frac{1}{2}}(\mathbf{w}_i^n, \mathbf{w}_{i+1}^n)| \right) \leq \tfrac{1}{2}\Delta x. \tag{1.68}$$

The main drawback of Godunov's scheme results from computing the exact solution of each nonlinear Riemann problem, which has a direct impact on calculation cost. It is therefore necessary to consider an approximation $\boldsymbol{\mathcal{W}}(\xi; \boldsymbol{w}_l, \boldsymbol{w}_r)$ to the Riemann problem centered at $x = x_0$, which satisfies the consistency with the conservation law

$$\int_{x_l}^{x_r} \boldsymbol{\mathcal{W}}(\xi; \boldsymbol{w}_l, \boldsymbol{w}_r) \, dx = (x_r - x_0)\boldsymbol{w}_r + (x_0 - x_l)\boldsymbol{w}_l + (t - t^n)(\boldsymbol{f}_l - \boldsymbol{f}_r), \tag{1.69}$$

as long as the complicated structure of the exact solution $\boldsymbol{w}(\xi; \boldsymbol{w}_l, \boldsymbol{w}_r)$ is contained in the control volume $(x_l, x_r) \times (t^n, t^n + \Delta t)$, $x_l \leq x_0 \leq x_r$ and $0 \leq t^n$. For convenience, from this point on, we assume $t^n = 0$; also note that $\boldsymbol{f}_l = \boldsymbol{f}(\boldsymbol{w}_l)$ and $\boldsymbol{f}_r = \boldsymbol{f}(\boldsymbol{w}_r)$. Then, using the approximations $\boldsymbol{\mathcal{W}}(\xi; \boldsymbol{w}_l, \boldsymbol{w}_r)$, Harten et. al (refer to [74]) define a Godunov-type scheme as

$$\mathbf{w}_i^{n+1} = \frac{1}{\Delta x}\int_{x_{i-\frac{1}{2}}}^{x_i} \boldsymbol{\mathcal{W}}_{i-\frac{1}{2}}(\xi) \, dx + \frac{1}{\Delta x}\int_{x_i}^{x_{i+\frac{1}{2}}} \boldsymbol{\mathcal{W}}_{i+\frac{1}{2}}(\xi) \, dx. \tag{1.70}$$

By applying the integral conservation law (1.54) over $\mathcal{R}_l = (x_l, x_0) \times (0, \Delta t)$ and $\mathcal{R}_r = (x_0, x_r) \times (0, \Delta t)$, two fluxes along the t-axis are obtained

$$\boldsymbol{\phi}_l(\boldsymbol{w}_l, \boldsymbol{w}_r) = \boldsymbol{f}_l - \frac{1}{\Delta t}\int_{x_l}^{x_0} (\boldsymbol{\mathcal{W}}(\xi; \boldsymbol{w}_l, \boldsymbol{w}_r) - \boldsymbol{w}_l) \, dx, \tag{1.71a}$$

$$\boldsymbol{\phi}_r(\boldsymbol{w}_l, \boldsymbol{w}_r) = \boldsymbol{f}_r + \frac{1}{\Delta t}\int_{x_0}^{x_r} (\boldsymbol{\mathcal{W}}(\xi; \boldsymbol{w}_l, \boldsymbol{w}_r) - \boldsymbol{w}_r) \, dx, \tag{1.71b}$$

respectively. Consistency with the conservation law (1.69) ensures that $\boldsymbol{\phi}_l = \boldsymbol{\phi}_r$, so that the Godunov-type scheme can be written in the form (1.55) with

$$\boldsymbol{\phi}_{x,i+\frac{1}{2}} = \boldsymbol{\phi}_i(\mathbf{w}_i^n, \mathbf{w}_{i+1}^n) = \boldsymbol{\phi}_{i+1}(\mathbf{w}_i^n, \mathbf{w}_{i+1}^n). \tag{1.72}$$

The following theorem, due to Harten and Lax [Thm. 2.1][73] (see also, [74]), confirms that this type of approximation is consistent (the theorem's proof is in the same paper). Here, it also has the additional purpose of summarizing and completing the previous statements in a formal manner.

Theorem 1.3.3 (Harten and Lax)**.** *Let $\boldsymbol{\mathcal{W}}(\xi; \boldsymbol{w}_l, \boldsymbol{w}_r)$ be an approximation to the solution of the Riemann problem that satisfies the following conditions:*

1. consistency with the integral form of the conservation law in the sense that

$$\int_{-\Delta x/2}^{\Delta x/2} \boldsymbol{\mathcal{W}}(\xi; \boldsymbol{w}_l, \boldsymbol{w}_r) \, dx = \tfrac{1}{2}\Delta x(\boldsymbol{w}_r + \boldsymbol{w}_l) + \Delta t(\boldsymbol{f}_l - \boldsymbol{f}_r), \tag{1.73}$$

for $\Delta x/2 > \Delta t \max|\lambda_{\pm,0}(\boldsymbol{w}_l, \boldsymbol{w}_r)|$, where $\boldsymbol{f}_l = \boldsymbol{f}(\boldsymbol{w}_l)$ and $\boldsymbol{f}_r = \boldsymbol{f}(\boldsymbol{w}_r)$;

2. consistency with the integral form of the entropy condition in the sense that

$$\int_{-\Delta x/2}^{\Delta x/2} \boldsymbol{\eta}(\boldsymbol{\mathcal{W}}(\xi; \boldsymbol{w}_l, \boldsymbol{w}_r))\, dx \leq \tfrac{1}{2}\Delta x(\boldsymbol{\eta}_r + \boldsymbol{\eta}_l) + \Delta t(\boldsymbol{q}_l - \boldsymbol{q}_r), \qquad (1.74)$$

for $\Delta x/2 > \Delta t \max|\lambda_{\pm,0}(\boldsymbol{w}_l, \boldsymbol{w}_r)|$, where $\boldsymbol{q}_l = \boldsymbol{q}(\boldsymbol{w}_l)$ and $\boldsymbol{q}_r = \boldsymbol{q}(\boldsymbol{w}_r)$.

Using the approximation to the Riemann problem, one can define a Godunov-type scheme as follows:

$$\mathbf{w}_i^{n+1} = \frac{1}{\Delta x}\int_0^{\Delta x/2} \boldsymbol{\mathcal{W}}\left(\xi; \mathbf{w}_{i-1}^n, \mathbf{w}_i^n\right) dx + \frac{1}{\Delta x}\int_{-\Delta x/2}^0 \boldsymbol{\mathcal{W}}\left(\xi; \mathbf{w}_i^n, \mathbf{w}_{i+1}^n\right) dx. \qquad (1.75)$$

Assertion. *If the conditions (1.73) and (1.74) are satisfied, the scheme (1.75) is in conservation form consistent with (1.64), and satisfies the entropy inequality*

$$\boldsymbol{\eta}_i^{n+1} \leq \boldsymbol{\eta}_i^n - \frac{\Delta t}{\Delta x}\left(\boldsymbol{q}_{x,i+\frac{1}{2}} - \boldsymbol{q}_{x,i-\frac{1}{2}}\right). \qquad (1.76)$$

Finally, we add that Godunov proposed the general approach of the reconstruct-evolve-average (REA) algorithm as a means to solve the Euler equations of gas dynamics [65, 90]. In point of fact, all Godunov-type schemes (note that Godunov's scheme is technically of Godunov type) are based on this algorithm:

Algorithm 1.3.4 (REA). *Given the cell averages (1.56) at a time level t^n,*

1. **reconstruct** *a piecewise polynomial function from all cell averages,*

2. **evolve** *the hyperbolic equation (exactly or approximately) with the initial data defined in the previous step,*

3. **average** *the evolved solution over the grid cells to obtain new cell averages.*

Repeat the process in the next time step.

1.3.2 MUSCL Reconstruction

The MUSCL (Monotonic Upstream-centered Scheme for Conservation Laws) approach was introduced by van Leer through a series of contributions [133, 134, 135, 136, 137] with the objective of constructing highly accurate numerical solutions for nonlinear conservation laws. Actually, the term comes from the fourth paper of the series, where he succeeded in constructing the first high-order, total variation diminishing (TVD) scheme having second-order spatial accuracy. Total variation in a discrete sense is essentially $TV(\mathrm{w}^*) = \sum_i |\mathrm{w}_{i+1}^* - \mathrm{w}_i^*|$ and a numerical method is said to be TVD if

$$TV(\mathrm{w}^{n+1}) \leq TV(\mathrm{w}^n). \qquad (1.77)$$

Actually, the MUSCL methodology follows the REA algorithm described above, knowing that in order to achieve more than first-order accuracy, a "better" reconstruction than the piecewise constant one must be used for the first step. By constructing

piecewise linear functions from cell averages, the reconstruction of the unknown variables at the interfaces for a structured mesh is

$$\mathbf{w}_i^{n,\pm} = \mathbf{w}_i^n \pm \tfrac{1}{2}\sigma_i^n \Delta x, \tag{1.78}$$

as depicted in Figure 1.4b, such that

$$\mathbf{w}_i^{n+1} = \mathbf{w}_i^n - \frac{\Delta t}{\Delta x}\left(\boldsymbol{\phi}_{x,i+\frac{1}{2}}(\mathbf{w}_i^{n,+},\mathbf{w}_{i+1}^{n,-}) - \boldsymbol{\phi}_{x,i-\frac{1}{2}}(\mathbf{w}_{i-1}^{n,+},\mathbf{w}_i^{n,-})\right). \tag{1.79}$$

For second-order MUSCL approximations, it is necessary to limit the slopes σ_i^n of the reconstruction, which can be done using *slope limiters*. Indeed, a slope limiter is nothing more than a continuous function $L : \mathbb{R}^d \times \mathbb{R}^d \to \mathbb{R}^d$ that is bounded, i.e.,

$$\exists M \in \mathbb{R},\, M > 0, \quad \text{s.t.} \quad \|L(\sigma_l,\sigma_r)\| \leq M \max(\|\sigma_l\|,\|\sigma_r\|), \tag{1.80}$$

and satisfies the consistency condition in the sense that $L(\bar{\sigma},\bar{\sigma}) = \bar{\sigma}$, for every $\bar{\sigma} \in \mathbb{R}^d$. Once this limiter has been chosen, we redefine the slope as

$$\sigma_i^n = L\left(\frac{\mathbf{w}_i^n - \mathbf{w}_{i-1}^n}{\Delta x}, \frac{\mathbf{w}_{i+1}^n - \mathbf{w}_i^n}{\Delta x}\right). \tag{1.81}$$

In this thesis, we employ different limiters such as such as the MC limiter [136], minmod limiter [118] or the positive preserving limiter [127]; other interesting ones are the Superbee [118] and the van Leer [134] limiters, among others.

CHAPTER 2

A Simple 2D Extension of the HLL Riemann Solver for Gas Dynamics

Introduction

In the context of Godunov-type methods [65, 74], the one-dimensional (1D) theory has had many years to evolve and give rise to interesting and powerful approximate Riemann solvers that are applied at cell interfaces. For the one-dimensional case, these interfaces are simply vertices connecting two coarse cells and the corresponding Riemann problem can be solved exactly for the Euler equations with the ideal gas equation of state, even though approximate solutions are more commonly used in practice. Thanks to strict hyperbolicity and entropy dissipation in shocks, a key concept used in the one-dimensional analysis is the fact that weak solutions evolve in time toward a non-interacting scattering state (decay of Glimm's interaction potential, see [62, 63, 99]).

Now, consider that in two dimensions the interfaces are defined as collections of vertices connected by edges. The Riemann problems at the vertices are genuinely multidimensional (MultiD), involving interactions of more than two coarse data, whereas the Riemann problems associated with the cell edges are locally one-dimensional. In principle, a proper multidimensional approximation should take into account interactions of both 1D and MultiD Riemann problems. Unfortunately, even for the Euler equations with the ideal gas equation of state, an adequate approximation of multidimensional Riemann problems is a challenging problem [2, 3], especially given the complexity of the nonlinear interaction of wave patterns [87, 95, 151]. As a matter of fact, the corresponding MultiD solutions do not systematically provide a non-interacting scattering state because of these complicated effects.

Put in the simplified context of the Euler equations with the ideal equation of state, for the two-dimensional Riemann problem, even under the premise that each jump between neighboring initial states projects one planar wave consisting of a single shock, rarefaction or contact discontinuity, the number of allowable distinct self-similar configurations can be up to 77 [122]. It is then unrealistic to expect that an exact MultiD

Riemann solver can be used as a building block for numerical schemes. Yet, we can still view the numerical flux as the one-dimensional flux across cell boundaries plus multidimensional corrections emanating from the corners (in the 2D case). In the Lagrangian context, the approximation of corner interactions has already been combined with one-dimensional fluxes to obtain robust approximations satisfying a discrete entropy inequality [49, 103, 104]. However, it is known that for most of the current flux based numerical strategies, approximations often neglect the corner corrections and only use one-dimensional wave characteristics, even when an operator splitting technique is not employed. We mention that several alternative strategies consisting of Riemann solver-free formulations are available, such as residual distribution schemes [44, 43], variational multiscale methods applied to finite element solutions [77], and Riemann-solvers-free central schemes [85, 86], among others, but are not within the scope of our work.

Our focus in this chapter is on Riemann based unsplit formulations taking into account the interactions associated to the "corner" boundaries. A nine state Riemann solver was formulated in [145] to obtain numerical approximations that include these interactions as constant states, extending the one-dimensional HLL theory [74] with Einfeldt's wave speed estimates [50] to two dimensions. Although his approach includes a valuable interpretation of the approximate structure of 2D solutions at a given time, it regrettably lacks explicit expressions that would enable a direct implementation. One year later, in another line of development, Brio et al. [26] proposed a multistate Riemann solver (defined at the corner) as a linear hyperbolic propagation of acoustic waves, which can be regarded as a partial correction to the 1D solver applied at the interfaces such that the final numerical flux results from a convex combination of purely one-dimensional and corner fluxes. However, the solver was solely developed for the Euler equations of gas dynamics and, given its linear nature, requires considerable reformulation for application to other systems of conservation laws. Recently, Balsara re-examined Wendroff's contribution and formulated a multidimensional solver in [9] and a more robust version in [10], which include, among other things, calculating the states and fluxes at a corner by means of the integral form of the conservation laws over a space-time volume that is essentially different from Wendroff's to facilitate the computation of the resulting equations in the subsonic case; to handle supersonic cases, slight modifications must be performed to the fluxes and/or signal speeds, nonetheless.

With all this in mind, we were motivated to combine ideas from existing methods with the enforcing of jump conditions, to design a strategy for the construction of simple MultiD Riemann solvers. In the subsequent section, we present all necessary background information about HLL Riemann solvers (both one- and two-dimensional) that serves to assist the understanding of the subject and introduce important concepts such as the advantageous space-time structure suggested by Wendroff [145]. In Section 2.2, we present our solver, which is suitably built as an extension of the HLL formalism to multidimensions and inevitably leads to the construction of an approximate profile of propagation consisting of constant states and representative of the complexity of the waves associated with the multidimensional Riemann problem. We make use of the consistency with the integral formulation through the Rankine-Hugoniot relations,

which hold across planar waves separating these constant states, to derive general closed-form expressions (in the sense of [9, 10]) for the fluxes. All expressions are, in fact, the solution of an overdetermined linear system resolved by the method of ordinary least squares and provide a straightforward implementation of our robust and stable scheme. Although we will restrict our attention to the case of the Euler equations for inviscid compressible gas flows in two space variables, all formalisms developed in this chapter can be extended to higher dimensions and applied to any system of conservation laws, e.g., the MHD equations (see Chapter 3). Next, the developed strategy is validated through applications to test problems in Section 2.3 and finally, concluding remarks are given in the last section.

2.1 HLL Riemann Solvers

One of the simplest Godunov-type schemes is the so-called HLL Riemann solver proposed by Harten et. al [74], where the exact Riemann fan is approximated by two waves containing a single constant state in between (see Figure 2.1). These waves propagate with speeds s_l and s_r denoting the smallest and largest signal speeds, the estimation of which will be detailed later in this section. As pointed out in [74], any scheme (1.55) remains consistent with (1.70) as long as the waves from one cell interface do not arrive at an adjacent interface during one time step, which translates to

$$\Delta t/\Delta x \max(|s_l|, |s_r|) \leq 1. \tag{2.1}$$

(a) Speeds   (b) States

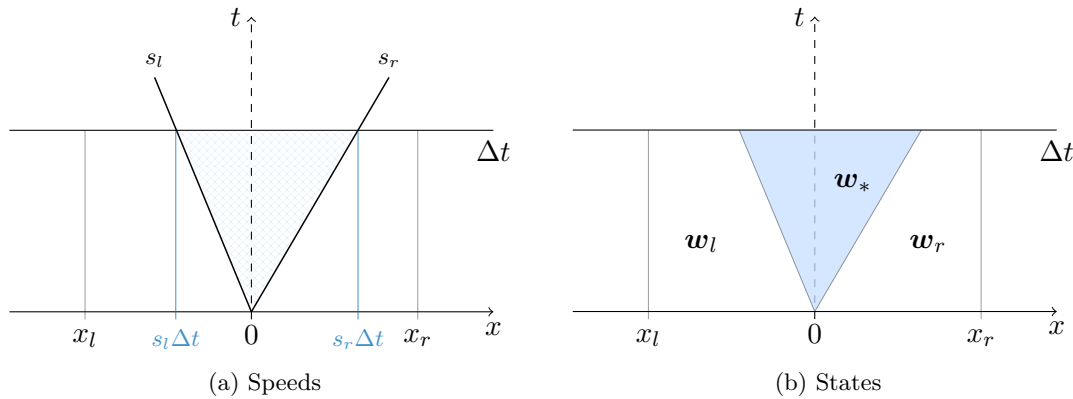FIGURE 2.1. One-dimensional HLL Riemann problems.

Thus, considering the previously mentioned configuration, the HLL approximate Riemann solver is defined as

$$\mathcal{W}^{hll}, \phi_x^{hll} = \begin{cases} \boldsymbol{w}_l, \boldsymbol{f}_l & \text{if } \xi < s_l, \\ \boldsymbol{w}_*, \boldsymbol{f}_* & \text{if } s_l < \xi < s_r, \\ \boldsymbol{w}_r, \boldsymbol{f}_r & \text{if } \xi > s_r, \end{cases} \tag{2.2}$$

with the self-similar variable $\xi = x/t$. The term $\boldsymbol{w}_*$ represents the average intermediate state between the two waves and can be derived from the conservation laws (1.69), i.e.,

$$\boldsymbol{w}_* = \frac{s_r \boldsymbol{w}_r - s_l \boldsymbol{w}_l + \boldsymbol{f}_l - \boldsymbol{f}_r}{s_r - s_l}. \tag{2.3}$$

Moreover, we are interested in the determination of the associated numerical flux. For this purpose, by applying the integral conservation laws (1.54) over two distinct rectangles $(x_l, 0) \times (0, \Delta t)$, $(0, x_r) \times (0, \Delta t)$, two fluxes along the t-axis are obtained

$$\boldsymbol{\phi}_l = \boldsymbol{f}_l - \frac{x_l}{\Delta t} \boldsymbol{w}_l - \frac{1}{\Delta t} \int_{x_l}^0 \boldsymbol{\mathcal{W}}^{hll} \left(\frac{x}{\Delta t}; \boldsymbol{w}_l, \boldsymbol{w}_r \right) dx, \tag{2.4a}$$

$$\boldsymbol{\phi}_r = \boldsymbol{f}_r - \frac{x_r}{\Delta t} \boldsymbol{w}_r + \frac{1}{\Delta t} \int_0^{x_r} \boldsymbol{\mathcal{W}}^{hll} \left(\frac{x}{\Delta t}; \boldsymbol{w}_l, \boldsymbol{w}_r \right) dx. \tag{2.4b}$$

Consistency with the conservation law (1.69) ensures that $\boldsymbol{\phi}_l = \boldsymbol{\phi}_r$. Let us now introduce some useful notation: for any constant $h \in \mathbb{R}$, we define

$$h^+ = \max(0, h) \quad \text{and} \quad h^- = \min(0, h), \tag{2.5}$$

recalling that $h = h^+ + h^-$. Employing this notation, we are able to rewrite (2.4) as

$$\boldsymbol{\phi}_l = \boldsymbol{f}_l + s_l^{-}(\boldsymbol{w}_* - \boldsymbol{w}_l), \quad \boldsymbol{\phi}_r = \boldsymbol{f}_r + s_r^{+}(\boldsymbol{w}_* - \boldsymbol{w}_r), \tag{2.6}$$

which are both useful to obtain an approximation to the numerical flux along the t-axis.

Hence, we substitute the state (2.3), with both signal speeds replaced by s_l^{-} and s_r^{+}, into any of the previous equations (2.6) to get

$$\boldsymbol{\phi}_x^{hll}(\boldsymbol{w}_l, \boldsymbol{w}_r) = \frac{s_r^{+} \boldsymbol{f}_l - s_l^{-} \boldsymbol{f}_r + s_l^{-} s_r^{+}(\boldsymbol{w}_r - \boldsymbol{w}_l)}{s_r^{+} - s_l^{-}}, \tag{2.7}$$

so the scheme can be written in the conservative form (1.55) simply by defining

$$\boldsymbol{\phi}_{x, i-\frac{1}{2}} = \boldsymbol{\phi}_x^{hll}(\mathbf{w}_{i-1}^n, \mathbf{w}_i^n) \quad \text{and} \quad \boldsymbol{\phi}_{x, i+\frac{1}{2}} = \boldsymbol{\phi}_x^{hll}(\mathbf{w}_i^n, \mathbf{w}_{i+1}^n). \tag{2.8}$$

Yet another equivalent and simpler way to construct the HLL intermediate state vector and flux relies on applying the Rankine-Hugoniot jump conditions across each of the waves. Specifically, we may think of these intermediate quantities as solutions of the linear system

$$\boldsymbol{f}_* = \boldsymbol{f}_l + s_l(\boldsymbol{w}_* - \boldsymbol{w}_l), \tag{2.9a}$$

$$\boldsymbol{f}_* = \boldsymbol{f}_r + s_r(\boldsymbol{w}_* - \boldsymbol{w}_r), \tag{2.9b}$$

i.e., the Rankine-Hugoniot conditions across the left and right waves, respectively. These conditions hold across curves of discontinuities and are mentioned here briefly for later reference in Section 2.2. Solving system (2.9) yields the state $\boldsymbol{w}_*$ (2.3) and the flux

$$\boldsymbol{f}_* = \frac{s_r \boldsymbol{f}_l - s_l \boldsymbol{f}_r + s_l s_r(\boldsymbol{w}_r - \boldsymbol{w}_l)}{s_r - s_l}. \tag{2.10}$$

Under the assumption of a *subsonic* solution where $s_l < 0 < s_r$, it is evident that $\boldsymbol{\phi}_x^{hll} = \boldsymbol{f}_*$. With a slight modification to the speeds, we then obtain the intercell flux (2.7).

Now, in order to completely determine the numerical fluxes previously described, an adequate choice of the wave speeds s_l and s_r is needed. In [50], Einfeldt derived approximations for the minimum and maximum physical signal velocities of the exact Riemann problem, generalized to

$$s_l = \min_{1 \leq \theta \leq \vartheta} \left(\min \left(\lambda_\theta(\boldsymbol{w}_l), \hat{\lambda}_\theta(\boldsymbol{w}_l, \boldsymbol{w}_r) \right) \right) \quad \text{and} \quad s_r = \max_{1 \leq \theta \leq \vartheta} \left(\max \left(\lambda_\theta(\boldsymbol{w}_r), \hat{\lambda}_\theta(\boldsymbol{w}_l, \boldsymbol{w}_r) \right) \right),$$

(2.11)

where λ_θ is the θ-th eigenvalue of the Jacobian matrix $\nabla_{\boldsymbol{w}} \boldsymbol{f}$ associated with system (1.2a) and $\hat{\lambda}_\theta$ is the θ-th eigenvalue of the Roe matrix (see [50, 117, 129]).

The HLL approach [74] together with Einfeldt's wave speed estimates (2.11) is not only effective and robust but also rather easy to implement. Several details regarding the scheme's ability to preserve the positivity of the internal energy and density throughout the computational process are given in [51, 74].

2.1.1 Two-Dimensional Systems

Due to our specific interest in two-dimensional gas dynamics, henceforth in this chapter we only consider system (1.20) in $d = 2$ dimensions with $\boldsymbol{x} = (x, y)$, $\boldsymbol{u} = (u, v)$ and denote $\boldsymbol{f}$ and $\boldsymbol{g}$ the fluxes $\boldsymbol{f}_1$ and $\boldsymbol{f}_2$, respectively. We then write

$$\partial_t \boldsymbol{w} + \partial_x \boldsymbol{f}(\boldsymbol{w}) + \partial_y \boldsymbol{g}(\boldsymbol{w}) = 0,$$

(2.12)

with

$$\boldsymbol{w} = \begin{pmatrix} \rho \\ \rho u \\ \rho v \\ \rho e \end{pmatrix}, \quad \boldsymbol{f}(\boldsymbol{w}) = \begin{pmatrix} \rho u \\ \rho u^2 + p \\ \rho u v \\ (\rho e + p) u \end{pmatrix}, \quad \boldsymbol{g}(\boldsymbol{w}) = \begin{pmatrix} \rho v \\ \rho v u \\ \rho v^2 + p \\ (\rho e + p) v \end{pmatrix}.$$

(2.13)

After Harten et al.'s contribution in [74], several extensions of their HLL scheme have been proposed to find approximate solutions to the above system and in this section we will carefully review two of them. However, following the developments in the one-dimensional case, we first establish the integral form of the conservation laws (2.12). Thus, for all control volumes $(x_a, x_b) \times (y_c, y_d) \times (t_1, t_2)$, the following integral form should hold:

$$\int_{x_a}^{x_b} \int_{y_c}^{y_d} \boldsymbol{w}(x, y, t_2) \, dy \, dx = \int_{x_a}^{x_b} \int_{y_c}^{y_d} \boldsymbol{w}(x, y, t_1) \, dy \, dx$$

$$+ \int_{t_1}^{t_2} \int_{y_c}^{y_d} \boldsymbol{f}(\boldsymbol{w}(x_a, y, t)) \, dy \, dt - \int_{t_1}^{t_2} \int_{y_c}^{y_d} \boldsymbol{f}(\boldsymbol{w}(x_b, y, t)) \, dy \, dt$$

$$+ \int_{t_1}^{t_2} \int_{x_a}^{x_b} \boldsymbol{g}(\boldsymbol{w}(x, y_c, t)) \, dx \, dt - \int_{t_1}^{t_2} \int_{x_a}^{x_b} \boldsymbol{g}(\boldsymbol{w}(x, y_d, t)) \, dx \, dt.$$

(2.14)

To find a numerical approximation, we break the spatial domain into rectangular grid cells with centers indexed as i, j, where i refers to the x-coordinate direction and

j to the y-coordinate direction. Here, $\Delta x = 1/N_x$ and $\Delta y = 1/N_y$ are the grid spacing such that $x_i = (i-1)\Delta x$ and $y_j = (j-1)\Delta y$, with $i = 1, \ldots, N_x$ and $j = 1, \ldots, N_y$, and as before, the corresponding cell interfaces are denoted by half integers. Once such a grid has been constructed, the average value of the gas dynamic state at time level t^n over a particular cell $\mathcal{C}_{i,j} = (x_{i-1/2}, x_{i+1/2}) \times (y_{j-1/2}, y_{j+1/2})$ can be defined as

$$\mathbf{w}_{i,j}^n = \frac{1}{|\mathcal{C}_{i,j}|} \int_{\mathcal{C}_{i,j}} \boldsymbol{w}(x,y,t^n)\, d\boldsymbol{x}, \tag{2.15}$$

where $|\mathcal{C}_{i,j}| = \Delta x \Delta y$, and applying the integral form (1.54) over $\mathcal{C}_{i,j} \times (t^n, t^{n+1})$ yields

$$\mathbf{w}_{i,j}^{n+1} = \mathbf{w}_{i,j}^n - \frac{\Delta t}{\Delta x}\left(\boldsymbol{\phi}_{x,i+\frac{1}{2},j} - \boldsymbol{\phi}_{x,i-\frac{1}{2},j}\right) - \frac{\Delta t}{\Delta y}\left(\boldsymbol{\phi}_{y,i,j+\frac{1}{2}} - \boldsymbol{\phi}_{y,i,j-\frac{1}{2}}\right), \tag{2.16}$$

with

$$\boldsymbol{\phi}_{x,i\pm\frac{1}{2},j} = \frac{1}{\Delta t} \int_{t^n}^{t^{n+1}} \int_{y_{j-\frac{1}{2}}}^{y_{j+\frac{1}{2}}} \boldsymbol{f}(\boldsymbol{w}(x_{i\pm\frac{1}{2}}, y, t))\, dy\, dt, \tag{2.17a}$$

$$\boldsymbol{\phi}_{y,i,j\pm\frac{1}{2}} = \frac{1}{\Delta t} \int_{t^n}^{t^{n+1}} \int_{x_{i-\frac{1}{2}}}^{x_{i+\frac{1}{2}}} \boldsymbol{g}(\boldsymbol{w}(x, y_{i\pm\frac{1}{2}}, t))\, dx\, dt. \tag{2.17b}$$

As noted before, any finite volume method based on a Godunov-type approach strongly depends on the exact or approximate solution of the Riemann problem. Conventional approaches based on one-dimensional Riemann solvers by direction consider an approximation for (2.16) of the form

$$\boldsymbol{\phi}_{x,i+\frac{1}{2},j} = \boldsymbol{\phi}_x(\mathbf{w}_{i,j}, \mathbf{w}_{i+1,j}) \quad \text{and} \quad \boldsymbol{\phi}_{y,i,j+\frac{1}{2}} = \boldsymbol{\phi}_y(\mathbf{w}_{i,j}, \mathbf{w}_{i,j+1}), \tag{2.18}$$

but tend to completely ignore the genuinely two-dimensional Riemann problems formed at the vertices (as depicted in Figure 2.2a). Since the one-dimensional theory was already introduced in the first chapter, we now focus on approximately solving the local 2D Riemann problem formed at the vertex $\boldsymbol{x}_{i+1/2,j+1/2} = (x_{i+1/2}, y_{j+1/2})$, i.e.,

$$\partial_t \boldsymbol{w} + \partial_x \boldsymbol{f}(\boldsymbol{w}) + \partial_y \boldsymbol{g}(\boldsymbol{w}) = 0, \quad \boldsymbol{w}_0(x,y) = \boldsymbol{w}_{i+1/2,j+1/2}(x,y,t^n), \tag{2.19}$$

having piecewise constant initial data

$$\boldsymbol{w}_{i+1/2,j+1/2}(x,y,t^n) = \begin{cases} \boldsymbol{w}_{sw} = \mathbf{w}_{i,j} & \text{if } x < x_{i+\frac{1}{2}}, y < y_{j+\frac{1}{2}}, \\ \boldsymbol{w}_{se} = \mathbf{w}_{i+1,j} & \text{if } x > x_{i+\frac{1}{2}}, y < y_{j+\frac{1}{2}}, \\ \boldsymbol{w}_{nw} = \mathbf{w}_{i,j+1} & \text{if } x < x_{i+\frac{1}{2}}, y > y_{j+\frac{1}{2}}, \\ \boldsymbol{w}_{ne} = \mathbf{w}_{i+1,j+1} & \text{if } x > x_{i+\frac{1}{2}}, y > y_{j+\frac{1}{2}}. \end{cases} \tag{2.20}$$

It is known that system (2.12) is invariant under scaling of the form $(x,y,t) \mapsto (\kappa x, \kappa y, \kappa t)$, for any constant $\kappa > 0$, and (2.19) has a similarity solution of the form

$\boldsymbol{w}(\xi, \eta; \boldsymbol{w}_{ne}, \boldsymbol{w}_{nw}, \boldsymbol{w}_{sw}, \boldsymbol{w}_{se})$, hereafter $\boldsymbol{w}(\xi, \eta)$, i.e., a function constant along ξ and η, with $\xi = (x - x_{i+1/2})/(t - t^n)$ and $\eta = (y - y_{j+1/2})/(t - t^n)$, and which is self-similar. Despite the reduction in the number of dimensions (from three to two in this case), the solution is expected to be fairly complex nonetheless, as demonstrated by Schulz-Rinne et al. [122]. Before proceeding with the wave model, some remarks are in order.

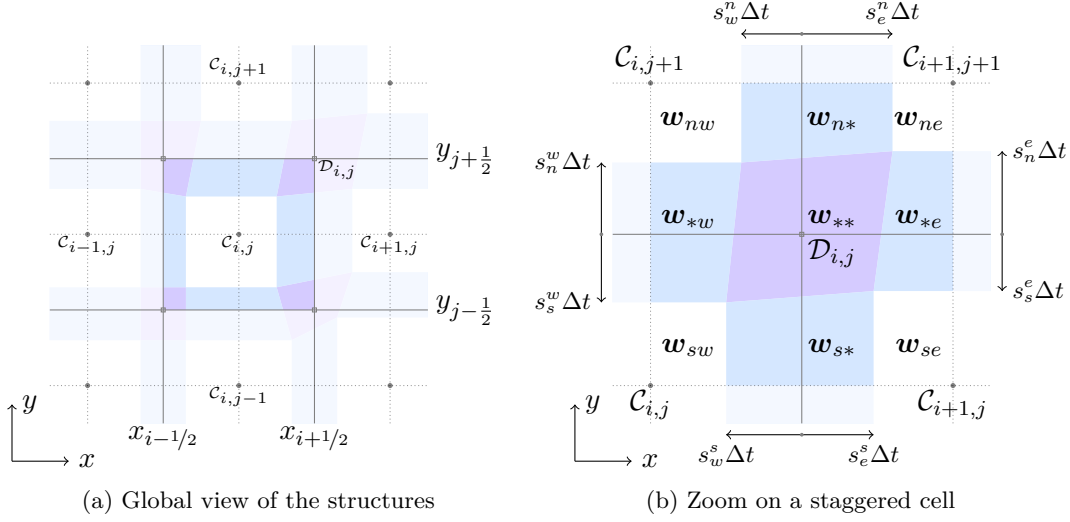(a) Global view of the structures   (b) Zoom on a staggered cell

FIGURE 2.2. Example of a solution's structure at time $t = \Delta t$, resulting from a series of one- and two-dimensional HLL Riemann problems on a rectangular mesh.

As previously mentioned, the solution of the initial value problem (2.19) is assumed to have a rather complex structure and one of the reasons for this stems from wave interactions taking place. A proper study requires considering the numerous combinations of initial data that are possible for this two-dimensional problem, and even under the premise that each jump between neighboring initial states projects one planar wave consisting of a single shock, rarefaction or contact discontinuity, the number of possible combinations for a polytropic gas reduces to nineteen [30, 87] (ignoring the sign of the slip lines, to fifteen [122]), and for each combination, the solution's complexity is evident in the conjectures of Zhang and Zheng [151] and in the numerical experiments [87, 122]. In both predicted and numerical results, we are able to perceive that the two-dimensional Riemann problem gives rise to a region of strong interaction consisting of a complex similarity solution. This interaction region can then be approximated in a way conceptually similar to that of the one-dimensional intermediate state in the context of the HLL method.

Thus, considering the definition of the local Riemann problem (2.19), it is apparent that the jump discontinuities at the cell's edges lead to two one-dimensional Riemann problems in the x-direction and two one-dimensional Riemann problems in the y-direction, and their effects on one another at the vertex give rise to the region of strong interaction. Since waves propagate with finite velocities, one can then approximately

delimit this interaction region by means of the wave model detailed in the subsequent paragraphs of this section.

Computing the one-dimensional HLL smallest and largest wave speed estimates with (2.11) for each of the previously discussed one-dimensional problems yields eight approximate signal velocities that determine the following vectors:

$$\boldsymbol{s}_{sw} = (s_w^s, s_s^w), \quad \boldsymbol{s}_{se} = (s_e^s, s_s^e), \quad \boldsymbol{s}_{nw} = (s_w^n, s_n^w), \quad \boldsymbol{s}_{ne} = (s_e^n, s_n^e), \qquad (2.21)$$

where s_w^n and s_e^n (respectively, s_w^s and s_e^s) are the left and right speeds for the 1D Riemann problem above (respectively, below) the x-axis, with equivalent definitions for the y-direction. Additionally, one can specify the minimal and maximal wave speeds

$$s_n = \max(s_n^e, s_n^w), \quad s_s = \min(s_s^e, s_s^w), \quad s_e = \max(s_e^n, s_e^s), \quad s_w = \min(s_w^n, s_w^s). \quad (2.22)$$

Solving the one-dimensional Riemann problems at the edges not only allows us to deduce the speeds (2.21) but also lets us derive expressions for the constant state $\boldsymbol{w}_*$ (2.3) and HLL fluxes (2.10) associated with each problem. We denote by $\boldsymbol{w}_{\mu*}$, $\mu = n$ or s, the state in the intermediate constant region of the one-dimensional Riemann problem with initial data set to $\boldsymbol{w}_l = \boldsymbol{w}_{\mu w}$ and $\boldsymbol{w}_r = \boldsymbol{w}_{\mu e}$. Analogous notations are used for $\boldsymbol{w}_{*\nu}$, $\nu = e$ or w, with initial states given by $\boldsymbol{w}_l = \boldsymbol{w}_{s\nu}$ and $\boldsymbol{w}_r = \boldsymbol{w}_{n\nu}$. One then has

$$\boldsymbol{w}_{\mu*} = \frac{s_e^\mu \boldsymbol{w}_{\mu e} - s_w^\mu \boldsymbol{w}_{\mu w} + \boldsymbol{f}_{\mu w} - \boldsymbol{f}_{\mu e}}{s_e^\mu - s_w^\mu}, \quad \mu = n \text{ or } s, \qquad (2.23a)$$

$$\boldsymbol{w}_{*\nu} = \frac{s_n^\nu \boldsymbol{w}_{n\nu} - s_s^\nu \boldsymbol{w}_{s\nu} + \boldsymbol{g}_{s\nu} - \boldsymbol{g}_{n\nu}}{s_n^\nu - s_s^\nu}, \qquad \nu = e \text{ or } w, \qquad (2.23b)$$

with corresponding HLL fluxes

$$\boldsymbol{f}_{\mu*} = \frac{s_e^\mu \boldsymbol{f}_{\mu w} - s_w^\mu \boldsymbol{f}_{\mu e} + s_w^\mu s_e^\mu (\boldsymbol{w}_{\mu e} - \boldsymbol{w}_{\mu w})}{s_e^\mu - s_w^\mu}, \quad \mu = n \text{ or } s, \qquad (2.24a)$$

$$\boldsymbol{g}_{*\nu} = \frac{s_n^\nu \boldsymbol{g}_{s\nu} - s_s^\nu \boldsymbol{g}_{n\nu} + s_s^\nu s_n^\nu (\boldsymbol{w}_{n\nu} - \boldsymbol{w}_{s\nu})}{s_n^\nu - s_s^\nu}, \qquad \nu = e \text{ or } w. \qquad (2.24b)$$

Denote now by $\mathbf{O} = (\boldsymbol{x}_0, t_0)$ a local origin in the space-time domain (x, y, t). For a 2D Riemann problem centered at this origin, the extent of its strong interaction region on the xy-plane at a time $t > t_0$ lies by construction within a quadrilateral with time-dependent vertices

$$\boldsymbol{X}_{sw}(t) = \boldsymbol{x}_0 + \boldsymbol{s}_{sw}t, \quad \boldsymbol{X}_{se}(t) = \boldsymbol{x}_0 + \boldsymbol{s}_{se}t, \quad \boldsymbol{X}_{nw}(t) = \boldsymbol{x}_0 + \boldsymbol{s}_{nw}t, \quad \boldsymbol{X}_{ne}(t) = \boldsymbol{x}_0 + \boldsymbol{s}_{ne}t, \qquad (2.25)$$

having assumed that $t_0 = 0$. For later convenience, at this stage we define the four points at some fixed small time $\Delta t > 0$

$$\mathbf{Q}_{sw} = (\boldsymbol{X}_{sw}(\Delta t), \Delta t), \ \mathbf{Q}_{se} = (\boldsymbol{X}_{se}(\Delta t), \Delta t), \ \mathbf{Q}_{nw} = (\boldsymbol{X}_{nw}(\Delta t), \Delta t), \ \mathbf{Q}_{ne} = (\boldsymbol{X}_{ne}(\Delta t), \Delta t), \qquad (2.26)$$

and specify a rectangular space-time control volume $\mathcal{Q} = \mathcal{R} \times (0, \Delta t)$ that contains these points (2.26), as well as the local origin $\mathbf{O}$. We define the rectangle $\mathcal{R} = (x_w, x_e) \times (y_s, y_n)$, with $x_w \le x_0 \le x_e$ and $y_s \le y_0 \le y_n$, and identify its four corners as

$$\boldsymbol{x}_{sw} = (x_w, y_s), \quad \boldsymbol{x}_{se} = (x_e, y_s), \quad \boldsymbol{x}_{nw} = (x_w, y_n), \quad \boldsymbol{x}_{ne} = (x_e, y_n). \qquad (2.27)$$

2.1.2 Wendroff's Nine-State Solver

Wendroff formulated in [145] a nine-state two-dimensional version of the three-state HLL Riemann solver, using the literal extension of Godunov's formulation (1.65) to two dimensions as its basis. However, given the absence of an exact solution to the initial value problem (2.19), he employed an approximation $\mathcal{W}(\xi, \eta; \boldsymbol{w}_{ne}, \boldsymbol{w}_{nw}, \boldsymbol{w}_{sw}, \boldsymbol{w}_{se})$, or $\mathcal{W}(\xi, \eta)$ for short, to obtain the two-dimensional analogue of (1.70) given by

$$
\begin{aligned}
\mathbf{w}_{i,j}^{n+1} = \; & \frac{1}{|\mathcal{C}_{i,j}|} \int_{x_{i-\frac{1}{2}}}^{x_i} \int_{y_{j-\frac{1}{2}}}^{y_j} \mathcal{W}\left(\frac{x - x_{i-\frac{1}{2}}}{\Delta t}, \frac{y - y_{j-\frac{1}{2}}}{\Delta t}; \mathbf{w}_{i,j}^n, \mathbf{w}_{i-1,j}^n, \mathbf{w}_{i-1,j-1}^n, \mathbf{w}_{i,j-1}^n \right) dy\, dx \\
& + \frac{1}{|\mathcal{C}_{i,j}|} \int_{x_{i-\frac{1}{2}}}^{x_i} \int_{y_j}^{y_{j+\frac{1}{2}}} \mathcal{W}\left(\frac{x - x_{i-\frac{1}{2}}}{\Delta t}, \frac{y - y_{j+\frac{1}{2}}}{\Delta t}; \mathbf{w}_{i,j+1}^n, \mathbf{w}_{i-1,j+1}^n, \mathbf{w}_{i-1,j}^n, \mathbf{w}_{i,j}^n \right) dy\, dx \\
& + \frac{1}{|\mathcal{C}_{i,j}|} \int_{x_i}^{x_{i+\frac{1}{2}}} \int_{y_{j-\frac{1}{2}}}^{y_j} \mathcal{W}\left(\frac{x - x_{i+\frac{1}{2}}}{\Delta t}, \frac{y - y_{j-\frac{1}{2}}}{\Delta t}; \mathbf{w}_{i+1,j}^n, \mathbf{w}_{i,j}^n, \mathbf{w}_{i,j-1}^n, \mathbf{w}_{i+1,j-1}^n \right) dy\, dx \\
& + \frac{1}{|\mathcal{C}_{i,j}|} \int_{x_i}^{x_{i+\frac{1}{2}}} \int_{y_j}^{y_{j+\frac{1}{2}}} \mathcal{W}\left(\frac{x - x_{i+\frac{1}{2}}}{\Delta t}, \frac{y - y_{j+\frac{1}{2}}}{\Delta t}; \mathbf{w}_{i+1,j+1}^n, \mathbf{w}_{i,j+1}^n, \mathbf{w}_{i,j}^n, \mathbf{w}_{i+1,j}^n \right) dy\, dx,
\end{aligned}
\tag{2.28}
$$

under the assumption that the approximate solutions at the vertices do not interact with each other during the time interval Δt provided the condition

$$
\Delta t \max_{\mathcal{R}=\mathcal{D}_{i,j}} \left(\max_{\substack{\mu=s,n \\ \nu=e,w}} \left(|s_\nu^\mu|, |s_\mu^\nu| \right) \right) \leq \min \left(\frac{\Delta x}{2}, \frac{\Delta y}{2} \right),
\tag{2.29}
$$

interpreting $\mathcal{D}_{i,j} = (x_i, x_{i+1}) \times (y_j, y_{j+1})$ as a staggered cell centered in $\boldsymbol{x}_{i+1/2,j+1/2}$, (see Figure 2.2b). Equation (2.28) can be regarded as

$$
\mathbf{w}_{i,j}^{n+1} = \mathbf{w}_{i,j}^n - \frac{\Delta t}{\Delta x} \left(\boldsymbol{\phi}_{x,i+\frac{1}{2},j}^{Wen,l} - \boldsymbol{\phi}_{x,i-\frac{1}{2},j}^{Wen,r} \right) - \frac{\Delta t}{\Delta y} \left(\boldsymbol{\phi}_{y,i,j+\frac{1}{2}}^{Wen,d} - \boldsymbol{\phi}_{y,i,j-\frac{1}{2}}^{Wen,u} \right),
\tag{2.30}
$$

where

$$
\begin{aligned}
\boldsymbol{\phi}_{x,i+\frac{1}{2},j}^{Wen,l} = \; & \boldsymbol{f}(\mathbf{w}_{i,j}^n) - \frac{1}{2\Delta y \Delta t} \int_{x_i}^{x_{i+\frac{1}{2}}} \int_{y_{j-\frac{1}{2}}}^{y_j} \left(\mathcal{W}\left(\frac{x - x_{i+\frac{1}{2}}}{\Delta t}, \frac{y - y_{j-\frac{1}{2}}}{\Delta t} \right) - \mathbf{w}_{i,j}^n \right) dy\, dx \\
& - \frac{1}{2\Delta y \Delta t} \int_{x_i}^{x_{i+\frac{1}{2}}} \int_{y_j}^{y_{j+\frac{1}{2}}} \left(\mathcal{W}\left(\frac{x - x_{i+\frac{1}{2}}}{\Delta t}, \frac{y - y_{j+\frac{1}{2}}}{\Delta t} \right) - \mathbf{w}_{i,j}^n \right) dy\, dx, \\
\boldsymbol{\phi}_{x,i-\frac{1}{2},j}^{Wen,r} = \; & \boldsymbol{f}(\mathbf{w}_{i,j}^n) + \frac{1}{2\Delta y \Delta t} \int_{x_{i-\frac{1}{2}}}^{x_i} \int_{y_{j-\frac{1}{2}}}^{y_j} \left(\mathcal{W}\left(\frac{x - x_{i-\frac{1}{2}}}{\Delta t}, \frac{y - y_{j-\frac{1}{2}}}{\Delta t} \right) - \mathbf{w}_{i,j}^n \right) dy\, dx \\
& + \frac{1}{2\Delta y \Delta t} \int_{x_{i-\frac{1}{2}}}^{x_i} \int_{y_j}^{y_{j+\frac{1}{2}}} \left(\mathcal{W}\left(\frac{x - x_{i-\frac{1}{2}}}{\Delta t}, \frac{y - y_{j+\frac{1}{2}}}{\Delta t} \right) - \mathbf{w}_{i,j}^n \right) dy\, dx, \\
\boldsymbol{\phi}_{y,i,j+\frac{1}{2}}^{Wen,d} = \; & \boldsymbol{g}(\mathbf{w}_{i,j}^n) - \frac{1}{2\Delta x \Delta t} \int_{x_{i-\frac{1}{2}}}^{x_i} \int_{y_j}^{y_{j+\frac{1}{2}}} \left(\mathcal{W}\left(\frac{x - x_{i-\frac{1}{2}}}{\Delta t}, \frac{y - y_{j+\frac{1}{2}}}{\Delta t} \right) - \mathbf{w}_{i,j}^n \right) dy\, dx \\
& - \frac{1}{2\Delta x \Delta t} \int_{x_i}^{x_{i+\frac{1}{2}}} \int_{y_j}^{y_{j+\frac{1}{2}}} \left(\mathcal{W}\left(\frac{x - x_{i+\frac{1}{2}}}{\Delta t}, \frac{y - y_{j+\frac{1}{2}}}{\Delta t} \right) - \mathbf{w}_{i,j}^n \right) dy\, dx,
\end{aligned}
$$

$$\phi_{y,i,j-\frac{1}{2}}^{Wen,u} = \boldsymbol{g}(\mathbf{w}_{i,j}^n) + \frac{1}{2\Delta x \Delta t} \int_{x_{i-\frac{1}{2}}}^{x_i} \int_{y_{j-\frac{1}{2}}}^{y_j} \left(\boldsymbol{\mathcal{W}}\left(\frac{x - x_{i-\frac{1}{2}}}{\Delta t}, \frac{y - y_{j-\frac{1}{2}}}{\Delta t} \right) - \mathbf{w}_{i,j}^n \right) dy\, dx$$

$$+ \frac{1}{2\Delta x \Delta t} \int_{x_i}^{x_{i+\frac{1}{2}}} \int_{y_{j-\frac{1}{2}}}^{y_j} \left(\boldsymbol{\mathcal{W}}\left(\frac{x - x_{i+\frac{1}{2}}}{\Delta t}, \frac{y - y_{j-\frac{1}{2}}}{\Delta t} \right) - \mathbf{w}_{i,j}^n \right) dy\, dx.$$

With our attention directed towards Wendroff's derivation of $\boldsymbol{\mathcal{W}}(\xi, \eta)$, we begin by analyzing the structure of a solution to the 2D Riemann problem (2.12, 2.20) at the planar faces of the space-time control volume $\mathcal{Q}$, illustrated in Figure 2.3a. The top surface of $\mathcal{Q}$ constitutes nine regions resulting from the finite propagation of waves, in accordance with the wave model introduced in the previous section, up to a small time Δt. For reference, we show this flat surface in Figure 2.3b and acknowledge the following: the central extent corresponds to the strong interaction region; the four corner zones are simply rectangles containing the undisturbed initial data $\boldsymbol{w}_{ne}, \boldsymbol{w}_{nw}, \boldsymbol{w}_{sw}$, and $\boldsymbol{w}_{se}$, written in a counterclockwise order starting from the top right quadrant in the xy-plane; and each of the remaining regions represents the total area covered at time Δt by the intermediate state (2.23) obtained from the application of a three-state HLL solver at the underlying edge. Let us here summarize the technique used by Wendroff to obtain an approximation for the former region. The central idea is to lump together all of the region's complicated structure into a constant state $\boldsymbol{w}_{**}$, in agreement with the one-dimensional approach presented in Section 2.1, and make use of the integral conservation laws (2.14) over $\mathcal{Q}$ to obtain its specific value and deduce the numerical fluxes, as well.

(a) Space-time control volume $\mathcal{Q} = \mathcal{R} \times (0, \Delta t)$ (b) Surface of $\mathcal{Q}$ in space and at time $t = \Delta t$
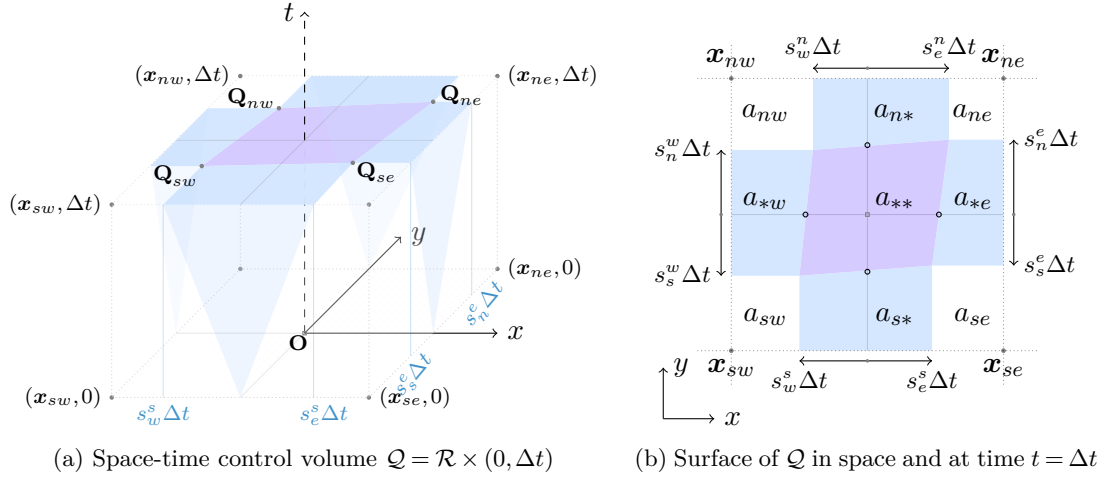
FIGURE 2.3. Structures formed by the outward propagation of waves from the staggered cell's origin $\mathbf{O}$ and edges, as suggested by Wendroff in [145].

Performing a simple geometric analysis of the top surface described in the previous paragraph, hereafter defined as $\mathcal{S} = \mathcal{R} \times \{t = \Delta t\}$, we note that the two-dimensional interactions are contained in the quadrilateral with vertices $\boldsymbol{X}_{sw}(\Delta t), \boldsymbol{X}_{se}(\Delta t), \boldsymbol{X}_{nw}(\Delta t)$, and $\boldsymbol{X}_{ne}(\Delta t)$, which can be located anywhere on $\mathcal{S}$. For this reason, to simplify the

developments and reduce coding difficulties, Wendroff adopts the notation (2.5) and proposes to reformulate (2.21) as

$$\boldsymbol{s}_{sw} = (s_w^{s-}, s_s^{w-}), \quad \boldsymbol{s}_{se} = (s_e^{s+}, s_s^{e-}), \quad \boldsymbol{s}_{nw} = (s_w^{n-}, s_n^{w+}), \quad \boldsymbol{s}_{ne} = (s_e^{n+}, s_n^{e+}), \qquad (2.31)$$

and as a result, relaxes every solution to the subsonic case in two-dimensions, which accounts for the introduction of additional numerical dissipation.

We are now in the position to formulate his explicit approximation of the solution for (2.19). At the small fixed time Δt, let $\mathcal{R}_{\mu\nu}$ ($\mu = n, *, s$, $\nu = e, *, w$) be the nine regions with corresponding areas $a_{\mu\nu}$, and then define

$$\boldsymbol{\mathcal{W}}\left(\frac{x-x_0}{\Delta t}, \frac{y-y_0}{\Delta t}\right) = \boldsymbol{w}_{\mu\nu} \quad \text{for all } (x,y) \in \mathcal{R}_{\mu\nu}, \qquad (2.32)$$

with the state $\boldsymbol{w}_{**}$ determined by solving the equation that results from applying the integral form of the conservation laws (2.14) on the control volume $\mathcal{Q}$, i.e.,

$$\sum_{\substack{\mu=s,*,n \\ \nu=e,*,w}} a_{\mu\nu} \boldsymbol{w}_{\mu\nu} = \delta x_{e-0}\, \delta y_{n-0}\, \boldsymbol{w}_{ne} + \delta x_{0-w}\, \delta y_{n-0}\, \boldsymbol{w}_{nw} \qquad (2.33)$$
$$+ \delta x_{0-w}\, \delta y_{0-s}\, \boldsymbol{w}_{sw} + \delta x_{e-0}\, \delta y_{0-s}\, \boldsymbol{w}_{se} - (\boldsymbol{f}_e - \boldsymbol{f}_w) - (\boldsymbol{g}_n - \boldsymbol{g}_s),$$

as long as $\mathcal{R}_{**} \neq 0$. Each flux on the right-hand side of the previous equation is obtained from a time-surface integral at the control volume's outer face α, see Figure 2.3a, e.g.,

$$\boldsymbol{f}_e = \tfrac{\Delta t}{2}\left((2y_u - y_0 - s_n^e \Delta t)\, \boldsymbol{f}_{ne} + (s_n^e - s_s^e)\, \Delta t \boldsymbol{f}_{*e} + (s_s^e \Delta t + y_0 - 2y_d)\, \boldsymbol{f}_{se}\right). \qquad (2.34)$$

We note that the author in [145] does not explicitly mention the procedure to define the transverse fluxes $\boldsymbol{f}_{*e}$, $\boldsymbol{f}_{*w}$, $\boldsymbol{g}_{n*}$ and $\boldsymbol{g}_{s*}$, but instead writes that $\boldsymbol{f}_{*e} = \boldsymbol{f}(\boldsymbol{w}_{*e})$ and $\boldsymbol{g}_{n*} = \boldsymbol{g}(\boldsymbol{w}_{n*})$, assuming analogous expressions for the other fluxes. Moreover, in (2.33), we used the abbreviations $\delta x_{\alpha-\beta}$ and $\delta y_{\alpha-\beta}$ to indicate the differences

$$\delta x_{\alpha-\beta} = x_\alpha - x_\beta \quad \text{and} \quad \delta y_{\alpha-\beta} = y_\alpha - y_\beta, \quad \alpha, \beta \in \{n, s, e, w, 0\}. \qquad (2.35)$$

Once the intermediate constant state is found from solving equation (2.33), the approximation (2.32) is properly defined in the subdomain $\mathcal{R} = \mathcal{D}_{i,j}$. If we repeat the process for each vertex of $\mathcal{C}_{i,j}$, we obtain the four approximations needed to calculate the value $\mathbf{w}_{i,j}^{n+1}$ (2.28).

However, despite the valuable wave model and the consistency with the integral form introduced by Wendroff, the resulting scheme is mainly first-order in both space and time and a higher-order version is not straightforward considering its general formulation. For some details regarding the difficulty in proving the positivity and stability of the method, as well as the behavior of entropy, we refer the reader to [145].

2.1.3 Balsara's Multidimensional HLL Solver

In 2010, eleven years after Wendroff's contribution to the recently growing collection of multidimensional solvers, Balsara [9] formulated a two-dimensional HLL solver that included closed-form, approximate expressions for the fluxes, thus providing a relatively

simple implementation of the resulting scheme. Two years later, the same author succeeded in constructing a more robust version of his own solver and presented it in the first pages of [10], and recently, extended it to unstructured meshes [11]. Here, we concisely detail the fundamental ideas behind the second paper [10], in a way that will be useful for future comparisons with the method proposed in this chapter.

(a) Surface at time $t = \Delta t$ of $\mathcal{Q}$

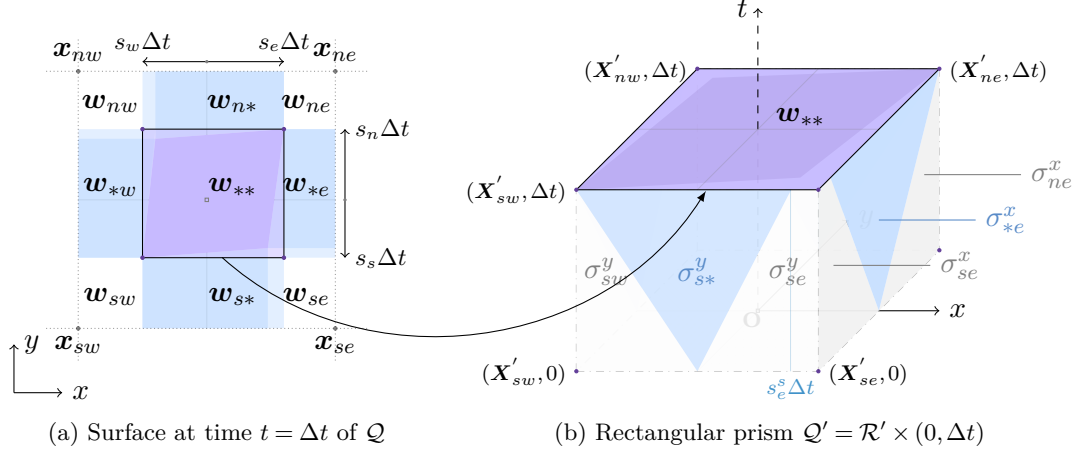(b) Rectangular prism $\mathcal{Q}' = \mathcal{R}' \times (0, \Delta t)$

FIGURE 2.4. Specific choice for the rectangle proposed by Balsara [9, 10], which bounds the strong interaction region arising from the two-dimensional interaction of waves at the origin **O**.

Once again, the interest lies in finding an approximate solution to the 2D Riemann problem (2.12, 2.20), now conveniently centered at the origin $\mathbf{O} = (\boldsymbol{x}_0, t_0)$ with $\boldsymbol{x}_0 = (0,0)$ and $t_0 = 0$. Balsara's proposal [10] involves a constant approximation of the two-dimensional interaction region's composite structure and under a subsonic condition, he assumes this region to be bounded at time $\Delta t > 0$ by the rectangle

$$\mathcal{R}' = (s_w \Delta t, s_e \Delta t) \times (s_s \Delta t, s_n \Delta t), \quad s_w, s_s < 0 \ \text{ and } \ s_n, s_e > 0, \tag{2.36}$$

with its vertices $\boldsymbol{X}'_{ne}$, $\boldsymbol{X}'_{nw}$, $\boldsymbol{X}'_{sw}$, and $\boldsymbol{X}'_{se}$ respectively located in the four known quadrants of the xy-plane. He then chooses the control volume $\mathcal{Q}'$ to be the rectangular prism formed with $\mathcal{R}'$ (2.36) as its base to make the forthcoming integral evaluations easier. Figure 2.4b aims to show this three-dimensional element graphically and Figure 2.4a might assist in visualizing how the interaction region is chosen.

Considering the control volume $\mathcal{Q}' = \mathcal{R}' \times (0, \Delta t)$ with $|\mathcal{R}'| = \Delta t^2 (s_e - s_w)(s_n - s_s)$, an algebraic expression for the constant state $\boldsymbol{w}_{**}$ can be found based on the integral form (2.14), namely

$$\begin{aligned}
|\mathcal{R}'|\boldsymbol{w}_{**} = {}& s_s s_w \Delta t^2 \boldsymbol{w}_{sw} - s_s s_e \Delta t^2 \boldsymbol{w}_{se} - s_n s_w \Delta t^2 \boldsymbol{w}_{nw} + s_n s_e \Delta t^2 \boldsymbol{w}_{ne} \\
& + \sigma^x_{sw} \boldsymbol{f}_{sw} + \sigma^x_{nw} \boldsymbol{f}_{nw} - \sigma^x_{ne} \boldsymbol{f}_{ne} - \sigma^x_{se} \boldsymbol{f}_{se} + \sigma^y_{sw} \boldsymbol{g}_{sw} + \sigma^y_{se} \boldsymbol{g}_{se} - \sigma^y_{nw} \boldsymbol{g}_{nw} - \sigma^y_{ne} \boldsymbol{g}_{ne} \\
& + \sigma^x_{*w} \boldsymbol{f}_{*w} - \sigma^x_{*e} \boldsymbol{f}_{*e} + \sigma^y_{s*} \boldsymbol{g}_{s*} - \sigma^y_{n*} \boldsymbol{g}_{n*},
\end{aligned} \tag{2.37}$$

denoting by $\sigma_{\mu e}^x$ and $\sigma_{\mu w}^x$, $\mu = n, *, s$, the areas of the trapezoidal or triangular sections generated by the slowest and fastest waves arising from each of the one-dimensional Riemann problems at the corresponding planar faces $x = s_e \Delta t$ and $x = s_w \Delta t$, as can be appreciated in Figure 2.4b. In an analogous manner, the areas of the zones formed at the outer surfaces $y = s_n \Delta t$ and $y = s_s \Delta t$ are respectively represented by $\sigma_{n\nu}^y$ and $\sigma_{s\nu}^y$, with $\nu = e, *, w$.

To solve for the state $\boldsymbol{w}_{**}$, we note that all variables in the right-hand side of equation (2.37) are known, with the exception of the fluxes appearing in the last line, i.e., the transverse fluxes introduced briefly in the prior section. Momentarily focusing on the one-dimensional Riemann problem above the x-axis with initial states $\boldsymbol{w}_l = \boldsymbol{w}_{nw}$ and $\boldsymbol{w}_r = \boldsymbol{w}_{ne}$, we realize that its solution provided by the HLL approximate Riemann solver yields the intermediate constant state $\boldsymbol{w}_{n*}$ (2.24) and normal flux $\boldsymbol{f}_{n*}$ (2.23), but not the transverse flux $\boldsymbol{g}_{n*}$. A similar scenario holds for each of the other one-dimensional Riemann problems. However, Balsara offers a solution in [10], which will be carefully summarized in the following paragraph.

Roughly, each transverse flux can be constructed using values extracted from the associated intermediate state and normal flux. Using the notation introduced in the first paragraphs of Chapter 1, where vector elements are designated by superscripts placed in brackets to avoid confusion with exponents, one constructs the transverse fluxes as

$$\boldsymbol{f}_{*\nu} = \begin{pmatrix} w_{*\nu}^{[2]} \\ g_{*\nu}^{[3]} + ((w_{*\nu}^{[2]})^2 - (w_{*\nu}^{[3]})^2)/w_{*\nu}^{[1]} \\ w_{*\nu}^{[3]} w_{*\nu}^{[2]}/w_{*\nu}^{[1]} \\ w_{*\nu}^{[2]} g_{*\nu}^{[4]}/w_{*\nu}^{[3]} \end{pmatrix}, \quad \boldsymbol{g}_{\mu*} = \begin{pmatrix} w_{\mu*}^{[3]} \\ w_{\mu*}^{[2]} w_{\mu*}^{[3]}/w_{\mu*}^{[1]} \\ f_{\mu*}^{[2]} + ((w_{\mu*}^{[3]})^2 - (w_{\mu*}^{[2]})^2)/w_{\mu*}^{[1]} \\ w_{\mu*}^{[3]} f_{\mu*}^{[4]}/w_{\mu*}^{[2]} \end{pmatrix}, \quad (2.38)$$

where $\nu = e$ or w and $\mu = n$ or s.

Now, the only unknown in equation (2.37) is $\boldsymbol{w}_{**}$, which can be expanded by substituting particular values for each of the zone areas at the four faces normal to the main directions x and y such that

$$
\begin{aligned}
\frac{|\mathcal{R}'|}{\Delta t^2} \boldsymbol{w}_{**} = {} & s_s s_w \boldsymbol{w}_{sw} - s_s s_e \boldsymbol{w}_{se} - s_n s_w \boldsymbol{w}_{nw} + s_n s_e \boldsymbol{w}_{ne} \\
& + s_s (\boldsymbol{f}_{se} - \boldsymbol{f}_{sw}) - s_n (\boldsymbol{f}_{ne} - \boldsymbol{f}_{nw}) + s_e (\boldsymbol{g}_{se} - \boldsymbol{g}_{ne}) - s_w (\boldsymbol{g}_{sw} - \boldsymbol{g}_{nw}) \\
& + \tfrac{1}{2} [s_s^w (\boldsymbol{f}_{sw} - \boldsymbol{f}_{*w}) - s_s^e (\boldsymbol{f}_{se} - \boldsymbol{f}_{*e}) - s_n^w (\boldsymbol{f}_{nw} - \boldsymbol{f}_{*w}) + s_n^e (\boldsymbol{f}_{ne} - \boldsymbol{f}_{*e})] \\
& + \tfrac{1}{2} [s_w^s (\boldsymbol{g}_{sw} - \boldsymbol{g}_{s*}) - s_e^s (\boldsymbol{g}_{se} - \boldsymbol{g}_{s*}) - s_w^n (\boldsymbol{g}_{nw} - \boldsymbol{g}_{n*}) + s_e^n (\boldsymbol{g}_{ne} - \boldsymbol{g}_{n*})] = d_1.
\end{aligned}
\quad (2.39)
$$

The focus now shifts from obtaining the interaction state to determining the associated fluxes $\boldsymbol{f}_{**}$ and $\boldsymbol{g}_{**}$. Balsara's approach to derive them is based on the arguments used to define the one-dimensional HLL flux along the t-axis by means of any of the two equations (2.4). In two dimensions, equivalent formulations can be found by employing the integral form (2.14) over sub-rectangular prisms obtained by partitioning the principal space-time control volume so that the time axis is positioned at a face. Among other choices, it can for instance be divided along the x- or y-axis to get four possible volumes $\mathcal{Q}_w' = (s_w \Delta t, 0) \times (s_s \Delta t, s_n \Delta t) \times (0, \Delta t)$, $\mathcal{Q}_s' = (s_w \Delta t, s_e \Delta t) \times (s_s \Delta t, 0) \times (0, \Delta t)$, $\mathcal{Q}_e' = (0, s_e \Delta t) \times (s_s \Delta t, s_n \Delta t) \times (0, \Delta t)$ and lastly, $\mathcal{Q}_n' = (s_w \Delta t, s_e \Delta t) \times (0, s_n \Delta t) \times (0, \Delta t)$.

Before proceeding, we remark that the assumed subsonic case ($s_w, s_s < 0$ and $s_n, s_e > 0$) guarantees that the inverted pyramidal structure, a consequence for the evolution of the rectangular interaction region from time 0 to Δt, contains the vertical time axis. One can therefore determine the two unknowns $\boldsymbol{f}_{**}$ and $\boldsymbol{g}_{**}$ by performing space-time integrations over any two of the above-mentioned volumes.
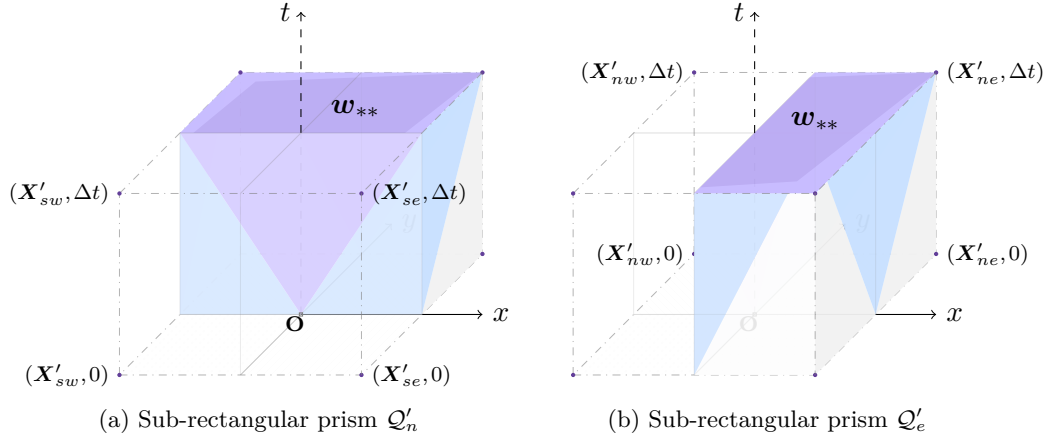

(a) Sub-rectangular prism $\mathcal{Q}'_n$ (b) Sub-rectangular prism $\mathcal{Q}'_e$

FIGURE 2.5. Sub-rectangular prisms used by Balsara [9, 10] to determine the x-flux $\boldsymbol{f}_{**}$ and y-flux $\boldsymbol{g}_{**}$ associated with the strong interaction region.

Choosing first $\mathcal{Q}'_e$, Balsara [9, 10] applies the integral conservation law (2.14) over this space-time volume to obtain the equality

$$
\begin{aligned}
s_e\,(s_n - s_s)\,\boldsymbol{w}_{**} &- \tfrac{1}{2}\,(s_n - s_s)\,\boldsymbol{f}_{**} \\
&= -s_s s_e\,\boldsymbol{w}_{se} + s_n s_e\,\boldsymbol{w}_{ne} + \tfrac{1}{2}\,[\,s_w^{s+}\boldsymbol{g}_{sw} - s_w^{n+}\boldsymbol{g}_{nw} + s_n\boldsymbol{\phi}_n^{hll} - s_s\boldsymbol{\phi}_s^{hll}\,] \\
&\quad + \tfrac{1}{2}\,[\,(2s_e - s_e^{s+})\boldsymbol{g}_{se} - (2s_e - s_e^{n+})\boldsymbol{g}_{ne} - (s_e^{n+} - s_w^{n+})\boldsymbol{g}_{n*} + (s_e^{s+} - s_w^{s+})\boldsymbol{g}_{s*}\,] \\
&\quad\quad - \tfrac{1}{2}\,[\,(-2s_s + s_s^e)\boldsymbol{f}_{se} + (2s_n - s_n^e)\boldsymbol{f}_{ne} + (s_n^e - s_s^e)\boldsymbol{f}_{*e}\,] = d_2,
\end{aligned}
\tag{2.40}
$$

having grouped the unknown quantities associated with the strong interaction region on the left-hand side. The flux $\boldsymbol{\phi}_\mu^{hll}$, $\mu = n$ or s, is to (2.24a) what the numerical flux along the t-axis (2.7) is to (2.10). In order to obtain the numerical y-flux $\boldsymbol{g}_{**}$, the integration of the conservation law (2.14) is performed over the volume $\mathcal{Q}'_n$ shown in Figure 2.5a, yielding the expression

$$
\begin{aligned}
s_n\,(s_e - s_w)\,\boldsymbol{w}_{**} &- \tfrac{1}{2}\,(s_e - s_w)\,\boldsymbol{g}_{**} \\
&= -s_n s_w\,\boldsymbol{w}_{nw} + s_n s_e\,\boldsymbol{w}_{ne} + \tfrac{1}{2}\,[\,s_s^{w+}\boldsymbol{f}_{sw} - s_s^{e+}\boldsymbol{f}_{se} + s_e\boldsymbol{\phi}_e^{hll} - s_w\boldsymbol{\phi}_w^{hll}\,] \\
&\quad + \tfrac{1}{2}\,[\,(2s_n - s_n^{w+})\boldsymbol{f}_{nw} - (2s_n - s_n^{e+})\boldsymbol{f}_{ne} - (s_n^{e+} - s_s^{e+})\boldsymbol{f}_{*e} + (s_n^{w+} - s_s^{w+})\boldsymbol{f}_{*w}\,] \\
&\quad\quad - \tfrac{1}{2}\,[\,(-2s_w + s_w^n)\boldsymbol{g}_{nw} + (2s_e - s_e^n)\boldsymbol{g}_{ne} + (s_e^n - s_w^n)\boldsymbol{g}_{n*}\,] = d_3,
\end{aligned}
\tag{2.41}
$$

written in terminology analogous to that described above.

Using Figure 2.5 as reference, we are able to understand why the wave speeds involving a plus sign, following the notation established in (2.5), are needed in the previous

equations. Basically, their introduction allows to handle supersonic cases provided they appear. For example, consider the situation where the x-directional Riemann problem with initial states $\boldsymbol{w}_{nw}$ and $\boldsymbol{w}_{ne}$ admits speed estimates $s_w^n < 0$ and $s_e^n > 0$, so that part of the required subsonic condition (2.36) is satisfied. Now, let us suppose that only the flow below the x-axis is supersonic with strictly positive wave speeds s_w^s, s_e^s. Note then that the terms $s_w^{s+}\boldsymbol{g}_{sw}$ and $(s_e^{s+} - s_w^{s+})\boldsymbol{g}_{s*}$ in equation (2.40) are non-zero, as they should be, providing the needed contributions to the appropriate estimation of $\boldsymbol{f}_{**}$.

The system of linear equations (2.39, 2.40, 2.41) can be easily expressed in matrix form $\boldsymbol{C}\mathbf{y} = \boldsymbol{d}$, specifically

$$\begin{pmatrix} \frac{1}{\Delta t^2}|\mathcal{R}'| & 0 & 0 \\ s_e(s_n - s_s) & -\frac{1}{2}(s_n - s_s) & 0 \\ s_n(s_e - s_w) & 0 & -\frac{1}{2}(s_e - s_w) \end{pmatrix} \begin{pmatrix} \boldsymbol{w}_{**} \\ \boldsymbol{f}_{**} \\ \boldsymbol{g}_{**} \end{pmatrix} = \begin{pmatrix} d_1 \\ d_2 \\ d_3 \end{pmatrix}, \qquad (2.42)$$

such that one is readily able to retrieve $\det \boldsymbol{C} = \frac{1}{4\Delta t^4}|\mathcal{R}'|^2$, which without any doubt is strictly positive as long as $|\mathcal{R}'| \neq 0$ (recall that $\Delta t \neq 0$). From standard linear algebra, one thus finds the inverse matrix

$$\boldsymbol{C}^{-1} = \frac{\Delta t^2}{|\mathcal{R}'|} \begin{pmatrix} 1 & 0 & 0 \\ 2\,s_e & -2(s_e - s_w) & 0 \\ 2\,s_n & 0 & -2(s_n - s_s) \end{pmatrix}, \qquad (2.43)$$

and compute the unique solution $\mathbf{y} = \boldsymbol{C}^{-1}\mathbf{d}$ for the subsonic case.

In the event that the underlying flow is supersonic in both x and y directions, Balsara solves for the intermediate state directly from equation (2.39) and explicitly defines $\boldsymbol{f}_{**}$ and $\boldsymbol{g}_{**}$ at point $(\boldsymbol{x}_0, \Delta t)$ as the properly upwinded fluxes

$$\boldsymbol{\mathcal{F}}_{**} = (\boldsymbol{f}_{**}, \boldsymbol{g}_{**}) = \begin{cases} (\,\boldsymbol{f}_{sw}\,,\,\boldsymbol{g}_{sw}\,) & \text{if } s_s \geq 0 \text{ and } s_w \geq 0, \\ (\,\boldsymbol{f}_{se}\,,\,\boldsymbol{g}_{se}\,) & \text{if } s_s \geq 0 \text{ and } s_e \leq 0, \\ (\,\boldsymbol{f}_{nw}\,,\,\boldsymbol{g}_{nw}\,) & \text{if } s_n \leq 0 \text{ and } s_w \geq 0, \\ (\,\boldsymbol{f}_{ne}\,,\,\boldsymbol{g}_{ne}\,) & \text{if } s_n \leq 0 \text{ and } s_e \leq 0, \end{cases} \qquad (2.44)$$

as given in [10, p. 7483]. On the same page, one also finds the expressions for the fluxes that are meant to be used in the remaining situations where the flow is fully supersonic in one of the two spatial directions, but subsonic in the other. For specific details concerning the appropriate use of $\boldsymbol{\mathcal{F}}_{**}$ at the cells' interfaces, see Section 2.2.4.2.

2.2 Simple Two-Dimensional HLL Riemann Solver

In this section, a simple method is developed to numerically approximate the solution of the two-dimensional Riemann problem (2.12, 2.20). Suitably built as an extension of the well-known HLL formalism to two dimensions, the scheme relies heavily on the proper utilization of Rankine-Hugoniot relations, which hold across the surfaces of discontinuity that emerge from the origin $\mathbf{O}$, to estimate the constant flux $\boldsymbol{\mathcal{F}}_{**}$. Hence, before embarking on the details, we must understand what these conditions are like in two dimensions.

2.2.1   Rankine-Hugoniot Relation in Two Dimensions

We are interested in the derivation of the Rankine-Hugoniot relation in two dimensions from a general point of view. The system of conservation laws in (2.12) can be rewritten as

$$\widetilde{\nabla} \cdot \boldsymbol{\mathcal{U}}^{[\theta]} = 0, \quad \theta = 1, \dots, \vartheta, \tag{2.45}$$

with $\widetilde{\nabla}$ the nabla operator in the physical space (x, y, t) and $\boldsymbol{\mathcal{U}}^{[\theta]} = (f^{[\theta]}, g^{[\theta]}, w^{[\theta]})$. Assume that $\boldsymbol{\mathcal{U}}^{[\theta]}$ is a bounded measurable function and divergence-free in a weak sense over an open region $\Omega \subset \mathbb{R}^2 \times (0, \infty)$ such that

$$\int_\Omega \widetilde{\nabla} \varphi \cdot \boldsymbol{\mathcal{U}}^{[\theta]} \, \mathrm{d}\boldsymbol{x} \, \mathrm{d}t = 0, \tag{2.46}$$

for all continuously differentiable test functions $\varphi : \Omega \to \mathbb{R}$ with compact support and for every $\theta \in \{1, \dots, \vartheta\}$.

Let us consider a two-dimensional smooth surface $\mathcal{S}$ that splits the region Ω into two open parts Ω_l and Ω_r. Suppose that $\boldsymbol{\mathcal{U}}^{[\theta]}$ is smooth in each of the parts' interiors and uniformly continuous up to $\mathcal{S}$, and also that it has limits along $\mathcal{S}$ from the left and from the right, denoted by $\boldsymbol{\mathcal{U}}_l^{[\theta]}$ and $\boldsymbol{\mathcal{U}}_r^{[\theta]}$. Thus, based on the Rankine-Hugoniot relation theorem presented in [152], equation (2.46) along $\mathcal{S}$ is equivalent to

$$\bar{\boldsymbol{n}} \cdot \left(\boldsymbol{\mathcal{U}}_r^{[\theta]} - \boldsymbol{\mathcal{U}}_l^{[\theta]} \right) = 0, \quad \theta = 1, \dots, \vartheta, \tag{2.47}$$

where $\bar{\boldsymbol{n}} = (n_x, n_y, n_t)$ is the unit normal of the surface, pointing from Ω_l to Ω_r. The previous equation in expanded form is $n_x(f_l^{[\theta]} - f_r^{[\theta]}) + n_y(g_l^{[\theta]} - g_r^{[\theta]}) + n_t(w_l^{[\theta]} - w_r^{[\theta]}) = 0$, but is most commonly expressed as

$$[\![n_x f^{[\theta]} + n_y g^{[\theta]}]\!] = \sigma [\![w^{[\theta]}]\!], \quad \theta = 1, \dots, \vartheta, \tag{2.48}$$

having defined $\sigma = -n_t$ and the jump

$$[\![(\cdot)]\!] = (\cdot)_r - (\cdot)_l. \tag{2.49}$$

For self-similar solutions, the discontinuity surface $\mathcal{S}$ described by an equation of the form $(a, b, c) \cdot (x, y, t) = 0$, may be identified by a similarity curve in the (ξ, η) plane having the form $\Gamma(\xi, \eta) = a\xi + b\eta + c = 0$ and its normal can easily be obtained as the gradient $\nabla \Gamma(\xi, \eta)$ in the physical space (x, y, t), i.e.,

$$\boldsymbol{n} = \left(\frac{\partial \Gamma}{\partial \xi} \frac{\partial \xi}{\partial x}, \frac{\partial \Gamma}{\partial \eta} \frac{\partial \eta}{\partial y}, \frac{\partial \Gamma}{\partial \xi} \frac{\partial \xi}{\partial t} + \frac{\partial \Gamma}{\partial \eta} \frac{\partial \eta}{\partial t} \right) = \frac{1}{t} (a, b, c). \tag{2.50}$$

Now that all the theoretical notions have been formally introduced, we can proceed with the complete description of the proposed scheme.

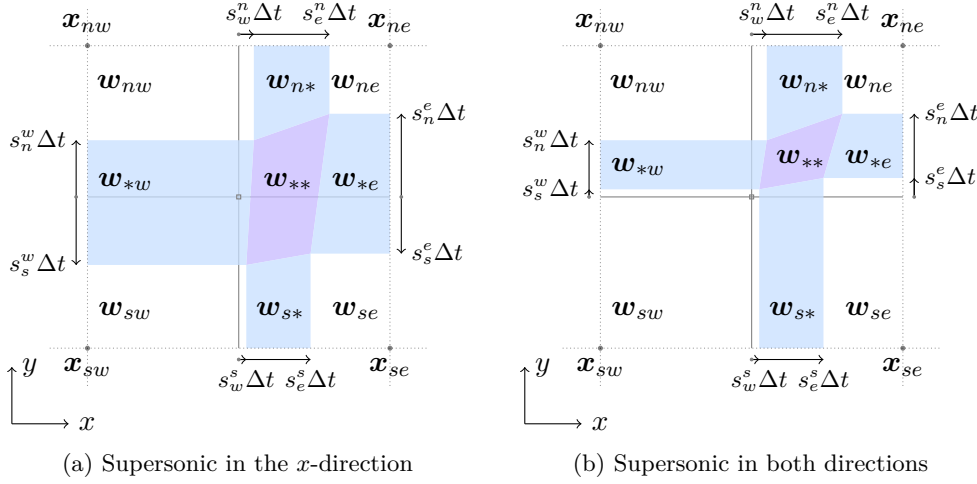(a) Supersonic in the x-direction   (b) Supersonic in both directions

FIGURE 2.6. Two examples of structures formed at time $t = \Delta t$ by outward propagating waves related to flows that are supersonic in at least one of the spatial directions.

2.2.2   Derivation of Intermediate States and Fluxes

Any approach that deliberately aims to extend the approximate Riemann solver of HLL type to two dimensions involves in some way the constant approximation of intermediate states, as is our case. Furthermore, we expect the solution of the two-dimensional Riemann problem (2.12, 2.20) to be self-similar, as was indicated in Section 2.1.1, and we need to ensure that an implementation of our method invariably satisfies this property.

We therefore base our wave model and space-time control volume $\mathcal{Q}$ that will be used in our forthcoming developments on the ones suggested by Wendroff in [145], accurately portrayed in Figure 2.3 and carefully detailed in Section 2.1.2 of this chapter. Our strong preference for his setup over other possible ones comes from the fact that it encloses not only subsonic but also supersonic flow structures, e.g., those shown in Figure 2.6, and provides the correct profile for the eventual use of jump conditions, which is readily seen from the fact that the associated discontinuity planes and their normals are self-similar. Moreover, the approximate Riemann solver is self-similar as long as the states defined in the nine non-overlapping subdomains (resulting from the evolution in time of initial data by virtue of flat space-time surfaces arising from an origin **O**) are self-similar themselves: indeed, constant values on self-similar subdomains are always self-similar, i.e., $\boldsymbol{w}_{sw}$, $\boldsymbol{w}_{se}$, $\boldsymbol{w}_{nw}$ and $\boldsymbol{w}_{ne}$ satisfy this property, and for the other states, self-similarity is achieved when $\boldsymbol{w}_{n*}$, $\boldsymbol{w}_{s*}$, $\boldsymbol{w}_{*e}$, $\boldsymbol{w}_{*w}$ and $\boldsymbol{w}_{**}$ are functions of ξ, ξ, η, η and (ξ, η), respectively.

Now, we take into account Balsara's approach to reformulate Wendroff's approximate, quadrangular wave model and make use of the consistency with the integral formulation through jump conditions to obtain the intermediate states and fluxes. However, contrary to the 1D HLL solver, the two-dimensional HLL derivation will only satisfy these jump conditions in a weak sense.

2.2.2.1   Strongly Interacting State

Regardless of the type, a flow characterized by the considered wave model forms specific patterns at the control volume's faces that can be generalized as follows: the bottom flat surface $t = t_0$ comprises the four rectangles determined by the initial states $\boldsymbol{w}_{ne}, \boldsymbol{w}_{nw}, \boldsymbol{w}_{sw}$, and $\boldsymbol{w}_{se}$, each in its corresponding quadrant; the top face $t = \Delta t$ consists of four trapezoids that result from applying the one-dimensional HLL [74] solver at the underlying edges as described in Section 2.1.2, four rectangles containing unaltered initial data, and a quadrilateral defined by the points $\mathbf{Q}_{sw}, \mathbf{Q}_{se}, \mathbf{Q}_{nw}$ and $\mathbf{Q}_{ne}$ (with speeds given in equation (2.21) for the general case) which bounds all two-dimensional interactions at time Δt that originated from $\mathbf{O}$; and each of the lateral faces retains a structure similar to that of Figure 2.1 created by a two-wave Riemann fan.

Therefore, all of the individual regions found at the rectangular prism's surfaces have simple geometric shapes and a computation of their areas does not pose a challenge. This facilitates the application of the integral conservation law (2.14) over it, i.e., over the discussed control volume $\mathcal{Q} = \mathcal{R} \times (0, \Delta t)$, providing a straightforward expression to obtain $\boldsymbol{w}_{**}$ given by

$$
\begin{aligned}
\sum_{\substack{\mu=s,*,n \\ \nu=e,*,w}} a_{\mu\nu}\boldsymbol{w}_{\mu\nu} = {}& x_r y_u \,\boldsymbol{w}_{ne} - x_l y_u \,\boldsymbol{w}_{nw} + x_l y_d \,\boldsymbol{w}_{sw} - x_r y_d \,\boldsymbol{w}_{se} \\
& - \tfrac{\Delta t}{2} \left[(2y_u - s_n^e \Delta t)\,\boldsymbol{f}_{ne} - (2y_u - s_n^w \Delta t)\,\boldsymbol{f}_{nw} + (2y_d - s_s^w \Delta t)\,\boldsymbol{f}_{sw} - (2y_d - s_s^e \Delta t)\,\boldsymbol{f}_{se} \right] \\
& - \tfrac{\Delta t}{2} \left[(2x_r - s_e^n \Delta t)\,\boldsymbol{g}_{ne} - (2y_l - s_w^n \Delta t)\,\boldsymbol{g}_{nw} + (2y_l - s_w^s \Delta t)\,\boldsymbol{g}_{sw} - (2x_r - s_e^s \Delta t)\,\boldsymbol{g}_{se} \right] \\
& - \tfrac{\Delta t^2}{2} \left[s_e^n \,(s_e^n - s_w^n)\,\boldsymbol{g}_{n*} - (s_e^s - s_w^s)\,\boldsymbol{g}_{s*} + (s_n^e - s_s^e)\,\boldsymbol{f}_{*e} - (s_n^w - s_s^w)\,\boldsymbol{f}_{*w} \right],
\end{aligned}
$$
$$(2.51)$$

where the origin $\mathbf{O}$ was set to $(0,0,0)$, taking $\boldsymbol{x}_0 = (0,0)$ and $t_0 = 0$, to make later computations simpler. We wish to note that the nine areas $a_{\mu\nu}$ ($\mu = n, *, s$, $\nu = e, *, w$) correspond to the previously identified regions located at the top face, which in turn has a total surface area $|\mathcal{R}| = \delta x_{e-w}\,\delta y_{n-s}$ since $\mathcal{R} = (x_w, x_e) \times (y_s, y_n)$, and it is rather easy to define the main quadrilateral's extent a_{**} as a remaining value, notably

$$
\begin{aligned}
a_{**} &= |\mathcal{R}| - a_{ne} - a_{n*} - a_{nw} - a_{*w} - a_{sw} - a_{s*} - a_{se} - a_{*e} \\
&= \tfrac{\Delta t^2}{2} \left[(s_e^n - s_w^s)(s_n^w - s_s^e) + (s_n^e - s_s^w)(s_e^s - s_w^n) \right].
\end{aligned}
\tag{2.52}
$$

Substituting then the constant one-dimensional intermediate states $\boldsymbol{w}_{n*}, \boldsymbol{w}_{s*}, \boldsymbol{w}_{*e}$ and $\boldsymbol{w}_{*w}$ defined in (2.23), in conjunction with the particular values of all areas having the form $a_{\mu\nu}$ such as a_{**} (2.52), into the left-hand side of equation (2.51) yields

$$
\begin{aligned}
\boldsymbol{w}_{**} = {}& \frac{1}{(s_e^n - s_w^s)(s_n^w - s_s^e) + (s_n^e - s_s^w)(s_e^s - s_w^n)} \, * \\
& \big[\, (s_n^w s_e^n + s_s^e s_e^n)\boldsymbol{w}_{ne} - (s_n^e s_w^n + s_s^s s_w^n)\boldsymbol{w}_{nw} + (s_s^e s_w^s + s_n^w s_s^s)\boldsymbol{w}_{sw} - (s_s^w s_e^s + s_n^e s_s^s)\boldsymbol{w}_{se} \\
& \quad - s_n^w \boldsymbol{f}_{ne} + s_n^e \boldsymbol{f}_{nw} - s_s^e \boldsymbol{f}_{sw} + s_s^w \boldsymbol{f}_{se} - (s_n^e - s_s^e)\boldsymbol{f}_{*e} + (s_n^w - s_s^w)\boldsymbol{f}_{*w} \\
& \quad - s_e^s \boldsymbol{g}_{ne} + s_w^s \boldsymbol{g}_{nw} - s_w^n \boldsymbol{g}_{sw} + s_e^n \boldsymbol{g}_{se} - (s_e^n - s_w^n)\boldsymbol{g}_{n*} + (s_e^s - s_w^s)\boldsymbol{g}_{s*} \, \big],
\end{aligned}
$$

$$(2.53)$$

after considerable algebraic manipulation. This formulation is only complete after appropriate definitions for the fluxes $\boldsymbol{f}_{*e}$, $\boldsymbol{f}_{*w}$, $\boldsymbol{g}_{n*}$ and $\boldsymbol{g}_{s*}$ have been furnished. For this end, we adopt the solution (2.38) proposed by Balsara, thoroughly detailed in Section 2.1.3, and construct each of these unknown transverse fluxes with values obtained from the corresponding normal flux and intermediate state.

Before turning to the determination of the flux $\boldsymbol{\mathcal{F}}_{**}$, we would like to point out that the strong interaction region in the xy-plane at time Δt is most likely delimited by a sonic line consisting of a circle or ellipse (see [152]) and well contained in the quadrilateral with vertices $\boldsymbol{X}_{sw}(\Delta t)$, $\boldsymbol{X}_{se}(\Delta t)$, $\boldsymbol{X}_{nw}(\Delta t)$, and $\boldsymbol{X}_{ne}(\Delta t)$ and area a_{**}. If a larger interaction region is considered, more dissipation is certainly introduced. For instance, in the case that all wave speeds relax to the minimal and maximal ones defined in equation (2.22), as in [9], the volume's top and bottom surfaces will be formed entirely of rectangular regions and the lateral faces of triangular parts, and equation (2.53) would reduce to

$$\boldsymbol{w}_{**} = \frac{\Delta t^2}{2|\mathcal{R}'|} * \big[\, 2s_n s_e \boldsymbol{w}_{ne} - 2s_n s_w \boldsymbol{w}_{nw} + 2s_s s_w \boldsymbol{w}_{sw} - 2s_s s_e \boldsymbol{w}_{se}$$
$$- s_n \left(\boldsymbol{f}_{ne} - \boldsymbol{f}_{nw}\right) - s_s \left(\boldsymbol{f}_{sw} - \boldsymbol{f}_{se}\right) - s_e \left(\boldsymbol{g}_{ne} - \boldsymbol{g}_{se}\right) - s_w \left(\boldsymbol{g}_{sw} - \boldsymbol{g}_{nw}\right)$$
$$- (s_n - s_s)\left(\boldsymbol{f}_{*e} - \boldsymbol{f}_{*w}\right) - (s_e - s_w)\left(\boldsymbol{g}_{n*} - \boldsymbol{g}_{s*}\right)\,\big],$$
$$(2.54)$$

with $\mathcal{R}' = (s_w \Delta t, s_e \Delta t) \times (s_s \Delta t, s_n \Delta t)$. By comparing this expression with the one derived by Balsara in [10], it is apparent that the dissimilarities arise from considering different wave configurations at the control volume's lateral faces. To be precise, using Figure 2.4b as reference, the approach described in Section 2.1.3 does not require each corner of the two-dimensional interaction region to exactly coincide with the sides of the two neighboring one-dimensional intermediate scopes, whereas the proposed technique essentially does to allow for the use of jump conditions, as will be explained in the immediate section. We remark that in the limit $s_\alpha^\beta \to s_\alpha$ for $\alpha, \beta \in \{n, s, e, w\}$, both equations (2.54) and (2.39) are nevertheless the same.

2.2.2.2 Fluxes from Jump Conditions

We will now restrict ourselves to the derivation of closed form expressions for both fluxes $\boldsymbol{f}_{**}$ and $\boldsymbol{g}_{**}$. Recall that for the one-dimensional case, we exposed in Section 2.1 the equivalence between the integral relation (1.69), also known as the consistency condition, and the use of Rankine-Hugoniot conditions across the outermost waves, as a means to recover the flux in the intermediate region. We wish to extend this latter concept to two dimensions.

Let us denote by $\bar{\boldsymbol{n}}_e = \boldsymbol{n}_e / \|\boldsymbol{n}_e\|$ the unit normal of the plane $\mathcal{S}_e$ that contains the three points $\mathbf{Q}_{se}$, $\mathbf{Q}_{ne}$, and $\mathbf{O}$, as illustrated in Figure 2.7. Without difficulty, we identify the distinct vectors $\overrightarrow{\mathbf{OQ}}_{ne} = (s_e^n \Delta t, s_n^e \Delta t, \Delta t)$ and $\overrightarrow{\mathbf{OQ}}_{se} = (s_e^s \Delta t, s_s^e \Delta t, \Delta t)$ that lie on the flat surface and determine their cross product to compute the normal $\boldsymbol{n}_e$, namely

$$\boldsymbol{n}_e = \overrightarrow{\mathbf{OQ}}_{ne} \times \overrightarrow{\mathbf{OQ}}_{se} = \Delta t^2 \left[(s_n^e - s_s^e)\,\mathbf{i} - (s_e^n - s_e^s)\,\mathbf{j} + (s_e^n s_s^e - s_n^e s_e^s)\,\mathbf{t} \right], \qquad (2.55)$$

with $\mathbf{i}$, $\mathbf{j}$ and $\mathbf{t}$ the standard basis in the physical space (x, y, t). The Rankine-Hugoniot condition across the discontinuity surface $\mathcal{S}_e$ is $\boldsymbol{n}_e \cdot (\boldsymbol{f}_{**} - \boldsymbol{f}_{*e}, \boldsymbol{g}_{**} - \boldsymbol{g}_{*e}, \boldsymbol{w}_{**} - \boldsymbol{w}_{*e}) = 0$,
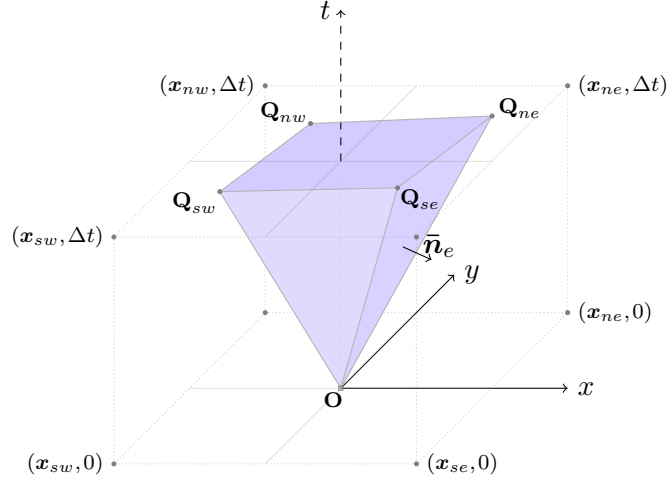
FIGURE 2.7. Planes in the interior of the space-time volume $\mathcal{Q}$.

obtained by means of equation (2.48), which can be rewritten as

$$(s_e^n s_s^e - s_n^e s_e^s)(\boldsymbol{w}_{*e} - \boldsymbol{w}_{**}) + (s_n^e - s_s^e)(\boldsymbol{f}_{*e} - \boldsymbol{f}_{**}) + (s_e^s - s_e^n)(\boldsymbol{g}_{*e} - \boldsymbol{g}_{**}) = 0. \qquad (2.56)$$

For the remaining directions, a similar procedure is employed to get the conditions across the corresponding planes, and a summary of all, including (2.56), is presented below:

$$\text{Ⓝ}\ \overbrace{(s_w^n s_n^e - s_n^w s_e^n)}^{\delta_1^w}(\boldsymbol{w}_{n*} - \boldsymbol{w}_{**}) + \overbrace{(s_n^w - s_n^e)}^{\delta_1^f}(\boldsymbol{f}_{n*} - \boldsymbol{f}_{**}) + \overbrace{(s_e^n - s_w^n)}^{\delta_1^g}(\boldsymbol{g}_{n*} - \boldsymbol{g}_{**}) = 0, \quad (2.57a)$$

$$\text{Ⓦ}\ \overbrace{(s_w^s s_n^w - s_s^w s_w^n)}^{\delta_2^w}(\boldsymbol{w}_{*w} - \boldsymbol{w}_{**}) + \overbrace{(s_s^w - s_n^w)}^{\delta_2^f}(\boldsymbol{f}_{*w} - \boldsymbol{f}_{**}) + \overbrace{(s_w^n - s_w^s)}^{\delta_2^g}(\boldsymbol{g}_{*w} - \boldsymbol{g}_{**}) = 0, \quad (2.57b)$$

$$\text{Ⓢ}\ \overbrace{(s_e^s s_s^w - s_s^e s_w^s)}^{\delta_3^w}(\boldsymbol{w}_{s*} - \boldsymbol{w}_{**}) + \overbrace{(s_s^e - s_s^w)}^{\delta_3^f}(\boldsymbol{f}_{s*} - \boldsymbol{f}_{**}) + \overbrace{(s_w^s - s_e^s)}^{\delta_3^g}(\boldsymbol{g}_{s*} - \boldsymbol{g}_{**}) = 0, \quad (2.57c)$$

$$\text{Ⓔ}\ \overbrace{(s_e^n s_s^e - s_n^e s_e^s)}^{\delta_4^w}(\boldsymbol{w}_{*e} - \boldsymbol{w}_{**}) + \overbrace{(s_n^e - s_s^e)}^{\delta_4^f}(\boldsymbol{f}_{*e} - \boldsymbol{f}_{**}) + \overbrace{(s_e^s - s_e^n)}^{\delta_4^g}(\boldsymbol{g}_{*e} - \boldsymbol{g}_{**}) = 0. \quad (2.57d)$$

Relations (2.57) form a system of linear equations and, since the specific value of the strongly interacting state $\boldsymbol{w}_{**}$ is completely determined by equation (2.53), we opt to rewrite it as

$$\delta_1^f \boldsymbol{f}_{**} + \delta_1^g \boldsymbol{g}_{**} = \delta_1^w(\boldsymbol{w}_{n*} - \boldsymbol{w}_{**}) + \delta_1^f \boldsymbol{f}_{n*} + \delta_1^g \boldsymbol{g}_{n*} = \boldsymbol{b}_1, \qquad (2.58a)$$

$$\delta_2^f \boldsymbol{f}_{**} + \delta_2^g \boldsymbol{g}_{**} = \delta_2^w(\boldsymbol{w}_{*w} - \boldsymbol{w}_{**}) + \delta_2^f \boldsymbol{f}_{*w} + \delta_2^g \boldsymbol{g}_{*w} = \boldsymbol{b}_2, \qquad (2.58b)$$

$$\delta_3^f \boldsymbol{f}_{**} + \delta_3^g \boldsymbol{g}_{**} = \delta_3^w(\boldsymbol{w}_{s*} - \boldsymbol{w}_{**}) + \delta_3^f \boldsymbol{f}_{s*} + \delta_3^g \boldsymbol{g}_{s*} = \boldsymbol{b}_3, \qquad (2.58c)$$

$$\delta_4^f \boldsymbol{f}_{**} + \delta_4^g \boldsymbol{g}_{**} = \delta_4^w(\boldsymbol{w}_{*e} - \boldsymbol{w}_{**}) + \delta_4^f \boldsymbol{f}_{*e} + \delta_4^g \boldsymbol{g}_{*e} = \boldsymbol{b}_4, \qquad (2.58d)$$

with the unknown fluxes on the left hand-side. It is evident that (2.58) is overdetermined, seeing that there are four equations to solve for two unknowns, and the method of ordinary least squares can be utilized to find a solution. Hence, we express the linear system (2.58) in the form $\boldsymbol{A}\mathbf{x} = \boldsymbol{b}$, by defining

$$\boldsymbol{A} = \begin{pmatrix} \delta_1^f & \delta_1^g \\ \delta_2^f & \delta_2^g \\ \delta_3^f & \delta_3^g \\ \delta_4^f & \delta_4^g \end{pmatrix}, \quad \mathbf{x} = \begin{pmatrix} \boldsymbol{f}_{**} \\ \boldsymbol{g}_{**} \end{pmatrix}, \quad \text{and} \quad \boldsymbol{b} = \begin{pmatrix} \delta_1^w(\boldsymbol{w}_{n*} - \boldsymbol{w}_{**}) + \delta_1^f\,\boldsymbol{f}_{n*} + \delta_1^g\,\boldsymbol{g}_{n*} \\ \delta_2^w(\boldsymbol{w}_{*w} - \boldsymbol{w}_{**}) + \delta_2^f\,\boldsymbol{f}_{*w} + \delta_2^g\,\boldsymbol{g}_{*w} \\ \delta_3^w(\boldsymbol{w}_{s*} - \boldsymbol{w}_{**}) + \delta_3^f\,\boldsymbol{f}_{s*} + \delta_3^g\,\boldsymbol{g}_{s*} \\ \delta_4^w(\boldsymbol{w}_{*e} - \boldsymbol{w}_{**}) + \delta_4^f\,\boldsymbol{f}_{*e} + \delta_4^g\,\boldsymbol{g}_{*e} \end{pmatrix}, \quad (2.59)$$

and write the normal equations in matrix notation as $\boldsymbol{A}^T\boldsymbol{A}\mathbf{x} = \boldsymbol{A}^T\boldsymbol{b}$. The least squares solution $\mathbf{x} = \boldsymbol{M}^{-1}\boldsymbol{A}^T\boldsymbol{b} = \boldsymbol{K}\boldsymbol{b}$, provided $\boldsymbol{M} = \boldsymbol{A}^T\boldsymbol{A}$ can be inverted, is the exact one if it exists or an approximate one if it does not.

Considering that $\boldsymbol{M}$ has in fact a strictly positive determinant (A.3) and is consequently nonsingular (see Annex A), we are thus able to get explicit forms for the fluxes in the interaction region as

$$\boxed{\begin{aligned} \boldsymbol{f}_{**} &= [k_{11}\,\boldsymbol{b}_1 + k_{12}\,\boldsymbol{b}_2 + k_{13}\,\boldsymbol{b}_3 + k_{14}\,\boldsymbol{b}_4]\,/\det\boldsymbol{M}, \\ \boldsymbol{g}_{**} &= [k_{21}\,\boldsymbol{b}_1 + k_{22}\,\boldsymbol{b}_2 + k_{23}\,\boldsymbol{b}_3 + k_{24}\,\boldsymbol{b}_4]\,/\det\boldsymbol{M}, \end{aligned}} \qquad \begin{aligned} &(2.60\text{a}) \\ &(2.60\text{b}) \end{aligned}$$

given in terms of the matrix elements

$$\begin{aligned} k_{11} &= \delta_1^f(\delta_2^{g\,2} + \delta_3^{g\,2} + \delta_4^{g\,2}) - \delta_1^g(\delta_2^f\delta_2^g + \delta_3^f\delta_3^g + \delta_4^f\delta_4^g), \\ k_{12} &= \delta_2^f(\delta_1^{g\,2} + \delta_3^{g\,2} + \delta_4^{g\,2}) - \delta_2^g(\delta_1^f\delta_1^g + \delta_3^f\delta_3^g + \delta_4^f\delta_4^g), \\ k_{13} &= \delta_3^f(\delta_1^{g\,2} + \delta_2^{g\,2} + \delta_4^{g\,2}) - \delta_3^g(\delta_1^f\delta_1^g + \delta_2^f\delta_2^g + \delta_4^f\delta_4^g), \\ k_{14} &= \delta_4^f(\delta_1^{g\,2} + \delta_2^{g\,2} + \delta_3^{g\,2}) - \delta_4^g(\delta_1^f\delta_1^g + \delta_2^f\delta_2^g + \delta_3^f\delta_3^g), \\ k_{21} &= \delta_1^g(\delta_2^{f\,2} + \delta_3^{f\,2} + \delta_4^{f\,2}) - \delta_1^f(\delta_2^f\delta_2^g + \delta_3^f\delta_3^g + \delta_4^f\delta_4^g), \\ k_{22} &= \delta_2^g(\delta_1^{f\,2} + \delta_3^{f\,2} + \delta_4^{f\,2}) - \delta_2^f(\delta_1^f\delta_1^g + \delta_3^f\delta_3^g + \delta_4^f\delta_4^g), \\ k_{23} &= \delta_3^g(\delta_1^{f\,2} + \delta_2^{f\,2} + \delta_4^{f\,2}) - \delta_3^f(\delta_1^f\delta_1^g + \delta_2^f\delta_2^g + \delta_4^f\delta_4^g), \\ k_{24} &= \delta_4^g(\delta_1^{f\,2} + \delta_2^{f\,2} + \delta_3^{f\,2}) - \delta_4^f(\delta_1^f\delta_1^g + \delta_2^f\delta_2^g + \delta_3^f\delta_3^g). \end{aligned} \qquad (2.61)$$

The advantage of the suggested formulation over existing ones is that it efficiently encloses all feasible subsonic or supersonic configurations for the two-dimensional interaction of waves associated with the Riemann problem (2.12, 2.20), while providing a single and perspicuous implementation of the approximate variables $\boldsymbol{w}_{**}$ (2.53) and $\boldsymbol{\mathcal{F}}_{**}$ (2.60).

If we regard the elements of the matrix $\boldsymbol{K}$ as weights, we notice that k_{11}, k_{13}, k_{22} and k_{24} become smaller as the strongly interaction region in the $t = \Delta t$ plane turns rectangular. In fact, studying once more the situation discussed at the end of the previous section where this region is a rectangle $\mathcal{R}'$, we perceive that in the limit $s_\alpha^\beta \to s_\alpha$ for $\alpha, \beta \in \{n, s, e, w\}$, $\delta_1^g = -\delta_3^g$, $\delta_4^f = -\delta_2^f$ and $\delta_1^f = \delta_3^f = \delta_2^g = \delta_4^g = 0$. This further implies that

the four mentioned weights become zero and $k_{12} = 2\delta_2^f \delta_1^{g2} = -k_{14}$, $k_{21} = 2\delta_1^g \delta_2^{f2} = -k_{23}$, allowing us to find

$$\boldsymbol{f}_{**} = \tfrac{1}{2}\left[(s_e + s_w)\boldsymbol{w}_{**} - s_e \boldsymbol{w}_{*e} - s_w \boldsymbol{w}_{*w} + \boldsymbol{f}_{*e} + \boldsymbol{f}_{*w}\right], \tag{2.62a}$$

$$\boldsymbol{g}_{**} = \tfrac{1}{2}\left[(s_n + s_s)\boldsymbol{w}_{**} - s_n \boldsymbol{w}_{n*} - s_s \boldsymbol{w}_{s*} + \boldsymbol{g}_{n*} + \boldsymbol{g}_{s*}\right], \tag{2.62b}$$

having substituted the quantities defined in (2.57). Equations (2.62) aid to confirm that our proposed approach is able to pick out the right ingredients for the determination of the numerical flux $\boldsymbol{\mathcal{F}}_{**}$. It is worth observing that for this particular case, $\boldsymbol{f}_{**}$ (respectively, $\boldsymbol{g}_{**}$) is simply the average of the jump conditions across the eastern and western (respectively, northern and southern) planes of the inverted rectangular pyramid, as expected.

The above analysis inspired us to develop alternative formulations to (2.60), which will be duly justified in the subsequent section. For all details pertaining the appropriate use of the resolved fluxes at the primary cells' interfaces, refer to Section 2.2.4.2.

2.2.3   Alternative Formulations

As the linear system (2.58) is mathematically overdetermined, we could theoretically propose infinitely many formulations to estimate $\boldsymbol{\mathcal{F}}_{**}$, not all of which would be sensible. However, in this spirit, we detail two of which will give reasonable solutions and yield shorter expressions than in (2.60), for later interpretation and implementation. The first method gives fluxes that are dependent on the intermediate state $\boldsymbol{w}_{**}$, as opposed to the ones provided by the second. In addition, we briefly present an alternative methodology that involves using the jump conditions to define the transverse fluxes $\boldsymbol{f}_{*e}$, $\boldsymbol{f}_{*w}$, $\boldsymbol{g}_{n*}$ and $\boldsymbol{g}_{s*}$, resulting in a linearly dependent system of equations.

Form I

We first calculate the difference between equations (2.58a) and (2.58c), and separately, the one between (2.58d) and (2.58b), to recover a system of two, not four, linear equations that can be written in condensed form as

$$\begin{pmatrix} \delta_1^f - \delta_3^f & \delta_1^g - \delta_3^g \\ \delta_4^f - \delta_2^f & \delta_4^g - \delta_2^g \end{pmatrix} \begin{pmatrix} \boldsymbol{f}_{**} \\ \boldsymbol{g}_{**} \end{pmatrix} = \begin{pmatrix} \boldsymbol{b}_1 - \boldsymbol{b}_3 \\ \boldsymbol{b}_4 - \boldsymbol{b}_2 \end{pmatrix}, \tag{2.63}$$

where the 2×2 real matrix on the left-hand side is denoted by $\boldsymbol{A}_I$. A straightforward substitution of the terms introduced in (2.57) into this matrix allows us to compute its determinant as $\det \boldsymbol{A}_I = -\frac{4}{\Delta t^2} a_{**}$, which is certainly less than zero on the assumption that both Δt and a_{**} are positive quantities. The unique solution of (2.63) is then

$$\begin{pmatrix} \boldsymbol{f}_{**} \\ \boldsymbol{g}_{**} \end{pmatrix} = -\frac{\Delta t^2}{4 a_{**}} \begin{pmatrix} s_e^s + s_w^s - s_e^n - s_w^n & s_w^n + s_w^s - s_e^n - s_e^s \\ s_s^e + s_s^w - s_n^e - s_n^w & s_n^w + s_s^w - s_n^e - s_s^e \end{pmatrix} \begin{pmatrix} \boldsymbol{b}_1 - \boldsymbol{b}_3 \\ \boldsymbol{b}_4 - \boldsymbol{b}_2 \end{pmatrix}. \tag{2.64}$$

By substituting the constant one-dimensional states and fluxes defined in (2.23) and

(2.24) into the terms $\boldsymbol{b}_1 - \boldsymbol{b}_3$ and $\boldsymbol{b}_4 - \boldsymbol{b}_2$, we obtain

$$
\begin{aligned}
\boldsymbol{b}_1 - \boldsymbol{b}_3 = {}& (s_n^w s_e^n + s_s^w s_e^s - s_w^n s_n^e - s_w^s s_s^e)\boldsymbol{w}_{**} - s_n^w s_e^n \boldsymbol{w}_{ne} + s_w^n s_e^s \boldsymbol{w}_{nw} + s_e^s s_w^s \boldsymbol{w}_{sw} - s_e^s s_s^w \boldsymbol{w}_{se} \\
& + s_n^w \boldsymbol{f}_{ne} - s_n^e \boldsymbol{f}_{nw} - s_s^e \boldsymbol{f}_{sw} + s_s^w \boldsymbol{f}_{se} - (s_w^n - s_e^n)\boldsymbol{g}_{n*} - (s_w^s - s_e^s)\boldsymbol{g}_{s*}, \\
\boldsymbol{b}_4 - \boldsymbol{b}_2 = {}& (s_n^e s_e^s + s_n^w s_w^s - s_s^e s_e^n - s_s^w s_w^n)\boldsymbol{w}_{**} - s_e^s s_n^e \boldsymbol{w}_{ne} - s_w^s s_n^w \boldsymbol{w}_{nw} + s_e^w s_n^n \boldsymbol{w}_{sw} + s_e^n s_s^e \boldsymbol{w}_{se} \\
& + s_e^s \boldsymbol{g}_{ne} + s_w^s \boldsymbol{g}_{nw} - s_w^n \boldsymbol{g}_{sw} - s_e^n \boldsymbol{g}_{se} - (s_s^e - s_n^e)\boldsymbol{f}_{*e} - (s_s^w - s_n^w)\boldsymbol{f}_{*w},
\end{aligned}
$$

so the fluxes $\boldsymbol{f}_{**}$ and $\boldsymbol{g}_{**}$ possess a clear and condensed form. Note that in the limit $s_\alpha^\beta \to s_\alpha$, with $\alpha, \beta \in \{n, s, e, w\}$, system (2.64) corresponds to (2.62).

Form II

We shall now describe a method that is built with the specific intention of eliminating the contribution of the resolved state $\boldsymbol{w}_{**}$ to the flux tensor $\boldsymbol{\mathcal{F}}_{**}$. We start by summing equation (2.57a) multiplied by δ_3^w and equation (2.57c) multiplied by $-\delta_1^w$, to get

$$
\begin{aligned}
(\delta_1^f \delta_3^w - \delta_3^f \delta_1^w)\boldsymbol{f}_{**} + (\delta_1^g \delta_3^w - \delta_3^g \delta_1^w)\boldsymbol{g}_{**} = {}& \delta_1^w \delta_3^w (\boldsymbol{w}_{n*} - \boldsymbol{w}_{s*}) + \delta_1^f \delta_3^w \boldsymbol{f}_{n*} \\
& - \delta_3^f \delta_1^w \boldsymbol{f}_{s*} + \delta_1^g \delta_3^w \boldsymbol{g}_{n*} - \delta_3^g \delta_1^w \boldsymbol{g}_{s*} = \boldsymbol{c}_1,
\end{aligned} \tag{2.66}
$$

and in an analogous manner, we multiply equation (2.57d) by δ_2^w and equation (2.57b) by $-\delta_4^w$ so that their sum gives

$$
\begin{aligned}
(\delta_4^f \delta_2^w - \delta_2^f \delta_4^w)\boldsymbol{f}_{**} + (\delta_4^g \delta_2^w - \delta_2^g \delta_4^w)\boldsymbol{g}_{**} = {}& \delta_4^w \delta_2^w (\boldsymbol{w}_{*e} - \boldsymbol{w}_{*w}) + \delta_4^f \delta_2^w \boldsymbol{f}_{*e} \\
& - \delta_2^f \delta_4^w \boldsymbol{f}_{*w} + \delta_4^g \delta_2^w \boldsymbol{g}_{*e} - \delta_2^g \delta_4^w \boldsymbol{g}_{*w} = \boldsymbol{c}_2.
\end{aligned} \tag{2.67}
$$

Using the same methodology as in **Form I**, we employ matrix notation to write both linear equations as

$$
\begin{pmatrix} \delta_1^f \delta_3^w - \delta_3^f \delta_1^w & \delta_1^g \delta_3^w - \delta_3^g \delta_1^w \\ \delta_4^f \delta_2^w - \delta_2^f \delta_4^w & \delta_4^g \delta_2^w - \delta_2^g \delta_4^w \end{pmatrix} \begin{pmatrix} \boldsymbol{f}_{**} \\ \boldsymbol{g}_{**} \end{pmatrix} = \begin{pmatrix} \boldsymbol{c}_1 \\ \boldsymbol{c}_2 \end{pmatrix}, \tag{2.68}
$$

with the square matrix denoted by $\boldsymbol{A}_{II}$, which, if invertible, allows us to find simple and compact representations for the fluxes $\boldsymbol{f}_{**}$ and $\boldsymbol{g}_{**}$. We wish to point out that in actual practice, we have not yet encountered a situation where $\boldsymbol{A}_{II}$ is singular. However, by removing $\boldsymbol{w}_{**}$ from the computation, we are eliminating a dissipation that might be needed in some problems.

It is interesting to observe the behavior of this method in the limit that has hitherto been considered ($s_\alpha^\beta \to s_\alpha$ for $\alpha, \beta \in \{n, s, e, w\}$), where

$$
\boldsymbol{f}_{**} = \frac{s_e \boldsymbol{f}_{*w} - s_w \boldsymbol{f}_{*e} + s_e s_w (\boldsymbol{w}_{*e} - \boldsymbol{w}_{*w})}{s_e - s_w} \quad \text{and} \quad \boldsymbol{g}_{**} = \frac{s_n \boldsymbol{g}_{s*} - s_s \boldsymbol{g}_{n*} + s_n s_s (\boldsymbol{w}_{n*} - \boldsymbol{w}_{s*})}{s_n - s_s}, \tag{2.69}
$$

which are clearly consistent and can be seen as one-dimensional HLL fluxes (2.10) with initial data that are HLL intermediate states themselves.

Alternative Jump Condition Approach

Until now, we have considered the transverse fluxes $\boldsymbol{f}_{*e}$, $\boldsymbol{f}_{*w}$, $\boldsymbol{g}_{n*}$ and $\boldsymbol{g}_{s*}$ as known variables constructed with values taken out from the associated normal flux and intermediate state (refer to equation (2.38) in Section 2.1.3). If we were to regard them as unknown elements instead, the total number of unknowns in Balsara's formulation (2.39, 2.40, 2.41) would increase to seven. Thus, our first approach to define a well-posed problem consisted in deriving four additional equations by enforcing the jump conditions between the intermediate state $\boldsymbol{w}_{**}$ and $\boldsymbol{w}_{n*}$, $\boldsymbol{w}_{*w}$, $\boldsymbol{w}_{s*}$, $\boldsymbol{w}_{*e}$, respectively, to obtain

$$\boldsymbol{g}_{n*} = \boldsymbol{g}_{**} + s_n(\boldsymbol{w}_{n*} - \boldsymbol{w}_{**}), \tag{2.70a}$$

$$\boldsymbol{f}_{*w} = \boldsymbol{f}_{**} + s_w(\boldsymbol{w}_{*w} - \boldsymbol{w}_{**}), \tag{2.70b}$$

$$\boldsymbol{g}_{s*} = \boldsymbol{g}_{**} + s_s(\boldsymbol{w}_{s*} - \boldsymbol{w}_{**}), \tag{2.70c}$$

$$\boldsymbol{f}_{*e} = \boldsymbol{f}_{**} + s_e(\boldsymbol{w}_{*e} - \boldsymbol{w}_{**}), \tag{2.70d}$$

i.e., equations (2.57) for a rectangular interaction region. Substitution of these fluxes into (2.39), (2.40), (2.41) yields a system with the same number of equations and unknowns.

However, given the complexity of the involved terms, the solution set of the linear system cannot be readily determined. In practice, we found that the associated matrix is almost always singular since the system is, in fact, ill-posed; for instance, if we assume the flow is subsonic everywhere and take $s_\alpha^\beta \to s_\alpha$ for $\alpha, \beta \in \{n, s, e, w\}$, we get

$$\begin{pmatrix} 0 & 0 & 0 \\ s_w(s_n - s_s) & 0 & 0 \\ s_s(s_e - s_w) & 0 & 0 \end{pmatrix} \begin{pmatrix} \boldsymbol{w}_{**} \\ \boldsymbol{f}_{**} \\ \boldsymbol{g}_{**} \end{pmatrix} = \begin{pmatrix} \tilde{d}_1 \\ \tilde{d}_2 \\ \tilde{d}_3 \end{pmatrix}. \tag{2.71}$$

2.2.3.1   Consistency

In the next few paragraphs, we give various statements concerning the consistency of the proposed numerical scheme, where $\boldsymbol{w}_{**}$ is defined by equation (2.53) and $\boldsymbol{\mathcal{F}}_{**}$ by (2.60). For this, let us define a state $\bar{\boldsymbol{w}}$ constant in $\boldsymbol{x} \in \mathbb{R}^2$, as well as $\bar{\boldsymbol{w}}_e$, $\bar{\boldsymbol{w}}_n$, $\bar{\boldsymbol{w}}_w$, and $\bar{\boldsymbol{w}}_s$ constant in $x > 0$, $y > 0$, $x < 0$ and $y < 0$, respectively, with the corresponding fluxes denoted in a similar way.

Given that the scheme is in conservative form, we need to verify if the numerical fluxes are consistent with the physical ones, i.e., if $\boldsymbol{f}_{**}(\bar{\boldsymbol{w}}, \bar{\boldsymbol{w}}, \bar{\boldsymbol{w}}, \bar{\boldsymbol{w}}) = \boldsymbol{f}(\bar{\boldsymbol{w}})$ and $\boldsymbol{g}_{**}(\bar{\boldsymbol{w}}, \bar{\boldsymbol{w}}, \bar{\boldsymbol{w}}, \bar{\boldsymbol{w}}) = \boldsymbol{g}(\bar{\boldsymbol{w}})$. Making use of equations (2.62) with the speeds defined as $s_e = s_n = s = -s_s = -s_w$, and recalling the fact that the one-dimensional HLL fluxes are consistent, e.g., $\boldsymbol{f}_{*e}(\bar{\boldsymbol{w}}, \bar{\boldsymbol{w}}) = \boldsymbol{f}(\bar{\boldsymbol{w}})$, we surely recover that these basic consistency equalities are satisfied.

In addition, if all variations occur in one spatial direction, as depicted in Figure 2.8, equation (2.53) reduces to an analogue of (2.3). For instance, if the variation is restricted to the y-direction, we are sure that $\bar{\boldsymbol{w}}_n = \boldsymbol{w}_{ne} = \boldsymbol{w}_{nw}$, $\bar{\boldsymbol{w}}_s = \boldsymbol{w}_{se} = \boldsymbol{w}_{sw}$, $\bar{\boldsymbol{\mathcal{F}}}_n = \boldsymbol{\mathcal{F}}_{ne} = \boldsymbol{\mathcal{F}}_{nw}$ and $\bar{\boldsymbol{\mathcal{F}}}_s = \boldsymbol{\mathcal{F}}_{se} = \boldsymbol{\mathcal{F}}_{sw}$, and the equality (2.53) changes into

$$\boldsymbol{w}_{**} = \frac{s_n \bar{\boldsymbol{w}}_n - s_s \bar{\boldsymbol{w}}_s - (\bar{\boldsymbol{g}}_n - \bar{\boldsymbol{g}}_s)}{s_n - s_s}. \tag{2.72}$$

(a) Variation in the x-direction   (b) Variation in the y-direction
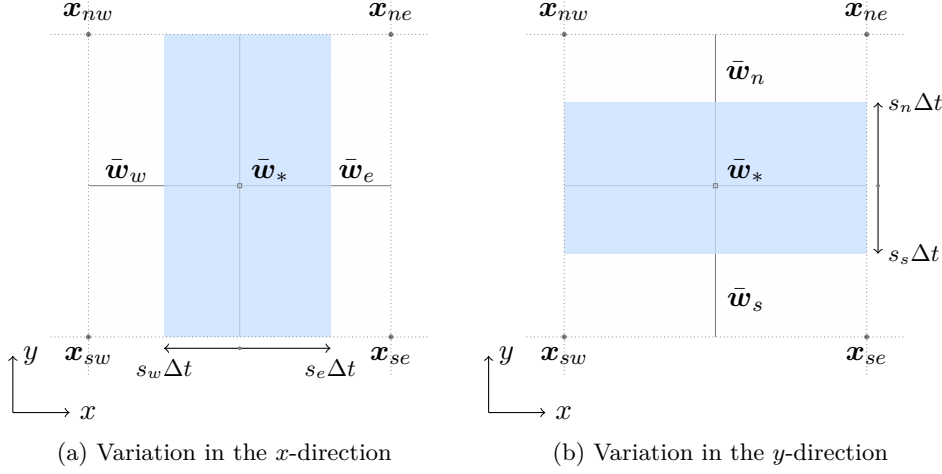
FIGURE 2.8. Two-dimensional variations restricted to a single spatial direction.

2.2.4   Extensions and Computational Remarks

The goal of this section is to exhibit a general representation of the proposed solver for two-dimensional meshes satisfying certain properties and simultaneously provide insight into its implementation. We then elaborate on how to assemble the total flux across the mesh edges or interfaces and on how to obtain a second-order version of the scheme.

2.2.4.1   Non-Rectangular Meshes

In the framework of finite volume methods, the technique presented in Section 2.2 naturally relies on integral relations that can be easily applied over any right prism in the physical space (x, y, t). So, let $\mathcal{T}$ be an admissible mesh defined over an open bounded region $\Omega \in \mathbb{R}^2$ in the sense of [54] (Definition 9.1) consisting of polygonal cells $\mathcal{C}_{\mathtt{c}} \in \mathcal{T}$ (with $\mathtt{c}$ a unique index), edges, and vertices; the latter belonging to a family denoted by $\mathcal{P}$. Moreover, for each vertex $\mathtt{p} \in \mathcal{P}$, we construct a dual convex cell $\mathcal{D}_{\mathtt{p}}$ by connecting the centers of the polygons that share this point and establish the space-time control volume $\mathcal{Q}_{\mathtt{p}} = \mathcal{D}_{\mathtt{p}} \times (0, \Delta t)$. An integration of (2.12) over this prism $\mathcal{Q}_{\mathtt{p}}$ then yields the expression

$$\int_{\mathcal{D}_{\mathtt{p}}} \boldsymbol{w}(\boldsymbol{x}, \Delta t) \, d\boldsymbol{x} - \int_{\mathcal{D}_{\mathtt{p}}} \boldsymbol{w}(\boldsymbol{x}, 0) \, d\boldsymbol{x} + \int_{\mathcal{Q}_{\mathtt{p}}} \nabla \cdot \boldsymbol{\mathcal{F}}(\boldsymbol{w}(\boldsymbol{x}, t)) \, d\boldsymbol{x} \, dt = 0, \qquad (2.73)$$

with $\boldsymbol{\mathcal{F}} = (\boldsymbol{f}, \boldsymbol{g})$ and $\boldsymbol{x} = (x, y)$, which is known to be equivalent to

$$\int_{\mathcal{D}_{\mathtt{p}}} \boldsymbol{w}(\boldsymbol{x}, \Delta t) \, d\boldsymbol{x} = \int_{\mathcal{D}_{\mathtt{p}}} \boldsymbol{w}(\boldsymbol{x}, 0) \, d\boldsymbol{x} - \int_{\mathcal{S}_{\mathtt{p}}} \boldsymbol{\mathcal{F}}(\boldsymbol{w}(s, t)) \cdot d\boldsymbol{\mathcal{S}}, \qquad (2.74)$$

by application of the divergence theorem, given $\mathcal{S}_{\mathtt{p}} = \partial \mathcal{D}_{\mathtt{p}} \times (0, \Delta t)$. For presentation purposes, we shall hereafter limit ourselves to the case where $\mathcal{D}_{\mathtt{p}}$ is a basic triangle.

(a) Global view of possible structures   (b) Zoom on a triangular dual cell
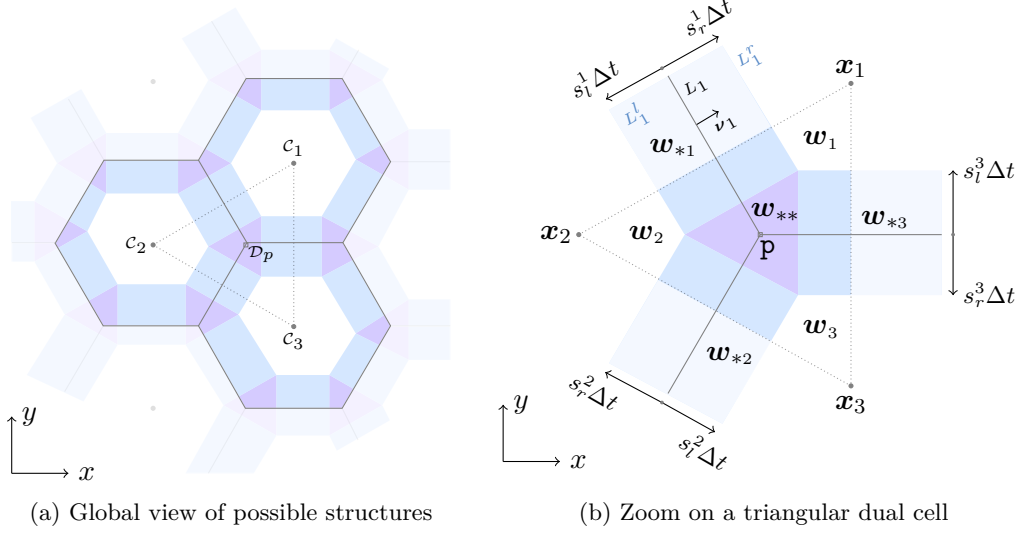
FIGURE 2.9. A solution example at time $t = \Delta t$, resulting from the application of HLL Riemann solvers at the interfaces and at the vertices of the underlying non-rectangular mesh.

However, we urge the reader to keep in mind that all subsequent developments can be readily generalized to any convex polygonal dual cell.

Thus, we consider the volume $\mathcal{Q}_\mathsf{p}$ to be a triangular prism, provided $\mathcal{D}_\mathsf{p}$ is adequately defined by joining together the three distinct centers

$$\boldsymbol{x}_\alpha = (x_\alpha, y_\alpha), \quad \alpha = 1, 2, 3, \tag{2.75}$$

of the corresponding primary cells $\mathcal{C}_\alpha$, as exemplified in Figure 2.9. Owing to its construction, the dual cell contains the vertex p that is evidently the intersection point of three edges L_α, for which we know their respective formulations and unit normals $\boldsymbol{\nu}_\alpha = (\nu_{\alpha x}, \nu_{\alpha y})$. We employ the notation L_α to designate the line segment having p as one of its endpoints and lying between $\boldsymbol{x}_\alpha$ and $\boldsymbol{x}_{\alpha+1}$, with the index α following a cyclic order such that for $\alpha = 3$, $\alpha + 1 = 1$.

As explained in Section 2.1.1, a constant state $\boldsymbol{w}_\alpha$ is assumed within each cell $\mathcal{C}_\alpha$ at the initial time $t_0 \geq 0$, for $\alpha = 1, 2, 3$. Using now Figure 2.9b as reference, it is evident that in order to obtain the desired values at the face $L_\alpha \times (t_0, t_0 + \Delta t)$ in the interior of $\mathcal{Q}_\mathsf{p}$, we must solve not only a one-dimensional Riemann problem in its normal direction, but also a local two-dimensional Riemann problem, involving initial data $\boldsymbol{w}_1$, $\boldsymbol{w}_2$ and $\boldsymbol{w}_3$, at the vertex p.

For the former, we identify as s_l^α and s_r^α the left and right Einfeldt's wave speeds in the direction of $\boldsymbol{\nu}_\alpha$, after making use of equation (2.11) with $\boldsymbol{w}_l = \boldsymbol{w}_{\alpha+1}$ and $\boldsymbol{w}_r = \boldsymbol{w}_\alpha$ (refer to Annex B.1 for implementation details). Moreover, solving the one-dimensional Riemann problems at the edges allows us to derive expressions for the constant state

$\boldsymbol{w}_{*\alpha}$ (2.3) and HLL fluxes (2.10) associated with each problem, i.e.,

$$\boldsymbol{w}_{*\alpha} = \frac{s_r^\alpha \boldsymbol{w}_\alpha - s_l^\alpha \boldsymbol{w}_{\alpha+1} + \boldsymbol{\nu}_\alpha \cdot (\boldsymbol{\mathcal{F}}_{\alpha+1} - \boldsymbol{\mathcal{F}}_\alpha)}{s_r^\alpha - s_l^\alpha}, \tag{2.76a}$$

$$\boldsymbol{f}_{*\alpha}^n = \frac{\boldsymbol{\nu}_\alpha \cdot (s_r^\alpha \boldsymbol{\mathcal{F}}_{\alpha+1} - s_l^\alpha \boldsymbol{\mathcal{F}}_\alpha) + s_l^\alpha s_r^\alpha (\boldsymbol{w}_\alpha - \boldsymbol{w}_{\alpha+1})}{s_r^\alpha - s_l^\alpha}, \tag{2.76b}$$

where $\boldsymbol{f}_{*\alpha}^n = \boldsymbol{\nu}_\alpha \cdot \boldsymbol{\mathcal{F}}_{*\alpha}$ is the flux perpendicular to the edge $\alpha \in \{1,2,3\}$. We recall that the transverse fluxes, denoted here as $\boldsymbol{f}_{*\alpha}^{n\perp} = (-\nu_{\alpha y}, \nu_{\alpha x}) \cdot (\boldsymbol{f}_{*\alpha}, \boldsymbol{g}_{*\alpha})$, can be constructed using values extracted from the associated normal flux (2.76b) and intermediate state (2.76a), as was done in Section 2.1.3. In addition, we easily recover the two parallel lines that bound the extent of $\boldsymbol{w}_{*\alpha}$ on the xy-plane at some time $t > t_0$, which are given by

$$L_\alpha^r(t) = \{(x,y) \mid \nu_{\alpha x} x + \nu_{\alpha y} y = s_r^\alpha (t - t_0)\}, \tag{2.77a}$$

$$L_\alpha^l(t) = \{(x,y) \mid \nu_{\alpha x} x + \nu_{\alpha y} y = s_l^\alpha (t - t_0)\}, \tag{2.77b}$$

having conveniently set $\mathsf{p} = (0,0)$ and recalling that $\|\boldsymbol{\nu}_\alpha\| = 1$. From now on, we also consider the time $t = \Delta t$ and $t_0 = 0$.

With regard to the 2D Riemann problem found at the origin $\mathbf{O} = (\mathsf{p}, 0)$, we specify a triangular region by connecting the vertices $\boldsymbol{X}_\alpha = (x_\alpha' \Delta t, y_\alpha' \Delta t)$, $\alpha = 1, 2, 3$, which are essentially the intersection points of the bounding lines $L_\alpha^l(\Delta t)$ and $L_{\alpha+1}^r(\Delta t)$ such that

$$x_\alpha' = \frac{s_r^{\alpha+1} \nu_{\alpha y} - s_l^\alpha \nu_{(\alpha+1)y}}{\nu_{(\alpha+1)x} \nu_{\alpha y} - \nu_{\alpha x} \nu_{(\alpha+1)y}} \quad \text{and} \quad y_\alpha' = \frac{s_l^\alpha \nu_{(\alpha+1)x} - s_r^{\alpha+1} \nu_{\alpha x}}{\nu_{(\alpha+1)x} \nu_{\alpha y} - \nu_{\alpha x} \nu_{(\alpha+1)y}}. \tag{2.78}$$

Let us note that all two-dimensional complex interactions emanating from $\mathbf{O}$ and projected onto the planar surface $t = \Delta t$, are well-contained in the previously mentioned triangle, which in turn generates an inverted triangular pyramid during its time evolution from 0 to Δt.

The previous statements facilitate the derivation of an algebraic equation to compute the constant state $\boldsymbol{w}_{**}$, when applying the integral conservation law (2.74) over the control volume $\mathcal{Q}_\mathsf{p}$. However, for the determination of the flux $\boldsymbol{f}_{**}$, we still need to provide the Rankine-Hugoniot relations that hold across the surfaces of discontinuities emerging from $\mathbf{O}$, following the approach carefully detailed in Section 2.2.2.2. We therefore start by identifying the points $\mathbf{Q}_\alpha = (\boldsymbol{X}_\alpha, \Delta t)$ and the normals

$$\boldsymbol{n}_\alpha = \overrightarrow{\mathbf{OQ}}_{\alpha+1} \times \overrightarrow{\mathbf{OQ}}_\alpha = \Delta t^2 \left[(y_{\alpha+1}' - y_\alpha') \mathbf{i} + (x_\alpha' - x_{\alpha+1}') \mathbf{j} + (x_{\alpha+1}' y_\alpha' - x_\alpha' y_{\alpha+1}') \mathbf{t} \right], \tag{2.79}$$

that will allow us to deduce the jump conditions for $\alpha = 1, 2, 3$ as

$$\overbrace{(x_{\alpha+1}' y_\alpha' - x_\alpha' y_{\alpha+1}')}^{\delta_\alpha^w}(\boldsymbol{w}_{*\alpha} - \boldsymbol{w}_{**}) + \overbrace{(y_{\alpha+1}' - y_\alpha')}^{\delta_\alpha^f}(\boldsymbol{f}_{*\alpha} - \boldsymbol{f}_{**}) + \overbrace{(x_\alpha' - x_{\alpha+1}')}^{\delta_\alpha^g}(\boldsymbol{g}_{*\alpha} - \boldsymbol{g}_{**}) = 0, \tag{2.80}$$

which can be written in the following form:

$$\delta_\alpha^f \boldsymbol{f}_{**} + \delta_\alpha^g \boldsymbol{g}_{**} = \delta_\alpha^w (\boldsymbol{w}_{*\alpha} - \boldsymbol{w}_{**}) + \delta_\alpha^f \boldsymbol{f}_{*\alpha} + \delta_\alpha^g \boldsymbol{g}_{*\alpha} = \boldsymbol{b}_\alpha, \quad \alpha = 1, 2, 3. \tag{2.81}$$

Clearly, relations (2.81) form once again an overdetermined system of linear equations, since there are more equations (three) than unknowns (two). In view of the method of ordinary least squares, we then express this system as $\boldsymbol{A}_\mathcal{T}\mathbf{x} = \boldsymbol{b}_\mathcal{T}$ by defining

$$\boldsymbol{A}_\mathcal{T} = \begin{pmatrix} \delta_1^f & \delta_1^g \\ \delta_2^f & \delta_2^g \\ \delta_3^f & \delta_3^g \end{pmatrix}, \quad \mathbf{x} = \begin{pmatrix} \boldsymbol{f}_{**} \\ \boldsymbol{g}_{**} \end{pmatrix}, \quad \text{and} \quad \boldsymbol{b}_\mathcal{T} = \begin{pmatrix} \delta_1^w(\boldsymbol{w}_{*1} - \boldsymbol{w}_{**}) + \delta_1^f \boldsymbol{f}_{*1} + \delta_1^g \boldsymbol{g}_{*1} \\ \delta_2^w(\boldsymbol{w}_{*2} - \boldsymbol{w}_{**}) + \delta_2^f \boldsymbol{f}_{*2} + \delta_2^g \boldsymbol{g}_{*2} \\ \delta_3^w(\boldsymbol{w}_{*3} - \boldsymbol{w}_{**}) + \delta_3^f \boldsymbol{f}_{*3} + \delta_3^g \boldsymbol{g}_{*3} \end{pmatrix}, \quad (2.82)$$

and look for the least squares solution $\mathbf{x} = \boldsymbol{M}_\mathcal{T}^{-1}\boldsymbol{A}_\mathcal{T}^T\boldsymbol{b}_\mathcal{T}$, provided $\boldsymbol{M}_\mathcal{T}$ is invertible. It is worth mentioning that in the general case when three or more edges ($\varepsilon \geq 3$) meet at the vertex $\mathbf{p}$, the matrix

$$\boldsymbol{M}_\mathcal{T} = \begin{pmatrix} \displaystyle\sum_{\alpha=1,\ldots,\varepsilon} \delta_\alpha^{f\,2} & \displaystyle\sum_{\alpha=1,\ldots,\varepsilon} \delta_\alpha^f \delta_\alpha^g \\ \displaystyle\sum_{\alpha=1,\ldots,\varepsilon} \delta_\alpha^f \delta_\alpha^g & \displaystyle\sum_{\alpha=1,\ldots,\varepsilon} \delta_\alpha^{g\,2} \end{pmatrix}, \quad (2.83)$$

has a determinant that can be expressed as the sum of square binomials of the form $(\delta_\alpha^f \delta_\beta^g - \delta_\beta^f \delta_\alpha^g)^2$, for all $\alpha, \beta \in \{1, 2, \ldots, \varepsilon\}$, which is geometrically proven to be strictly positive as long as the area of the interaction region a_{**} is not zero.

Hence, we confirm that the proposed approach is simple enough to be applied on any admissible mesh, yielding useful closed expressions for $\boldsymbol{w}_{**}$ and $\boldsymbol{\mathcal{F}}_{**}$. Our strategy only relies on geometry to define the structures' areas that are formed by the outward propagation of waves from the origin $\mathbf{O}$ and edges L_α in order to compute the intermediate state. In fact, the estimation of the fluxes is entirely algebraic, as opposed to the extension of Balsara's multidimensional HLL solver to unstructured meshes [11], which relies heavily on geometry to calculate both $\boldsymbol{w}_{**}$ and $\boldsymbol{\mathcal{F}}_{**}$.

2.2.4.2   Flux Assembling at Faces

The assembling of the total flux at the cells' faces is an important aspect that has to be carefully considered. Although we perform the subsequent study focusing on the rectangular mesh used in Section 2.2, we note that all formalisms developed here can be easily adapted to other configurations such as the ones presented in the previous section.

After analyzing the structures shown in Figures 2.2a and 2.9a, we can infer that the final expression will be a convex combination of one-and two-dimensional fluxes, as in [9, 26, 85]. Each flux at an edge of the primary cell $\mathcal{C}_{i,j}$ can be obtained from the surface average of the flux normal to the underlying space-time face, e.g.,

$$\phi_{x,i+\frac{1}{2},j} = \frac{1}{\Delta y \, \Delta t} \int_{y_{j-\frac{1}{2}}}^{y_{j+\frac{1}{2}}} \int_0^{\Delta t} \boldsymbol{\mathcal{F}}(\boldsymbol{w}(x_{i+\frac{1}{2}}, y, t)) \cdot \bar{\boldsymbol{n}}_{i+\frac{1}{2}} \, dt \, dy, \quad (2.84)$$

being $\bar{\boldsymbol{n}}_{i+1/2} = (1, 0)$ the unit normal vector of $\mathcal{S}_{i+1/2} = (y_{j-1/2}, y_{j+1/2}) \times (0, \Delta t)$.

In the subsonic case, the above definite integral can be evaluated by considering the contributions at the face coming from the one- and two-dimensional Riemann solvers

initially applied at the cell's edge and vertices, respectively. The averaged flux becomes

$$\phi_{x,i+\frac{1}{2},j} = \theta_{s,i+\frac{1}{2},j+\frac{1}{2}} \, \phi^{hll2D}_{x,i+\frac{1}{2},j+\frac{1}{2}} + \theta_{y,i+\frac{1}{2},j} \, \phi^{hll}_{x,i+\frac{1}{2},j} + \theta_{n,i+\frac{1}{2},j-\frac{1}{2}} \, \phi^{hll2D}_{x,i+\frac{1}{2},j-\frac{1}{2}}, \qquad (2.85)$$

with

$$\theta_{s,i+\frac{1}{2},j+\frac{1}{2}} = \tfrac{\Delta t}{2\,\Delta y}|\hat{s}_{s,i+\frac{1}{2},j+\frac{1}{2}}|, \quad \theta_{n,i+\frac{1}{2},j-\frac{1}{2}} = \tfrac{\Delta t}{2\,\Delta y}|\hat{s}_{n,i+\frac{1}{2},j-\frac{1}{2}}|,$$

$$\text{and} \quad \theta_{y,i+\frac{1}{2},j} = 1 - \theta_{s,i+\frac{1}{2},j+\frac{1}{2}} - \theta_{n,i+\frac{1}{2},j-\frac{1}{2}}.$$

It is obvious that the weights $\theta_{s,i+1/2,j+1/2}$ and $\theta_{n,i+1/2,j-1/2}$ determine the amount of two-dimensional contributions that the total flux at the cell's face will possess, and they are directly linked through the time step with the CFL number used in practice (for details regarding the associated CFL condition, we refer the reader to [9, p. 1977] where it is fully explained). We remark that a simpler alternative to (2.85) is fixing the weights to the coefficients in Simpson's rule, used to numerically integrate the average of $\boldsymbol{\mathcal{F}}(\boldsymbol{w}(x_{i+1/2}, y, \Delta t)) \cdot \bar{\boldsymbol{n}}_{i+1/2}$ over the edge $(y_{j-1/2}, y_{j+1/2})$, yielding

$$\phi_{x,i+\frac{1}{2},j} = \tfrac{1}{6}\phi^{hll2D}_{x,i+\frac{1}{2},j+\frac{1}{2}} + \tfrac{4}{6}\phi^{hll}_{x,i+\frac{1}{2},j} + \tfrac{1}{6}\phi^{hll2D}_{x,i+\frac{1}{2},j-\frac{1}{2}}. \qquad (2.86)$$

Let us note that in equations (2.85) and (2.86), we have employed new variables that need to be appropriately defined. First, the element having the superscript "*hll*" is essentially the one-dimensional numerical flux described in equation (2.8), but with a two-dimensional index instead, such that $\phi^{hll}_{x,i+1/2,j} = \phi^{hll}_x(\mathbf{w}^n_{i,j}, \mathbf{w}^n_{i+1,j})$. In a similar manner, we specify

$$\phi^{hll2D}_{x,i+\frac{1}{2},j+\frac{1}{2}} = \phi^{hll2D}_x(\mathbf{w}^n_{i+1,j+1}, \mathbf{w}^n_{i,j+1}, \mathbf{w}^n_{i,j}, \mathbf{w}^n_{i+1,j}), \qquad (2.87a)$$

$$\phi^{hll2D}_{x,i+\frac{1}{2},j-\frac{1}{2}} = \phi^{hll2D}_x(\mathbf{w}^n_{i+1,j}, \mathbf{w}^n_{i,j}, \mathbf{w}^n_{i,j-1}, \mathbf{w}^n_{i+1,j-1}), \qquad (2.87b)$$

where $\phi^{hll2D}_{x,m,n}$ is the local flux $\boldsymbol{f}_{**}$ of the two-dimensional Riemann problem defined at the vertex $\boldsymbol{x}_{m,n}$, with analogous considerations for the y direction. Next, the wave speeds denoted by $\hat{s}_\alpha$, for $\alpha \in \{n, s, e, w\}$, are determined from the intersection of the interaction region with the x- and y-axes at time Δt (notice the circles pictured in Figure 2.3b of Section 2.1.2), specifically

$$\hat{s}_n = s^w_n - s^n_w\left(\frac{s^w_n - s^e_n}{s^n_w - s^n_e}\right), \qquad \hat{s}_s = s^e_s - s^s_e\left(\frac{s^e_s - s^w_s}{s^s_e - s^s_w}\right),$$

$$\hat{s}_w = s^s_w - s^w_s\left(\frac{s^n_w - s^s_w}{s^w_n - s^w_s}\right), \qquad \hat{s}_e = s^n_e - s^e_n\left(\frac{s^s_e - s^n_e}{s^e_s - s^e_n}\right),$$

$$(2.88)$$

and in the limit $s^\beta_\alpha \to s_\alpha$ for $\alpha, \beta \in \{n, s, e, w\}$, $\hat{s}_\alpha = s_\alpha$.

Equations (2.85) and (2.86) are strictly valid only for a flow that is subsonic everywhere. However, if we reformulate our signal speeds defined in (2.21) as s^{n+}_e, s^{e+}_n, s^{n-}_w, s^{w+}_n, s^{s-}_w, s^{w-}_s s^{s+}_e, and s^{e-}_s, and utilize them to recover all one- and two-dimensional states and fluxes associated with our multidimensional Riemann solver (2.23, 2.24, 2.38, 2.53, 2.60), we are able to account for supersonic situations and employ both (2.85) and

(2.86) without any additional adjustments. Another way to deal with supersonic situations is to approximately define the fluxes $\phi_{x,m,n}^{hll2D}$ and $\phi_{y,m,n}^{hll2D}$ as the upwinded fluxes at the space-time point $(\boldsymbol{x}_{m,n}, \Delta t)$, as given in [10, p. 7483] and partially described in equation (2.44). Henceforth, we use the term *Simpson assembling* to denominate equation (2.86) together with these upwinded 2D fluxes.

The most accurate approach to handle supersonic flows is to manually track the position of the interaction region and deduce the actual elements that contribute to the total flux at each of the cell's faces. For instance, on examining the configuration shown in Figure 2.6a, it is clear that for this example, $\boldsymbol{f}_{**}$ does not have an effect in the total flux assembled at the vertical edge, and choosing $\boldsymbol{f}_{*w}$ when assembling would certainly be more accurate. For this, we choose to introduce a new expression

$$\phi_{x,i+\frac{1}{2},j} = \widetilde{\theta}_{s,i+\frac{1}{2},j+\frac{1}{2}}\, \widetilde{\phi}_{x,i+\frac{1}{2},j+\frac{1}{2}}^{hll2D} + \widetilde{\theta}_{y,i+\frac{1}{2},j}\, \phi_{x,i+\frac{1}{2},j}^{hll} + \widetilde{\theta}_{n,i+\frac{1}{2},j-\frac{1}{2}}\, \widetilde{\phi}_{x,i+\frac{1}{2},j-\frac{1}{2}}^{hll2D}, \qquad (2.89)$$

where

$$\widetilde{\theta}_{s,i+\frac{1}{2},j+\frac{1}{2}} = \frac{\Delta t}{2\,\Delta y}|\tilde{s}_{s,i+\frac{1}{2},j+\frac{1}{2}}|, \quad \widetilde{\theta}_{n,i+\frac{1}{2},j-\frac{1}{2}} = \frac{\Delta t}{2\,\Delta y}|\tilde{s}_{n,i+\frac{1}{2},j-\frac{1}{2}}|,$$

$$\text{and} \quad \widetilde{\theta}_{y,i+\frac{1}{2},j} = 1 - \widetilde{\theta}_{s,i+\frac{1}{2},j+\frac{1}{2}} - \widetilde{\theta}_{n,i+\frac{1}{2},j-\frac{1}{2}}.$$

The x-directional flux $\widetilde{\phi}_{x,m,n}^{hll2D}$ needs to be regarded as a convex combination of local fluxes associated to the nine states, characterized by $\mathcal{L}_{m,n} = \{**, n*, s*, *e, *w, ne, nw, sw, se\}$, of the two-dimensional Riemann solver centered at $\boldsymbol{x}_{m,n}$, i.e.,

$$\widetilde{\phi}_{x,i+\frac{1}{2},j+\frac{1}{2}}^{hll2D} = \widetilde{\phi}_x^{hll2D}(\mathbf{w}_{i+1,j+1}^n, \mathbf{w}_{i,j+1}^n, \mathbf{w}_{i,j}^n, \mathbf{w}_{i+1,j}^n) = \sum_{(\mu\nu)\in\mathcal{L}_{i+\frac{1}{2},j+\frac{1}{2}}} \beta_{y,\mu\nu}\, \boldsymbol{f}_{\mu\nu}, \qquad (2.90a)$$

$$\widetilde{\phi}_{x,i+\frac{1}{2},j-\frac{1}{2}}^{hll2D} = \widetilde{\phi}_x^{hll2D}(\mathbf{w}_{i+1,j}^n, \mathbf{w}_{i,j}^n, \mathbf{w}_{i,j-1}^n, \mathbf{w}_{i+1,j-1}^n) = \sum_{(\mu\nu)\in\mathcal{L}_{i+\frac{1}{2},j-\frac{1}{2}}} \beta_{y,\mu\nu}\, \boldsymbol{f}_{\mu\nu}, \qquad (2.90b)$$

and $\beta_{y,\mu\nu} \geq 0$, $\sum \beta_{y,\mu\nu} = 1$, with similar equations and notation for the y-direction. Each coefficient $\beta_{y,\mu\nu}$ corresponds to the fraction of the interaction surface associated to the local state $\mu\nu$. In a subsonic configuration, notice that $\beta_{y,**} = 1$ and all others are zero.

Equation (2.89) will now be referred to as *manual assembling* and in Annex B.2, we provide the specific details for the implementation of (2.89, 2.90) with the help of pseudocode. There, observe that the third algorithm corresponds to the approximate (due to some simplifications) 2D analogue of ϕ_x^{hll} (2.2).

2.2.4.3   Predictor-Corrector Scheme of Second-Order Accuracy

The first-order scheme is now complete and the next step is to define an appropriate second-order extension. This is achieved by means of a simple predictor-corrector approach similar to the one proposed by Balsara in [9, 10], which roughly consists of using the two-dimensional Riemann solver for both steps involved in the algorithm. A consequence of employing this solver in the corrector step is the introduction of more isotropy into the simulation. Instead, "our use of the multidimensional Riemann solver in the predictor step has the happy consequence of raising the maximal CFL number", in the

words of the author of [10], and we add the phrase "when needed". For some problems, e.g., the ones presented in Section 2.3.2, the multidimensional contributions are not needed in the predictor step in order to have a high CFL number in the corresponding simulations. However, for certain test cases, such as the double Mach reflection and Sedov problems, these contributions are needed to be able to use the CFL 0.90.

Thus, in the predictor step, the vector $\boldsymbol{w}$ is spatially reconstructed from the center of the primary cell to its corners or vertices following a MUSCL-type approach, i.e., using piecewise linear interpolations with slope limiters such as the MC limiter [136], minmod [118] or the positive preserving limiter [127]. The reconstruction provides the four states that are necessary to solve the multidimensional Riemann solver (2.23, 2.24, 2.38, 2.53, 2.60) at each corner, yielding the x- and y-directional fluxes that will contribute to the assembling at the cell's faces. Now, to avoid the appearance of spurious solutions for certain second-order simulations, we propose employing

$$\boldsymbol{\phi}_{x,i+\frac{1}{2},j} = \widetilde{\theta}_{y,i+\frac{1}{2},j+\frac{1}{2}}\ \widetilde{\boldsymbol{\phi}}^{hll2D}_{x_s,i+\frac{1}{2},j+\frac{1}{2}} + \widetilde{\theta}_{y,i+\frac{1}{2},j}\ \widetilde{\boldsymbol{\phi}}^{hll}_{x,i+\frac{1}{2},j} + \widetilde{\theta}_{y,i+\frac{1}{2},j-\frac{1}{2}}\ \widetilde{\boldsymbol{\phi}}^{hll2D}_{x_n,i+\frac{1}{2},j-\frac{1}{2}}, \quad (2.91)$$

where

$$\widetilde{\theta}_{y,i+\frac{1}{2},j\pm\frac{1}{2}} = \tfrac{\zeta\Delta t}{2\,\Delta y}\max(|\tilde{s}_{s,i+\frac{1}{2},j\pm\frac{1}{2}}|,|\tilde{s}_{n,i+\frac{1}{2},j\pm\frac{1}{2}}|)\ \text{ and }\ \widetilde{\theta}_{y,i+\frac{1}{2},j} = 1 - \widetilde{\theta}_{y,i+\frac{1}{2},j+\frac{1}{2}} - \widetilde{\theta}_{y,i+\frac{1}{2},j-\frac{1}{2}},$$

with analogous expressions for the other main direction. We note that we have introduced new variables "$hll2D$" which are defined in a way similar to (2.90) but with a different subscript that denotes the location relative to the local vertices (we refer the reader to Algorithm 4 in Annex B.2 for more details regarding their precise definition). Moreover, the flux $\widetilde{\boldsymbol{\phi}}^{hll}_{x,i+1/2,j}$ at the center of the face is simply the average of the nearest two x-directional HLL fluxes, one initially computed below the vertex $\boldsymbol{x}_{i+1/2,j+1/2}$ and the other above $\boldsymbol{x}_{i+1/2,j-1/2}$, as partial inputs for our two-dimensional Riemann solver. We then utilize the total assembled fluxes to estimate the vector of conservative variables at the half time step $t^n + \zeta\,\Delta t$, with $\zeta = 1/2$.

For the corrector step, we repeat the operations carried out in the predictor step but having set $\zeta = 1$. The slopes computed at time t^n are now applied to spatially reconstruct variables that are centered both in time and space, i.e., the output of the predictor step. In the coming section, we will present several numerical tests that were obtained with this simple yet second-order accurate predictor-corrector approach. First-order approximations can be obtained using the same computer code, by performing only one step with unreconstructed states and $\zeta = 1$.

2.3   Numerical Results

The purpose of this section is to validate our scheme with several multidimensional test problems on a uniform rectangular mesh. The numerical implementation of our solver and Balsara's [10] (hereafter referred to as BAL2012) has been done in the HERACLES code [66] for astrophysical fluid flows. By having a common computational framework, we can fairly compare the accuracy and robustness of both methods.

We note that employing *Simpson assembling* at the cells' faces for our solver yields almost the exact same results as BAL2012, for which this type of assembling is the default

for second-order simulations, and thus, unless stated otherwise, we opt to display our method's solutions with the *manual assembling* (2.91). All tests were run with a CFL number of 0.9 and making use of the predictor-corrector scheme mentioned in Section 2.2.4.3. As for the choice of slope limiters, we applied the MC limiter [136] for all except the last (Section 2.3.4), where minmod [118] was utilized instead.

2.3.1 Accuracy Analysis

We wish to estimate the rate at which the L^1 error for the proposed scheme decreases as the numerical grid is refined. For this, we consider the initial density profile [81]

$$\rho_0(x,y) = 1 + 0.2\sin(\pi(x+y)), \tag{2.92}$$

		Scheme with *Manual Asmb.*		Scheme with *Simpson Asmb.*	
Order	Resolution	L^1 error	L^1 order	L^1 error	L^1 order
1st	25×25	4.8975e-01		4.9536e-01	
	50×50	4.1098e-01	0.25	4.2679e-01	0.21
	100×100	2.8650e-01	0.52	3.0515e-01	0.48
	200×200	1.7279e-01	0.73	1.8704e-01	0.71
	400×400	9.5487e-02	0.86	1.0429e-01	0.84
	800×800	5.0278e-02	0.93	5.5167e-02	0.92
	1600×1600	2.5808e-02	0.96	2.8383e-02	0.96
2nd MM [118]	25×25	2.0198e-01		2.1682e-01	
	50×50	6.5074e-02	1.63	6.7657e-02	1.68
	100×100	2.8358e-02	1.20	3.0418e-02	1.15
	200×200	7.8803e-03	1.85	8.4898e-03	1.84
	400×400	2.1739e-03	1.86	2.3589e-03	1.85
	800×800	5.9648e-04	1.87	6.4860e-04	1.86
	1600×1600	1.5876e-04	1.91	1.7275e-04	1.91
2nd PP [127]	25×25	7.7416e-02		7.9507e-02	
	50×50	2.5379e-02	1.61	2.3234e-02	1.77
	100×100	5.5017e-03	2.21	5.1137e-03	2.18
	200×200	1.1486e-03	2.26	1.0969e-03	2.22
	400×400	2.3008e-04	2.32	2.2597e-04	2.28
	800×800	4.5417e-05	2.34	4.5906e-05	2.30
	1600×1600	8.9790e-06	2.34	9.4001e-06	2.29
2nd MC [136]	25×25	3.2846e-02		4.2989e-02	
	50×50	4.4552e-03	2.88	5.8172e-03	2.89
	100×100	8.8114e-04	2.34	1.0172e-03	2.52
	200×200	2.0742e-04	2.09	2.1494e-04	2.24
	400×400	4.8755e-05	2.09	4.8707e-05	2.14
	800×800	1.1452e-05	2.09	1.1523e-05	2.08
	1600×1600	2.7050e-06	2.08	2.7568e-06	2.06

TABLE 2.1. L^1 density errors and orders of accuracy for the wave advection test, using our proposed scheme with different slope limiters.

together with the velocities and pressure defined in Section 4.1 of [98], i.e., $u_0 = 1$, $v_0 = -0.5$ and $p_0 = 1$. The simulation is run to time $t = 4$, which corresponds to the time it takes for the wave to be advected once around the periodic domain spanning $[0, 2] \times [0, 2]$. The final state is then compared with the analytical one.

In Table 2.1, the accuracy results for our scheme are summarized. For both assembling methods being compared, the L^1 density errors decrease as the numerical resolution increases and we are able to see that the lowest values are obtained when the MC limiter and *manual assembling* are present. In addition, we observe that second-order accuracy is reached when any of the three selected limiters are used, as was previously mentioned in Section 2.2.4.3. We mention that our method with *Simpson assembling* not only gives roughly the same results as BAL2012 (e.g., differences after the seventh or eight decimal place for the MC limiter results) but also takes the same amount of CPU time to complete with HERACLES.

1D HLL Solvers Only

	25×25	50×50	100×100	200×200	400×400	800×800	1600×1600
L^1 error	4.2162 e-02	6.5289e-03	1.3566e-03	3.5122e-04	8.7975e-05	2.1608e-05	5.2697e-06
L^1 order		2.69	2.27	1.95	2.00	2.03	2.04

TABLE 2.2. Density errors measured in the L^1 norm for the wave advection test using the MC limiter and one-dimensional HLL Riemann solvers in both the predictor and corrector steps.

The advantage, in terms of accuracy, of taking into account the multidimensional contributions for this problem is evident when we compare the rows corresponding to the MC limiter in Table 2.1 with those of Table 2.2. The latter were obtained utilizing only 1D HLL Riemann solvers in both steps of the predictor-corrector algorithm.

2.3.2 Multidimensional Riemann Problems
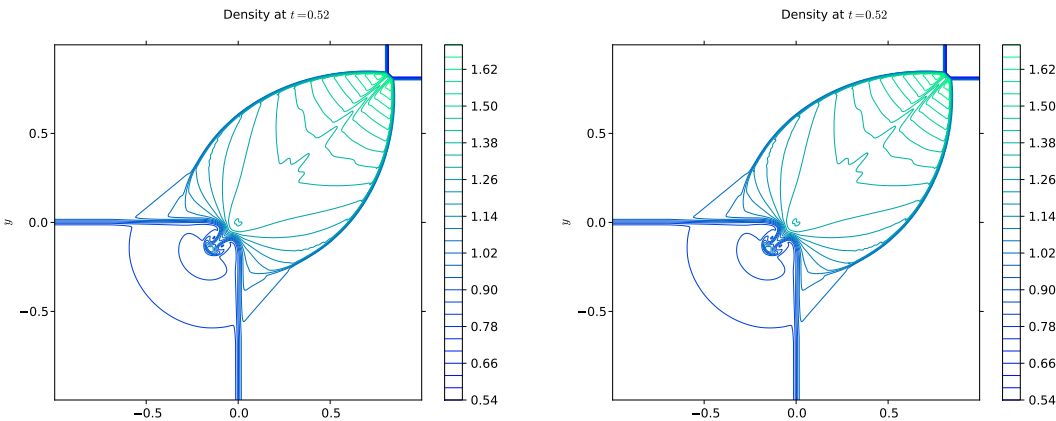
FIGURE 2.10. Density variable ρ obtained using BAL2012 (left, ρ:0.53-1.72) and our scheme (right, ρ:0.53-1.71) for the MultiD RP1; computations performed on a 400×400 grid and 30 contour lines displayed from 0.54 to 1.70 with a step of 0.04.

Firstly, we consider the two-dimensional problem described in [26, p. 183], with initial data given in Table 2.3 (left). This Riemann problem (RP) initially consists of two contact discontinuities J and two forward shock waves $\overrightarrow{S}$, specifically $\overrightarrow{S}_{21} J_{32} J_{34} \overrightarrow{S}_{41}$ borrowing the notation used in [122]. In general, we expect that both slip lines encounter the sonic circle of the constant state in the third quadrant of the xy-plane and bend to end in spirals inside the subsonic area of the circle's portion lying in this quadrant. In addition, from the interaction of the shocks $\overrightarrow{S}_{21}$ and $\overrightarrow{S}_{41}$, we await the appearance of a pair of three-shock configurations, such that part of the subsonic area is bounded by two joining Mach shocks and two reflected shocks.

Multidimensional Riemann Problems 1 & 2

Quadrant	$\rho_0(x,y)$	$u_0(x,y)$	$v_0(x,y)$	$p_0(x,y)$	$\rho_0(x,y)$	$u_0(x,y)$	$v_0(x,y)$	$p_0(x,y)$
$x>0,\ y>0$	0.5313	0.0	0.0	0.4	1.0	0.75	-0.5	1.0
$x<0,\ y>0$	1.0	0.7276	0.0	1.0	2.0	0.75	0.5	1.0
$x<0,\ y<0$	0.8	0.0	0.0	1.0	1.0	-0.75	0.5	1.0
$x>0,\ y<0$	1.0	0.0	0.7276	1.0	3.0	-0.75	-0.5	1.0
Computational domain: $[-1,1] \times [-1,1]$; Free-flow boundary conditions								

TABLE 2.3. Initial data for the first MultiD RP described in [26] and the sixth of [86].

Multidimensional Riemann Problems 3 & 4

Quadrant	$\rho_0(x,y)$	$u_0(x,y)$	$v_0(x,y)$	$p_0(x,y)$	$\rho_0(x,y)$	$u_0(x,y)$	$v_0(x,y)$	$p_0(x,y)$
$x>0,\ y>0$	1.0	0.1	-0.3	1.0	1.5	0.0	0.0	1.5
$x<0,\ y>0$	0.5197	-0.6259	-0.3	0.4	0.5323	1.206	0.0	0.3
$x<0,\ y<0$	0.8	0.1	-0.3	0.4	0.1379	1.206	1.206	0.029
$x>0,\ y<0$	0.5313	0.1	0.4276	0.4	0.5323	0.0	1.206	0.3
Computational domain: $[-1,1] \times [-1,1]$; Free-flow boundary conditions								

TABLE 2.4. Initial data for the fifteenth MultiD RP described in [86] and the second of [10].

By means of the contour plots shown in Figures 2.10 and 2.11, we can analyze the solutions of this MultiD Riemann problem, computed on uniform grids of 400^2 and 1000^2 cells, for both methods being compared. All results follow the expected behavior described in the above paragraph, with the additional property of being symmetric with respect to the $x = y$ line, as was also anticipated. There is no significant difference between the plots obtained with the *manual assembling* and those of BAL2012 for this particular test. Let us note that the low resolution of the contact discontinuities is not surprising given that both methods are based on the two-wave model of the HLL Riemann solver.

Next, we study the multidimensional Riemann problem $\overrightarrow{J_{21} J_{32} J_{34} J_{41}}$ that involves nothing more than slip line initial data, summarized on the right of Table 2.3. Particularly, we expect the solutions to have a vortex-type structure that turns in clockwise direction, with contact discontinuities spiraling around the center, and this is the case for the numerical results presented in Figure 2.12. We can observe that the ripples cre-
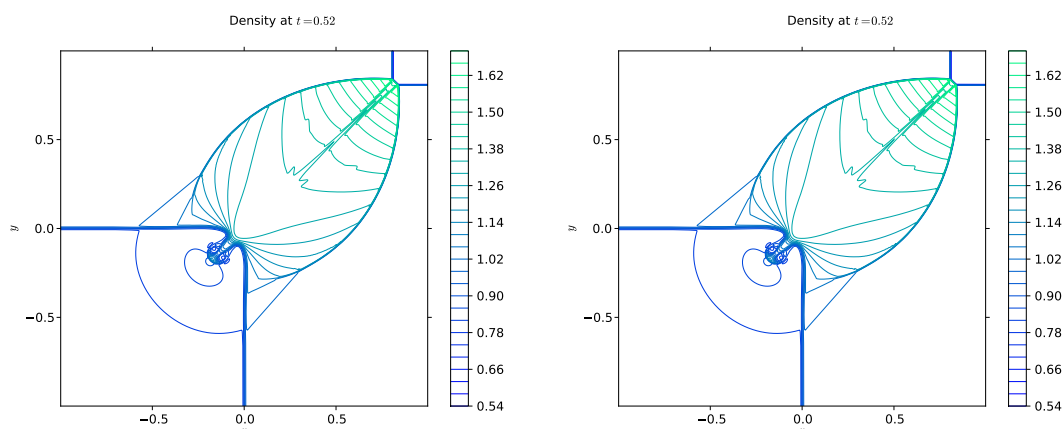
FIGURE 2.11. The density computed with BAL2012 (left) and our scheme (right) for MultiD RP1, using 1000×1000 cells on 64 processors; contour lines chosen as in Fig. 2.10 (ρ:0.53-1.73).

ated in the first and third quadrants of the left plot have comparable resolution to those found in [86, 87, 122]. The detail of the ripples and slip lines is greatly improved when the number of zones is increased, e.g., to one million cells, as shown in the right image. We wish to mention that once again there is no visible difference between the contours obtained with our scheme and the ones acquired with BAL2012, and this is the reason why we only display the former.
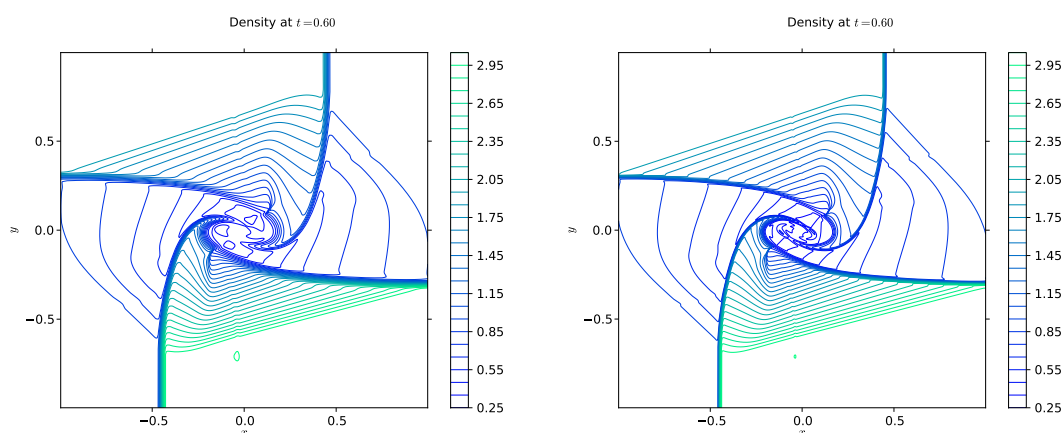
FIGURE 2.12. Density ρ obtained using our scheme for MultiD RP2 on 400×400 (left, ρ:0.23-3.07) and 1000×1000 (right, ρ:0.16-3.06) grids; 29 contour lines displayed from 0.25 to 3.05 with a step of 0.10.

The initial configuration of the third MultiD Riemann problem is given in Table 2.4 (left) and corresponds to $\overrightarrow{R}_{21} J_{32} J_{34} \overleftarrow{S}_{41}$. Both contact discontinuities bend after getting in the subsonic area and are expected to end in a spiral. The rarefaction, instead, turns backward in front of the shock wave, ending at the slip line J_{34}. As there are no significant
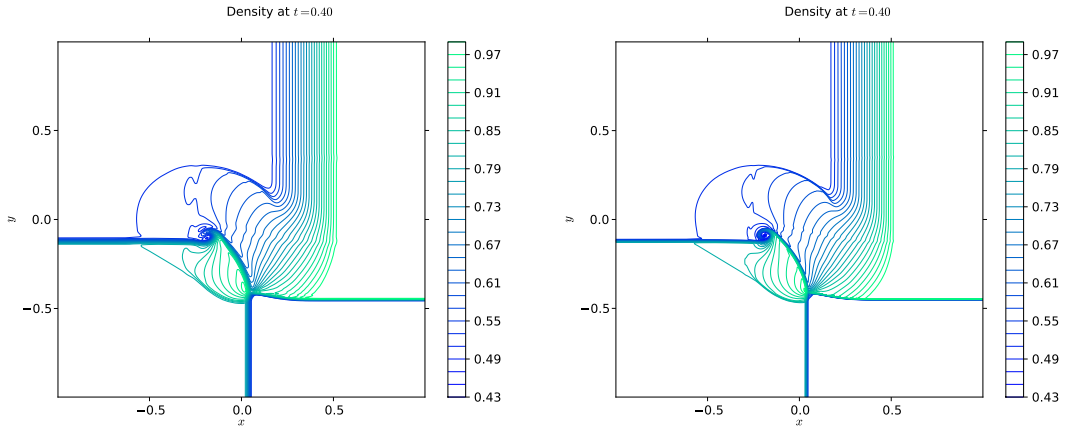
FIGURE 2.13. Contour plots of ρ using our scheme for MultiD RP3 on 400×400 (left, ρ:0.49-1.02) and 1000×1000 (right, ρ:0.42-1.01) grids; 29 contours from 0.43 to 0.99 with a step 0.02.

differences between the plots obtained with the two schemes being compared, Figure 2.13 only shows those corresponding to our approach. The results for the 400^2 mesh are satisfactory and comparable to [86], obviously improved when the grid is refined.
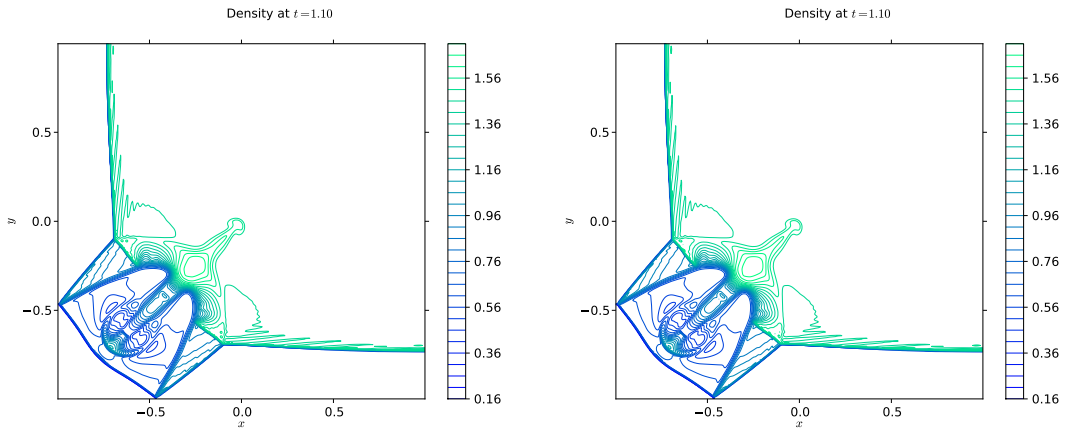
FIGURE 2.14. Contour plots of the density ρ obtained employing BAL2012 (left) and our scheme (right) for the MultiD RP4; computations done on a 400×400 grid and 32 contour lines displayed from 0.16 to 1.71 with a step of 0.05 (ρ:0.14-1.76).

Our last multidimensional Riemann problem, initially consisting of four backward shock waves $\overleftarrow{S}_{21} \overleftarrow{S}_{32} \overleftarrow{S}_{34} \overleftarrow{S}_{41}$, is the most severe of the tests presented in this subsection. Its initial and boundary conditions are given in Table 2.4 (right). The expected behavior of this problem is properly specified in Configuration 3 of [122]. Here, we briefly mention that during its time evolution, the solution develops a double Mach reflection and a shock propagates in the southwest direction at a 45-degree angle to the grid lines. This can be appreciated in Figures 2.14 and 2.15, where we display the density variable ρ at
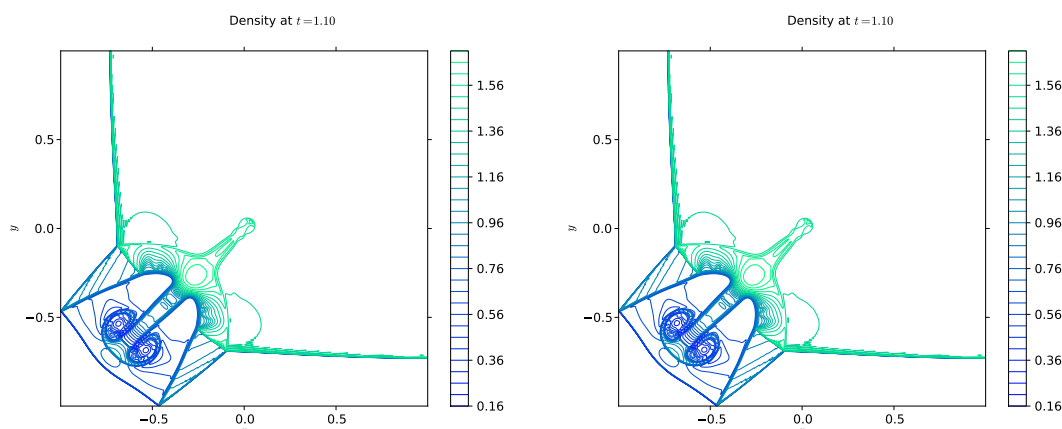
FIGURE 2.15. Density estimated with BAL2012 (left) and our scheme (right) for MultiD RP4, using 1000×1000 cells on 64 proc.; contours chosen as in Fig. 2.14 (ρ:0.14-1.75).

time $t = 1.1$ by means of contour plots obtained with our scheme and BAL2012, on two different meshes. Clearly, the region of strong and complex interactions associated with the problem is located in the third quadrant, where we are able to observe a well-resolved mushroom cap (especially in the finer grid where it is sharp), which is consistent with expectations. Once more, all solutions are visually symmetric with respect to $x = y$.
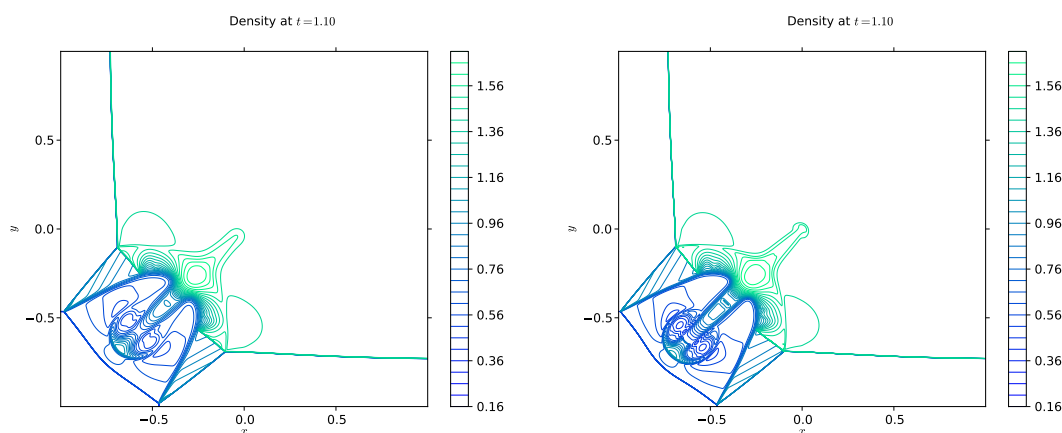
FIGURE 2.16. First-order density results for MultiD RP4 obtained with our scheme on 4000×4000 (left, 512 processors) and 10000×10000 (right, 1024 processors) cells; contours chosen as in Fig. 2.14 (ρ:0.14-1.75).

We wish to note that if we do not properly assemble the flux at each cell's faces for this problem, second-order computations will suffer from the spurious solution known as the carbuncle phenomenon. In fact, prevention of this instability is what inspired us to derive and recommend equation (2.91) instead of (2.85) for the assembling (Algorithms 3 and 2 in Annex B.2, respectively). For first-order approximations, both mentioned

expressions are equivalent; the results shown in Figure 2.16 were created using extremely fine meshes of 16 and 100 million cells, proving the robustness of the first-order scheme.

2.3.3 Double Mach Reflection

The double Mach reflection problem proposed by Woodward and Colella [148] starts off as a Mach 10 oblique shock in air encountering a reflecting wall. Using the set-up originally given in [148], we run the simulation until the final time $t = 0.2$ for the range of resolutions considered by Balsara [9, 10], i.e., grids consisting of 960×240, 1920×480 and 2400×600 zones, spanning the domain $[0, 4] \times [0, 1]$.

Figure 2.17 shows twenty-five density contours obtained with the two methods being compared, on the above-mentioned meshes. We are able to see that the jet formed by the double Mach reflection is well captured, especially on the finest grid; in all plots, we can observe the slipping contact line that leads around to the forward moving Mach stem, which rolls-up creating a vortex head. For the single-step Eulerian MUSCL results found in Figure 9e of [148], Woodward and Colella provided an explanation for the oscillations and noise present near the slowly moving shock, which we now quote as it directly applies to our case: "the shocks are extremely thin, but this thinness has permitted a numerical instability to generate noise where the shocks move slowly and are nearly aligned with the mesh". However, despite this noise, all results are satisfactory.
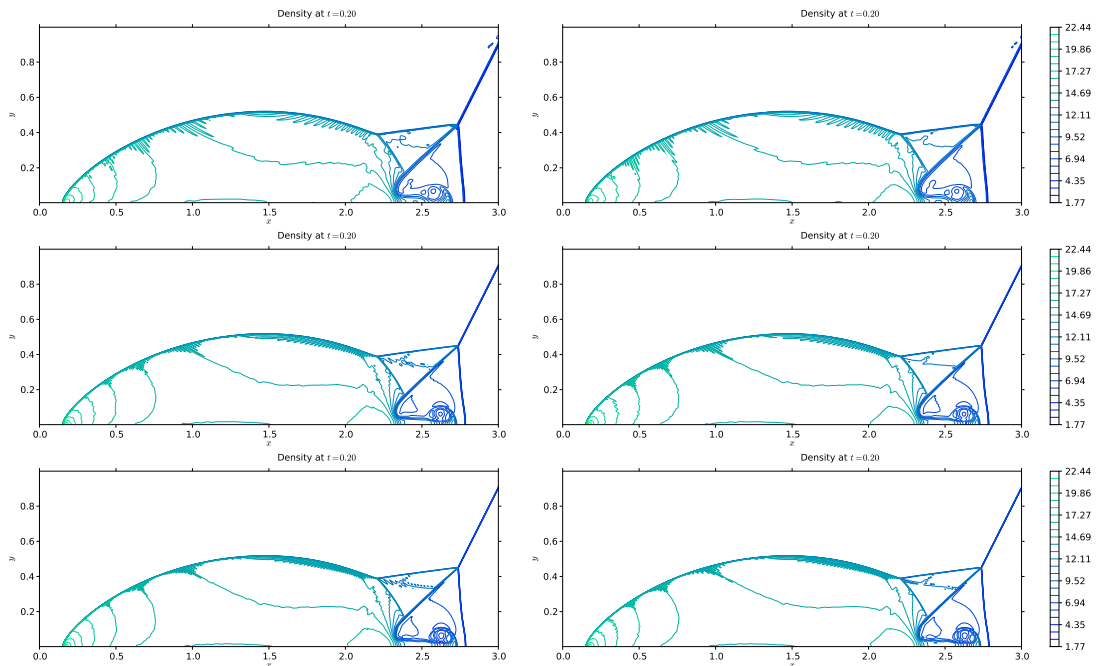
FIGURE 2.17. Results for the double Mach reflection problem obtained with BAL2012 (left) and our scheme (right), using 25 density contours ranging from 1.77 to 22.44 with a constant step; computations performed on 960×240 (top), 1920×480 (middle) and 2400×600 (bottom) meshes, 64 processors. All results have been plotted up to $x = 3$.

2.3.4 Sedov Explosion

The multidimensional blast test presented by Sedov in 1946 [123] comprises an intense explosion resulting from a punctual quantity of energy placed in the center of the numerical domain. We then expect the solution to be a strong spherical shock propagating outwards towards the boundaries, which are set to be periodic.

(a) 1D HLL RS   (b) BAL2012   (c) Our Scheme
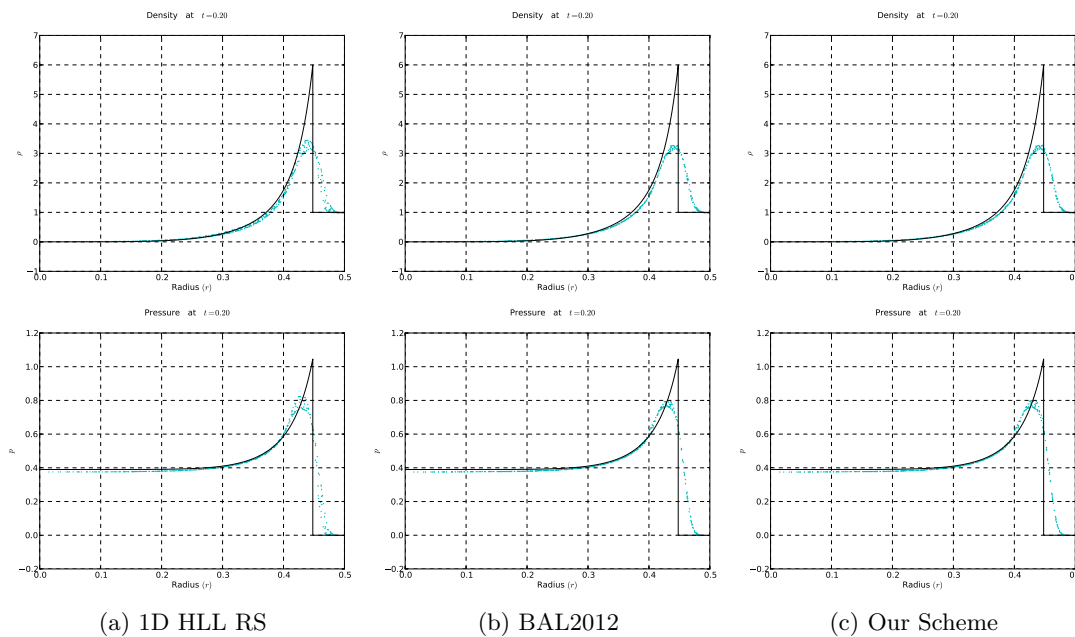
FIGURE 2.18. Scatter plots for three different methods compared with the analytical time dependent solution of the density (top) and pressure (bottom); computations performed on a 65×65 grid.

For this problem, both the ambient gas density and the explosion energy are initially set to unity. The latter is deposited in the central cell of a 65×65 or 129×129 grid covering the computational domain $[-0.5, 0.5] \times [-0.5, 0.5]$ and the simulations are run until a time $t = 0.2$, i.e., before the shock reaches the boundaries. The grid is purposely chosen coarse to be able to easily detect the anisotropic behavior commonly observed when performing this test with traditional Godunov codes. The results shown in Figures 2.18 and 2.19 for BAL2012 and our scheme were obtained using *Simpson assembling*, in order to reiterate the fact that both methods yield almost identical numerical solutions when this type of assembling is employed, and they are surely more isotropic than those obtained with the conventional second order HLL scheme. In addition, Figure 2.19 aids in understanding that the more we refine the grid, the more the corresponding solutions will resemble the analytical ones.
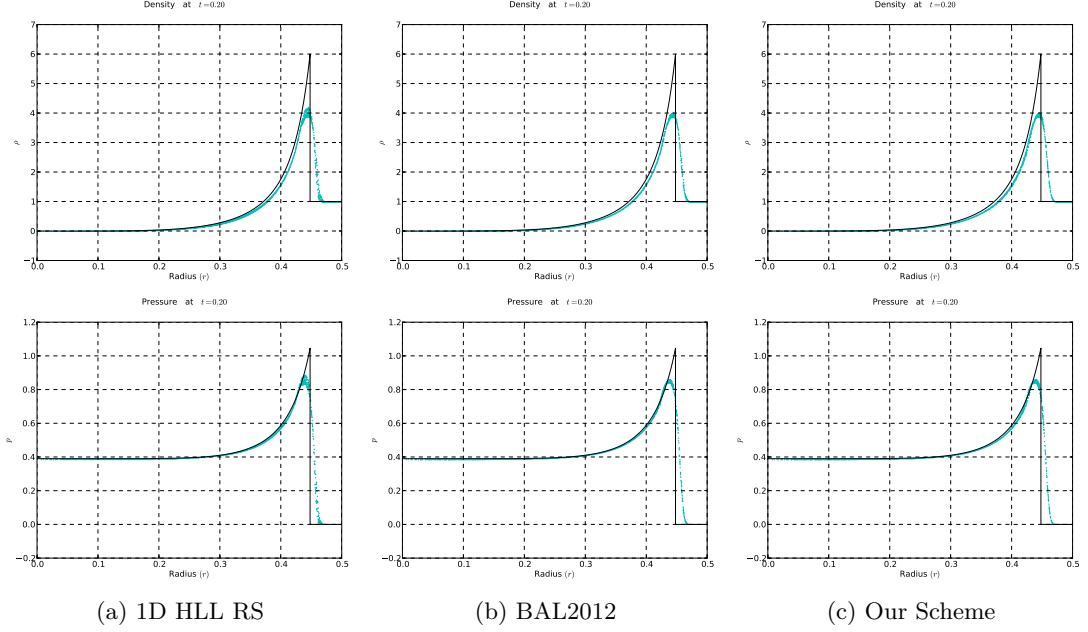
FIGURE 2.19. Density (top) and pressure (bottom) scatter plots compared with analytical solutions represented as solid lines, using three methods; computations done on a 129×129 grid.

2.4   Conclusions

We have described a simple multidimensional Riemann solver for compressible homogeneous flows governed by the Euler system of equations. The associated numerical strategy defines an approximate profile of 2D Riemann problems composed of plane waves and makes use of Rankine-Hugoniot conditions as a guideline to adequately derive constant state approximations on both sides of the discontinuities. The MultiD solver is a two-dimensional extension of the well-known HLL scheme for the four-quadrant Riemann problem that generalizes the 2D solver proposed by Balsara [9, 10]. For the considered approximate profile consisting of nine constant states, jump conditions led to an overdetermined system that we solved using a least squares approximation. Notwithstanding, the derived numerical 2D fluxes look remarkably similar to the typical HLL flux and all formulations reduce to those of the 1D solver when the initial Riemann data model a one-dimensional flow.

Sample numerical results presented in this chapter show the effectiveness and robustness of the proposed methodology when applied to subsonic and supersonic flows. For the latter, particular attention must be paid when assembling the total flux at the cells' faces with varying weights; therefore, we have provided a straightforward and robust assembling approach, comparable to that which uses weights fixed to the coefficients in Simpson's rule for all time steps. In addition to the simplicity, we also propose a generalization to unstructured grids with a formulation that is mostly algebraic rather than geometrical and, following this line, we argue that there is a way to derive an HLL solver

for Riemann problems with an arbitrary number of initial constant states connected at a single point.

Jump conditions can be improved by designing complex profiles so that the Rankine-Hugoniot relations define an invertible system with intermediate states and associated fluxes as unknowns. Moreover, given that the consistency with the integral formulation through these relations holds in three dimensions as well, we believe that a genuine three-dimensional solver can readily be obtained in future work. Extensions of more complex solvers such as the HLLE and HLLC are also feasible.

CHAPTER 3

Divergence-Free MHD Simulations

Introduction

Given the ubiquity of electrically conducting fluids in presence of magnetic fields and the simplicity of the model, MHD has widespread application in both astrophysics and magnetic confinement fusion (see [31, 42]). In the field of plasma physics, the MHD model is used to treat plasma as a single conducting fluid and describe different phenomena using macroscopic quantities and a corresponding system of conservation laws. Experimentally, these modelled phenomena are found to closely approximate aspects of real plasma behavior, such as MHD equilibria, Alfvén waves, and field line freezing [42], among others.

Therefore, it is not surprising that in the last few decades, the desire of performing highly efficient MHD simulations has become increasingly important. According to P. Janhunen [80], in order to have robust and accurate solutions, an optimal scheme for the associated equations should meet the following four requirements: exactly conserve the mass, momentum, and specific energy; preserve the positivity of the pressure and density under all circumstances; have as little numerical dissipation as possible; and satisfy the solenoidal property of the magnetic field as accurately as possible. The latter refers to guaranteeing the constraint $\nabla \cdot \boldsymbol{B} = 0$, while maintaining the conservation form of the fundamental physical laws, and is directly linked to the other requirements. Indeed, special care needs to be taken to satisfy and control this property on any numerical scheme, even if the magnetic field is initially divergence-free. Failure to do so may result in non-linear numerical instabilities and discretization errors increasing over time, manifesting themselves as discrepancies in the simulations, e.g., incorrect jump conditions, wrong propagation speed of discontinuities, appearance of unphysical effects such as plasma transport orthogonal to the magnetic field and negative pressures and/or densities (see, for instance, [12, 24, 45, 130]).

The conservation law formulation of the magnetohydrodynamic equations allows the use of Godunov-type schemes for their solution, and as a consequence, several strategies in multidimensional Godunov-type MHD codes and several algorithms that can be com-

bined with shock-capturing Godunov-type base schemes have been developed with the aim of maintaining the divergence-free property when performing numerical simulations [130]. In this chapter, we focus on the divergence cleaning and constrained transport (CT) methods. The latter, originally introduced by Evans and Hawley [52] (and considered to be a modification of the renowned Yee framework [150] for Maxwell's equations to the context of magnetohydrodynamic flows), involves the use of a staggered magnetic field with components defined at cell interfaces, thus providing a natural expression for the induction equation in conservative form. Hence, the combination of the CT framework with the Godunov one is an attractive solution, see [9, 10, 12, 41, 52, 58, 61], and this is the reason why it is the default technique used here in order to perform MHD simulations. Tóth [130] showed that the staggered representation of the magnetic field is not necessary in the formulation of constrained transport methods and various unstaggered variants have been proposed in recent years (see, for instance, [56, 75, 119]). However, our interest lies in conventional constrained transport techniques which involve the estimation of the electric field at corners and zone edges in two and three dimensions, respectively. Londrillo and Del Zanna [100] showed that these electric fields should be obtained as solutions of two-dimensional Riemann problems in order to obtain a stable numerical solution and fortunately, we have already derived a 2D HLL Riemann solver in the previous chapter that can be easily applied in this situation. We note though that several alternative methods have been developed in [12, 52, 100, 101, 130], among others, but are not examined here except for that of Fromang et al. [58], which we adopt for our numerical simulations and which we modify for our purposes.

In general, the staggered collocation of magnetic and electric field variables makes the use of CT method in unstructured grids rather laborious and costly. This had led to the development of alternative methods, such as divergence cleaning ones, and since one of our future goals is to design a high order finite volume approximation for hyperbolic conservation laws in curvilinear unstructured grids, we believe that other methods that do not involve a staggered formulation are simpler to extend to unstructured meshes (given an existing structured mesh code) as an initial step for testing and validating. Among the different existing techniques, we choose to investigate the hyperbolic cleaning method introduced by Dedner et al. [45]. We mention that the main advantage of using this method is that it is easy to implement, since it is completely based on the cell-centered discretizations favored in Godunov schemes, and thus allows highly accurate solutions with reduced computational effort.

This chapter is organized as follows. In the next section, we review and stress the importance of maintaining the divergence-free constraint at all times when performing numerical simulations of ideal MHD flows. Some background theory on the main approaches that have been proposed to control this constraint and some comments on standard notation are given briefly in the same section. The details of the hyperbolic divergence cleaning method and the constrained transport methods are presented in Sections 3.2 and 3.3, respectively. Several numerical tests are presented and discussed in Section 3.4, where we compare both considered methods with selected problems that aim to put in evidence their advantages and disadvantages; first numerical results obtained

with the 2D Riemann problem are also presented there. Finally, concluding remarks are given in the last section.

3.1 The Divergence-Free Condition

Let us consider the ideal MHD equations (1.33) and the closure equation (1.35). The constraint $\nabla \cdot \boldsymbol{B} = 0$ is not necessary in the time evolution in the sense that if the magnetic field is assumed at the initial time step to be divergence-free, then an exact solution to the MHD equations will satisfy this condition for all times $t > 0$. For smooth solutions, this is guaranteed by the evolution equation (1.33d), since taking the divergence of the equivalent equation (1.36) and recalling that $\nabla \cdot (\nabla \times \cdot) \equiv 0$, gives

$$\partial_t (\nabla \cdot \boldsymbol{B}) = 0. \tag{3.1}$$

As a result, from an analytical point of view, we sometimes find in the literature that equation (1.34) is regarded as an involution rather than a constraint, as in [13, 75]. Ideally, when performing numerical simulations, we would expect this particular equation to remain zero at all times. This is the case in one dimension, where the constraint becomes $\partial_x B_x = 0$ and the evolution equation for B_x in (1.33d), decoupled from the other equations, is reduced to $\partial_t B_x = 0$; hence, an initial $\partial_x B_x(\cdot, 0) = 0$ leads to $\partial_x B_x(\cdot, t) = 0$ for all times $t > 0$. However, the matter is more complicated for multidimensional MHD flows, and as detailed by the work of Brackbill and Barnes [24], numerical discretization errors have an impact on the time evolution in the following way:

$$\partial_t (\nabla \cdot \boldsymbol{B}) = 0 + \mathcal{O}\left((\Delta x)^m, (\Delta t)^n\right), \tag{3.2}$$

where Δx and Δt are respectively the space and time discretization steps and $m, n \geq 1$, related to the order of accuracy. In the same paper, Brackbill and Barnes show the importance of choosing an appropriate discretization of $\nabla \cdot \boldsymbol{B} = 0$ in order to avoid the emergence of unwanted and unphysical effects in the MHD system. Basically, if $\nabla \cdot \boldsymbol{B} \neq 0$, the magnetic force $\boldsymbol{F}$ defined by

$$\boldsymbol{F} = \nabla \cdot (\boldsymbol{B} \otimes \boldsymbol{B}) - \tfrac{1}{2} \nabla (\boldsymbol{B} \cdot \boldsymbol{B}) = \boldsymbol{J} \times \boldsymbol{B}, \tag{3.3}$$

will not in general disappear in the direction of the magnetic field, i.e.,

$$\boldsymbol{F} \cdot \boldsymbol{B} = (\nabla \cdot \boldsymbol{B})(\boldsymbol{B} \cdot \boldsymbol{B}) \neq 0. \tag{3.4}$$

Therefore, the behavior of the system may become unphysical due to an increase of spurious forcing, leading to instabilities. In general, the effects of not controlling the numerical errors arising from the discrete form of the divergence-free constraint have been well-documented in the literature, and interesting examples and conclusions can be found in [12, 24, 45, 130], as well as in Section 3.4 in this chapter. For the moment, we only mention that, from a numerical point of view, $\nabla \cdot \boldsymbol{B} = 0$ represents a constraint which cannot be safely ignored.

Besides the constrained transport and hyperbolic divergence cleaning techniques that will be explained in the immediate sections, two other interesting methods that aim to

maintain this constraint are the projection scheme and Powell's eight-wave formulation. The former [24] relies on the projection of the approximate magnetic field $\boldsymbol{B}^*$ (variables with a star superscript usually denote predicted values) computed with the base multidimensional MHD scheme into the subspace of divergence-free fields after each time step, specifically

$$\boldsymbol{B}^{n+1} = \boldsymbol{B}^* + \nabla\psi, \tag{3.5}$$

where ψ satisfies a Poisson equation

$$\Delta\psi = -\nabla \cdot \boldsymbol{B}^*. \tag{3.6}$$

Tóth [130] demonstrated that an appropriate implementation of this scheme preserves the conservative and other important properties of the base MHD scheme. However, since the solution requires a global elliptic solver per time step on a problem that is hyperbolic by nature, this might be "especially computationally inefficient in the case of adaptively refined grids" [75].

On the other hand, the eight-wave formulation was originally suggested by Powell in [112] and is based on an eight-wave structure for the Riemann problem, hence its name. In fact, the eighth wave is associated with the propagation of $\nabla \cdot \boldsymbol{B}$ and is added at the expense of introducing source terms proportional to this quantity at the PDE level (refer to Chapter 1). Although the deviations from the conservation are small in many situations, the scheme is nonetheless nonconservative and in problems containing strong shocks, the source terms might become significant enough to produce incorrect jump conditions and consequently, incorrect results away from the discontinuity (see [130] for a deeper analysis of the method).

3.1.1 Some Comments on Notation and Discretization

In this subsection, we introduce the notation as a standard for the numerical approximations of both the divergence cleaning and constrained transport techniques. First, we consider a uniform numerical grid in a three-dimensional ($d = 3$) domain with $\boldsymbol{x} = (x,y,z)$. If we integrate the system of conservation laws given in equation (1.1a) over a grid cell $\mathcal{C}_{i,j,k} = (x_{i-1/2}, x_{i+1/2}) \times (y_{j-1/2}, y_{j+1/2}) \times (z_{k-1/2}, z_{k+1/2})$ and over a time step (t^n, t^{n+1}), we obtain the following expression:

$$\mathbf{w}_{i,j,k}^{n+1} = \mathbf{w}_{i,j,k}^n - \frac{\Delta t}{\Delta x} \left(\boldsymbol{\phi}_{x,i+\frac{1}{2},j,k} - \boldsymbol{\phi}_{x,i-\frac{1}{2},j,k} \right) \tag{3.7}$$
$$- \frac{\Delta t}{\Delta y} \left(\boldsymbol{\phi}_{y,i,j+\frac{1}{2},k} - \boldsymbol{\phi}_{y,i,j-\frac{1}{2},k} \right) - \frac{\Delta t}{\Delta z} \left(\boldsymbol{\phi}_{z,i,j,k+\frac{1}{2}} - \boldsymbol{\phi}_{z,i,j,k-\frac{1}{2}} \right),$$

where Δx, Δy and Δz are the mesh sizes in each direction. We mention that in equation (3.7), both $\mathbf{w}_{i,j,k}^n$ and $\mathbf{w}_{i,j,k}^{n+1}$ are once again cell-averaged values of $\boldsymbol{w}(x,y,z,t^n)$ and $\boldsymbol{w}(x,y,z,t^{n+1})$, respectively, and the fluxes are obtained by a time-surface average (as was done in Sections 1.3 and 2.1.1 for the one- and two-dimensional case), namely

$$\mathbf{w}_{i,j,k}^n = \frac{1}{|\mathcal{C}_{i,j,k}|} \int_{\mathcal{C}_{i,j,k}} \boldsymbol{w}(x,y,z,t^n) \, d\boldsymbol{x}, \tag{3.8}$$

$$\boldsymbol{\phi}_{x,i\pm\frac{1}{2},j,k} = \frac{1}{\Delta t} \int_{t^n}^{t^{n+1}} \int_{y_{j-\frac{1}{2}}}^{y_{j+\frac{1}{2}}} \int_{z_{k-\frac{1}{2}}}^{z_{k+\frac{1}{2}}} \boldsymbol{f}(\boldsymbol{w}(x_{i\pm\frac{1}{2}},y,z,t))\, dy\, dz\, dt, \tag{3.9a}$$

$$\boldsymbol{\phi}_{y,i,j\pm\frac{1}{2},k} = \frac{1}{\Delta t} \int_{t^n}^{t^{n+1}} \int_{x_{i-\frac{1}{2}}}^{x_{i+\frac{1}{2}}} \int_{z_{k-\frac{1}{2}}}^{z_{k+\frac{1}{2}}} \boldsymbol{g}(\boldsymbol{w}(x,y_{i\pm\frac{1}{2}},z,t))\, dx\, dz\, dt, \tag{3.9b}$$

$$\boldsymbol{\phi}_{z,i,j,k\pm\frac{1}{2}} = \frac{1}{\Delta t} \int_{t^n}^{t^{n+1}} \int_{x_{i-\frac{1}{2}}}^{x_{i+\frac{1}{2}}} \int_{y_{j-\frac{1}{2}}}^{y_{j+\frac{1}{2}}} \boldsymbol{h}(\boldsymbol{w}(x,y,z_{i\pm\frac{1}{2}},t))\, dx\, dy\, dt. \tag{3.9c}$$

Recall that in conventional Godunov-type schemes, the numerical fluxes in equation (3.7) are evaluated by solving Riemann problems in the normal direction $\bar{\boldsymbol{n}}$ at each cell interface, and for MHD we will consider an approximation

$$\boldsymbol{\phi}_{x,i+\frac{1}{2},j,k} = \boldsymbol{\phi}_x(\mathbf{w}_{i,j,k}, \mathbf{w}_{i+1,j,k}; \boldsymbol{B} \cdot \bar{\boldsymbol{n}}_{x,i+\frac{1}{2},j,k}), \tag{3.10a}$$

$$\boldsymbol{\phi}_{y,i,j+\frac{1}{2},k} = \boldsymbol{\phi}_y(\mathbf{w}_{i,j,k}, \mathbf{w}_{i,j+1,k}; \boldsymbol{B} \cdot \bar{\boldsymbol{n}}_{y,i,j+\frac{1}{2},k}), \tag{3.10b}$$

$$\boldsymbol{\phi}_{z,i,j,k+\frac{1}{2}} = \boldsymbol{\phi}_z(\mathbf{w}_{i,j,k}, \mathbf{w}_{i,j,k+1}; \boldsymbol{B} \cdot \bar{\boldsymbol{n}}_{z,i,j,k+\frac{1}{2}}). \tag{3.10c}$$

This scheme directly applied to the MHD system of equations does not naturally achieve the divergence-free property.

3.2   Hyperbolic Divergence Cleaning

When all variables defined in the hyperbolic system (1.33) are defined in the same position, a cleaning technique is needed to enforce the constraint $\nabla \cdot \boldsymbol{B} = 0$. The hyperbolic divergence cleaning method suggested by Dedner et al. [45] is based on coupling the divergence constraint (1.34) to the evolution equation for the magnetic field (1.33d) by introducing a new scalar function or generalized Lagrangian multiplier (GLM) ψ. Then, both of the mentioned equations, are replaced by

$$\partial_t \boldsymbol{B} + \nabla \cdot (\boldsymbol{B} \otimes \boldsymbol{u} - \boldsymbol{u} \otimes \boldsymbol{B}) + \nabla \psi = 0, \tag{3.11}$$

$$\mathrm{D}(\psi) + \nabla \cdot \boldsymbol{B} = 0, \tag{3.12}$$

with $\mathrm{D}(\cdot)$ being a linear differential operator. Henceforth, the resulting system (1.33a, 1.33b, 1.33c, 3.11, 3.12) is called the generalized Lagrange multiplier (GLM) formulation of the MHD equations, or simply, GLM-MHD. Dedner et al. analyzed different possibilities for D and found that a satisfactory approximation to the original system may be obtained by choosing a mixed hyperbolic/parabolic ansatz, which will be explained in detail in Section 3.2.1. Additionally, in order to obtain a good numerical approximation, it is necessary to choose adequate initial and boundary conditions for the unphysical variable ψ (see Section 3.2.3). We keep the notation used by Dedner et al. with few minor changes.

3.2.1   Linear Differential Operator D

From equations (3.11) and (3.12), one can deduce that for any choice of D and for sufficiently smooth solutions, the divergence of the magnetic field and the scalar function ψ satisfy the same equation, namely

$$\partial_t \mathrm{D}(\nabla \cdot \boldsymbol{B}) - \Delta(\nabla \cdot \boldsymbol{B}) = 0, \tag{3.13}$$

$$\partial_t \mathrm{D}(\psi) \quad - \Delta\psi \quad = 0. \tag{3.14}$$

Parabolic Correction

Defining the linear differential operator as

$$\mathrm{D}(\psi) = \frac{1}{c_p^2}\psi, \tag{3.15}$$

with $c_p \in (0,\infty)$, and using it in (3.14) yields the heat equation $\partial_t\psi - c_p^2\Delta\psi = 0$. Hence, this type of correction allows for the perturbations in the magnetic field to be dissipated and smoothed out, if appropriate boundary conditions are defined. However, the explicit approximation to the MHD equations using a parabolic correction presents certain difficulties due to the restrictions imposed on the parameter c_p by stability conditions. Since we are only interested in explicit schemes, we study more suitable operators proposed by Dedner et al. [45].

Hyperbolic Correction

One obtains a hyperbolic correction by choosing

$$\mathrm{D}(\psi) = \frac{1}{c_h^2}\partial_t\psi, \tag{3.16}$$

with $c_h \in (0,\infty)$. Substituting (3.16) into (3.14) gives the wave equation $\partial_{tt}^2\psi - c_h^2\Delta\psi = 0$. Thus, local divergence errors are transported to the boundary with finite speed c_h. Now, expressing equation (3.12) in terms of the hyperbolic correction, yields

$$\partial_t\psi + c_h^2(\nabla \cdot \boldsymbol{B}) = 0, \tag{3.17}$$

which is an attractive result since the resulting GLM-MHD system is purely hyperbolic.

Mixed Correction

Formally, this approach is nothing but the combination of the parabolic and hyperbolic corrections, with the linear differential operator defined by

$$\mathrm{D}(\psi) = \frac{1}{c_h^2}\partial_t\psi + \frac{1}{c_p^2}\psi, \tag{3.18}$$

where c_p and c_h are the parabolic and hyperbolic constants previously defined. Direct substitution of this correction into (3.14) leads to $\partial_{tt}^2\psi + c_h^2/c_p^2\,\partial_t\psi = c_h^2\Delta\psi$, i.e., the telegraph equation, which implies that the errors associated to the divergence of the

magnetic field are both transported with speed c_h and damped with time and distance. Following the same approach used for the other corrections, from (3.14), one gets

$$\partial_t \psi + c_h^2 (\nabla \cdot \boldsymbol{B}) = -\frac{c_h^2}{c_p^2} \psi, \qquad (3.19)$$

where it is evident that the damping comes now from a source term.

3.2.2 Eigensystem of the GLM-MHD Equations

The complete GLM-MHD system with the mixed correction (3.18) can be written in the following form:

$$\partial_t \begin{pmatrix} \rho \\ \rho\boldsymbol{u} \\ \boldsymbol{B} \\ \rho e \\ \psi \end{pmatrix} + \nabla \cdot \begin{pmatrix} \rho\boldsymbol{u} \\ \rho\boldsymbol{u} \otimes \boldsymbol{u} + \left(p + \frac{1}{2}\boldsymbol{B}\cdot\boldsymbol{B}\right)\mathbf{I} - \boldsymbol{B}\otimes\boldsymbol{B} \\ \boldsymbol{B}\otimes\boldsymbol{u} - \boldsymbol{u}\otimes\boldsymbol{B} + \psi\mathbf{I} \\ \left(\rho e + p + \frac{1}{2}\boldsymbol{B}\cdot\boldsymbol{B}\right)\boldsymbol{u} - (\boldsymbol{u}\cdot\boldsymbol{B})\boldsymbol{B} \\ c_h^2\boldsymbol{B} \end{pmatrix} = \begin{pmatrix} 0 \\ 0 \\ 0 \\ 0 \\ -\frac{c_h^2}{c_p^2}\psi \end{pmatrix}, \qquad (3.20)$$

where $\mathbf{I}$ is a 3×3 identity matrix. This system, with a source term only in the equation for the unphysical variable ψ, can be written in compact form as

$$\partial_t \hat{\boldsymbol{w}} + \nabla \cdot \boldsymbol{\mathcal{G}}(\hat{\boldsymbol{w}}) = \hat{\boldsymbol{s}}(\hat{\boldsymbol{w}}), \qquad (3.21)$$

with $\hat{\boldsymbol{w}} = (\rho, \rho\boldsymbol{u}, \boldsymbol{B}, \rho e, \psi)^T$ and the flux function $\boldsymbol{\mathcal{G}} = (\hat{\boldsymbol{f}}, \hat{\boldsymbol{g}}, \hat{\boldsymbol{h}})$. Note that, in the limiting case where $c_p \to \infty$, the mixed correction reduces to the hyperbolic one and $\hat{\boldsymbol{s}}(\hat{\boldsymbol{w}}) = 0$. Moreover, given the primitive variables $\hat{\boldsymbol{v}} = (\rho, u_x, u_y, u_z, B_x, B_y, B_z, p, \psi)^T$, the homogeneous version of equation (3.21) may be rewritten in the quasilinear form

$$\partial_t \hat{\boldsymbol{v}} + \boldsymbol{A}_{\hat{f}}(\hat{\boldsymbol{v}})\partial_x \hat{\boldsymbol{v}} + \boldsymbol{A}_{\hat{g}}(\hat{\boldsymbol{v}})\partial_y \hat{\boldsymbol{v}} + \boldsymbol{A}_{\hat{h}}(\hat{\boldsymbol{v}})\partial_z \hat{\boldsymbol{v}} = 0, \qquad (3.22)$$

where, for example,

$$\boldsymbol{A}_{\hat{f}}(\hat{\boldsymbol{v}}) = \begin{pmatrix} u_x & \rho & 0 & 0 & 0 & 0 & 0 & 0 & 0 \\ 0 & u_x & 0 & 0 & -\frac{B_x}{\rho} & \frac{B_y}{\rho} & \frac{B_z}{\rho} & \frac{1}{\rho} & 0 \\ 0 & 0 & u_x & 0 & -\frac{B_y}{\rho} & -\frac{B_x}{\rho} & 0 & 0 & 0 \\ 0 & 0 & 0 & u_x & -\frac{B_z}{\rho} & 0 & -\frac{B_x}{\rho} & 0 & 0 \\ 0 & 0 & 0 & 0 & 0 & 0 & 0 & 0 & 1 \\ 0 & B_y & -B_x & 0 & -u_y & u_x & 0 & 0 & 0 \\ 0 & B_z & 0 & -B_x & -u_z & 0 & u_x & 0 & 0 \\ 0 & \gamma p & 0 & 0 & (\gamma-1)\boldsymbol{u}\cdot\boldsymbol{B} & 0 & 0 & u_x & (1-\gamma)B_x \\ 0 & 0 & 0 & 0 & c_h^2 & 0 & 0 & 0 & 0 \end{pmatrix}. \qquad (3.23)$$

In the matrix $\boldsymbol{A}_{\hat{f}}$ defined above, it is possible to decouple the equations for B_x and ψ from the remaining system and solve them independently. Thus, for a one-dimensional

problem, one obtains the following decoupled system of equations:

$$\partial_t \begin{pmatrix} B_x \\ \psi \end{pmatrix} + \begin{pmatrix} 0 & 1 \\ c_h^2 & 0 \end{pmatrix} \partial_x \begin{pmatrix} B_x \\ \psi \end{pmatrix} = \begin{pmatrix} 0 \\ 0 \end{pmatrix}. \tag{3.24}$$

Additionally, given $\hat{\boldsymbol{v}}' = (\rho, u_x, u_y, u_z, B_y, B_z, p)^T$, one can define the matrix $\boldsymbol{A}'_{\hat{f}}(\hat{\boldsymbol{v}}')$ by removing the fifth and ninth rows and columns from $\boldsymbol{A}_{\hat{f}}(\hat{\boldsymbol{v}})$. Considering B_x as a constant parameter, the following quasilinear system is obtained:

$$\partial_t \hat{\boldsymbol{v}}' + \boldsymbol{A}'_{\hat{f}}(\hat{\boldsymbol{v}}')\partial_x \hat{\boldsymbol{v}}' = 0. \tag{3.25}$$

Matrix $\boldsymbol{A}'_{\hat{f}}$ is diagonalizable and has seven eigenvalues corresponding to one entropy wave traveling with speed $\lambda_5 = u_x$; two Alfvén waves traveling with speed $\lambda_{3,7} = u_x \mp c_a$; and four magneto-acoustic waves, two fast and two slow with speeds $\lambda_{2,8} = u_x \mp c_f$ and $\lambda_{4,6} = u_x \mp c_s$, respectively, where

$$c_a = \frac{|B_x|}{\sqrt{\rho}}, \qquad c_{f,s}^2 = \frac{1}{2}\left(\frac{\gamma p + \boldsymbol{B} \cdot \boldsymbol{B}}{\rho} \pm \sqrt{\left(\frac{\gamma p + \boldsymbol{B} \cdot \boldsymbol{B}}{\rho}\right)^2 - 4\frac{\gamma p B_x^2}{\rho^2}}\right). \tag{3.26}$$

From the decoupled system, the eigenvalues $\lambda_{1,9} = \mp c_h$ are obtained, which turn out to be distinct from the eigenvalues of $\boldsymbol{A}'_{\hat{f}}$ for a sufficiently large c_h. Consequently, the matrix $\boldsymbol{A}_{\hat{f}}$ has nine eigenvalues, such that

$$\lambda_1 \le \lambda_2 \le \lambda_3 \le \lambda_4 \le \lambda_5 \le \lambda_6 \le \lambda_7 \le \lambda_8 \le \lambda_9.$$

One can draw analogous results for the matrices $\boldsymbol{A}_{\hat{g}}$ and $\boldsymbol{A}_{\hat{h}}$; thus, system (3.20) is hyperbolic (see Definition 1.2.1).

3.2.3 Numerical Approximation

In the previous paragraphs, the eigenvalues $\lambda_{1,9} = \mp c_h$ were obtained from the decoupled system, where the constant c_h represents the propagation speed of local divergence errors. Thus, c_h is chosen to be the maximum signal speed compatible with the time step Δt, such that

$$c_h = \max_{\mathcal{C}_{i,j,k}}\left(|u_x| + c_{f_x}, |u_y| + c_{f_y}, |u_z| + c_{f_z}\right), \tag{3.27}$$

where c_{f_x}, c_{f_y} and c_{f_z} are the fast magneto-acoustic speeds in the three directions. The time increment is restricted by the Courant-Friedrichs-Levy (CFL) condition $c_{cfl} \in (0,1)$ in the following way:

$$\Delta t = c_{cfl}\frac{\min(\Delta x, \Delta y, \Delta z)}{c_h}. \tag{3.28}$$

By attempting to solve equation (3.21) using a Godunov-type approach, it is necessary to find a numerical flux for the GLM-MHD system and one can start by deriving it for the hyperbolic one, i.e., system (3.21) with no source terms. First, notice that for

arbitrary left and right states (B_{xl}, ψ_l) and (B_{xr}, ψ_r), the Godunov flux of system (3.24) can be computed exactly since

$$\begin{pmatrix} \widetilde{B}_x \\ \widetilde{\psi} \end{pmatrix} = \begin{pmatrix} \frac{1}{2}(B_{xl} + B_{xr}) - \frac{1}{2c_h}(\psi_r - \psi_l) \\ \frac{1}{2}(\psi_l + \psi_r) - \frac{c_h}{2}(B_{xr} - B_{xl}) \end{pmatrix},$$

and the numerical flux $(\widetilde{\psi}, c_h^2 \widetilde{B}_x)^T$ is derived. For the remaining system, one can therefore use an approximate Riemann solver $\mathcal{W}$ for the one-dimensional MHD equations with the normal component of the magnetic field defined by $\widetilde{B}_x$. Hence, the numerical flux $\boldsymbol{\phi}_x$ that we employ for our numerical simulations has the following form:

$$\boldsymbol{\phi}_x = (\boldsymbol{\phi}_x^{hlld}(\hat{\boldsymbol{w}}_l, \hat{\boldsymbol{w}}_r; \widetilde{B}_x), 0)^T + (0, 0, 0, 0, \widetilde{\psi}, 0, 0, 0, c_h^2 \widetilde{B}_x)^T, \tag{3.29}$$

and analogous expressions can be found for $\boldsymbol{\phi}_y$ and $\boldsymbol{\phi}_z$. Moreover, for the mixed GLM-MHD system, which considers the source terms in the right-hand side of system (3.20), an operator-splitting approach is used. Thus, in the source step, the initial value problem

$$\partial_t \psi = -\frac{c_h^2}{c_p^2} \psi, \tag{3.30}$$

is solved, for which the initial condition ψ^* is the output of the previous step. Integrating exactly for a time increment Δt, yields

$$\psi^{n+1} = \psi^* \exp(-\Delta t \, c_h^2 / c_p^2). \tag{3.31}$$

Dedner et al. recommend fixing the value $c_r = c_p^2/c_h = 0.18$. Mignone and Tzeferacos [106] (see also [113]) argue that this quantity c_r is not dimensionless (indeed, it has units of length) and propose to introduce an additional parameter $\alpha = \Delta h / c_r$ such that

$$\psi^{n+1} = \psi^* \exp(-\alpha \, c_h \, \Delta t / \Delta h), \tag{3.32}$$

with $\Delta h = \min(\Delta x, \Delta y, \Delta z)$. Their numerical experiments indicate that divergence errors are minimized if $\alpha \in [0, 1]$.

Boundary Conditions

For the magnetohydrodynamic variables considered in system (1.33), the initial and boundary conditions are chosen according to the specific physical settings of the problem under consideration, but for the variable ψ, one is free to prescribe them. Given its nature, a good choice for the initial value of the unphysical variable is $\psi_0 = 0$. Regarding the particular choice of the boundary condition, Dedner et al. recommend assuming that the behavior of ψ and ρ is identical at the boundary, making the implementation quite simple and straightforward on an existing code.

3.3   Constrained Transport

The constrained transport (CT) method, introduced by Evans and Hawley [52] in 1988, is a numerical scheme that applies a staggered mesh to evolve the induction equation

while maintaining the divergence-free property of the magnetic field to machine round-off error precision. The approach relies on rewriting Faraday's law (1.36) using Stokes' theorem to obtain

$$\frac{d}{dt}\int_{\mathcal{S}}\boldsymbol{B}\cdot d\boldsymbol{S} = -\oint_{\partial\mathcal{S}}\boldsymbol{E}\cdot d\boldsymbol{l},\tag{3.33}$$

where $\mathcal{S}$ is the surface of a cell bounded by the closed contour $\partial\mathcal{S}$; thus, the divergence constraint is conserved in the integral sense.

3.3.1   Staggered Mesh Discretization

The staggered mesh formulation simply consists in defining the magnetic field components at cell interfaces, the electric fields at zone corners (in two dimensions) or edges (in three dimensions), and all the hydrodynamic variables at the cell centers. The main justification for using a strategy of this type is that it allows to define an inherently divergence-free method.
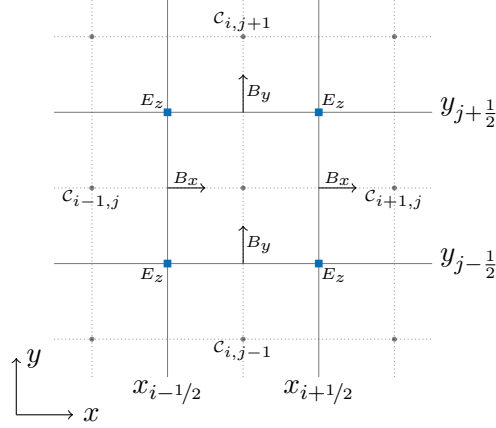
FIGURE 3.1. Two-dimensional staggering in the constrained transport approach.

Recalling equation (3.33), it is clear that a discrete version of Stokes' theorem may be used to evolve in time a magnetic field that has a staggered representation. On this account, let us consider the primary cell $\mathcal{C}_{i,j}$ in two dimensions with the volume-averaged hydrodynamic variables given in (2.15). Figure 3.1 shows the collocation of the magnetic and electric fields for this case, with B_x and B_y defined on the interface centers to which they are orthogonal. Therefore, we define the staggered magnetic field variables $B^n_{x,i-1/2,j}$, $B^n_{x,i+1/2,j}$, $B^n_{y,i,j-1/2}$ and $B^n_{y,i,j+1/2}$, as surface-averaged values over each cell's face, e.g.,

$$B^n_{x,i-\frac{1}{2},j} = \frac{1}{\Delta y}\int_{y_{j-\frac{1}{2}}}^{y_{j+\frac{1}{2}}} B_x(x_{i-\frac{1}{2}},y,t^n)\,dy.\tag{3.34}$$

In Figure 3.1, we also observe that the z-component of the electric field is located at the

corners; the induction equation can then be discretized along the cell edges, yielding

$$B_{x,i-\frac{1}{2},j}^{n+1} = B_{x,i-\frac{1}{2},j}^{n} - \frac{\Delta t}{\Delta y}\left(E_{z,i-\frac{1}{2},j+\frac{1}{2}}^{*} - E_{z,i-\frac{1}{2},j-\frac{1}{2}}^{*}\right), \tag{3.35a}$$

$$B_{x,i+\frac{1}{2},j}^{n+1} = B_{x,i+\frac{1}{2},j}^{n} - \frac{\Delta t}{\Delta y}\left(E_{z,i+\frac{1}{2},j+\frac{1}{2}}^{*} - E_{z,i+\frac{1}{2},j-\frac{1}{2}}^{*}\right), \tag{3.35b}$$

$$B_{y,i,j-\frac{1}{2}}^{n+1} = B_{y,i,j-\frac{1}{2}}^{n} + \frac{\Delta t}{\Delta x}\left(E_{z,i+\frac{1}{2},j-\frac{1}{2}}^{*} - E_{z,i-\frac{1}{2},j-\frac{1}{2}}^{*}\right), \tag{3.35c}$$

$$B_{y,i,j+\frac{1}{2}}^{n+1} = B_{y,i,j+\frac{1}{2}}^{n} + \frac{\Delta t}{\Delta x}\left(E_{z,i+\frac{1}{2},j+\frac{1}{2}}^{*} - E_{z,i-\frac{1}{2},j+\frac{1}{2}}^{*}\right). \tag{3.35d}$$

If the numerical divergence $\nabla \cdot \boldsymbol{B}$ for cell $\mathcal{C}_{i,j}$ at time t^n is defined as

$$(\nabla \cdot \boldsymbol{B})_{i,j}^{n} = \frac{B_{x,i+1/2,j}^{n} - B_{x,i-1/2,j}^{n}}{\Delta x} + \frac{B_{y,i,j+1/2}^{n} - B_{y,i,j-1/2}^{n}}{\Delta y}, \tag{3.36}$$

it is quite easy to show that an initial $(\nabla \cdot \boldsymbol{B})_{i,j}^{n} = 0$ leads to $(\nabla \cdot \boldsymbol{B})_{i,j}^{n+1} = 0$, with machine round-off error accuracy, i.e., the staggered approach maintains the constraint equation to machine round-off (see [52, 130]).

3.3.2 Numerical Methodology

Now, we proceed to briefly describe a general finite volume time-update strategy with the purpose of showing the main steps needed to evolve all state variables over one time step, considering the underlying staggered mesh formulation.

At the beginning of the time step, the hydrodynamic variables are defined at the center of the cells and the staggered magnetic field at the corresponding interface centers (see Figure 3.1). Let us denote by $\mathbf{w}_{i,j,k}^{n} = (\rho_{i,j,k}^{n}, \rho_{i,j,k}^{n}\boldsymbol{u}_{i,j,k}^{n}, \rho_{i,j,k}^{n}e_{i,j,k}^{n}, \boldsymbol{B}_{i,j,k}^{n})^{T}$ the vector of centered variables, where the magnetic field $\boldsymbol{B}_{i,j,k}^{n}$ may be approximately obtained in the following way:

$$B_{x,i,j,k}^{n} = \frac{B_{x,i-1/2,j,k}^{n} + B_{x,i+1/2,j,k}^{n}}{2}, \quad B_{y,i,j,k}^{n} = \frac{B_{y,i,j-1/2,k}^{n} + B_{y,i,j+1/2,k}^{n}}{2},$$

$$\text{and} \quad B_{z,i,j,k}^{n} = \frac{B_{z,i,j,k-1/2}^{n} + B_{z,i,j,k+1/2}^{n}}{2}. \tag{3.37}$$

One is then able to find the fluxes (3.10) by means of an adequate Riemann solver for MHD (see [25, 27, 72, 107, 97]); for instance, employing the HLLD solver [107] so that

$$\phi_{x,i+\frac{1}{2},j,k} = \phi_{x}^{hlld}(\mathbf{w}_{i,j,k}, \mathbf{w}_{i+1,j,k}; B_{x,i+1/2,j,k}), \tag{3.38a}$$

$$\phi_{y,i,j+\frac{1}{2},k} = \phi_{y}^{hlld}(\mathbf{w}_{i,j,k}, \mathbf{w}_{i,j+1,k}; B_{y,i,j+1/2,k}), \tag{3.38b}$$

$$\phi_{z,i,j,k+\frac{1}{2}} = \phi_{z}^{hlld}(\mathbf{w}_{i,j,k}, \mathbf{w}_{i,j,k+1}; B_{z,i,j,k+1/2}), \tag{3.38c}$$

to make the update of the state vector $\mathbf{w}_{i,j,k}^{n}$ using expression (3.7) and obtain $\mathbf{w}_{i,j,k}^{n+1}$.

What remains at this point is to update the constituents of $\boldsymbol{B}$ at the faces. The main idea consists in constructing an approximation to the electric field (1.37) at the edges

and use it to update the face centered magnetic fields, in a way similar to that shown in example (3.35). Note that in three dimensions, equation (3.35b) becomes

$$B^{n+1}_{x,i+\frac{1}{2},j,k} = B^n_{x,i+\frac{1}{2},j,k} - \frac{\Delta t}{\Delta y}\left(E^*_{z,i+\frac{1}{2},j+\frac{1}{2},k} - E^*_{z,i+\frac{1}{2},j-\frac{1}{2},k}\right) + \frac{\Delta t}{\Delta z}\left(E^*_{y,i+\frac{1}{2},j,k+\frac{1}{2}} - E^*_{y,i+\frac{1}{2},j,k-\frac{1}{2}}\right),$$
(3.39)

with similar expressions for the other magnetic field components. Thus, it is necessary to find an appropriate estimation for all terms of the form $E^*_{x,m,n,l}$, $E^*_{y,m,n,l}$, and $E^*_{z,m,n,l}$, and since it is of our interest to find second-order approximations, we will henceforth address the estimation in this context.

Accordingly, we refer the reader to [58] for details regarding the algorithm, based on the MUSCL-Hancock scheme [129, 134], that is used in HERACLES [66] to perform second-order numerical simulations of astrophysical magnetohydrodynamics. Here, we review the key aspects that are needed to characterize the upwinded value of the *z*-component of the electric field $\boldsymbol{E}$ at an edge or, more precisely, the time- and line-averaged electromotive force (EMF)

$$E^*_{z,i+\frac{1}{2},j+\frac{1}{2},k} = \frac{1}{\Delta z\,(t^* - t^n)}\int_{t^n}^{t^*}\int_{z_{k-\frac{1}{2}}}^{z_{k+\frac{1}{2}}} E_z(x_{i+\frac{1}{2}}, y_{j+\frac{1}{2}}, z, t)\, dz\, dt.$$
(3.40)

The scheme [58] follows a predictor-corrector approach, and in the C-MUSCL predictive step [128], this EMF is spatially interpolated on cell edges at time t^n by employing simple arithmetic means of the magnetic and velocity field variables, namely,

$$E^n_{z,i+\frac{1}{2},j+\frac{1}{2},k} = \bar{u}_{x,i+\frac{1}{2},j+\frac{1}{2},k}\,\bar{B}_{y,i+\frac{1}{2},j+\frac{1}{2},k} - \bar{u}_{y,i+\frac{1}{2},j+\frac{1}{2},k}\,\bar{B}_{x,i+\frac{1}{2},j+\frac{1}{2},k},$$
(3.41)

with

$$\bar{u}_{x,i+\frac{1}{2},j+\frac{1}{2},k} = \tfrac{1}{4}\left(u^n_{x,i,j,k} + u^n_{x,i+1,j,k} + u^n_{x,i,j+1,k} + u^n_{x,i+1,j+1,k}\right),$$
(3.42a)

$$\bar{u}_{y,i+\frac{1}{2},j+\frac{1}{2},k} = \tfrac{1}{4}\left(u^n_{y,i,j,k} + u^n_{y,i+1,j,k} + u^n_{y,i,j+1,k} + u^n_{y,i+1,j+1,k}\right),$$
(3.42b)

$$\bar{B}_{x,i+\frac{1}{2},j+\frac{1}{2},k} = \tfrac{1}{2}\left(B^n_{x,i+1/2,j,k} + B^n_{x,i+1/2,j+1,k}\right),$$
(3.42c)

$$\bar{B}_{y,i+\frac{1}{2},j+\frac{1}{2},k} = \tfrac{1}{2}\left(B^n_{y,i,j+1/2,k} + B^n_{y,i+1,j+1/2,k}\right).$$
(3.42d)

It is important to note that this reconstruction is second-order accurate and is only used to update the staggered magnetic field from time t^n to $t^{n+1/2}$ (see equation (3.39)), which in turn serves to compute the cell-centered magnetic field at time $t^{n+1/2}$ with (3.37); more details can be found in [128].

Then, for the induction corrector step, one is required to estimate the EMF that will be used for the final update of the magnetic field components. Londrillo and Del Zanna [100] showed that they should be obtained as solutions of the two-dimensional Riemann problems (defined at the edges) in order to obtain a stable numerical solution and we have derived a 2D HLL Riemann solver that can be easily applied in this situation, as will be seen in the coming part. We note though that several alternative methods have been developed in [12, 52, 58, 100, 101, 130], among others, but are not examined here.

3.3.3 Application of the Simple 2D HLL RS for the Electric Field

Essentially, the state vector of predicted variables $\mathbf{w}_{i,j,k}^{n+1/2}$ is spatially reconstructed from the center of each primary cell to its edges following the MUSCL approach, as was done in Section 2.2.4.3, providing the four states that are needed to solve a two-dimensional Riemann solver at each edge. Moreover, given that the magnetic field components of the staggered magnetic field are already defined on the interface centers at time $t^{n+1/2}$, we reconstruct the two longitudinal variables to the edges using face-centered TVD slopes as in equations (30) and (31) of [58], and subsequently, obtain the corresponding values for the cell-centered magnetic field after spatially averaging.

We have now all the necessary ingredients to compute the desired EMFs by applying the simple two-dimensional HLL Riemann solver from Chapter 2 (and thus complete the numerical description given in the previous subsection). For this, we begin by rewriting the ideal Ohm's law (1.37) and the evolution equation for the magnetic field (1.33d) in expanded forms, to get

$$\boldsymbol{E} = \begin{pmatrix} E_x \\ E_y \\ E_z \end{pmatrix} = \begin{pmatrix} u_z B_y - u_y B_z \\ u_x B_z - u_z B_x \\ u_y B_x - u_x B_y \end{pmatrix} \tag{3.43}$$

and the subsystem

$$\partial_t \begin{pmatrix} B_x \\ B_y \\ B_z \end{pmatrix} + \partial_x \begin{pmatrix} 0 \\ u_x B_y - u_y B_x \\ u_x B_z - u_z B_x \end{pmatrix} + \partial_y \begin{pmatrix} u_y B_x - u_x B_y \\ 0 \\ u_y B_z - u_z B_y \end{pmatrix} + \partial_z \begin{pmatrix} u_z B_x - u_x B_z \\ u_z B_y - u_y B_z \\ 0 \end{pmatrix} = 0, \tag{3.44}$$

respectively, where $(B_x, B_y, B_z)^T = (w^{[6]}, w^{[7]}, w^{[8]})^T$. As realized by Balsara and Spicer [12], there exists a dualism between the fluxes of the conservative formulation (3.44) and the components of the electric field (3.43), specifically

$$E_x = -g^{[8]} = h^{[7]}, \quad E_y = f^{[8]} = -h^{[6]}, \quad E_z = -f^{[7]} = g^{[6]}, \tag{3.45}$$

from which it is relative easy to determine the following averages (see [10]):

$$E_x = \tfrac{1}{2}\left(h^{[7]} - g^{[8]}\right), \quad E_y = \tfrac{1}{2}\left(f^{[8]} - h^{[6]}\right), \quad E_z = \tfrac{1}{2}\left(g^{[6]} - f^{[7]}\right). \tag{3.46}$$

Once more, we turn our attention to the z-component of the electric field, noting that equivalent formulations can also be found for the other components. Since our interest lies in properly characterizing the upwinded value of E_z at an edge $(\boldsymbol{x}_0, \Delta t)$, we define

$$E_z = \begin{cases} \bar{X}(\boldsymbol{f}_{ne}, \boldsymbol{g}_{ne}) & \text{if } s_n < 0 \quad \text{and } s_e < 0, \\ \bar{X}(\boldsymbol{f}_{nw}, \boldsymbol{g}_{nw}) & \text{if } s_n < 0 \quad \text{and } s_w > 0, \\ \bar{X}(\boldsymbol{f}_{sw}, \boldsymbol{g}_{sw}) & \text{if } s_s > 0 \quad \text{and } s_w > 0, \\ \bar{X}(\boldsymbol{f}_{se}, \boldsymbol{g}_{se}) & \text{if } s_s > 0 \quad \text{and } s_e < 0, \\ \bar{X}(\boldsymbol{f}_{n*}, \boldsymbol{g}_{n*}) & \text{if } s_n < 0 \quad \text{and } s_w < 0 < s_e, \\ \bar{X}(\boldsymbol{f}_{s*}, \boldsymbol{g}_{s*}) & \text{if } s_s > 0 \quad \text{and } s_w < 0 < s_e, \\ \bar{X}(\boldsymbol{f}_{*e}, \boldsymbol{g}_{*e}) & \text{if } s_s < 0 < s_n \text{ and } s_e < 0, \\ \bar{X}(\boldsymbol{f}_{*w}, \boldsymbol{g}_{*w}) & \text{if } s_s < 0 < s_n \text{ and } s_w > 0, \\ \bar{X}(\boldsymbol{f}_{**}, \boldsymbol{g}_{**}) & \text{if } s_s < 0 < s_n \text{ and } s_w < 0 < s_e, \end{cases} \tag{3.47}$$

where

$$\bar{X}(\boldsymbol{f}_{\mu\nu}, \boldsymbol{g}_{\mu\nu}) = \tfrac{1}{2}\left(g_{\mu\nu}^{[6]} - f_{\mu\nu}^{[7]}\right), \tag{3.48}$$

with $g_{**}^{[6]}$ and $f_{**}^{[7]}$ defined in (2.60) and the other fluxes in (2.24,2.38), for the ideal MHD equations. Given that only one value is calculated per cell edge at a time step, the face-centered magnetic field satisfies the divergence constraint exactly according to the considered numerical divergence (3.36).

3.4 Numerical Results

The numerical implementation of the methods presented in this chapter has been done in the same software [66] so that we are able to compare the accuracy and robustness of the hyperbolic divergence cleaning and constrained transport techniques in a fair manner. In this section, we present a series of selected test problems, some of which require the divergence of the cell-centered magnetic field to be computed numerically. For this reason, we define

$$(\nabla \cdot \boldsymbol{B})_{i,j,k}^n = \frac{B_{x,i+1,j,k}^n - B_{x,i-1,j,k}^n}{2\Delta x} + \frac{B_{y,i,j+1,k}^n - B_{y,i,j-1,k}^n}{2\Delta y} + \frac{B_{z,i,j,k+1}^n - B_{z,i,j,k-1}^n}{2\Delta z}, \tag{3.49}$$

i.e., the numerical divergence for cell $\mathcal{C}_{i,j,k}$ at time t^n.

For second order approximations, we extend the hyperbolic cleaning scheme by using the MUSCL-Hancock Method (MHM), see [129, 134], whereas in the constrained transport case, the approach of Fromang et al. [58] (that is based on the MHM method) is employed. As for the choice of slope limiters, we use two different ones: the minmod limiter [118] when comparing both methods since it is known to ensure the positivity of the solution in multiple space dimensions; and the MC limiter [136], when employing our constrained transport variant (that relies on the 2D HLL Riemann problem to estimate the electric fields) to be consistent with the hydrodynamic tests. For the latter, all results were obtained with a CFL of 0.90.

3.4.1 Advection in B_x

This problem, summarized in Table 3.1, has a non-zero initial divergence of the magnetic field. Thus, the purpose of performing tests for this unphysical problem is to determine whether the divergence cleaning technique is robust enough or not and we show results obtained using the first order hyperbolic and mixed GLM approaches.

$\rho_0(x,y)$	$u_{x0}(x,y)$	$u_{y0}(x,y)$	$u_{z0}(x,y)$	$B_{x0}(x,y)$	$B_{y0}(x,y)$	$B_{z0}(x,y)$	$p_0(x,y)$
1	1	1	0	$r(x^2+y^2)/\sqrt{4\pi}$	0	$1/\sqrt{4\pi}$	6.0

Advection in B_x

Computational domain: $[-0.5, 1.5] \times [-0.5, 1.5]$; Periodic boundary conditions

Peak: $r(s) = \begin{cases} 4096s^4 - 128s^2 + 1 & \text{if } s \in [0, 0.125], \\ 0 & \text{otherwise} \end{cases}$

TABLE 3.1. Initial data for the peak in B_x problem described in [45].

(a) $t = 0.25$ (b) $t = 0.50$ (c) $t = 0.75$ (d) $t = 1.00$
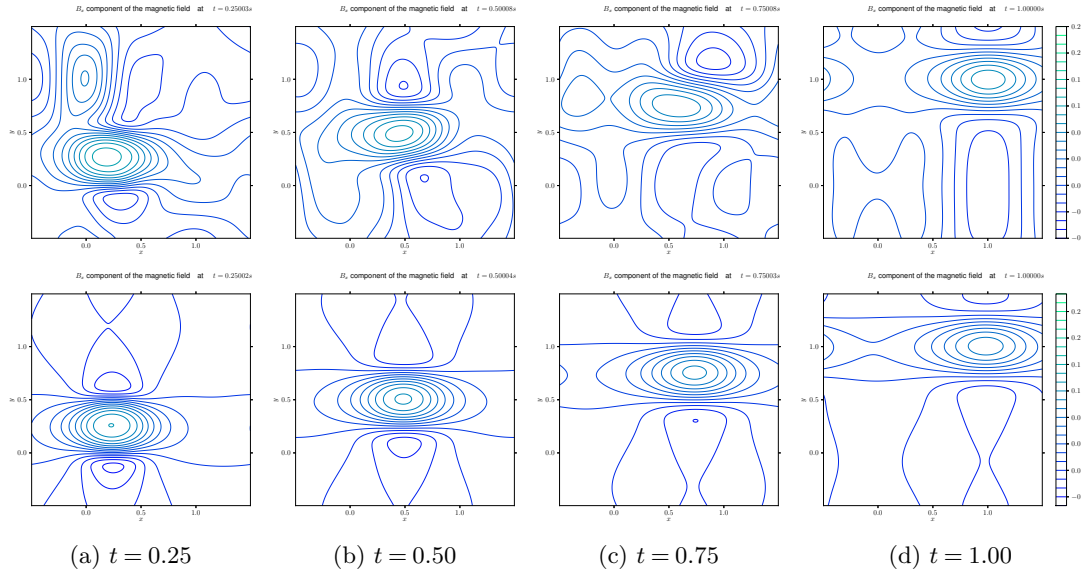
FIGURE 3.2. Isolines of B_x obtained with the HLLD scheme. The computations are performed with 256×256 cells for hyperbolic and mixed GLM approaches (from top to bottom).

In the contour plots shown in Figure 3.2, we can perceive that during the time evolution, the initial peak in B_x decreases in height for both the hyperbolic and mixed cleaning, but is well advected with the flow velocity nonetheless. The mixed GLM solutions do not show the complex wave interactions seen in the hyperbolic case, because of the additional damping. Additionally, this problem also allows to find the optimal value for the ratio $c_p^2/c_h = 0.18$ [45] (see Figure 3.3).

(a) 64×64 cells   (b) 128×128 cells   (c) 256×256 cells
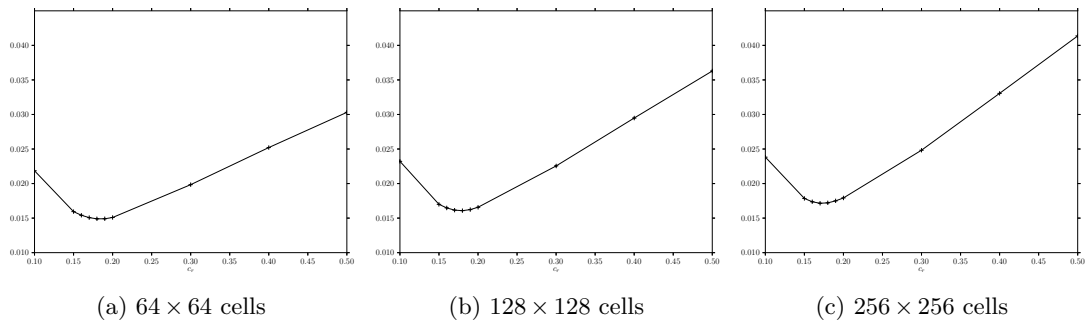
FIGURE 3.3. Time averages of the total divergence obtained with the HLLD scheme for problem 3.4.1 using different values of $c_r = c_p^2/c_h$. The optimal value is about 0.18, independent of the grid resolution.

3.4.2 Orszag-Tang

The Orszag-Tang vortex is a standard and well-known two-dimensional test for MHD codes. It describes a periodic fluid configuration, with initial conditions in Table 3.2, that leads to a system of supersonic MHD turbulence. As a result, this problem allows to test a method's ability to handle such turbulence and MHD shocks.

Orszag-Tang

$\rho_0(x,y)$	$u_{x0}(x,y)$	$u_{y0}(x,y)$	$u_{z0}(x,y)$	$B_{x0}(x,y)$	$B_{y0}(x,y)$	$B_{z0}(x,y)$	$p_0(x,y)$
γ^2	$-\sin(2\pi y)$	$\sin(2\pi x)$	0	$-\sin(2\pi y)$	$\sin(4\pi x)$	0	γ
Computational domain: $[0,1] \times [0,1]$; Periodic boundary conditions								

TABLE 3.2. Initial data for the Orszag-Tang vortex described in [106].

First, comparing the hyperbolic divergence cleaning with the constrained transport approach (without utilizing the 2D HLL Riemann solver), we show density distributions at times $t = 0.5$ and $t = 1.0$ in Figure 3.4, where we can visualize the formation of small scale vortices and turbulence.

(a) No correction   (b) Hyperbolic GLM   (c) Mixed GLM   (d) Constrained Transport
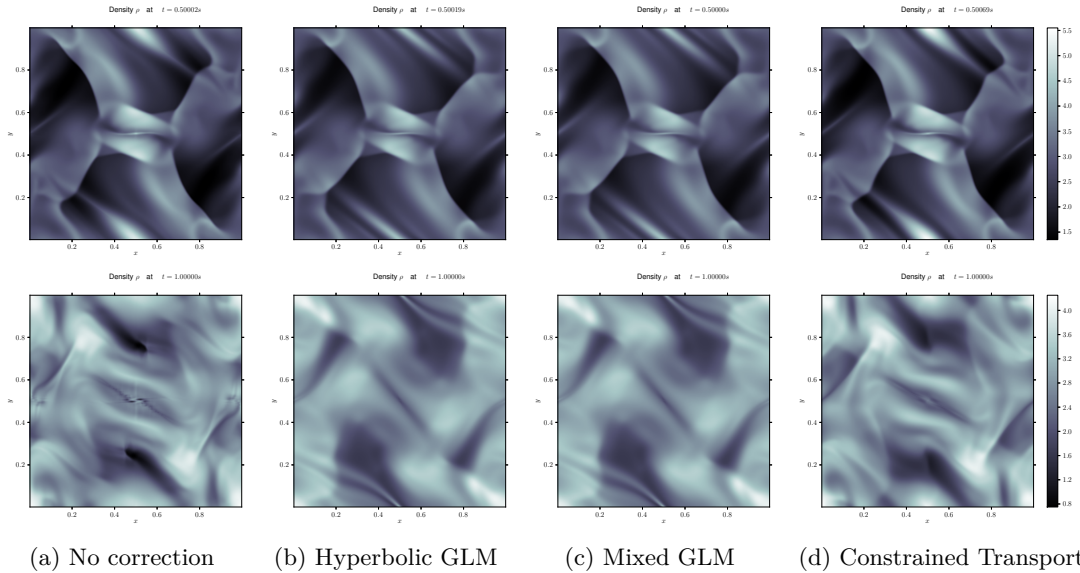
FIGURE 3.4. 2D density plots, first order in both space and time, for the Orszag-Tang system using 256×256 points at times $t = 0.5$ (top) and $t = 1.0$ (bottom).

In Figure 3.5, the evolution of the L^1 norm and maximum value of the divergence is plotted for different cell-centered techniques. It is evident that the measured L^1 errors for the hyperbolic and mixed approaches seem to converge to zero as time increases, while those obtained without correction tend to increase with time. We note that a second order simulation with no correction is not possible to obtain since the blow-up of divergence errors causes the crash of the simulation. Finally, in Figure 3.6 (left), we show horizontal cuts at $y = 0.3125$ of the pressure distribution, and find no perceivable

difference between the hyperbolic and mixed GLM techniques. Moreover, the same figure allows to conclude that the constrained transport method solves this problem more accurately than the divergence cleaning techniques presented in this chapter.
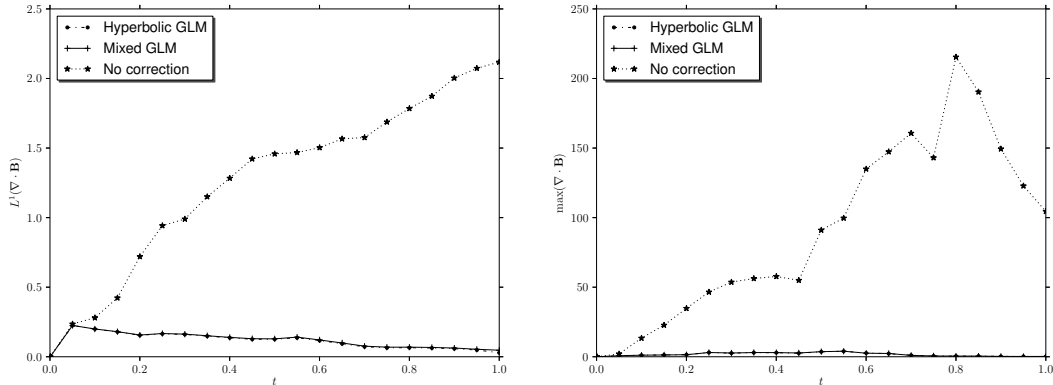
FIGURE 3.5. $L^1(\nabla \cdot \boldsymbol{B})$ (left) and $\max(\nabla \cdot \boldsymbol{B})$ (right) obtained with the HLLD scheme for the Orszag-Tang vortex; computations performed using a cell-centered approach on 256×256 cells.
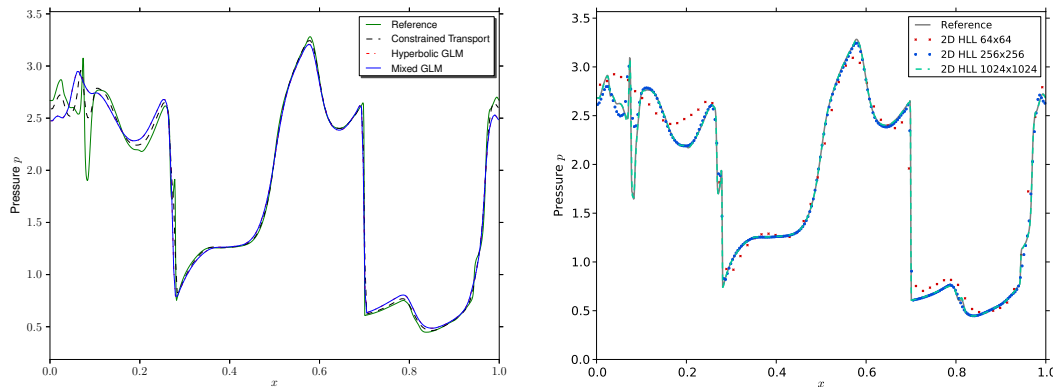
FIGURE 3.6. One-dimensional pressure distribution along $y = 0.3125$ for the Orszag-Tang system at time $t = 0.5$ employing several methods for comparison (left) and the CT method described in Section 3.3 (right); the solid line gives a reference solution obtained only with Roe Riemann solvers (see [58]) on a fine grid of 1024×1024 cells.

Now, we test the proposed constrained transport approach of Section 3.3.3. Density (respectively, pressure) plots for different mesh sizes at times $t = 0.5$ and $t = 1.0$ are shown in Figure 3.7 (respectively, Figure 3.8), where we can visualize the formation of small-scale vortices, as well as turbulence, and the development of a current sheet in the center of the domain (most evident in the very fine grids of 1024^2 and 2048^2 cells). We wish to add that these variables ρ and p remained positive for the entire simulation. All results follow the expected behavior and are symmetric under a rotation of π radians; the good agreement between our results and the ones obtained in previous investigations, such as in [41, 58, 101, 106, 107, 130], is satisfactory. Moreover, in Figure 3.6(right), we display horizontal cuts of the gas pressure at $y = 0.3125$ and note that no spurious oscillations are visible.

(a) 256×256 cells   (b) 512×512 cells   (c) 1024×1024 cells   (d) 2048×2048 cells
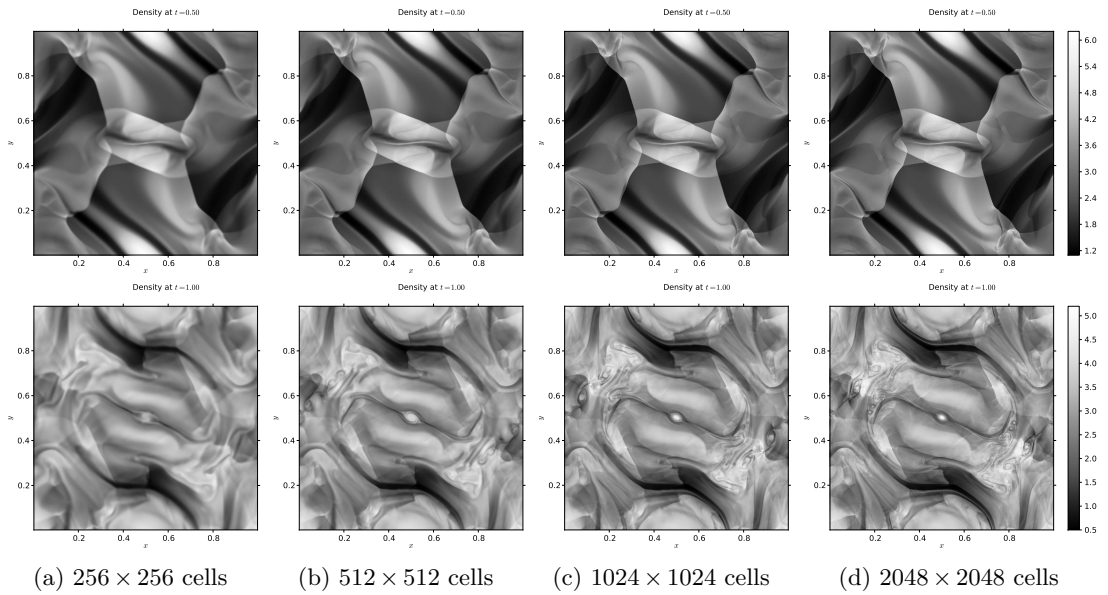
FIGURE 3.7. Grayscale density plots for the Orszag-Tang system using the CT approach of Section 3.3 at $t = 0.5$ (top) and $t = 1.0$ (bottom); density ranges: 1.05-6.22, 1.06-6.23, 1.06-6.23, 1.06-6.23 (top, left to right) and 0.60-4.55, 0.51-4.60, 0.47-5.20, 0.50-5.25 (bottom, left to right).

(a) 256×256 cells   (b) 512×512 cells   (c) 1024×1024 cells   (d) 2048×2048 cells
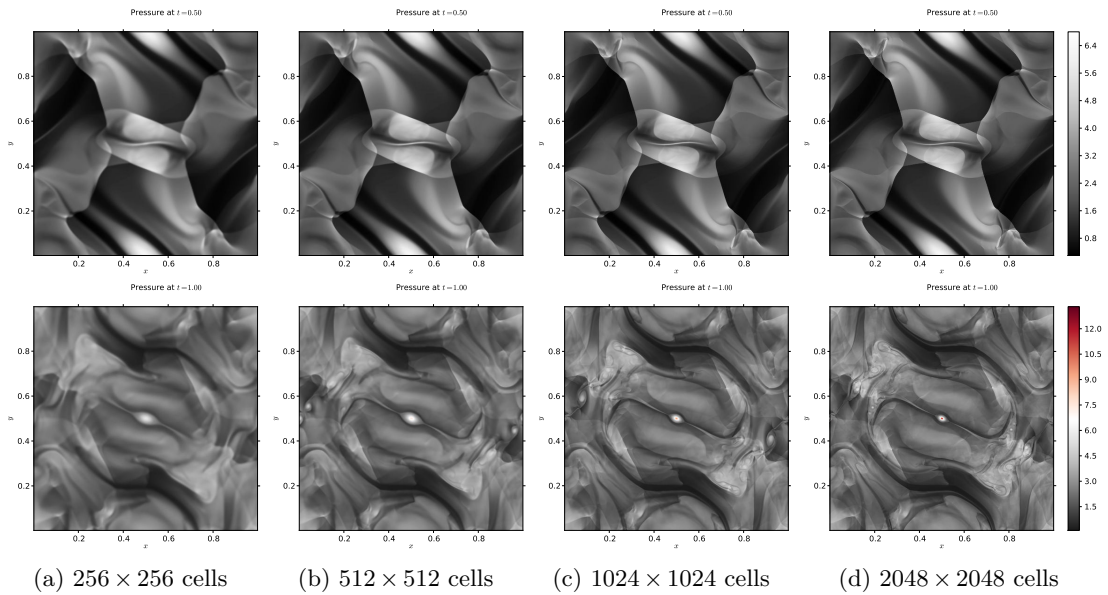
FIGURE 3.8. Grayscale 2D plots of the pressure p for Orszag-Tang at times $t = 0.5$ (top) and $t = 1.0$ (bottom), obtained with the constrained transport scheme (Section 3.3); pressure ranges: 0.28-6.39, 0.29-6.40, 0.29-6.41, 0.29-6.77 (top, left to right) and 0.12-5.61, 0.10-7.53, 0.09-9.47, 0.09-13.34 (bottom, left to right).

3.4.3   Blast Wave in Three Dimensions

The evolution of a 3D blast wave in a low plasma beta medium helps to demonstrate the method's robustness and the code's ability to handle strong shocks and rarefactions in multidimensions. This test was originally introduced in the two-dimensional context by [12] and later extended to three dimensions (see [9, 10, 61, 124], among others), and it is the most severe of the problems presented in this chapter. It consists of the explosion of an overpressurized region in the center of the domain over an exterior low β ambient medium. We then expect the solution to be a strong shock wave propagating outwards towards the boundaries, which are set to be periodic, and a rarefaction propagating inwards, evacuating the overpressurized region. Let us note that the beta of a plasma is simply the ratio of the pressure to the magnetic one, i.e., $\beta = p/p_m$.

Here, we consider the settings described in [9], where the 3D computational domain is $[-0.5, 0.5] \times [-0.5, 0.5] \times [-0.5, 0.5]$, with a resolution of 129^3. The problem is initialized with a unit density and a uniform magnetic field $\boldsymbol{B}_0 = (40/\sqrt{12\pi}, 40/\sqrt{12\pi}, 40/\sqrt{12\pi})$ everywhere in the domain. The gas pressure is set to 1000 within a central sphere of radius 0.1 and is fixed to 0.1 outside of this sphere such that $\beta \approx 0.00157$. The test is run until a time $t = 0.013$, with the method proposed in Section 3.3.3, the positivity preserving limiter [127] and $\gamma = 1.4$. The contour plots shown in Figure 3.9 correspond to the density, energy density, magnitude of the magnetic field, magnitude of the velocity vector, gas pressure and total pressure in the $z = 0$ plane at this time, and we notice that the contours are visually symmetric with respect to $x = y$.

One of the main difficulties encountered when numerically simulating this low beta problem lies in maintaining the positivity of the gas pressure and density (specially the former), and this is the reason why in the literature, one finds variants that tend to increase the value of β, e.g., by decreasing the magnitude of the magnetic field [124] or increasing the value of the ambient gas pressure [61], to make this test less stringent. Given that p is determined by subtracting both the magnetic and kinetic energies from the total energy density (and multiplying by the term $\gamma - 1$), a numerical error in the estimation of the magnetic field can be significant enough to produce a negative pressure for low beta plasmas. Thus, in our code, we make use of the energy density correction described in [12, p. 277], which put in our notation becomes

$$(\rho e)_{i,j,k}^{n+1} = (\rho e)_{i,j,k}^{n+1} - \tfrac{1}{2}(|\boldsymbol{B}_{i,j,k}^{hlld,n+1}|^2 - |\boldsymbol{B}_{i,j,k}^{n+1}|^2) \tag{3.50}$$

where

$$\boldsymbol{B}_{i,j,k}^{n+1} = \tfrac{1}{2}\left(B_{x,i-1/2,j,k}^{n+1} + B_{x,i+1/2,j,k}^{n+1},\; B_{y,i,j-1/2,k}^{n+1} + B_{y,i,j+1/2,k}^{n+1},\; B_{z,i,j,k-1/2}^{n+1} + B_{z,i,j,k+1/2}^{n+1} \right)^T,$$

to preserve the pressure positivity of this blast wave problem, as can be appreciated in Figures 3.9 and 3.10 for two different mesh sizes, with p ranging from 0.10 to 61.22 and 0.10 to 65.35, respectively. The value $\boldsymbol{B}_{i,j,k}^{hlld,n+1}$ in the previous equation corresponds to the magnetic field obtained as output of the one-dimensional (HLLD) Riemann solver. We add that the price to pay for using this correction is a small loss of the conservation of total energy density (see Table 3.3).
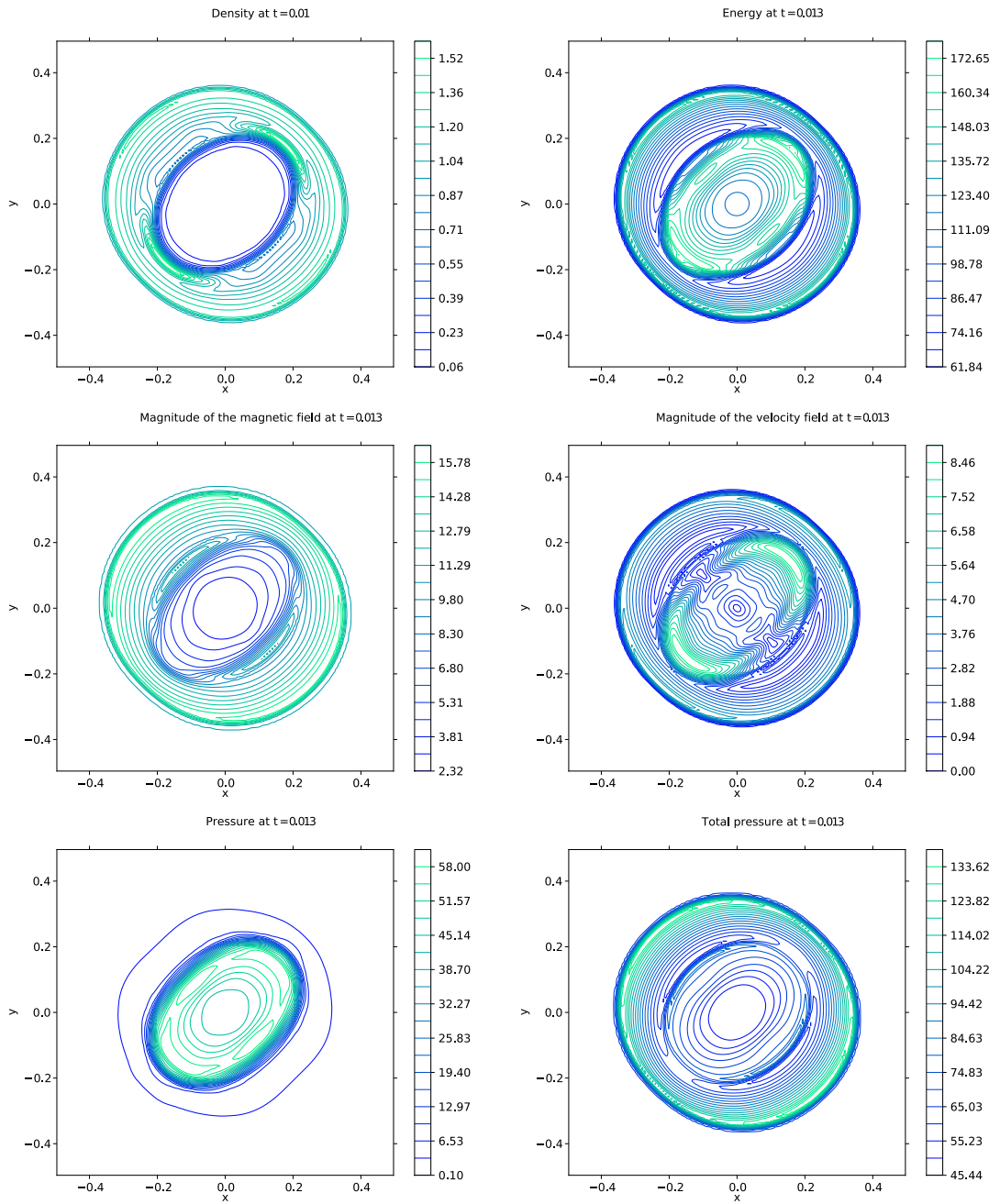
FIGURE 3.9. Contour plots of the density ($\rho : 0.06 - 1.60$), energy density ($\rho e : 61.84 - 178.81$), magnitude of the magnetic field ($|\boldsymbol{B}| : 2.32 - 16.53$), magnitude of the velocity vector ($|\boldsymbol{u}| : 0.00 - 8.93$), gas pressure ($p : 0.10 - 61.22$) and total pressure ($p_t = p + p_m : 45.44 - 138.51$) in the midplane $z = 0$ using the constrained transport scheme of Section 3.3 on a $129 \times 129 \times 129$ grid; 20 contour lines are displayed with a constant step.
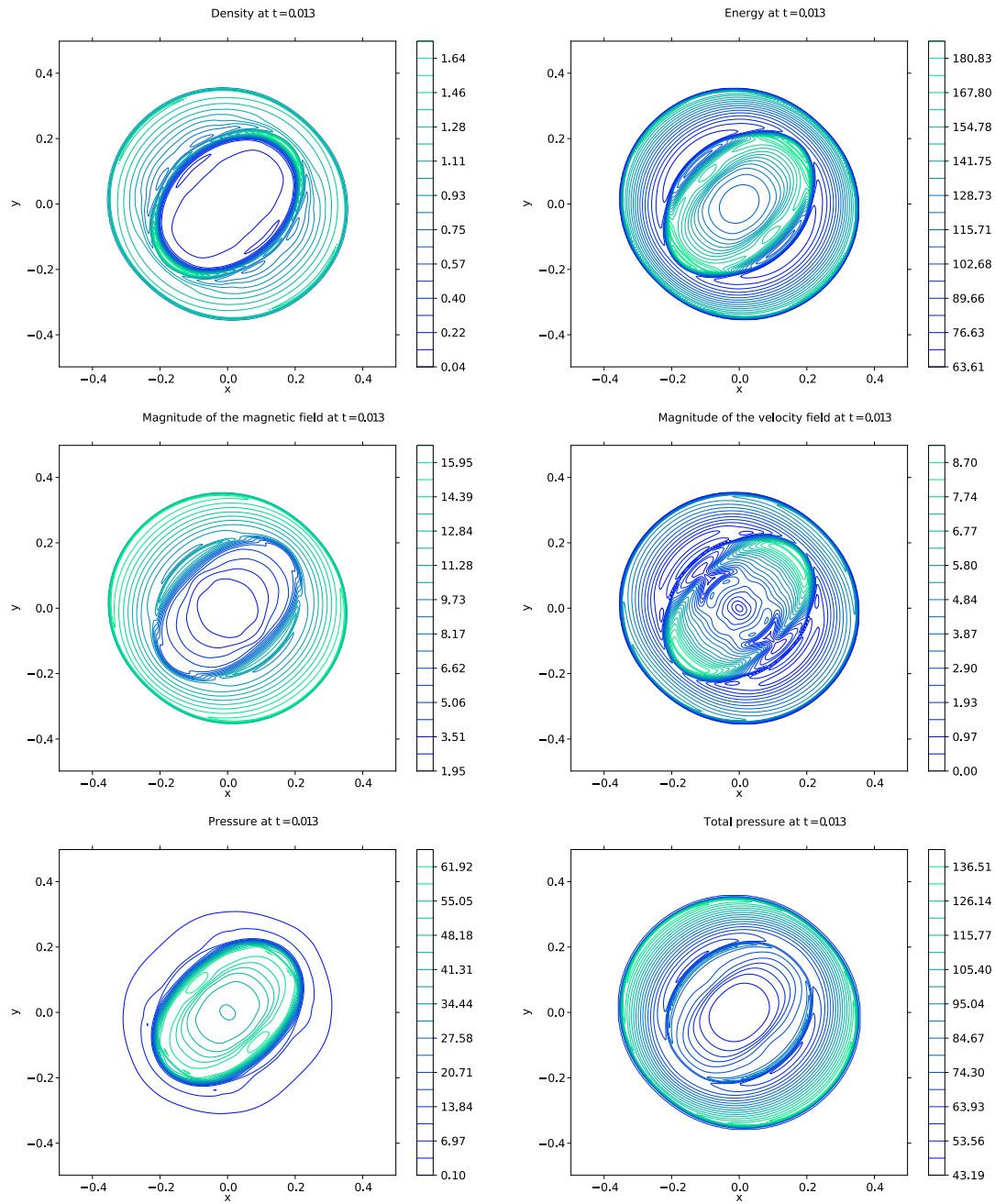
FIGURE 3.10. Density ($\rho : 0.04 - 1.73$), energy density ($\rho e : 63.61 - 187.34$), magnitude of $\boldsymbol{B}$ ($|\boldsymbol{B}| : 1.95 - 16.72$), magnitude of the velocity field ($|\boldsymbol{u}| : 0.00 - 9.19$), gas pressure ($p : 0.10 - 65.35$) and total pressure ($p_t : 43.19 - 141.69$) in the plane $z = 0$ obtained with the CT approach of Section 3.3 on a 257^3 grid; 20 contour lines are displayed with a constant step.

Loss of the Total Energy Conservation

0.0000	0.0013	0.0026	0.0039	0.0053	0.0065	0.0078	0.0091	0.0105	0.0118	0.0130
74.4446	74.4297	74.4193	74.4147	74.4129	74.4146	74.4180	74.4221	74.4272	74.4318	74.4363

TABLE 3.3. Total energy density for the three-dimensional blast problem using 129^2 cells (bottom row) at different times t (top row).

3.4.4   Magnetized Rotor Problem

Another test that is well-known in magnetohydrodynamics is the rotor problem, originally described by Balsara and Spicer (BS) in [12]. However, Gábor Tóth made an accurate observation in [130] and brought up the difference found in the plots provided by BS and their proposed setup. For this reason, and because we wish to make proper comparisons, we choose to use Tóth's "second rotor problem" (thoroughly detailed in his paper) as reference. Here, we only mention that this test consists of a "dense, rapidly spinning cylinder, in the center of an initially stationary, light ambient fluid" [9].
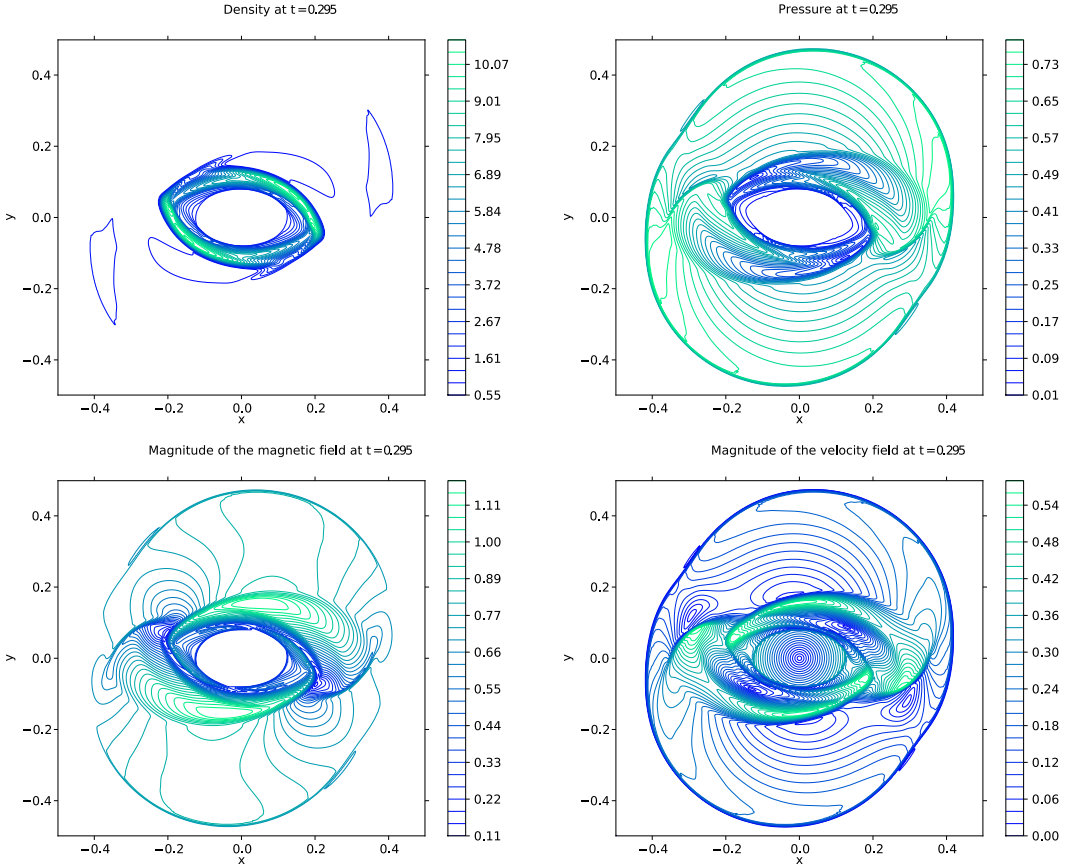
FIGURE 3.11. The density ($\rho : 0.55 - 10.77$), pressure ($p : 0.01 - 0.78$), magnitude of $\boldsymbol{B}$ ($|\boldsymbol{B}|$: $0.11 - 1.18$) and magnitude of the velocity vector ($|\boldsymbol{u}| : 0.00 - 0.58$) computed using the proposed CT scheme with 400×400 cells; 30 contour lines are displayed with a constant step.

The results obtained using a 400×400 grid have been successfully reproduced (see Figure 3.11) with the constrained transport method of Section 3.3.3 and are comparable to those obtained in [130, Fig. 19] (we mention that the comparison is not difficult as we have displayed the same number of contours for the final time $t = 0.249$ as in Tóth's paper). In addition, we also ran this problem on grids of 1000×1000 and 4000×4000 cells and found no outstanding difference between the two; we show the results for the latter in Figure 3.11 and note that the pressure remained positive throughout the computation without the need of employing the fix mentioned in Section 3.4.3.
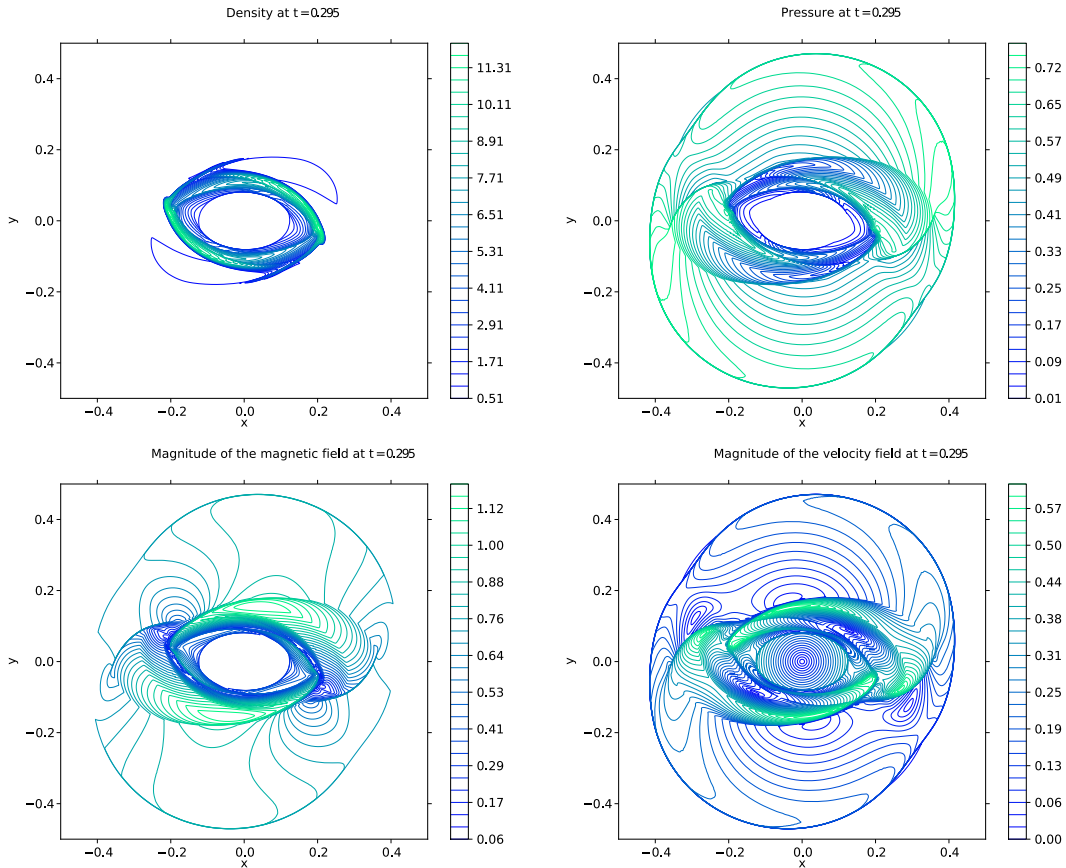
FIGURE 3.12. Contour plots of the density ($\rho : 0.51 - 12.11$), pressure ($p : 0.01 - 0.78$), magnitude of the magnetic field ($|\boldsymbol{B}| : 0.06 - 1.19$) and magnitude of the velocity vector ($|\boldsymbol{u}| : 0.00 - 0.61$) computed using the proposed CT scheme with 4000^2 cells; 30 contour lines are displayed with a constant step.

3.4.5 Kelvin-Helmholtz Instability

As a final test, we study the nonlinear evolution of the two-dimensional MHD Kelvin-Helmholtz instability [106] resulting from velocity shear. The setup for this problem is summarized in Table 3.4, where y_0 is the steepness of the shear, M the Mach number, c_a

the Alfvén speed, and $u_y^p(x,y)$ the single-mode perturbation introduced into the system at the initial time. Our interest in this test lies in demonstrating the scheme's ability to evolve the perturbation into nonlinear turbulence, while maintaining a divergence-free magnetic field.

<div align="center">

Kelvin-Helmholtz Instability

$\rho_0(x,y)$	$u_{x0}(x,y)$	$u_{y0}(x,y)$	$u_{z0}(x,y)$	$B_{x0}(x,y)$	$B_{y0}(x,y)$	$B_{z0}(x,y)$	$p_0(x,y)$
1	$\frac{M}{2}\tanh\left(\frac{y}{y_0}\right)$	0	0	$c_a\cos(\theta)\sqrt{\rho}$	0	$c_a\sin(\theta)\sqrt{\rho}$	$\frac{1}{\gamma}$
	$y_0 = 1/20,$	$M = 1,$	$\theta = \pi/3,$	$c_a = 0.1$			

Computational domain: $[0,1] \times [-1,1]$; Reflecting boundaries (top & bottom), periodic (left & right)

Single mode perturbation: $u_y^p(x,y) = 0.01\sin(2\pi x)\exp(-y^2/\sigma^2)$, with $\sigma = 0.1$

</div>

TABLE 3.4. Initial data for the Kelvin-Helmholtz instability described in [106].

The left plot in Figure 3.13 shows the L^1 norm of the divergence $\nabla \cdot \boldsymbol{B}$ at different times for the methods that use a cell-centered collocation. For the case without correction, a blow-up of divergence errors occurs, causing the simulation to crash. This problem is then addressed by adding a divergence cleaning technique. Additionally, on the right plot, we present the time evolution of the L^1 norm of the total energy density ρe, a conserved quantity in the MHD equations. However, for the constrained transport method, there is a slight loss of the conservation at the level of discretization error.
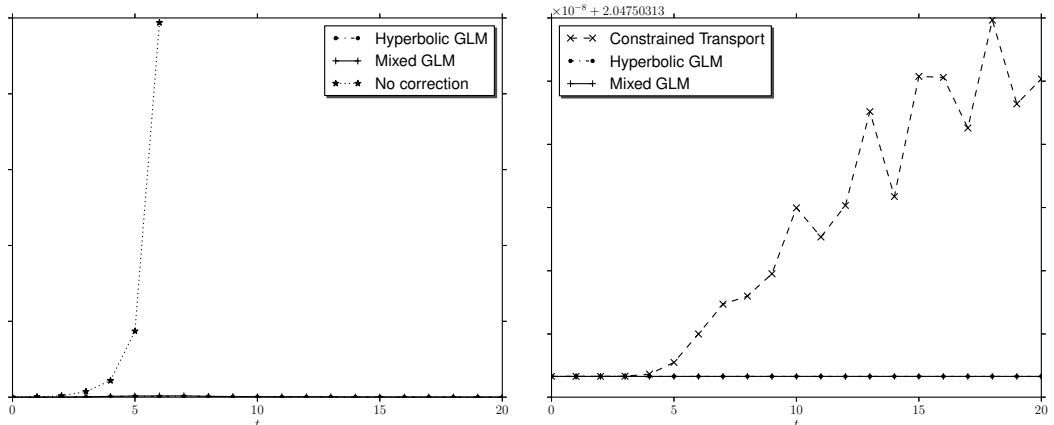
FIGURE 3.13. $L^1(\nabla \cdot \boldsymbol{B})$ (left) and $L^1(\rho e)$ (right) obtained with the HLLD scheme for the Kelvin-Helmholtz instability. The computations are performed using 256×256 points.

Now, the simulation is run using the constrained transport approach of Section 3.3.3 and the MC limiter [136] until the final time $t = 20.0$ and on computational grids consisting of 64×128, 128×256 and 256×512 cells, spanning the domain $[0,1] \times [-1,1]$. Several evolution plots for the ratio of the poloidal field strength and the toroidal component, i.e., $(B_x^2 + B_y^2)^{1/2}/B_z$, are shown in Figure 3.15. There, we are able to observe that the instability has been realistically captured (see [57, 105]), especially on the finest grid: the typical vortex associated with this instability develops and the magnetic field,

frozen into the fluid, grows; then, as noted in [106], the field amplification is prevented by tearing mode instabilities ($t \gtrsim 8.0$) and strong fluid motions are generated by transient reconnection events, followed by a saturation stage. Thus, the three phases in the instability's evolution [105] can be seen clearly in our results.

3.5 Conclusions

In this chapter, we have investigated and compared two different methods that aim to maintain the divergence-free property of the magnetic field, a constraint that cannot be ignored without having consequences.

The method proposed by Dedner et al. [45] prescribes a hyperbolic equation that allows for the divergence errors to be propagated to the boundary of the domain. The same authors recommend using a small variation of this approach, the mixed GLM ansatz, which offers both propagation and damping of the errors. The advantage of the divergence cleaning technique is that it is easy to implement as it is based on the cell-centered formulation favored in the Godunov approach. However, one of its disadvantages is that it depends on tunable parameters.

On the other hand, the constrained transport (CT) approach, originally introduced by Evans and Hawley [52], relies on a staggered formulation of the magnetic and electric fields. One clear advantage of this method is its inherently divergence-free magnetic field. Moreover, it does not have tunable parameters, as in the hyperbolic divergence cleaning technique. However, this method is harder to implement and it sometimes presents loss of the conservation of the total energy density.

Through the different numerical test cases, we have shown that the implementation of the hyperbolic divergence cleaning approach in the HERACLES code was successful, as well as that of the proposed constrained transport approach that uses the 2D HLL Riemann solver to estimate the electric field. We were able to reproduce quantitatively results obtained by other authors and found that both methods are robust and efficient. Although we find that the hyperbolic divergence cleaning generates more diffusive results than the constrained transport, the simplicity of the method makes it an attractive technique for our future work in the design of a high order finite volume approximation for hyperbolic conservation laws in curvilinear unstructured grids.

(a) $t = 5$

(b) $t = 8$

(c) $t = 12$

(d) $t = 20$
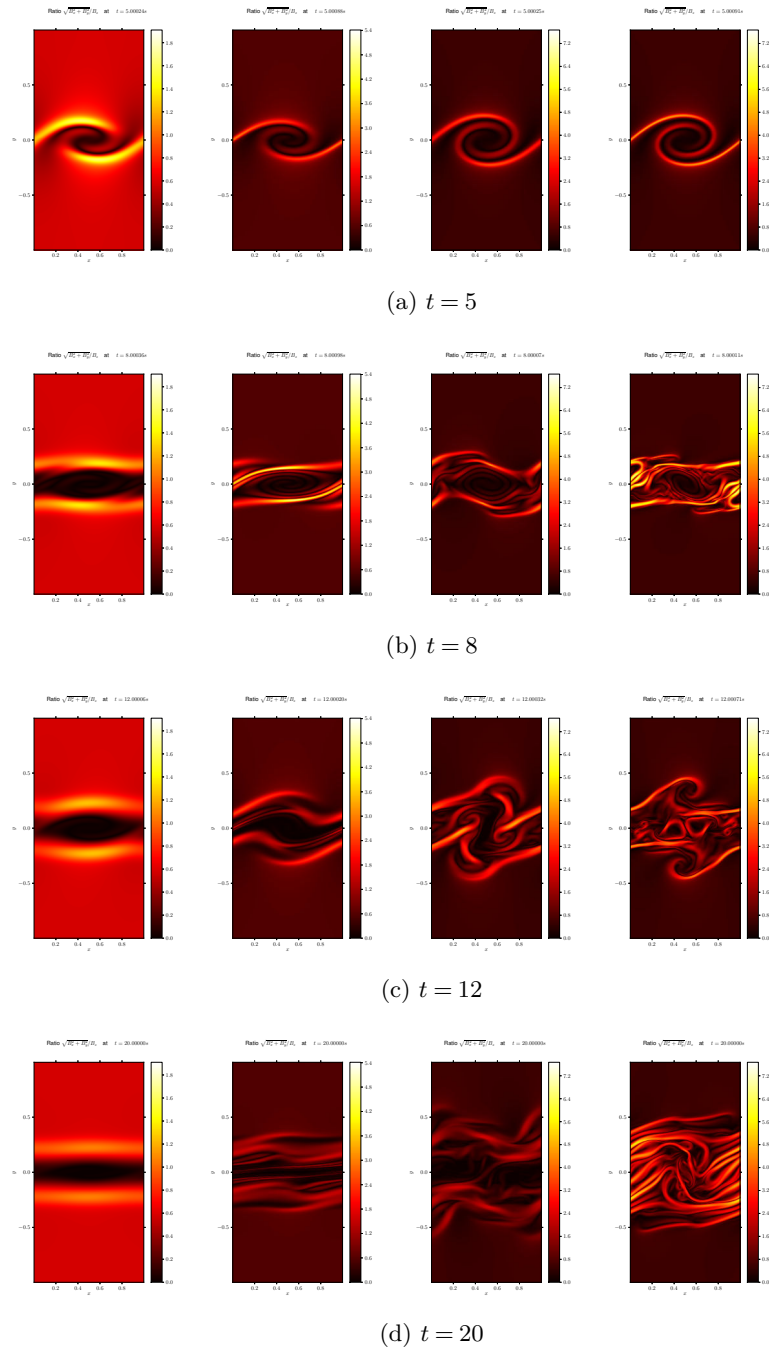
FIGURE 3.14. Evolution of the Kelvin-Helmholtz instability obtained with the HLLD scheme for the mixed GLM, constrained-transport, second order mixed GLM, and second order constrained-transport (from left to right). The results for the hyperbolic GLM (not shown) are almost identical to those obtained with the mixed GLM technique. The plots show the ratio of the poloidal field strength and the toroidal component, i.e., $(B_x^2 + B_y^2)^{1/2}/B_z$. The computations are done on a mesh of 256×512 points and show that results obtained with the hyperbolic divergence technique are the most diffusive.

(a) 64×128 cells (b) 128×256 cells (c) 256×512 cells
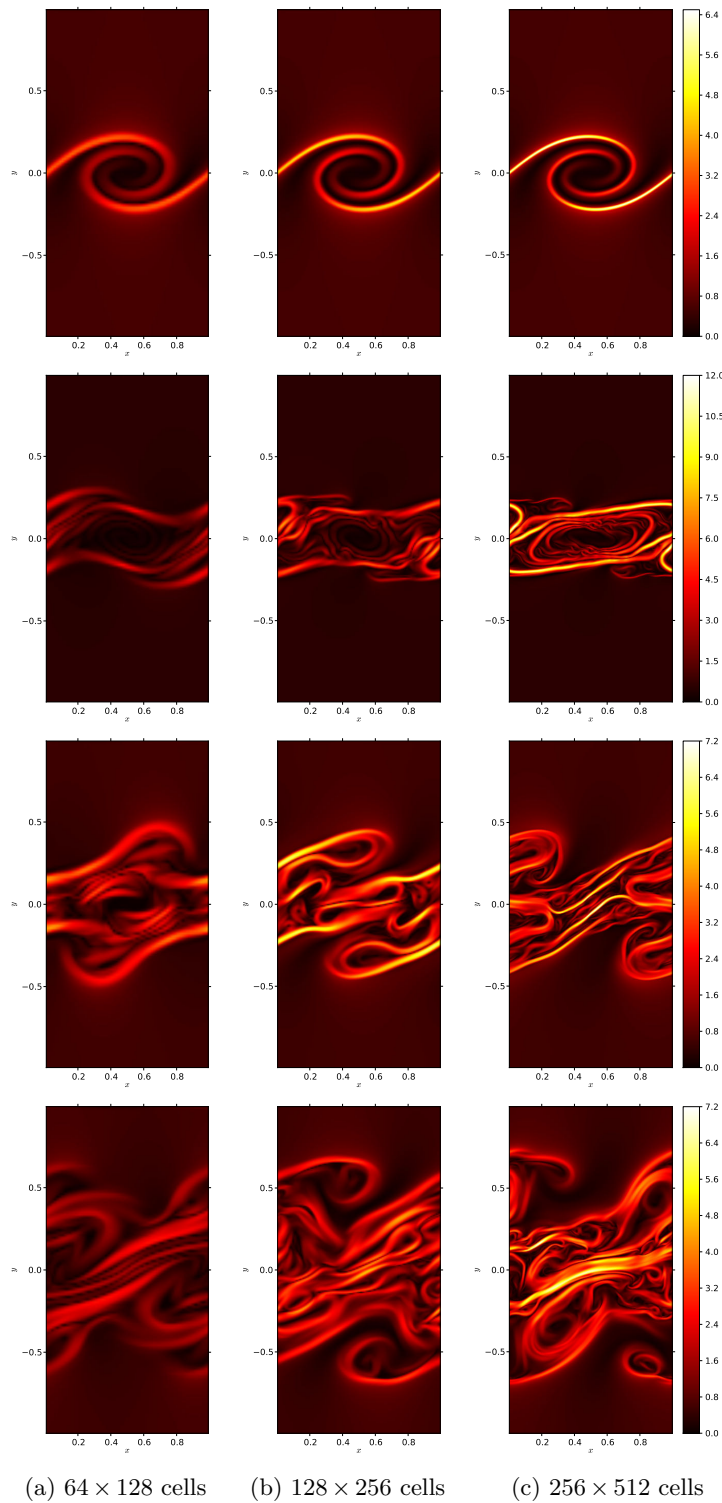
FIGURE 3.15. Evolution of the Kelvin-Helmholtz instability in a 2D computational domain with the constrained transport approach described in Section 3.3. The plots show the ratio $(B_x^2 + B_y^2)^{1/2}/B_z$ at times $t = 5.0, 8.0, 12.0, 20.0$ (top to bottom) on 8 processors.

<div align="right">

CHAPTER 4

</div>

A Relaxation Scheme for Inviscid Flows Under Gravitational Influence

Introduction

Gravitational flows are widely found in the field of astrophysics and their study is a matter of great interest to the scientific community. In stellar physics, numerous of these flows reach steady or quasi-steady states characterized by a balance between gravitational forces and distinct forces, such as pressure gradients. In some other areas, e.g., physical cosmology, the former forces are largely dominant over the latter ones. Therefore, in view of numerical simulations, the proper treatment of gravitational effects related to a vast range of problems presents a challenge.

We are particularly interested in astrophysical flows modeled by the Euler equations (1.20) with gravity source terms derived from a potential Φ, the evolution of which is described by a Poisson equation. Thus, the associated solutions are governed by the Euler-Poisson model, given by the following system of nonlinear partial differential equations:

$$
\begin{cases}
\partial_t(\rho) + \nabla \cdot (\rho \boldsymbol{u}) = 0, \\
\partial_t(\rho \boldsymbol{u}) + \nabla \cdot (\rho \boldsymbol{u} \otimes \boldsymbol{u}) + \nabla p = -\rho \nabla \Phi, \\
\partial_t(\rho e) + \nabla \cdot ((\rho e + p)\boldsymbol{u}) = -\rho \boldsymbol{u} \cdot \nabla \Phi, \\
\Delta \Phi = 4\pi G \rho,
\end{cases}
\tag{4.1}
$$

where ρ, $\boldsymbol{u}$ and e are the density, d-dimensional velocity and specific total energy already introduced in Section 1.2.1. The universal gravitational constant G is approximately equal to $6.67 \times 10^{-11} m^3 kg^{-1} s^{-2}$ and the gravitational potential Φ is always a smooth function since it is the solution of the Laplace equation. The thermodynamic pressure p is governed by a suitable equation of state of the form (1.21), and as usual (see [64, 146]), it is assumed to satisfy

$$
c^2 = \partial_\rho p(\rho, \epsilon) + \frac{p(\rho, \epsilon)}{\rho^2} \partial_\epsilon p(\rho, \epsilon) > 0,
\tag{4.2}
$$

with c denoting the speed of sound.

Due to its importance, several numerical strategies can be adopted to solve system (4.1) and for simplicity of notation, we first write it in compact form as

$$\begin{cases} \partial_t \boldsymbol{w} + \nabla \cdot \boldsymbol{\mathcal{F}}(\boldsymbol{w}) + \boldsymbol{\mathcal{B}}(\boldsymbol{w})\nabla\Phi = 0, \\ \Delta\Phi = 4\pi G\rho, \end{cases} \tag{4.3}$$

with

$$\boldsymbol{w} = \begin{pmatrix} \rho \\ \rho\boldsymbol{u} \\ \rho e \end{pmatrix}, \quad \boldsymbol{\mathcal{F}}(\boldsymbol{w}) = \begin{pmatrix} \rho\boldsymbol{u} \\ \rho\boldsymbol{u}\otimes\boldsymbol{u} + p\,\mathbf{I} \\ (\rho e + p)\boldsymbol{u} \end{pmatrix}, \quad \boldsymbol{\mathcal{B}}(\boldsymbol{w}) = \rho\begin{pmatrix} \mathbf{0}^T \\ \mathbf{I} \\ \boldsymbol{u}^T \end{pmatrix}, \tag{4.4}$$

where $\mathbf{0} = (0,\ldots,0)^T$ is the null vector in $\mathbb{R}^d$. Here, $\boldsymbol{\mathcal{B}}: \mathcal{V} \to \mathbb{R}^\vartheta \times \mathbb{R}^d$ represents the gravitational contribution when multiplied by the gradient of the gravitational potential $(\nabla\Phi)$, with $\vartheta = 2+d$. Moreover, we define the convex set of admissible state vectors by

$$\mathcal{V} = \left\{ \boldsymbol{w} \in \mathbb{R}^\vartheta; \quad \rho > 0,\ \boldsymbol{u} \in \mathbb{R}^d,\ \epsilon = e - \frac{|\boldsymbol{u}|^2}{2} > 0 \right\}. \tag{4.5}$$

System (4.3) is completed with appropriate initial and boundary conditions. In the field of astrophysics, it is common to find isolated boundary conditions for the potential Φ, i.e., the potential gets approximated by a multipolar development of the mass distribution at the boundary (see [79]). For the initial data, we define both $\boldsymbol{w}(\boldsymbol{x},0) = \boldsymbol{w}_0(\boldsymbol{x})$ and $\Phi(\boldsymbol{x},0) = \Phi_0(\boldsymbol{x})$, chosen according to the specific physical settings of the problem being considered.

The Euler-Poisson system of equations is certainly a commonly used plasma physics model and an abundant literature is devoted to its application in this context (see, for instance, [39, 40, 46, 47, 48, 55, 96, 110]). In fact, the model is used to describe ions and electrons flows which are usually highly dynamic. A particular issue resides in the quasi-neutral limit where the Poisson equation becomes singular and the derivation of efficient numerical schemes becomes a complex task: the space and time scales of the solution tend toward zero, leading to severe consistency and stability criteria. In order to overcome this difficulty, Degond et al. [39, 40, 47, 48] (see also [46]) proposed a reformulation of the Poisson equation which is not singular in this limit. The resulting numerical scheme resolves successfully all the plasma regimes (particularly attractive when different ones are present in a single domain). However, simulations of plasma flows are not the purpose of the work presented in this chapter and we will restrict our attention to gravitational flows of astrophysical fluid dynamics, where the Poisson equation never bears singularities. The main challenge then consists in discretizing the gravitational effects governed by $\boldsymbol{\mathcal{B}}(\boldsymbol{w})\nabla\Phi$. We note that in the limit of a steady flow, the first equation of system (4.3) gives

$$\nabla \cdot \boldsymbol{\mathcal{F}}(\boldsymbol{w}) = -\boldsymbol{\mathcal{B}}(\boldsymbol{w})\nabla\Phi, \tag{4.6}$$

and a major difficulty lies in the design of a numerical scheme that preserves this asymptotic regime accurately.

Hence, using an operator splitting approach (Yanenko splitting, first-order, or Strang splitting, second-order accurate) and in the context of the first-order decomposition, we choose to solve equation (4.3) in two steps. First, being $\boldsymbol{w} \in \mathcal{V}$ an unknown state vector and Φ an *a priori* given gravitational potential, the following nonlinear hyperbolic system is considered:

$$\partial_t \boldsymbol{w} + \nabla \cdot \boldsymbol{\mathcal{F}}(\boldsymbol{w}) + \boldsymbol{\mathcal{B}}(\boldsymbol{w}) \nabla \Phi = 0, \tag{4.7}$$

which is clearly in nonconservative form and the method used to solve it will be our primary focus. Once the solution has been found, the second step consists in using the element ρ of the obtained $\boldsymbol{w}$ to solve the elliptic Poisson equation

$$\Delta \Phi = 4\pi G \rho, \tag{4.8}$$

by means of a classical second-order finite difference approach. Therefore, the operator splitting approach allows to decompose (4.3) into two subproblems and treat equations (4.7) and (4.8) individually, which are hyperbolic and elliptic, respectively.

Now, several numerical strategies can be adopted in view of solving (4.7). The first idea [89] is to decompose the solution into a hydrostatic steady part governed by system (4.6) and an acoustic dynamic part described by the Euler equations without source terms (1.20). Although classical Godunov-type based numerical schemes can be used to approximate the latter, the overall technique tends to become much too complex in three dimensions or when a complete implicit formulation is required because of system (4.6) resolution. The second idea consists in constructing a Godunov-type solver that takes into account the gravitational effects. A full conservative reformulation of (4.7) proposed in another context [7] (see also Chièze [33]) could be used, e.g., by introducing the specific energy $e_\Phi = e + \Phi$ to rewrite the last equation of (4.7) in conservative form. However, the nonlinearities involved in this formulation's differential operators make the approach of little interest from a scientific computing perspective.

Another approach comes from the work of Greenberg et al. [69, 68] where the potential form of the source term is used with some benefits to derive well-balanced schemes. Such a numerical procedure has been widely improved in the literature (see, for instance, [23, 59, 60, 82, 111] for the shallow-water equations, [19] in the framework of radiative transfer or [5] for extensions of the Kerr-Debye model), and constitutes a relevant alternative to discretize (4.7). However, the nonlinear Riemann problem involved by this approach is too sophisticated in the present framework to be directly considered. Hence, the extension of this technique to the present context is obtained by involving a relaxation scheme. This relaxation technique is adopted to introduce relevant linearizations and thus derive a Suliciu-type relaxation solver for the Euler-Poisson system. From now on, we note that the obtained scheme is not well-balanced in the sense of [69, 68], but the steady states will be approximated with a better accuracy than with standard fractional step splitting approaches. We mention that a large part of this work was done in collaboration with B. Braconnier and C. Berthon [140].

This chapter is organized as follows. In Section 4.1, we detail the derivation of the one-dimensional relaxation model used to approximate the solutions of the system under consideration. One of the benefits of the proposed model, in which the pressure

is a supplementary variable and the Poisson equation is transformed into a hyperbolic equation with a penalty parameter, is that it ensures a strong coupling between the Euler equations and the gravitational potential. The details of the Riemann solution associated with the homogeneous relaxation model are presented in Section 4.2, and its subsequent section is then devoted to the derivation of the relaxation scheme. The resulting Riemann solver provides better robustness compared to other approaches available in the same software and is capable of preserving gravitational equilibria when required. Several numerical tests are presented and discussed in Section 4.4. Finally, concluding remarks are given in the last section.

4.1 Derivation of the One-Dimensional Relaxation Model

In this section, we consider the numerical approximation of the hyperbolic-elliptic coupled system (4.3). Following a strategy similar to that employed in [108, 109] to obtain the constrained formulation of Maxwell's equations and in [45] to couple the divergence-free constraint on the magnetic field with the ideal magnetohydrodynamic equations (refer to Section 3.2), we introduce a new parameter $c_h \geq 0$ and transform the elliptic equation $\nabla \cdot (\nabla \Phi) = 4\pi G \rho$ to an approximate hyperbolic system with an augmented variable $\boldsymbol{\kappa} = \nabla \Phi$. Thus, we get

$$\begin{cases} \partial_t(\rho) & + \nabla \cdot (\rho \boldsymbol{u}) & = 0, \\ \partial_t(\rho \boldsymbol{u}) & + \nabla \cdot (\rho \boldsymbol{u} \otimes \boldsymbol{u}) + \nabla p + \rho \nabla \Phi & = 0, \\ \partial_t(\rho e) & + \nabla \cdot ((\rho e + p) \boldsymbol{u}) + \rho \boldsymbol{u} \cdot \nabla \Phi & = 0, \\ \frac{1}{c_h} \partial_t(\Phi) + \nabla \cdot \boldsymbol{\kappa} & = -c_h \int_0^t 4\pi G \rho \, d\tau, \\ \frac{1}{c_h} \partial_t(\boldsymbol{\kappa}) + \nabla \Phi & = 0. \end{cases} \tag{4.9}$$

This reformulated system is globally hyperbolic with a source term under integral form. For sufficiently smooth solutions, combining the last two equations yields the nonhomogenous wave equation

$$\frac{1}{c_h^2} \partial_{tt} \Phi - \nabla \cdot (\nabla \Phi) = 4\pi G \rho. \tag{4.10}$$

Note that when the parameter c_h tends towards zero, we formally recover both that $\partial_{tt} \Phi = \mathcal{O}(c_h^2)$ and $\nabla \cdot \nabla \Phi = 4\pi G \rho + \mathcal{O}(c_h^2)$. For the moment, we only assume that $c_h \ll 1$.

We focus now on the numerical approximation of system (4.9). For the sake of mathematical simplicity, we begin our analysis by studying the one-dimensional subsystem

$$\begin{cases} \partial_t(\rho) & + \partial_x(\rho u) & = 0, \\ \partial_t(\rho u) & + \partial_x(\rho u^2 + p) + \rho \partial_x \Phi & = 0, \\ \partial_t(\rho e) & + \partial_x((\rho e + p)u) + \rho u \partial_x \Phi & = 0, \end{cases} \tag{4.11}$$

i.e., system (4.7) in one dimension. By making use of the definitions given in (4.4) and denoting the first element of $\boldsymbol{\mathcal{B}}$ by $\boldsymbol{b}$, we are able to write (4.11) under the form

$$\partial_t \boldsymbol{w} + \partial_x \boldsymbol{f}(\boldsymbol{w}) + \boldsymbol{b}(\boldsymbol{w}) \partial_x \Phi = 0, \tag{4.12}$$

where the 1D state vector $\boldsymbol{w} = (\rho, \rho u, \rho e)^T$ belongs to the phase space defined by (4.5) ($\vartheta = 3$ since $d = 1$).

As mentioned in the introduction of this chapter, particular attention must be given to the proper discretization of the gravity terms. Thus, we propose to derive a relaxation scheme, a classical numerical approach widely spread across the literature considering fluid flow simulations [4, 16, 17, 18, 32, 92]. Motivated by the work of Jin-Xin [83] and Bouchut [23], (see [14, 36, 29] as well), we choose to approximate the weak solutions of (4.12) by the weak solutions of a relaxation system, designed to render the Riemann problem easily solvable. According to Coquel and Perthame [36] (see also [14, 20], for instance), most of the nonlinearities of the initial system, called *relaxation equilibrium system*, must be preserved by the relaxation system to enforce accuracy of the resulting numerical scheme.

After the influential work of Suliciu [125, 126] (see [4, 16, 17, 18, 32, 28, 92] for several interesting extensions), the pressure p is relaxed with an approximation π governed by an adequate evolution equation supplemented by a relaxation source term. Such an evolution law can be deduced from the commonly known pressure equation (e.g., refer to [64]) given by

$$\partial_t p + u \partial_x p + \rho c^2 \partial_x u = 0, \tag{4.13}$$

with the sound speed c satisfying (4.2). Let us underline that the above relation does not depend on the gravitational potential Φ. From (4.13), we suggest the evolution equation

$$\partial_t \pi + u \partial_x \pi + \frac{a^2}{\rho} \partial_x u = \frac{1}{\delta}(p - \pi), \tag{4.14}$$

to govern the additional variable π. As the parameter δ tends to zero, a relaxation equilibrium limit characterized by $\pi = p$ is reached. Concerning the relaxation parameter a, we will eventually consider a sub-characteristic Whitham condition [147] to fix its value. It is evident that the choice of a plays an important role in the stability and robustness of the scheme, as will be seen in Section 4.4.

Now, we propose to introduce a relaxation procedure to approximate the potential Φ. We start by writing the last two equations of the integro-differential system (4.9) in their one-dimensional form

$$\begin{cases} \partial_t \Phi + c_h \partial_x \kappa = -c_h^2 \int_0^t 4\pi G \rho \, d\tau, \\ \partial_t \kappa + c_h \partial_x \Phi = 0, \end{cases} \tag{4.15}$$

and their combination as $1/c_h^2 \, \partial_{tt}\Phi - \partial_{xx}\Phi = 4\pi G \rho$ (see equation (4.10)). The relaxation system, which ensures adequate coupling of the Poisson and Euler equations, is then

$$\begin{cases} \partial_t (\rho) + \partial_x (\rho u) = 0, \\ \partial_t (\rho u) + \partial_x (\rho u^2 + \pi) + \rho \partial_x \Phi = 0, \\ \partial_t (\rho e) + \partial_x ((\rho e + \pi)u) + \rho u \partial_x \Phi = 0, \\ \partial_t (\pi) + u \partial_x \pi + \frac{a^2}{\rho} \partial_x u = \frac{1}{\delta}(p - \pi), \\ \partial_t (\Phi) + c_h \partial_x \kappa = -c_h^2 \int_0^t 4\pi G \rho \, d\tau, \\ \partial_t (\kappa) + c_h \partial_x \Phi = 0. \end{cases} \tag{4.16}$$

Note that if we study the last two equations of (4.16) or system (4.15) in the limit $c_h = 0$, we obtain $\partial_t \Phi = 0$ and $\partial_{xx}\Phi = 4\pi G\rho$, consistent with the first-order decomposition described at the beginning of this chapter. Therefore, in this asymptotic case, we suggest to relax the gravitational potential Φ by replacing it with a new variable ψ governed by

$$\partial_t \psi = \frac{1}{\delta}(\Phi - \psi), \tag{4.17}$$

so that in the general case, the complete relaxation system becomes

$$\begin{cases} \partial_t(\rho) + \partial_x(\rho u) &= 0, \\ \partial_t(\rho u) + \partial_x(\rho u^2 + \pi) + \rho\partial_x\psi &= 0, \\ \partial_t(\rho e) + \partial_x((\rho e + \pi)u) + \rho u\partial_x\psi = 0, \\ \partial_t(\rho\pi) + \partial_x((\rho\pi + a^2)u) &= \frac{\rho}{\delta}(p - \pi), \\ \partial_t(\psi) + \partial_x(c_h\kappa) &= \frac{1}{\delta}(\Phi - \psi) - c_h^2\int_0^t 4\pi G\rho\,d\tau, \\ \partial_t(\kappa) + \partial_x(c_h\Phi) &= 0, \end{cases} \tag{4.18}$$

where the fourth equation is easily obtained from (4.14), i.e., multiply it by ρ and make use of the density equation. Setting the general relaxed state to $\hat{\boldsymbol{w}} = (\rho, \rho u, \rho e, \rho\pi, \Phi, \kappa)^T$, we can put (4.18) in the form

$$\partial_t\hat{\boldsymbol{w}} + \partial_x\hat{\boldsymbol{f}}(\hat{\boldsymbol{w}}) + \hat{\boldsymbol{b}}(\hat{\boldsymbol{w}})\partial_x\Phi = \frac{1}{\delta}\hat{\boldsymbol{s}}_0(\hat{\boldsymbol{w}}) + c_h\hat{\boldsymbol{s}}_1(\hat{\boldsymbol{w}}). \tag{4.19}$$

In the asymptotic situation $c_h = 0$, the previous system of equations reduces to a smaller one that corresponds exclusively to subsystem (4.11), where Φ is now an *a priori* given function, solution to the Poisson equation $\partial_{xx}\Phi = 4\pi G\rho$. We have

$$\begin{cases} \partial_t(\rho) + \partial_x(\rho u) &= 0, \\ \partial_t(\rho u) + \partial_x(\rho u^2 + \pi) + \rho\partial_x\psi &= 0, \\ \partial_t(\rho e) + \partial_x((\rho e + \pi)u) + \rho u\partial_x\psi = 0, \\ \partial_t(\rho\pi) + \partial_x((\rho\pi + a^2)u) &= \frac{\rho}{\delta}(p - \pi), \\ \partial_t(\psi) &= \frac{1}{\delta}(\Phi - \psi). \end{cases} \tag{4.20}$$

Let us stress out that as δ tends to zero, $\pi = p$ and $\Phi = \psi$, and the evolution equations for $(\rho, \rho u, \rho e)^T$ are thus equivalently to those found in (4.11). Moreover, by defining $\boldsymbol{w}_\delta = (\rho, \rho u, \rho e, \rho\pi, \psi)^T \in \mathcal{V}_\delta$, with $\mathcal{V}_\delta$ the set of admissible relaxation state vectors, namely

$$\mathcal{V}_\delta = \left\{\boldsymbol{w}_\delta \in \mathbb{R}^5; \quad \rho > 0,\ u \in \mathbb{R},\ \epsilon = e - u^2/2 > 0,\ \pi \in \mathbb{R},\ \psi \in \mathbb{R}\right\},$$

we propose a compact form representation of (4.20) written in terms of the relaxed variables as follows:

$$\partial_t\boldsymbol{w}_\delta + \partial_x\boldsymbol{f}_\delta(\boldsymbol{w}_\delta) + \boldsymbol{b}_\delta(\boldsymbol{w}_\delta)\partial_x\psi = \frac{1}{\delta}\boldsymbol{s}_\delta(\boldsymbol{w}_\delta), \tag{4.21}$$

with

$$\boldsymbol{f}_\delta(\boldsymbol{w}_\delta) = \begin{pmatrix} \rho u \\ \rho u^2 + \pi \\ (\rho e + \pi)u \\ (\rho\pi + a^2)u \\ 0 \end{pmatrix}, \quad \boldsymbol{b}_\delta(\boldsymbol{w}_\delta) = \begin{pmatrix} 0 \\ \rho \\ \rho u \\ 0 \\ 0 \end{pmatrix}, \quad \boldsymbol{s}_\delta(\boldsymbol{w}_\delta) = \begin{pmatrix} 0 \\ 0 \\ 0 \\ \rho(p - \pi) \\ \Phi - \psi \end{pmatrix}. \tag{4.22}$$

In the coming section, we will present the solution of the Riemann problem for the relaxation model (4.21) with a vanishing relaxation source term. Relevant choices of the parameter a are then specified to enforce a suitable positive preserving property.

4.2   Solution $\boldsymbol{\mathcal{W}}_\delta$ of the Riemann Problem

We consider the algebra of system (4.20) and propose to perform a simple change of variables. If we introduce the state vector $\boldsymbol{v}_\delta$ defined as

$$\boldsymbol{v}_\delta = (\rho, u, \epsilon, \pi, \psi)^T, \tag{4.23}$$

and omit the source term, system $(4.20)_{\delta=\infty}$ can be reformulated to

$$\partial_t \boldsymbol{v}_\delta + \boldsymbol{A}_\delta(\boldsymbol{v}_\delta) \partial_x \boldsymbol{v}_\delta = 0, \tag{4.24}$$

with

$$\boldsymbol{A}_\delta(\boldsymbol{v}_\delta) = \begin{pmatrix} u & \rho & 0 & 0 & 0 \\ 0 & u & 0 & \frac{1}{\rho} & 1 \\ 0 & \frac{\pi}{\rho} & u & 0 & 0 \\ 0 & \frac{a^2}{\rho} & 0 & u & 0 \\ 0 & 0 & 0 & 0 & 0 \end{pmatrix}. \tag{4.25}$$

A direct computation gives $\lambda_0 = 0$, $\lambda_u^1 = \lambda_u^2 = u$ and $\lambda_\pm = u \pm a/\rho$ as eigenvalues of the above matrix $\boldsymbol{A}_\delta(\boldsymbol{v}_\delta)$. One alternative way to specify these values relies on a simple analysis of the full relaxation system $(4.19)_{\delta=\infty}$ after a specific change of variables has taken place:

$$\partial_t \hat{\boldsymbol{v}} + \hat{\boldsymbol{A}}(\hat{\boldsymbol{v}}) \partial_x \hat{\boldsymbol{v}} = c_h \hat{\boldsymbol{s}}_1(\hat{\boldsymbol{v}}), \tag{4.26}$$

where $\hat{\boldsymbol{v}} = (\rho, u, \epsilon, \pi, \psi, \kappa)^T$ and

$$\hat{\boldsymbol{A}}(\hat{\boldsymbol{v}}) = \begin{pmatrix} u & \rho & 0 & 0 & 0 & 0 \\ 0 & u & 0 & \frac{1}{\rho} & 1 & 0 \\ 0 & \frac{\pi}{\rho} & u & 0 & 0 & 0 \\ 0 & \frac{a^2}{\rho} & 0 & u & 0 & 0 \\ 0 & 0 & 0 & 0 & 0 & c_h \\ 0 & 0 & 0 & 0 & c_h & 0 \end{pmatrix}, \tag{4.27}$$

which is clearly diagonalizable and with real eigenvalues $\pm c_h$, u, $u \pm a/\rho$. Hitherto, we have only assumed $c_h \ll 1$; now, we also suppose that $c_h \leq |u|$ (see Figure 4.1). Then, it is evident that in the limit $c_h = 0$, equation (4.26) reduces to (4.24), as was already explained in the previous section, and the waves associated with $\pm c_h$ become a single stationary one. In fact, following the pioneering work of Greenberg-LeRoux [69, 68], we have purposely introduced a source term in the associated Riemann solver which naturally comes with a stationary wave (see also [23]).
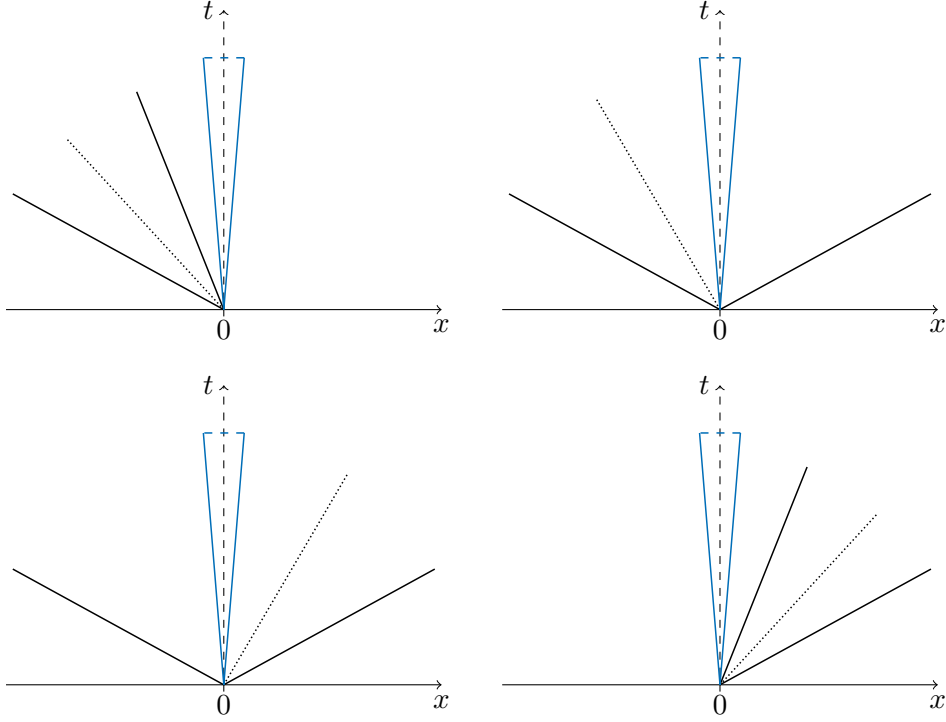
FIGURE 4.1. Solution structure of the Riemann problem for the general system (4.26) without any source terms, i.e., for $\partial_t \hat{\boldsymbol{v}} + \hat{\boldsymbol{A}}(\hat{\boldsymbol{v}}) \partial_x \hat{\boldsymbol{v}} = 0$.

Using common notation, the eigenvectors of $\boldsymbol{A}_\delta(\boldsymbol{v}_\delta)$ are

$$\mathbf{r}_0 = \begin{pmatrix} \rho^2 \\ -u\rho \\ \pi \\ a^2 \\ (u^2\rho^2 - a^2)/\rho \end{pmatrix}, \quad \mathbf{r}_u^1 = \begin{pmatrix} 1 \\ 0 \\ 0 \\ 0 \\ 0 \end{pmatrix}, \quad \mathbf{r}_u^2 = \begin{pmatrix} 0 \\ 0 \\ 1 \\ 0 \\ 0 \end{pmatrix}, \quad \mathbf{r}_\pm = \begin{pmatrix} \rho^2 \\ \pm a \\ \pi \\ a^2 \\ 0 \end{pmatrix} \quad (4.28)$$

with $\mathbf{r}_u^1$ and $\mathbf{r}_u^2$ associated to the double eigenvalue u, henceforth denoted only by the symbol λ_u. From simple calculations, we deduce that all the characteristics fields of (4.24) are linearly degenerate and we complete the algebra of this system by exhibiting the Riemann invariants. Let us recall that the Riemann invariants $\mathcal{I}$ associated with the eigenvector $\mathbf{r}$ are defined as $\nabla \mathcal{I} \cdot \mathbf{r} = 0$, and after straightforward computations, with the setting of $\tilde{\pi} = \pi + a^2/\rho$ and $\tilde{\epsilon} = \epsilon - \pi^2/(2a^2)$, we find them across each wave:

1. For the λ_0-wave, we have

$$\frac{\mathrm{d}\rho}{\rho^2} = \frac{\mathrm{d}u}{-u\rho} = \frac{\mathrm{d}\epsilon}{\pi} = \frac{\mathrm{d}\pi}{a^2} = \frac{\mathrm{d}\psi}{(u^2\rho^2 - a^2)/\rho},$$

which leads to

$$\mathcal{I}_0^1 = \rho u, \quad \mathcal{I}_0^2 = \tilde{\pi}, \quad \mathcal{I}_0^3 = \tilde{\epsilon}, \quad \mathcal{I}_0^4 = \psi + \frac{u^2}{2} - \frac{a^2}{2\rho^2}. \quad (4.29)$$

2. For the λ_u-wave, we have

$$\frac{\mathrm{d}u}{0} = \frac{\mathrm{d}\pi}{0} = \frac{\mathrm{d}\psi}{0},$$

which leads to

$$\mathcal{I}_u^1 = u, \quad \mathcal{I}_u^2 = \pi, \quad \mathcal{I}_u^3 = \psi. \tag{4.30}$$

3. For the $\lambda_\pm$-waves, we have

$$\frac{\mathrm{d}\rho}{\rho^2} = \frac{\mathrm{d}u}{\pm a} = \frac{\mathrm{d}\epsilon}{\pi} = \frac{\mathrm{d}\pi}{a^2} = \frac{\mathrm{d}\psi}{0},$$

which leads to

$$\mathcal{I}_\pm^1 = u \pm \frac{a}{\rho}, \quad \mathcal{I}_\pm^2 = \tilde{\pi}, \quad \mathcal{I}_\pm^3 = \tilde{\epsilon}, \quad \mathcal{I}_\pm^4 = \psi. \tag{4.31}$$

Let us introduce some notation for the sake of simplicity. It is known that the specific volume τ is the reciprocal of the density, namely $\tau = 1/\rho$. Therefore, several of the quantities previously defined can be written in terms of τ instead of ρ. In addition, given two constant values $(\cdot)_l$ and $(\cdot)_r$, we take again into consideration the jump function (2.49) of Chapter 2.

Fix now two admissible states $\boldsymbol{w}_{\delta l}$ and $\boldsymbol{w}_{\delta r}$ in $\mathcal{V}_\delta$ to define the initial data of the Riemann problem for system $(4.20)_{\delta=\infty}$, specifically

$$\boldsymbol{w}_{\delta 0}(x, 0) = \begin{cases} \boldsymbol{w}_{\delta l} & \text{if } x < x_0, \\ \boldsymbol{w}_{\delta r} & \text{if } x > x_0, \end{cases} \tag{4.32}$$

assuming $x_0 = 0$ for convenience. We need to find the solution to (4.24) with Riemann initial data expressed as

$$\boldsymbol{v}_{\delta 0}(x, 0) = \begin{cases} \boldsymbol{v}_l = \boldsymbol{v}_{\delta l} & \text{if } x < 0, \\ \boldsymbol{v}_r = \boldsymbol{v}_{\delta r} & \text{if } x > 0. \end{cases} \tag{4.33}$$

Given that all eigenvalues are linearly degenerate, we can compute the exact solution $\mathcal{W}_\delta$ to the Riemann problem, which has four wave speeds and three intermediate states. To evaluate these intermediate constant states, we make use of the Riemann invariants that are continuous across the contact discontinuity associated with a particular eigenvector. Note that the speeds of the stationary, contact, slowest and fastest waves will henceforth be denoted by s_0, s_m, s_l and s_r, respectively.

The characterization of the solution is conditioned by the knowledge of the wave ordering, which is not straightforward. By construction, the wave speeds are

$$s_0 = 0, \quad s_l = u_l - a\tau_l, \quad s_r = u_r + a\tau_r, \tag{4.34}$$

and since $\tau_l > 0$ and $\tau_r > 0$, we find that the difference $s_r - s_l = u_r - u_l + a(\tau_r + \tau_l)$ is positive as long as a is large enough. From a numerical point of view, the choice of the parameter a is crucial since it governs (in a way to be defined) the numerical diffusion

involved in the scheme. As a consequence, choosing an a too large will produce a very viscous scheme while choosing it too small will lead to an unstable scheme. As usual, the parameter a cannot be smaller than the exact impedance $Z = \rho c$ involved in the initial system (4.11) (see [16, 23, 29]).

Because $s_r > s_l$ for large enough values of a, the wave order problem then comes from the position of s_r, s_l and s_m compared to the stationary wave s_0. Thus, to cover all possibilities, we set the wave speed

$$\sigma = \frac{u_l + u_r}{2} - \frac{[\![\pi]\!]}{2a}, \tag{4.35}$$

which corresponds to the velocity in the intermediate region of the Suliciu relaxation model used to approximate the solution of the Riemann problem for the Euler equations (see Bouchut [23], for instance). Like so, only four distinct cases are possible and they are studied below. In all of them, the intermediate velocity σ can easily be recovered by setting $[\![\psi]\!] = 0$. Recall that we consider only small values of $[\![\psi]\!]$, making this a valid approach to segregate the second and third cases.

4.2.1 Case I: $s_l > 0$

In this case, we suppose that the wave ordering is $s_0 = 0 < s_l < s_m < s_r$. Thus, we search for the exact Riemann solution having the following structure:

$$
\begin{aligned}
\boldsymbol{v}_l &= (\ \tau_l, \ u_l, \ \tilde{\pi}_l, \ \tilde{\epsilon}_l, \ \psi_l \ )^T \\
\boldsymbol{v}_l^* &= (\ \tau_l^*, \ u_l^*, \ \tilde{\pi}_l^*, \ \tilde{\epsilon}_l^*, \ \psi_l^* \ )^T \\
\boldsymbol{v}_l^{**} &= (\ \tau_l^{**}, u_l^{**}, \tilde{\pi}_l^{**}, \tilde{\epsilon}_l^{**}, \psi_l^{**})^T \\
\boldsymbol{v}_r^* &= (\ \tau_r^*, \ u_r^*, \ \tilde{\pi}_r^*, \ \tilde{\epsilon}_r^*, \ \psi_r^* \ )^T \\
\boldsymbol{v}_r &= (\ \tau_r, \ u_r, \ \tilde{\pi}_r, \ \tilde{\epsilon}_r, \ \psi_r \ )^T
\end{aligned}
$$
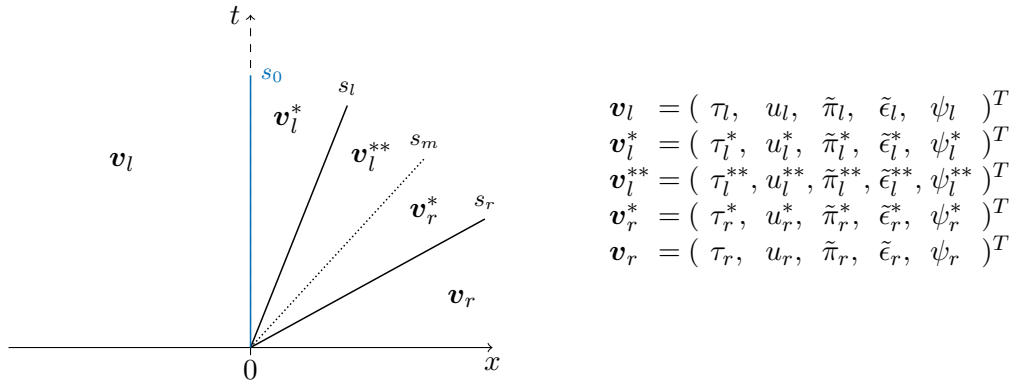
The unknowns that compose this solution are then determined by considering the system given by the continuity of the Riemann invariants (4.29, 4.30, 4.31) across each field. We can easily derive the equalities $\psi_r = \psi_r^* = \psi_l^{**} = \psi_l^*$ and

$$\tilde{\pi}_l = \tilde{\pi}_l^* = \tilde{\pi}_l^{**}, \qquad \tilde{\pi}_r = \tilde{\pi}_r^*, \tag{4.36a}$$

$$\tilde{\epsilon}_l = \tilde{\epsilon}_l^* = \tilde{\epsilon}_l^{**}, \qquad \tilde{\epsilon}_r = \tilde{\epsilon}_r^*. \tag{4.36b}$$

Since the velocity and the term π are constant across the s_m-wave, we have

$$s_m = u_l^{**} = u_r^*, \qquad \pi_l^{**} = \pi_r^*, \tag{4.37}$$

respectively. Additionally, across the s_0-wave, we have two more relations

$$u_l/\tau_l = u_l^*/\tau_l^*, \tag{4.38a}$$

$$\psi_l + \tfrac{1}{2}[(u_l)^2 - (a\,\tau_l)^2] = \psi_l^* + \tfrac{1}{2}[(u_l^*)^2 - (a\,\tau_l^*)^2], \tag{4.38b}$$

and across the waves with speeds s_l and s_r, we get

$$u_l^* - a\,\tau_l^* = u_l^{**} - a\,\tau_l^{**}, \tag{4.38c}$$

$$u_r^* + a\,\tau_r^* = u_r + a\,\tau_r. \tag{4.38d}$$

Equation (4.38a) can be rewritten as

$$u_l^* = u_l\,\tau_l^*/\tau_l. \tag{4.39}$$

We substitute both this relation (4.39) and the equality given by $\psi_l^* = \psi_r$ into equation (4.38b) to produce $(\tau_l^*)^2 = (\tau_l)^2 - 2\,[\![\psi]\!] / ((u_l/\tau_l)^2 - a^2)$. Since the specific volume τ_l^* has to be positive, we derive the expression

$$\tau_l^* = \tau_l\sqrt{1 - \frac{2\,[\![\psi]\!]}{(u_l)^2 - (a\,\tau_l)^2}}. \tag{4.40}$$

Recall that $\tilde{\pi} = \pi + a^2\tau$. We express the right hand sides of (4.36a) in this form and, consequently, obtain $\tilde{\pi}_l = \pi_l^{**} + a^2\tau_l^{**}$ and $\tilde{\pi}_r = \pi_r^* + a^2\tau_r^*$. By performing algebraic manipulations on these two equations and making use of the second equation in (4.37), we are able to define

$$\tau_r^* = \tau_l^{**} + \frac{[\![\tilde{\pi}]\!]}{a^2}. \tag{4.41}$$

Now, substitution of u_l^* from (4.39) into (4.38c) gives

$$u_l^{**} = (u_l/\tau_l - a)\tau_l^* + a\,\tau_l^{**} = s_m, \tag{4.42}$$

and use of the relation $u_r^* = u_r + a\,\tau_r - a\,\tau_r^* = s_m$ derived from (4.38d) leads to

$$\tau_l^{**} = \tfrac{1}{a}\left(u_r + a\,\tau_r - a\,\tau_r^* - (u_l/\tau_l - a)\tau_l^* \right). \tag{4.43}$$

Then, by utilizing (4.41) and (4.43), we obtain the values

$$\tau_l^{**} = \frac{1}{2a}\left(s_r - s_l\sqrt{1 - \frac{2\,[\![\psi]\!]}{(u_l)^2 - (a\,\tau_l)^2}} - \frac{[\![\tilde{\pi}]\!]}{a} \right), \tag{4.44a}$$

$$\tau_r^* = \frac{1}{2a}\left(s_r - s_l\sqrt{1 - \frac{2\,[\![\psi]\!]}{(u_l)^2 - (a\,\tau_l)^2}} + \frac{[\![\tilde{\pi}]\!]}{a} \right). \tag{4.44b}$$

We skip the computation for the other variables since they can be easily deduced from one another. However, from (4.40), we find the necessary condition

$$[\![\psi]\!] < \tfrac{1}{2}\left((u_l)^2 - (a\,\tau_l)^2 \right), \tag{4.45}$$

where $(u_l)^2 - (a\,\tau_l)^2 > 0$ since $s_l > 0$, i.e., $u_l + a\,\tau_l > u_l - a\,\tau_l > 0$. Additionally, in order for τ_l^{**} and τ_r^* to be positive, the following condition must be satisfied:

$$|[\![\tilde{\pi}]\!]| < a\left(s_r - s_l\sqrt{1 - \frac{2\,[\![\psi]\!]}{(u_l)^2 - (a\,\tau_l)^2}} \right). \tag{4.46}$$

If this condition is not met, to avoid the appearance of vacuum, we decide to degenerate the s_l-wave by choosing a larger value of a such that $s_l < 0 < s_r$, $\sigma > 0$ and, therefore, switch to the subsequent case.

4.2.2   Case II: $s_l < 0 < s_r$, $\sigma > 0$

Assume that the exact solution follows the wave ordering given by $s_l < s_0 < s_m < s_r$, which implies looking for the exact Riemann solution of the form:

$$
\begin{aligned}
\boldsymbol{v}_l &= (\ \tau_l, \quad u_l, \quad \tilde{\pi}_l, \quad \tilde{\epsilon}_l, \quad \psi_l \quad)^T \\
\boldsymbol{v}_l^* &= (\ \tau_l^*, \quad u_l^*, \quad \tilde{\pi}_l^*, \quad \tilde{\epsilon}_l^*, \quad \psi_l^* \quad)^T \\
\boldsymbol{v}_l^{**} &= (\ \tau_l^{**}, \ u_l^{**}, \ \tilde{\pi}_l^{**}, \ \tilde{\epsilon}_l^{**}, \ \psi_l^{**} \quad)^T \\
\boldsymbol{v}_r^* &= (\ \tau_r^*, \quad u_r^*, \quad \tilde{\pi}_r^*, \quad \tilde{\epsilon}_r^*, \quad \psi_r^* \quad)^T \\
\boldsymbol{v}_r &= (\ \tau_r, \quad u_r, \quad \tilde{\pi}_r, \quad \tilde{\epsilon}_r, \quad \psi_r \quad)^T
\end{aligned}
$$
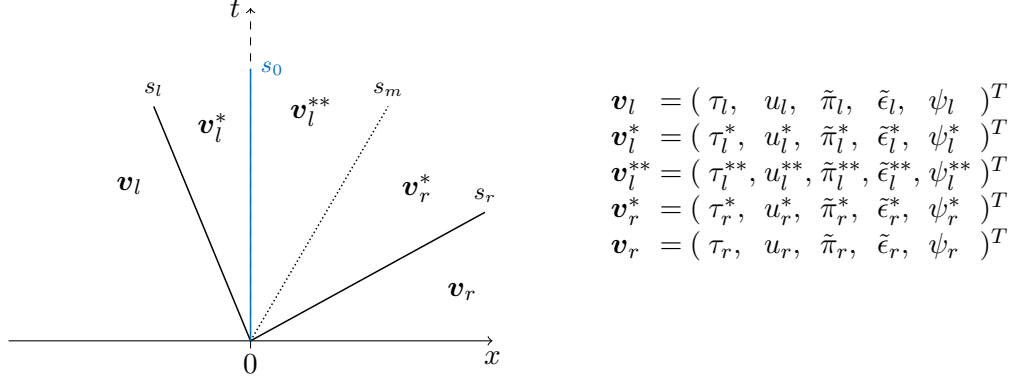
Once again, by employing the continuity of the Riemann invariants (4.29, 4.30, 4.31) across each field, we are able to specify several expressions

$$u_l - a\,\tau_l = u_l^* - a\,\tau_l^*, \tag{4.47a}$$

$$u_l^*/\tau_l^* = u_l^{**}/\tau_l^{**}, \tag{4.47b}$$

$$\psi_l^* + \tfrac{1}{2}[(u_l^*)^2 - (a\,\tau_l^*)^2] = \psi_l^{**} + \tfrac{1}{2}[(u_l^{**})^2 - (a\,\tau_l^{**})^2], \tag{4.47c}$$

$$u_r^* + a\,\tau_r^* = u_r + a\,\tau_r, \tag{4.47d}$$

and obtain, without difficulty, the equalities

$$\psi_r = \psi_r^* = \psi_l^{**}, \qquad \psi_l = \psi_l^*, \tag{4.48a}$$

$$\tilde{\pi}_l = \tilde{\pi}_l^* = \tilde{\pi}_l^{**}, \qquad \tilde{\pi}_r = \tilde{\pi}_r^*, \tag{4.48b}$$

$$\tilde{\epsilon}_l = \tilde{\epsilon}_l^* = \tilde{\epsilon}_l^{**}, \qquad \tilde{\epsilon}_r = \tilde{\epsilon}_r^*. \tag{4.48c}$$

Moreover, since the velocity and the variable π are constant across the s_m-wave, we find

$$s_m = u_l^{**} = u_r^*, \qquad \pi_l^{**} = \pi_r^*. \tag{4.49}$$

Before proceeding, we wish to note that equation (4.47b) can be rewritten to solve for the velocity u_l^* as

$$u_l^* = u_l^{**}\,\tau_l^*/\tau_l^{**}. \tag{4.50}$$

Direct substitution of the previous relation (4.50) and the values of $\psi_l^* = \psi_l$ and $\psi_l^{**} = \psi_r$ into equation (4.47c) yields

$$\left(\frac{\tau_l^*}{\tau_l^{**}}\right)^2 = 1 + \frac{2\,[\![\psi]\!]}{(u_l^{**})^2 - (a\,\tau_l^{**})^2}. \tag{4.51}$$

In addition, from (4.47a) and (4.50), we get the expression

$$\frac{\tau_l^*}{\tau_l^{**}} = \frac{u_l - a\,\tau_l}{u_l^{**} - a\,\tau_l^{**}}. \tag{4.52}$$

By expanding now the right hand sides of (4.48b), having in mind that $\tilde{\pi} = \pi + a^2 \tau$, we recover $\tilde{\pi}_l = \pi_l^{**} + a^2 \tau_l^{**}$ and $\tilde{\pi}_r = \pi_r^* + a^2 \tau_r^*$. We perform algebraic manipulations on these two equations and also utilize the one on the right of (4.49) to derive

$$\tau_r^* = \tau_l^{**} + \frac{[\![\tilde{\pi}]\!]}{a^2}, \tag{4.53}$$

that can be substituted into (4.47d) to give

$$u_l^{**} = u_r^* = \alpha - a\,\tau_l^{**}, \tag{4.54}$$

with

$$\alpha = s_r - \frac{[\![\tilde{\pi}]\!]}{a}. \tag{4.55}$$

Next, upon substitution of relations (4.54) and (4.52) into equation (4.51), we obtain the second-order polynomial

$$(\alpha - 2a\,\tau_l^{**})^2 + \tfrac{2}{\alpha}[\![\psi]\!](\alpha - 2a\,\tau_l^{**}) - (s_l)^2 = 0, \tag{4.56}$$

which has two real roots, i.e.,

$$\tau_l^{**} = \frac{1}{2a}\left(\alpha + \frac{[\![\psi]\!]}{\alpha} \pm \sqrt{\left(\frac{[\![\psi]\!]}{\alpha}\right)^2 + (s_l)^2} \right). \tag{4.57}$$

The suitable root is chosen by considering physical criteria. Recall that the specific volume τ_l^{**} has to be a positive quantity. Therefore, we select the solution capable of restoring the Riemann solution to the Suliciu model as $[\![\psi]\!]$ tends to zero, namely,

$$\tau_l^{**} = \frac{1}{2a}\left(\alpha + \frac{[\![\psi]\!]}{\alpha} + \sqrt{\left(\frac{[\![\psi]\!]}{\alpha}\right)^2 + (s_l)^2} \right), \tag{4.58a}$$

and as a result,

$$\tau_r^* = \frac{1}{2a}\left(\left(s_r + \frac{[\![\tilde{\pi}]\!]}{a}\right) + \frac{[\![\psi]\!]}{\alpha} + \sqrt{\left(\frac{[\![\psi]\!]}{\alpha}\right)^2 + (s_l)^2} \right). \tag{4.58b}$$

An easy substitution of τ_l^{**} into (4.54) leads to

$$s_m = \frac{1}{2}\left(\alpha - \frac{[\![\psi]\!]}{\alpha} - \sqrt{\left(\frac{[\![\psi]\!]}{\alpha}\right)^2 + (s_l)^2} \right). \tag{4.59}$$

Let us note that if α is large enough such that $|[\![\psi]\!]| \ll |\alpha|$, then the value of the speed s_m is approximately

$$\tfrac{1}{2}(\alpha - |s_l|) = \tfrac{1}{2}(u_l + u_r - \tfrac{1}{a}[\![\pi]\!]) = \sigma. \tag{4.60}$$

Now, by performing steps similar to the ones used to find τ_l^{**}, we find the second-order polynomial

$$(s_l + 2a\,\tau_l^*)^2 - \tfrac{2}{s_l}[\![\psi]\!](s_l + 2a\,\tau_l^*) - \alpha^2 = 0, \tag{4.61}$$

which is used to obtain an expression for τ_l^*. Hence, after some algebraic manipulations, we are able to find

$$\tau_l^* = \frac{1}{2a}\left(-s_l + \frac{[\![\psi]\!]}{s_l} + \mathrm{sgn}(\alpha)\sqrt{\left(\frac{[\![\psi]\!]}{s_l}\right)^2 + \alpha^2}\right). \tag{4.62}$$

Again, we omit the computation for the remaining unknowns since they can be easily deduced from one another.

4.2.3   Case III: $s_l < 0 < s_r$, $\sigma < 0$

In this case, we assume that the wave ordering is $s_l < s_m < s_0 < s_r$, and we look for the exact Riemann solution having the structure:
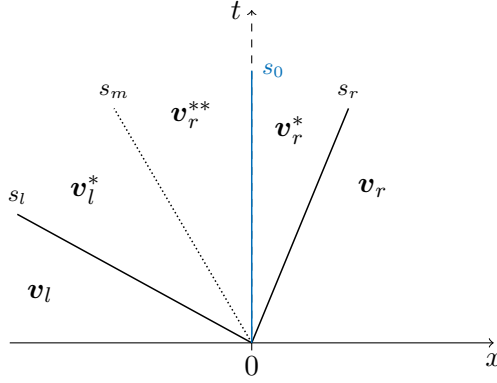
$$
\begin{aligned}
\boldsymbol{v}_l &= (\;\tau_l,\;\; u_l,\;\; \tilde{\pi}_l,\;\; \tilde{\epsilon}_l,\;\; \psi_l\;\;)^T\\
\boldsymbol{v}_l^* &= (\;\tau_l^*,\;\; u_l^*,\;\; \tilde{\pi}_l^*,\;\; \tilde{\epsilon}_l^*,\;\; \psi_l^*\;)^T\\
\boldsymbol{v}_r^{**} &= (\;\tau_r^{**},\, u_r^{**},\, \tilde{\pi}_r^{**},\, \tilde{\epsilon}_r^{**},\, \psi_r^{**}\,)^T\\
\boldsymbol{v}_r^* &= (\;\tau_r^*,\;\; u_r^*,\;\; \tilde{\pi}_r^*,\;\; \tilde{\epsilon}_r^*,\;\; \psi_r^*\;)^T\\
\boldsymbol{v}_r &= (\;\tau_r,\;\; u_r,\;\; \tilde{\pi}_r,\;\; \tilde{\epsilon}_r,\;\; \psi_r\;\;)^T
\end{aligned}
$$

The continuity of the Riemann invariants (4.29, 4.30, 4.31) across the linearly degenerate fields reads

$$u_l - a\,\tau_l = u_l^* - a\,\tau_l^*, \tag{4.63a}$$

$$u_r^*/\tau_r^* = u_r^{**}/\tau_r^{**}, \tag{4.63b}$$

$$\psi_r^* + \tfrac{1}{2}[(u_r^*)^2 - (a\,\tau_r^*)^2] = \psi_r^{**} + \tfrac{1}{2}[(u_r^{**})^2 - (a\,\tau_r^{**})^2], \tag{4.63c}$$

$$u_r^* + a\,\tau_r^* = u_r + a\,\tau_r, \tag{4.63d}$$

and

$$\psi_l = \psi_l^* = \psi_r^{**}, \qquad \psi_r = \psi_r^*, \tag{4.64a}$$

$$\tilde{\pi}_r = \tilde{\pi}_r^* = \tilde{\pi}_r^{**}, \qquad \tilde{\pi}_l = \tilde{\pi}_l^*, \tag{4.64b}$$

$$\tilde{\epsilon}_r = \tilde{\epsilon}_r^* = \tilde{\epsilon}_r^{**}, \qquad \tilde{\epsilon}_l = \tilde{\epsilon}_l^*. \tag{4.64c}$$

Across the wave with speed s_m, we also have the relations

$$s_m = u_r^{**} = u_l^*, \qquad \pi_r^{**} = \pi_l^*. \tag{4.65}$$

In order to find the solution for this case, we use a methodology similar to the one presented in Section 4.2.2 (**Case II**), and derive the specific volumes

$$\tau_r^* = \frac{1}{2a}\left(s_r + \frac{[\![\psi]\!]}{s_r} - \mathrm{sgn}(\beta)\sqrt{\left(\frac{[\![\psi]\!]}{s_r}\right)^2 + \beta^2}\right), \tag{4.66a}$$

$$\tau_r^{**} = \frac{1}{2a}\left(-\beta + \frac{[\![\psi]\!]}{\beta} + \sqrt{\left(\frac{[\![\psi]\!]}{\beta}\right)^2 + (s_r)^2}\right), \tag{4.66b}$$

$$\tau_l^* = \frac{1}{2a}\left(-\left(s_l + \frac{[\![\tilde{\pi}]\!]}{a}\right) + \frac{[\![\psi]\!]}{\beta} + \sqrt{\left(\frac{[\![\psi]\!]}{\beta}\right)^2 + (s_r)^2}\right), \tag{4.66c}$$

with β specified later in (4.67). We omit here the computation for the remaining unknowns, which easily follows from the relations defined in (4.63)-(4.65). However, due to its importance, we give the solution for $s_m = u_r^{**} = u_l^*$, with $u_l^* = s_l + a\tau_l^*$, as:

$$s_m = \frac{1}{2}\left(\beta + \frac{[\![\psi]\!]}{\beta} + \sqrt{\left(\frac{[\![\psi]\!]}{\beta}\right)^2 + (s_r)^2}\right), \quad \beta = s_l - \frac{[\![\tilde{\pi}]\!]}{a}. \tag{4.67}$$

If β is large enough such that $|[\![\psi]\!]| \ll |\beta|$, then the value of the wave speed s_m is approximately $\frac{1}{2}(\beta + |s_r|) = \frac{1}{2}(u_l + u_r - \frac{1}{a}[\![\pi]\!])$, and consequently, one recovers the term σ defined in equation (4.35).

4.2.4   Case IV: $s_r < 0$

Suppose that the exact solution follows the wave ordering $s_l < s_m < s_r < s_0 = 0$ and is composed of five constant states: $\boldsymbol{v}_l$, $\boldsymbol{v}_l^*$, $\boldsymbol{v}_r^{**}$, $\boldsymbol{v}_r^*$, and $\boldsymbol{v}_r$.
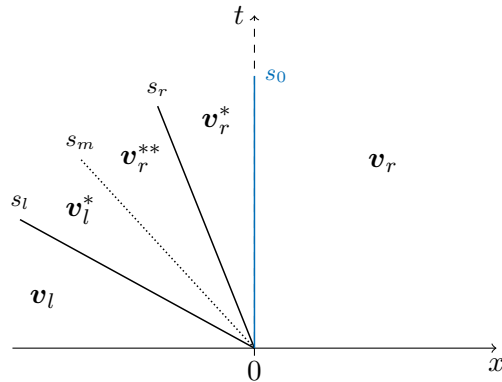
$$
\begin{aligned}
\boldsymbol{v}_l &= (\ \tau_l, \quad u_l, \quad \tilde{\pi}_l, \quad \tilde{\epsilon}_l, \quad \psi_l \ )^T \\
\boldsymbol{v}_l^* &= (\ \tau_l^*, \quad u_l^*, \quad \tilde{\pi}_l^*, \quad \tilde{\epsilon}_l^*, \quad \psi_l^* \ )^T \\
\boldsymbol{v}_r^{**} &= (\ \tau_r^{**}, \ u_r^{**}, \ \tilde{\pi}_r^{**}, \ \tilde{\epsilon}_r^{**}, \ \psi_r^{**} \ )^T \\
\boldsymbol{v}_r^* &= (\ \tau_r^*, \quad u_r^*, \quad \tilde{\pi}_r^*, \quad \tilde{\epsilon}_r^*, \quad \psi_r^* \ )^T \\
\boldsymbol{v}_r &= (\ \tau_r, \quad u_r, \quad \tilde{\pi}_r, \quad \tilde{\epsilon}_r, \quad \psi_r \ )^T
\end{aligned}
$$

By means of the trivial Riemann invariants, we search for the Riemann solution having the structure presented above. We first derive the simple equalities

$$\psi_l = \psi_l^* = \psi_r^{**} = \psi_r^*, \quad \tilde{\pi}_r = \tilde{\pi}_r^* = \tilde{\pi}_r^{**}, \quad \tilde{\pi}_l = \tilde{\pi}_l^*, \quad \tilde{\epsilon}_r = \tilde{\epsilon}_r^* = \tilde{\epsilon}_r^{**}, \quad \tilde{\epsilon}_l = \tilde{\epsilon}_l^*, \tag{4.68}$$

and then the relations

$$u_l - a\,\tau_l = u_l^* - a\,\tau_l^*, \tag{4.69a}$$

$$u_r/\tau_r = u_r^*/\tau_r^*, \tag{4.69b}$$

$$\psi_r + \tfrac{1}{2}[(u_r)^2 - (a\,\tau_r)^2] = \psi_r^* + \tfrac{1}{2}[(u_r^*)^2 - (a\,\tau_r^*)^2], \tag{4.69c}$$

$$u_r^* + a\,\tau_r^* = u_r^{**} + a\,\tau_r^{**}. \tag{4.69d}$$

Moreover, across the s_m-wave, we also obtain the useful expressions

$$s_m = u_r^{**} = u_l^*, \qquad \pi_r^{**} = \pi_l^*, \tag{4.70}$$

and using an approach similar to the one presented in **Case I**, we find the values for the following specific volumes:

$$\tau_r^* = \tau_r\sqrt{1 + \frac{2\,[\![\psi]\!]}{(u_r)^2 - (a\,\tau_r)^2}}, \tag{4.71a}$$

$$\tau_r^{**} = \frac{1}{2a}\left(-s_l + s_r\sqrt{1 + \frac{2\,[\![\psi]\!]}{(u_r)^2 - (a\,\tau_r)^2}} + \frac{[\![\tilde{\pi}]\!]}{a}\right), \tag{4.71b}$$

$$\tau_l^* = \frac{1}{2a}\left(-s_l + s_r\sqrt{1 + \frac{2\,[\![\psi]\!]}{(u_r)^2 - (a\,\tau_r)^2}} - \frac{[\![\tilde{\pi}]\!]}{a}\right). \tag{4.71c}$$

Once more, we decide to skip the computation details for the other variables since they can be simply deduced from one another. Yet, from (4.71a), we extract the necessary condition

$$[\![\psi]\!] > -\tfrac{1}{2}\left((u_r)^2 - (a\,\tau_r)^2\right). \tag{4.72}$$

It is worth recalling that $s_r < 0$; therefore, $u_r - a\,\tau_r < u_r + a\,\tau_r < 0$ and the quantity $(u_r)^2 - (a\,\tau_r)^2$ is strictly positive. Now, for τ_r^{**} and τ_l^* to be positive specific volumes, we must satisfy the following condition:

$$|[\![\tilde{\pi}]\!]| < a\left(-s_l + s_r\sqrt{1 + \frac{2\,[\![\psi]\!]}{(u_r)^2 - (a\,\tau_r)^2}}\right). \tag{4.73}$$

If this condition is not met, in order to avoid the appearance of vacuum, we degenerate the s_r-wave by choosing a larger value of a such that we can switch to **Case III**.

Review of Necessary Conditions

Summarizing the necessary conditions from **Cases II** and **III** yields

$$|[\![\psi]\!]| < \min\left(|\alpha|, |\beta|\right).$$

and for **Cases I** and **IV**, we must consider

$$|[\![\psi]\!]| < \tfrac{1}{2}\min\left((u_r)^2 - (a\,\tau_r)^2,\ (u_l)^2 - (a\,\tau_l)^2\right).$$

Thus, we confirm that the solver is robust for small values of $[\![\psi]\!]$. In Annex B.3, we provide several implementation details with regard to the proposed approach and its four cases, and simultaneously, specify the values of all the associated unknowns.

4.3 One-Dimensional Relaxation Scheme

Based on the relaxation model (4.21), we now present the main steps involved in the numerical time-update strategy employed to approximate the solution of the initial value problem

$$\begin{cases} \partial_t \boldsymbol{w} + \partial_x \boldsymbol{f}(\boldsymbol{w}) + \boldsymbol{b}(\boldsymbol{w})\partial_x \Phi = 0, \\ \partial_{xx}\Phi = 4\pi G\rho, \\ \boldsymbol{w}(x,0) = \boldsymbol{w}_0(x), \ \Phi(x,0) = \Phi_0(x). \end{cases} \tag{4.74}$$

As mentioned in Section 4.1, we apply a first-order operator splitting approach to decompose (4.74) into two subsystems: the Euler equations with gravity source terms and the Poisson equation. We consider a uniform numerical grid with a total of N_x cells $\mathcal{C}_i = (x_{i-1/2}, x_{i+1/2})$ of size Δx and time increments Δt such that $t^{n+1} = t^n + \Delta t$, using the notation introduced in Section 1.3 for a one-dimensional finite volume discretization.

4.3.1 Euler Equations with Gravity Source Terms

In this part, $\boldsymbol{w}$ is the unknown vector and the gravitational potential Φ is an *a priori* given function. Hence, we suppose for the moment that for each time step t^n, the approximate potential Φ_h is known, namely,

$$\Phi_h(x,t^n) = \sum_{i=1,\dots,N_x} \Phi_i^n \chi_{i,j}(x) \quad \text{with} \quad \chi_{i,j}(x) = \begin{cases} 1 & \text{if } x \in \mathcal{C}_i, \\ 0 & \text{if } x \notin \mathcal{C}_i. \end{cases} \tag{4.75}$$

Moreover, we assume that at the same time t^n, a piecewise constant approximate solution denoted by $\boldsymbol{w}_h(x,t^n)$ is also known:

$$\boldsymbol{w}_h(x,t^n) = \sum_{i=1,\dots,N_x} \mathbf{w}_i^n \chi_{i,j}(x). \tag{4.76}$$

The obtained approximations are then evolved in time using a two-step splitting technique, which will be described in detail subsequently.

First Step: Evolution in Time ($\delta = \infty$)

At the beginning of the time step t^n, we construct the initial data

$$\boldsymbol{w}_{\delta h}(x,t^n) = (\rho_i^n, (\rho u)_i^n, (\rho e)_i^n, (\rho \pi)_i^n = \rho_i^n p_i^n, \psi_i^n = \Phi_i^n)^T, \quad x \in \mathcal{C}_i, \tag{4.77}$$

which coincides with a relaxation equilibrium state as $\pi_i^n = p_i^n$ and $\psi_i^n = \Phi_i^n$ are set. Then, for all $t \in (0, \Delta t)$, we look for the weak solutions $\boldsymbol{w}_{\delta h}(x,t^n + t)$ of the Cauchy problem

$$\partial_t \boldsymbol{w}_\delta + \partial_x \boldsymbol{f}_\delta(\boldsymbol{w}_\delta) + \boldsymbol{b}_\delta(\boldsymbol{w}_\delta)\partial_x \psi = 0, \tag{4.78}$$

subject to the previously defined initial data $\boldsymbol{w}_{\delta h}(x,t^n)$. We wish to point out that equation (4.78) is in fact the relaxation model (4.21) without the source terms, i.e., with $\delta = \infty$. Now, the solution $\boldsymbol{w}_{\delta h}(x,t^n + t)$ is approximated as a superposition of

non-interacting Riemann solutions emerging at each interface $x_{i+1/2}$ for positive times t smaller than Δt, satisfying the restriction

$$\Delta t \max_{i=1,\dots,N_x}\left(|\lambda_{-,i+\frac{1}{2}}|,|\lambda_{+,i-\frac{1}{2}}|\right) \leq \frac{\Delta x}{2}, \tag{4.79}$$

where $\lambda_{-,i+1/2}$ and $\lambda_{+,i+1/2}$ are estimates of the slowest and fastest wave speeds, respectively. The description and details of these waves were given in Section 4.2, as well as the Riemann solution $\boldsymbol{\mathcal{W}}_\delta$ for the relaxation model (4.78).

In order to enforce a suitable positive preserving property, we discuss relevant criteria for the correct characterization of the parameter a. Thus, given two constant states $(\mathbf{w}_\delta)_i^n$ and $(\mathbf{w}_\delta)_{i+1}^n$ separated by a discontinuity at $x = x_{i+1/2}$, this parameter is defined locally at each interface as

$$a_{i+\frac{1}{2}} = a_0 \max\left(\rho_i^n c_i^n, \rho_{i+1}^n c_{i+1}^n\right), \tag{4.80}$$

with a_0 a positive constant, the value of which is fixed according to the specific physical settings of the problem addressed so all robustness conditions described in the previous section are satisfied. Unless specified otherwise, we use $a_0 = 1.05$ for our numerical simulations. In this manner, the Riemann solution depends not only on the left and right states $(\mathbf{w}_\delta)_i^n$ and $(\mathbf{w}_\delta)_{i+1}^n$, but also on the parameter a. Then, we write

$$\boldsymbol{w}_{\delta h}(x,t^n+t) = \boldsymbol{\mathcal{W}}_\delta\left(\frac{x-x_{i+\frac{1}{2}}}{t};(\mathbf{w}_\delta)_i^n,(\mathbf{w}_\delta)_{i+1}^n,a_{i+\frac{1}{2}}\right), \quad x \in (x_i,x_{i+1}), \quad t \in (0,\Delta t),$$

and its projection over the piecewise constant functions as

$$\begin{aligned}
(\mathbf{w}_\delta)_i^{n+1,-} &= \frac{1}{\Delta x}\int_{x_{i-\frac{1}{2}}}^{x_{i+\frac{1}{2}}} \boldsymbol{w}_{\delta h}\left(x,t^{n+1}\right)dx \\
&= \frac{1}{\Delta x}\int_{x_{i-\frac{1}{2}}}^{x_i} \boldsymbol{\mathcal{W}}_\delta\left(\frac{x-x_{i-\frac{1}{2}}}{\Delta t};(\mathbf{w}_\delta)_{i-1}^n,(\mathbf{w}_\delta)_i^n,a_{i-\frac{1}{2}}\right)dx \\
&\quad + \frac{1}{\Delta x}\int_{x_i}^{x_{i+\frac{1}{2}}} \boldsymbol{\mathcal{W}}_\delta\left(\frac{x-x_{i+\frac{1}{2}}}{\Delta t};(\mathbf{w}_\delta)_i^n,(\mathbf{w}_\delta)_{i+1}^n,a_{i+\frac{1}{2}}\right)dx.
\end{aligned} \tag{4.81}$$

Let us note that because of the potential source term, the standard conservative flux balance cannot be reached. However, making use of the formalism introduced by Harten, Lax and van Leer [74], we define

$$\begin{aligned}
\mathbf{f}_l\left((\mathbf{w}_\delta)_i^n,(\mathbf{w}_\delta)_{i+1}^n\right) =& \boldsymbol{f}_\delta\left((\mathbf{w}_\delta)_i^n\right) \\
&- \frac{1}{\Delta t}\int_{x_i}^{x_{i+\frac{1}{2}}}\left(\boldsymbol{\mathcal{W}}_\delta\left(\frac{x-x_{i+\frac{1}{2}}}{\Delta t};(\mathbf{w}_\delta)_i^n,(\mathbf{w}_\delta)_{i+1}^n,a_{i+\frac{1}{2}}\right)-(\mathbf{w}_\delta)_i^n\right)dx, \\
\mathbf{f}_r\left((\mathbf{w}_\delta)_i^n,(\mathbf{w}_\delta)_{i+1}^n\right) =& \boldsymbol{f}_\delta\left((\mathbf{w}_\delta)_{i+1}^n\right) \\
&+ \frac{1}{\Delta t}\int_{x_{i+\frac{1}{2}}}^{x_{i+1}}\left(\boldsymbol{\mathcal{W}}_\delta\left(\frac{x-x_{i+\frac{1}{2}}}{\Delta t};(\mathbf{w}_\delta)_i^n,(\mathbf{w}_\delta)_{i+1}^n,a_{i+\frac{1}{2}}\right)-(\mathbf{w}_\delta)_{i+1}^n\right)dx,
\end{aligned}$$

such that

$$(\mathbf{w}_\delta)_i^{n+1,-} = (\mathbf{w}_\delta)_i^n - \frac{\Delta t}{\Delta x} \left(\mathbf{f}_l \left((\mathbf{w}_\delta)_i^n, (\mathbf{w}_\delta)_{i+1}^n \right) - \mathbf{f}_r \left((\mathbf{w}_\delta)_{i-1}^n, (\mathbf{w}_\delta)_i^n \right) \right). \tag{4.82}$$

Second Step: Relaxation Equilibrium ($\delta = 0$)

This step of the scheme consists in solving $\partial_t \mathbf{w}_\delta = \frac{1}{\delta} \mathbf{s}_\delta(\mathbf{w}_\delta)$, with initial data defined by the piecewise constant approximation $(\mathbf{w}_\delta)_i^{n+1,-}$. As δ tends to zero, the updated approximate equilibrium solution is given by

$$\mathbf{w}_i^{n+1} = \left(\rho_i^{n+1,-}, (\rho u)_i^{n+1,-}, (\rho e)_i^{n+1,-} \right)^T, \tag{4.83}$$

and we enforce $\pi_i^{n+1} = p_i^{n+1}$ and $\psi_i^{n+1} = \Phi_i^{n+1}$ to recover a relaxation equilibrium.

4.3.2 Poisson Equation

This second part consists in using the first component of $\mathbf{w}_i^{n+1}$, i.e., ρ_i^{n+1}, to solve the Poisson equation and thus obtain Φ_i^{n+1}. The discretization of $\partial_{xx}\Phi = 4\pi G\rho$ by means of a second-order finite difference approach yields a tridiagonal matrix. There are numerous ways of solving the resulting matrix equation that can be categorized into direct and iterative methods.

4.3.3 Summary and Additional Remarks

Now, involving the usual framework of finite volume methods, the complete relaxation scheme is summarized below:

$$\mathbf{w}_i^{n+1} = \mathbf{w}_i^n - \frac{\Delta t}{\Delta x} \left(\phi_{x,i+\frac{1}{2}}^l - \phi_{x,i-\frac{1}{2}}^r \right), \tag{4.84}$$

where

$$\phi_{x,i+\frac{1}{2}}^l = \mathbf{f}_l \left(\boldsymbol{w}_\delta(\mathbf{w}_i^n), \boldsymbol{w}_\delta(\mathbf{w}_{i+1}^n) \right), \tag{4.85a}$$

$$\phi_{x,i+\frac{1}{2}}^r = \mathbf{f}_r \left(\boldsymbol{w}_\delta(\mathbf{w}_i^n), \boldsymbol{w}_\delta(\mathbf{w}_{i+1}^n) \right), \tag{4.85b}$$

with $\boldsymbol{w}_\delta(\mathbf{w}_i^n) = (\mathbf{w}_\delta)_i^n$ defined according to the relaxation equilibrium, i.e., $\pi_i^n = p_i^n$ and $\psi_i^n = \Phi_i^n$. Indeed, considering the projection step and the relaxation system solution, the numerical fluxes can be written as functions of the relaxation equilibrium states

$$\phi_{x,i+\frac{1}{2}}^l = \phi_{x,i+\frac{1}{2}}^l(\rho_i^n, u_i^n, (\rho e)_i^n, \Phi_i^n, \ \rho_{i+1}^n, u_{i+1}^n, (\rho e)_{i+1}^n, \Phi_{i+1}^n), \tag{4.86a}$$

$$\phi_{x,i+\frac{1}{2}}^r = \phi_{x,i+\frac{1}{2}}^r(\rho_i^n, u_i^n, (\rho e)_i^n, \Phi_i^n, \ \rho_{i+1}^n, u_{i+1}^n, (\rho e)_{i+1}^n, \Phi_{i+1}^n). \tag{4.86b}$$

Let us remark that we kept the notation $\phi_{x,i+1/2}^\alpha$ (with $\alpha \in \{l,r\}$) for the fluctuations, on account of the numerical scheme not being a conservative one. In fact, the nonconservative operator, coming from $\boldsymbol{b}(\boldsymbol{w})\partial_x\Phi$ in (4.12), is null except at the interfaces $x_{i+1/2}$ because of the evolution equation (4.17) that governs the relaxation potential. In Section 4.2, we have clearly shown that the continuity of the flux function is lost across any interface.

4.4   Numerical Results

The purpose of this section is to illustrate the interest of the proposed relaxation solver for the Euler-Poisson model. To address numerical issues, several astrophysical tests are performed: in the first four, we consider a fluid subject to a constant external gravitational field, and in the last, we numerically recover the *Lane-Emden equation* [84] which describes the hydrostatic equilibrium of a self-gravitating star.

The relaxation strategy has been implemented in the code HERACLES [66]. For second-order approximations, we extend the scheme by using the MUSCL-Hancock Method (MHM), see [129], and as for the choice of slope limiters, we employ the mono-tonized central (MC) one [136], unless stated otherwise. Let us note, though, that no slope limiting is used for the gravitational potential in order to have a proper potential jump at each cell interface, as is also done in [102].

When needed, the relaxation scheme is compared with the standard fractional step splitting method (hereafter referred to as *standard method*). This approach also consists on treating subsystems (4.7) and (4.8) individually, with the sole difference being that the former subsystem is simply solved by splitting it into

$$\partial_t \boldsymbol{w} + \nabla \cdot \boldsymbol{\mathcal{F}}(\boldsymbol{w}) = 0, \tag{4.87a}$$

$$\partial_t \boldsymbol{w} \qquad\qquad = -\boldsymbol{\mathcal{B}}(\boldsymbol{w})\nabla\Phi. \tag{4.87b}$$

4.4.1   One-Dimensional Equilibrium Flow

As a first test, we consider a one-dimensional equilibrium flow with a relatively simple setup. In this case, we neglect the gravitational interactions between particles and suppose that they are subject to a uniform gravitational field. With a potential of the form $\phi(x) = gx$ and constant $g > 0$, the flow satisfies the relation $\partial_x p = -\rho g$. We then suppose that the fluid is governed by an isentropic equation of state $p = c^2\rho$ so we obtain the equilibrium $\rho_{eq}(x) = \rho_0 \exp\left(-gx/c^2\right)$, with $\rho_0 = 10kg$, $c = 1\,ms^{-1}$ and $g = 10\,ms^{-2}$. From this relation, we can define the characteristic scales associated to this experiment: the gravitational length $L_{ref} = c^2/g$ and time $T_{ref} = (L_{ref}/g)^{1/2}$.
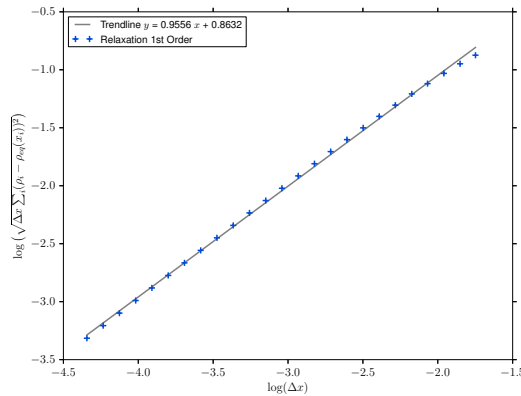
FIGURE 4.2. Accuracy of the relaxation method in the case of an isentropic hydrostatic atmosphere in a constant gravitational field.

In order to illustrate the accuracy of the relaxation method, we intend to compute this equilibrium flow and perform an error analysis in the L^2 norm. The experiment is then initialized on a computational domain $x \in [0,1]\,m$ consisting of $N = 1000$ uniform cells and is run a sufficiently long time $T = 50s \gg T_{ref} = 0.1\,s$, with a CFL number of 0.5. Homogenous and non-homogenous Dirichlet boundary conditions are set for ρ and u, respectively, to ensure the hydrostatic equilibrium. Figure 4.2 displays the L^2 error of the estimated density compared to the analytical solution ρ_{eq} for different mesh sizes Δx in a log-log scale. The slope of the error gives the order of accuracy of the method: using the least squares approach, we obtain a linear fit $y = 0.9556\,x + 0.8632$ and thus, the order is approximately 0.96.

(a) L^2 error (b) L^2 norm of the velocity
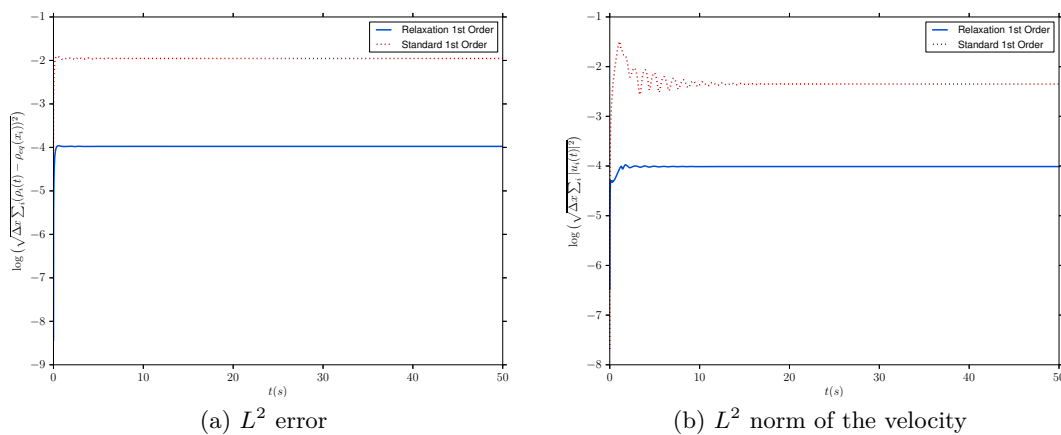
FIGURE 4.3. Results in logarithmic scale for the one-dimensional hydrostatic atmosphere with 1000 cells; solid line: proposed relaxation method ($a_0 = 1.0$), dotted line: *standard method*. Since the same half CFL condition (4.79) is used, the total number of time steps for both methods is of the same order of magnitude, specifically, 1.001×10^5 and 1.006×10^5 steps for the relaxation and standard methods, respectively.

Figure 4.3 shows the evolution in time of the L^2 error for the density (left) and the L^2 norm of the velocity (right), in logarithmic scales. We can observe that the L^2 error grows exponentially for a short time and then stabilizes itself, and this holds true for both methods being compared. Note that both the error and residual velocity are considerably smaller for the relaxation method than for a standard fractional step splitting method. Therefore, the relaxation scheme clearly enables a better approximation of the equilibrium solution ρ_{eq}.

4.4.2 Perturbed One-Dimensional Isothermal Equilibrium

LeVeque and Bale [91] first proposed this test to determine a method's ability to capture perturbed near-equilibrium solutions. The problem consists of an ideal gas in isothermal equilibrium. A small perturbation to the pressure is introduced and its behavior is then examined over time. The initial conditions and perturbation are given in Table 4.1.

Perturbed Isothermal Equilibrium

$\rho_0(x)$	$u_0(x)$	$p_0(x)$	Gravity potential
e^{-x}	0.0	e^{-x}	$\Phi(x) = gx$, with $g = 1.0$

Computational domain: $[0,1]$;   Fixed boundary conditions

Initial perturbed pressure: $p(x,0) = p_0(x) + \eta e^{-100(x-0.5)^2}$, with $0 < \eta \ll 1$

TABLE 4.1. Initial data for the 1D isothermal equilibrium described in [91].

The test is initialized on a computational domain $x \in [0,1]$ consisting of 100 evenly spaced cells, with the initial perturbation centered at $x = 0.5$. Three different values for the perturbation amplitude η are considered: $\eta = 0.01$, $\eta = 0.001$ and $\eta = 0.0001$. For the middle one, it has been already demonstrated in [91] that the *standard method* is not able to correctly capture the perturbed pressure nor maintain the boundary values, and here, we attempt to reproduce the observed numerical behavior.
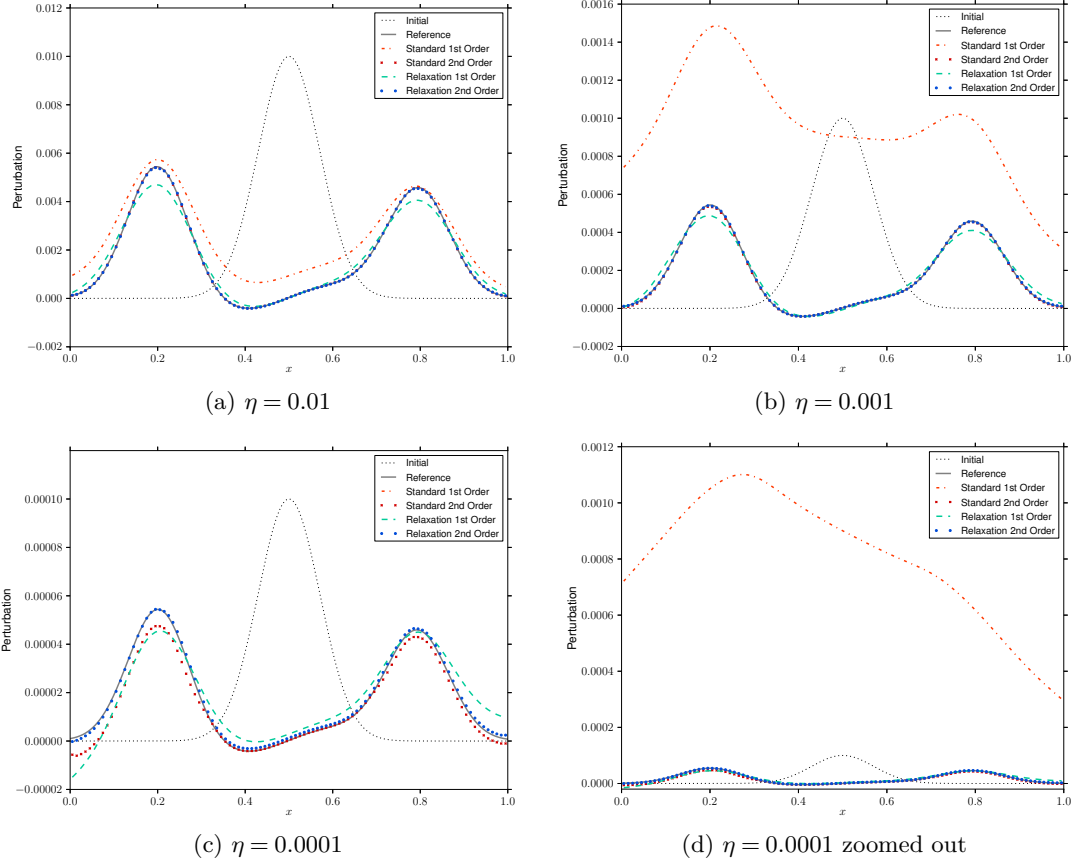
FIGURE 4.4. Comparison of the standard and relaxation schemes for the perturbed isothermal equilibrium test at time $t = 0.25$ and with $N_x = 100$. For the relaxation method, $a_0 = 0.83$ and $a_0 = 2.01$ were used for first- and second-order, respectively. The solid gray line gives a reference solution obtained with the second-order relaxation scheme on a finer mesh of 4000 zones.

We run this test and the perturbation $p(x,t) - p_0(x)$ at time $t = 0.25$ is shown in Figure 4.4. The perturbation at the initial time is indicated by the dashed line and the reference solution obtained with the second-order relaxation method using a higher resolution is included with a solid gray line. Second-order results show that both methods implemented in HERACLES [66] are able to capture the correct solution. First-order results are more dissipative and we can perceive that the standard method fails to capture the perturbation, specially when $\eta = 0.0001$, as seen in Figures 4.4c and 4.4d. The advantages of the proposed relaxation scheme are then adequately demonstrated by performing this test.

4.4.3 Sod Shock Tube Under Gravitational Influence

Now, we consider the Sod shock tube problem under a gravitational field, as described in [102, 149]. The main advantage of this test is that it consists of a relatively simple initial setup, summarized in Table 4.2.
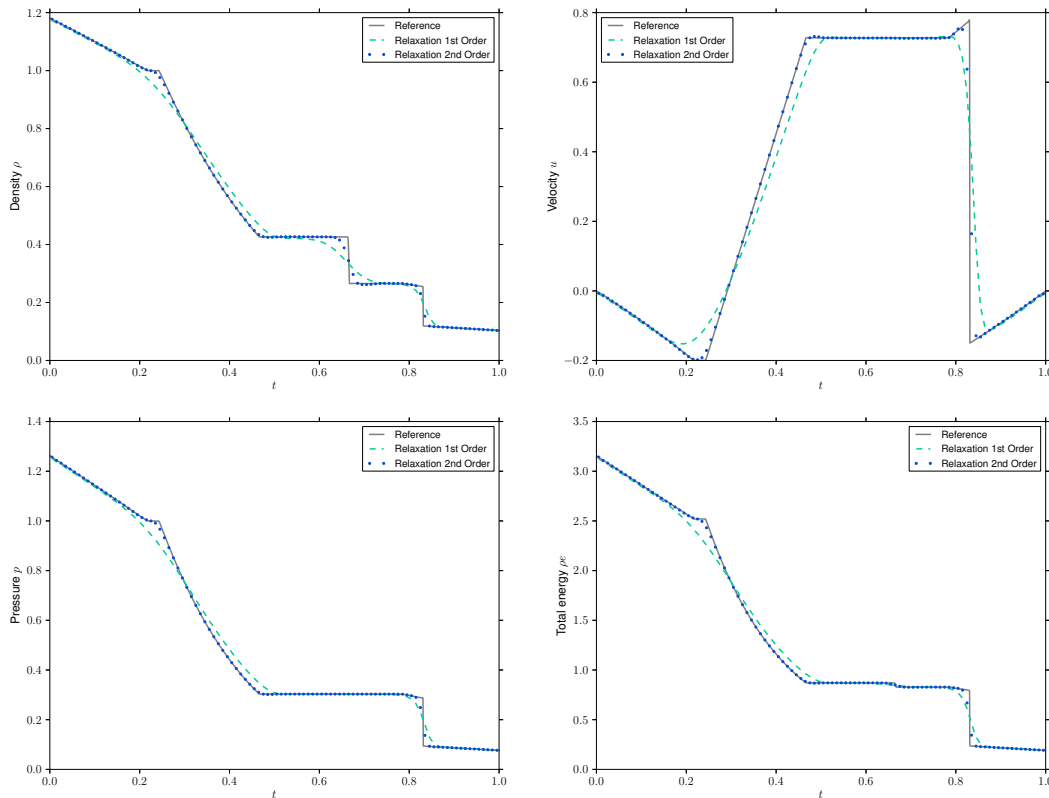
FIGURE 4.5. Several distributions obtained with the relaxation scheme proposed in this paper for Test 4.4.3 at time $t = 0.2$, using $N_x = 100$ cells and $a_0 = 1.0$. The results are compared with a reference solution obtained using the second-order algorithm on a finer grid of 4000 cells.

The test is then run to time $t = 0.2$ on a coarse grid composed of 100 cells using the relaxation scheme presented in Section 4.3. Figure 4.5 shows the corresponding density, velocity, pressure, and total energy density plots, compared with a reference solution

Shock Tube with Gravity

	$\rho_0(x)$	$u_0(x)$	$p_0(x)$	Gravity potential
$x \leq 0.5$	1.000	0.0	1.0	$\Phi(x) = gx$, with $g = 1.0$
$x > 0.5$	0.125	0.0	0.1	
	Computational domain: $[0,1]$; Reflecting boundaries			

TABLE 4.2. Initial data for the Sod shock tube under a gravitational field described in [102].

computed on a refined grid of 4000 cells. Due to the existence of a gravitational field, the first plot in the series shows how the density profile is pushed towards the left and the velocity plot reveals the development of negative velocities. As expected, the first-order results are the most diffusive given that the initial discontinuities are spread out over several zones. Second-order results are clearly more accurate and satisfying, and demonstrate that the relaxation scheme is able to capture shocks correctly.

4.4.4 Two- and Three-Dimensional Rayleigh-Taylor Instability

As a fourth test, we consider the Rayleigh-Taylor instability occurring as a consequence of a heavy fluid driven into a lighter one under the acceleration of a gravitational field, both in two and three dimensions.

(a) 800×200 points   (b) 8000×2000 points (256 proc.)
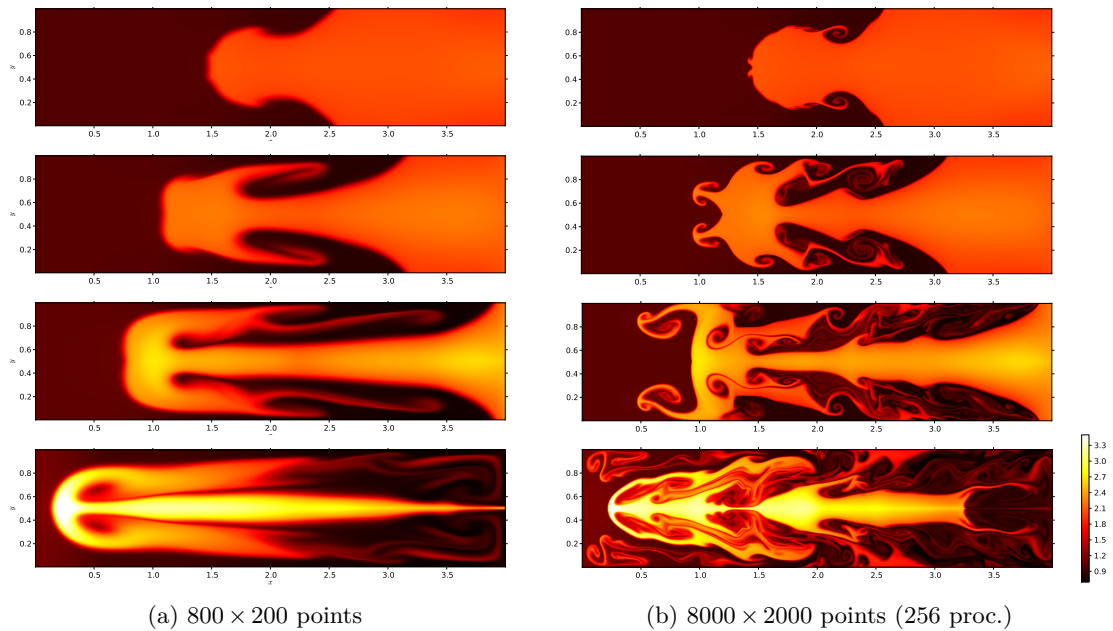
FIGURE 4.6. Rayleigh-Taylor instability computed with the proposed relaxation scheme in a 2D computational domain. The results are given at times $t = 2.4\,s, 4.0\,s, 5.6\,s, 7.2\,s$ (top to bottom).

First, we wish to carry out this experiment in the two-dimensional plane approximation (translational invariance along the z-axis). The derived numerical method given by

(a) Minmod ($\rho : 0.73 - 3.46$)

(b) MC limiter ($\rho : 0.71 - 3.36$)

(c) Superbee ($\rho : 0.80 - 3.19$)

(d) Positivity preserving ($\rho : 0.75 - 3.33$)
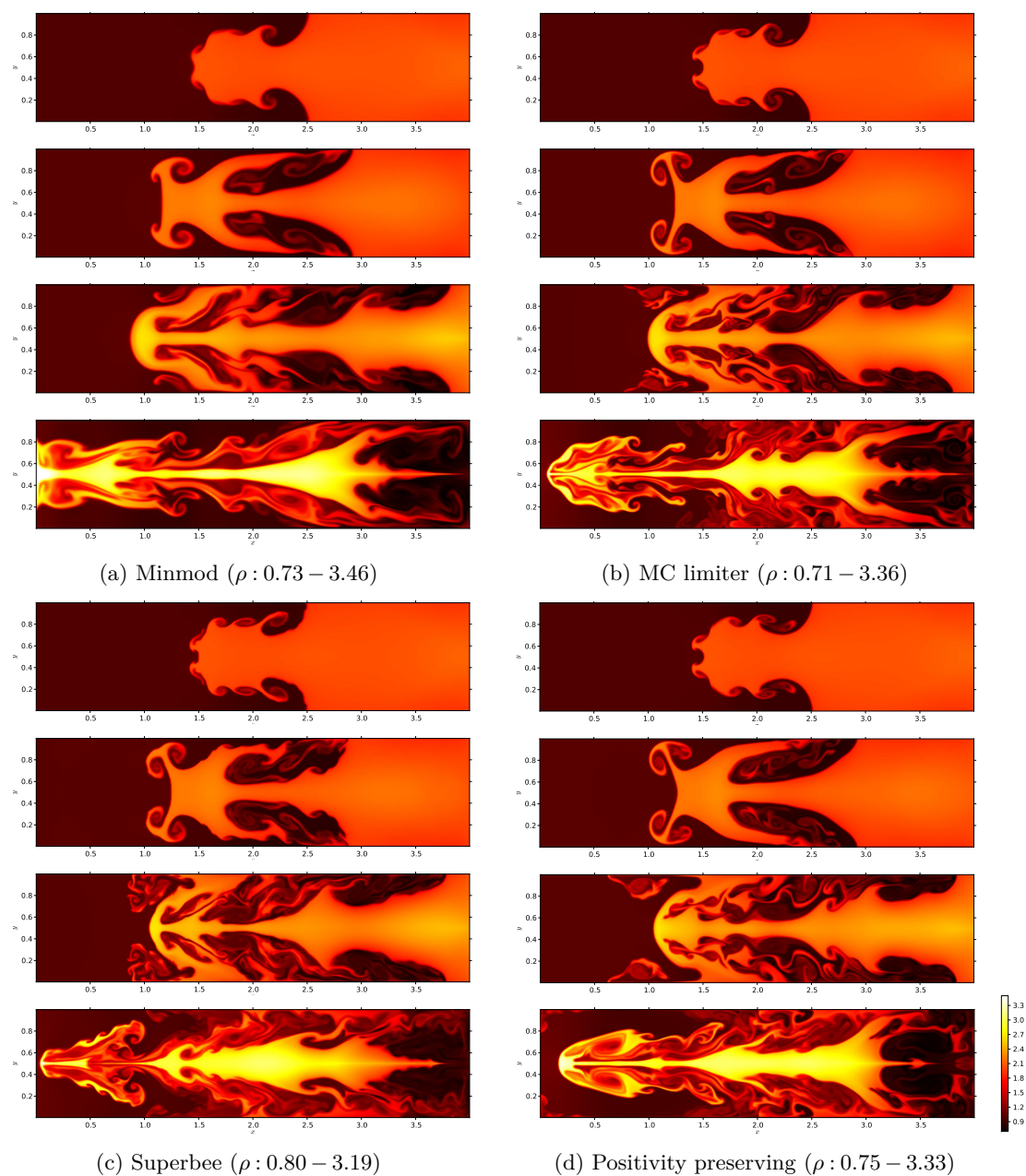
FIGURE 4.7. Rayleigh-Taylor instability computed with a MUSCL-type second-order extension of the relaxation scheme using different limiters. The computations are performed with 800×200 cells and the results are given at times $t = 2.4\,s$, $4.0\,s$, $5.6\,s$, $7.2\,s$ (top to bottom).

(4.84) is easily extended to consider 2D simulations, and as is usual, we suggest

$$\mathbf{w}_{i,j}^{n+1} = \mathbf{w}_{i,j}^{n} - \frac{\Delta t}{\Delta x}\left(\boldsymbol{\phi}_{x,i+\frac{1}{2},j}^{l} - \boldsymbol{\phi}_{x,i-\frac{1}{2},j}^{r}\right) - \frac{\Delta t}{\Delta y}\left(\boldsymbol{\phi}_{y,i,j+\frac{1}{2}}^{l} - \boldsymbol{\phi}_{y,i,j-\frac{1}{2}}^{r}\right), \qquad (4.88)$$

where $\phi^\alpha_{x,m,n}$ and $\phi^\alpha_{y,m,n}$ are the numerical fluxes in the x- and y-directions, respectively, with $\alpha \in \{l, r\}$ (refer to equation (4.85)). Moreover, the gravity potential is governed by $\Phi(x, y) = gx$, with $g = 1.0 \, m \, s^{-2}$. Initially, the two-dimensional computational domain $[0, L_x] \times [0, L_y]$ contains two fluids of different densities separated by an unstable interface

$$x = \tfrac{1}{2} L_x \left(1 - \tfrac{1}{10} cos[(\tfrac{y}{L_y} - \tfrac{1}{2})\pi] \right). \tag{4.89}$$

We set the densities on the right and on the left of this discontinuity to $\rho_l = 1.0 \, kg \, m^{-3}$ and $\rho_r = 2.0 \, kg \, m^{-3}$, respectively. After fixing the lengths to $L_x = 4.0 \, m$ and $L_y = 1.0 \, m$, we run this unsteady problem with imposed reflecting boundary conditions on two grids composed of 800×200 and 8000×2000 cells and using a CFL number of 0.5. The results are displayed in Figure 4.6, with the density ranging from 0.70 to 3.50. A graphical comparison indicates that a more accurate solution is obtained using the finer grid, which is not surprising.

Additionally, given that the approximately first-order scheme is too diffusive, we perform second-order computations employing four different limiters: minmod [118], MC [136], superbee [118], and the positivity preserving limiter [127]. We then use the mesh composed of 160000 cells to obtain the plots shown in Figure 4.7, where it is clear that the use of the minmod (respecitvely, MC) limiter yields the most (respectively, least) dissipative results for this particular experiment. In all of the simulations (including the first-order ones), we perceive the formation of the expected Rayleigh-Taylor *mushroom cap* and the development of side rolls along the evolution. In general, we observe that the Rayleigh-Taylor instability has been successfully reproduced in two dimensions.

3D Rayleigh-Taylor

	$\rho_0(x)$	$\boldsymbol{u}_0(x)$	$p_0(x)$	Gravity potential
$z \leq S(x, y)$	1	0	$10 - z$	$\Phi(x, y, z) = gz$, with $g = 1.0$
$z > S(x, y)$	2	0	$10 - 2z + S(x, y)$	
Computational domain: $[0, L_x] \times [0, L_y] \times [0, L_z]$ with $L_x = L_y = 1$, $L_z = 4$; Reflecting boundaries				
Interface: $S(x, y) = \tfrac{1}{2} L_z \left(1 - \tfrac{1}{10} \cos[(\tfrac{x}{L_x} - \tfrac{1}{2})\pi] \right) \left(1 - \tfrac{1}{10} \cos[(\tfrac{y}{L_y} - \tfrac{1}{2})\pi] \right)$				

TABLE 4.3. Initial data for the 3D Rayleigh-Taylor instability (SI units).

Now, let us consider this instability in three dimensions, extending the numerical approach (4.84) to 3D, i.e.,

$$\mathbf{w}^{n+1}_{i,j,k} = \mathbf{w}^n_{i,j,k} - \frac{\Delta t}{\Delta x} \left(\phi^l_{x,i+\frac{1}{2},j,k} - \phi^r_{x,i-\frac{1}{2},j,k} \right) \tag{4.90}$$
$$- \frac{\Delta t}{\Delta y} \left(\phi^l_{y,i,j+\frac{1}{2},k} - \phi^r_{y,i,j-\frac{1}{2},k} \right) - \frac{\Delta t}{\Delta z} \left(\phi^l_{z,i,j,k+\frac{1}{2}} - \phi^r_{z,i,j,k-\frac{1}{2}} \right),$$

using notation analogous to that of equation (4.88). The test, with initial data summarized in Table 4.3, is run using the MC limiter [136] on a fine grid of $200 \times 200 \times 800$ cells. Several snapshots of the density evolution are displayed in Figure 4.8, where once again, we are able to evidence the development of the mushroom cap and secondary Kelvin-Helmholtz instabilities along its edge. The test has been successfully reproduced.

(a) $t = 1.2$ (b) $t = 2.2$ (c) $t = 3.2$ (d) $t = 4.2$ (e) $t = 5.2$
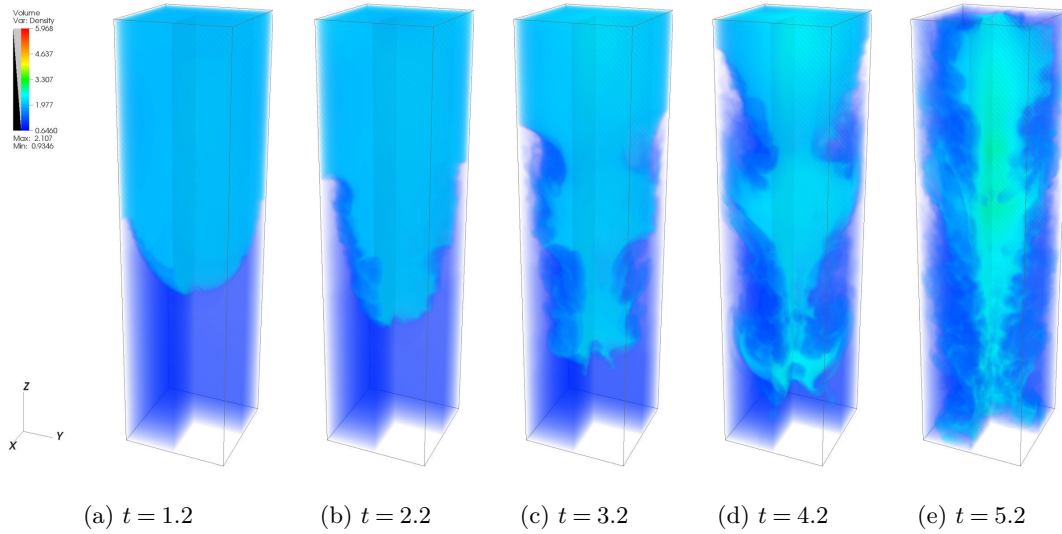
FIGURE 4.8. Rayleigh-Taylor instability computed with a second-order extension of the relaxation scheme on 1024 processors and using $200 \times 200 \times 800$ cells ($a_0 = 1.05$).

4.4.5 Equilibrium of a Self-Gravitating Compressible Fluid

In this context, we rewrite system (4.1) in spherical coordinates (r, θ, φ), assuming rotational invariance around the axes $\boldsymbol{e}_\theta$ and $\boldsymbol{e}_\varphi$, and obtain

$$\begin{cases} \partial_t(\rho) + \frac{1}{r^2}\partial_r(r^2\rho u_r) = 0, \\ \partial_t(\rho u_r) + \frac{1}{r^2}\partial_r(r^2\rho u_r^2) + \partial_r p = -\rho\partial_r\Phi, \\ \frac{1}{r^2}\partial_r(r^2\partial_r\Phi) = 4\pi G\rho. \end{cases} \tag{4.91}$$

For this last test, we consider a self-gravitational fluid at hydrostatic equilibrium, governed by the polytropic equation of state $p = \kappa\rho^\gamma = \kappa\rho^{1+\frac{1}{n}}$, where κ is the polytropic constant, γ the adiabatic exponent and n the polytropic index. Interestingly, this equilibrium flow can be characterized by the *Lane-Emden equation* [84], derived below.

First, assuming the fluid to be at hydrostatic equilibrium, i.e., $\partial_t = 0$ and $u_r = 0$, reduce system (4.91) to

$$\begin{cases} \partial_r(p) = -\rho\partial_r\Phi, \\ \frac{1}{r^2}\partial_r(r^2\partial_r\Phi) = 4\pi G\rho. \end{cases} \tag{4.92}$$

Combine the momentum equation with the polytropic relation and then perform a space integration to obtain a relation that links the fluid density to the potential, namely

$$\rho = \left(\frac{-\Phi}{(n+1)\kappa}\right)^n. \tag{4.93}$$

Using the Poisson equation, find the following second-order ordinary differential equation for the potential:

$$\partial_r^2(\Phi) + \frac{2}{r}\partial_r(\Phi) = 4\pi G\left(\frac{-\Phi}{(n+1)\kappa}\right)^n. \tag{4.94}$$

Now, define

$$z = Ar, \quad w = \frac{\Phi}{\Phi_c} = \left(\frac{\rho}{\rho_c}\right)^{\frac{1}{n}}, \quad A^2 = \frac{4\pi G \left(-\Phi_c\right)^{n-1}}{(n+1)^n \, \kappa^n} = \frac{4\pi G}{(n+1)\, \kappa} \left(\rho_c\right)^{\frac{n-1}{n}},$$

where Φ_c and ρ_c are the potential and the density at the center of the domain, respectively, so that the differential equation (4.94) becomes the *Lane-Emden equation* [84]

$$\frac{1}{z^2} \, \partial_z \left(z^2 \partial_z w\right) + w^n = 0. \tag{4.95}$$

We are only interested in solutions to the ordinary differential equation (4.95) that are finite at the center $z = 0$. Thus, we assume that $w(z,n)$ is a solution that fulfills the central boundary conditions $w(0,n) = 1$ and $\partial_z w(0,n) = 0$. Additionally, for $n = 0,1,5$, we have

$$w(z, n=0) = 1 - \frac{z^2}{6}, \quad w(z, n=1) = \frac{sin(z)}{z}, \quad w(z, n=5) = \frac{1}{\sqrt{1 + z^2/3}}. \tag{4.96}$$

Later on, we will validate the relaxation method with a polytropic gas $n = 1$. However, in order to reproduce this experiment, the numerical codes must be extended to the spherical finite volume formulation. For this, we propose to integrate system (4.91) over the space-time domain $\mathcal{C}_i \times (t^n, t^{n+1})$, with $\mathcal{C}_i = (r_{i-1/2}, r_{i+1/2}) \times (0, \pi) \times (0, 2\pi)$. Using the elementary volume expression $dv = r^2 \sin\theta \, dr \, d\theta \, d\varphi$, we integrate the time differential terms using a finite volume approach and get

$$\int_{\mathcal{C}_i} \int_{t^n}^{t^{n+1}} \partial_t(\rho) \, dt \, dv = |\mathcal{C}_i| \left(\rho_i^{n+1} - \rho_i^n\right),$$

$$\int_{\mathcal{C}_i} \int_{t^n}^{t^{n+1}} \partial_t(\rho u_r) \, dt \, dv = |\mathcal{C}_i| \left((\rho u_r)_i^{n+1} - (\rho u_r)_i^n\right),$$

where the cell's volume is $|\mathcal{C}_i| = 4\pi(r_{i+1/2}^3 - r_{i-1/2}^3)/3$. The integration of the divergence terms gives

$$\int_{\mathcal{C}_i} \int_{t^n}^{t^{n+1}} \frac{1}{r^2} \partial_r(r^2 \rho u_r) \, dt \, dv = 4\pi \int_{t^n}^{t^{n+1}} \int_{r_{i-\frac{1}{2}}}^{r_{i+\frac{1}{2}}} \partial_r(r^2 \rho u_r) \, dr \, dt$$

$$= 4\pi \Delta t \left(r_{i+\frac{1}{2}}^2 (\rho u_r)_{i+\frac{1}{2}}^l - r_{i-\frac{1}{2}}^2 (\rho u_r)_{i-\frac{1}{2}}^r\right),$$

and

$$\int_{\mathcal{C}_i} \int_{t^n}^{t^{n+1}} \frac{1}{r^2} \partial_r(r^2 \rho u_r^2) \, dt \, dv = 4\pi \Delta t \left(r_{i+\frac{1}{2}}^2 (\rho u_r^2)_{i+\frac{1}{2}}^l - r_{i-\frac{1}{2}}^2 (\rho u_r^2)_{i-\frac{1}{2}}^r\right),$$

with $(\cdot)_{i+1/2}^\alpha$, $\alpha \in \{l, r\}$, already defined for the relations (4.85). For the gradient terms, we note that $\rho \partial_r \Phi = 0$ on the integration domain so that we approximate the pressure differential integration as follows:

$$\int_{\mathcal{C}_i} \int_{t^n}^{t^{n+1}} (\partial_r(p) + \rho \partial_r(\Phi)) \, dt \, dv \approx 4\pi r_i^2 \int_{t^n}^{t^{n+1}} \int_{r_{i-\frac{1}{2}}}^{r_{i+\frac{1}{2}}} \partial_r(p) \, dr \, dt = 4\pi r_i^2 \Delta t \left((p)_{i+\frac{1}{2}}^l - (p)_{i-\frac{1}{2}}^r\right).$$

The numerical scheme associated with the first two equations of system (4.91) and the relaxation method is thus given by

$$
\begin{cases}
\dfrac{\rho_i^{n+1} - \rho_i^n}{\Delta t} + 3\,\dfrac{r_{i+1/2}^2(\rho u_r)_{i+1/2}^l - r_{i-1/2}^2(\rho u_r)_{i-1/2}^r}{r_{i+1/2}^3 - r_{i-1/2}^3} = 0, \\[2ex]
\dfrac{(\rho u_r)_i^{n+1} - (\rho u_r)_i^n}{\Delta t} + 3\,\dfrac{r_{i+1/2}^2(\rho u_r^2)_{i+1/2}^l - r_{i-1/2}^2(\rho u_r^2)_{i-1/2}^r}{r_{i+1/2}^3 - r_{i-1/2}^3} + 3\,\dfrac{r_i^2\left((p)_{i+1/2}^l - (p)_{i-1/2}^r\right)}{r_{i+1/2}^3 - r_{i-1/2}^3} = 0,
\end{cases}
\tag{4.97a}
$$

and for the Poisson equation, we propose an implicit scheme deduced from the integration over the volume $\mathcal{C}_i$, i.e.,

$$
\frac{3r_{i+1/2}^2}{\Delta r\left(r_{i+1/2}^3 - r_{i-1/2}^3\right)}\Phi_{i+1}^{n+1} - \frac{3\left(r_{i+1/2}^2 + r_{i-1/2}^2\right)}{\Delta r\left(r_{i+1/2}^3 - r_{i-1/2}^3\right)}\Phi_i^{n+1} + \frac{3r_{i-1/2}^2}{\Delta r\left(r_{i+1/2}^3 - r_{i-1/2}^3\right)}\Phi_{i-1}^{n+1} = 4\pi G\rho_i^n.
\tag{4.97b}
$$

In order to make numerical comparisons, the *standard method* in spherical coordinates is then introduced. The first step is devoted to the resolution of system (4.91) with $\partial_r\Phi = 0$ by making use of the relaxation scheme in the spherical formulation $(4.97a)_{\psi_l = \psi_r = 0}$. For the second step, we solve

$$
\begin{cases}
\partial_t(\rho) = 0, \\
\partial_t(\rho u_r) = -\rho\partial_r\Phi, \\
\frac{1}{r^2}\partial_r\left(r^2\partial_r\Phi\right) = 4\pi G\rho.
\end{cases}
\tag{4.98}
$$

As a numerical test, we consider a polytropic gas of index $n = 1$, with its initial state summarized in Table 4.4. The number of grid cells is set to 100 and the final time of the experiment to 1.0×10^7. Since the evolution of the potential is described by the Poisson equation in spherical symmetry, we choose to solve equation (4.97b) with Dirichlet boundary conditions on the one-dimensional domain by means of a standard LU method at each time step (since efficiency is not required at the present time).

Self-Gravitational Fluid at Hydrostatic Equilibrium - $n = 1$

ρ_c	$\rho_0(r)$	$u_{r0}(r)$	$p_0(r)$	Gravity potential
10.0	$\rho_e(r)$	0.0	$\kappa\left(\rho_e(r)\right)^2$	$\Phi_0(r) = -2\kappa\,\rho_e(r)$
Computational domain: $[0, L_r]$ with $L_r = 6.0 \times 10^5$; Fixed boundary conditions				
Solution to the *Lane-Emden equation*: $\rho_e(r) = \rho_c * \sin(z)/(z)$ with $z = A\,r = \sqrt{4\pi G/(2\kappa)}\,r$				

TABLE 4.4. Initial data for the self-gravitational fluid at hydrostatic equilibrium with the polytropic constant $\kappa = 1000$.

The numerical densities for both schemes, compared with the exact solution $\rho_e(r)$, at the final simulation time $t = 1.0 \times 10^7$ are displayed in Figure 4.9(a). Additionally, we observe the evolution of the parasitic currents during the simulation in Figure 4.9(b). This plot of the evolution in time of the L^2 norm of the velocity, in logarithmic scale,

(a) Density at time $t = 1.0 \times 10^7$ (b) L^2 norm of the velocity
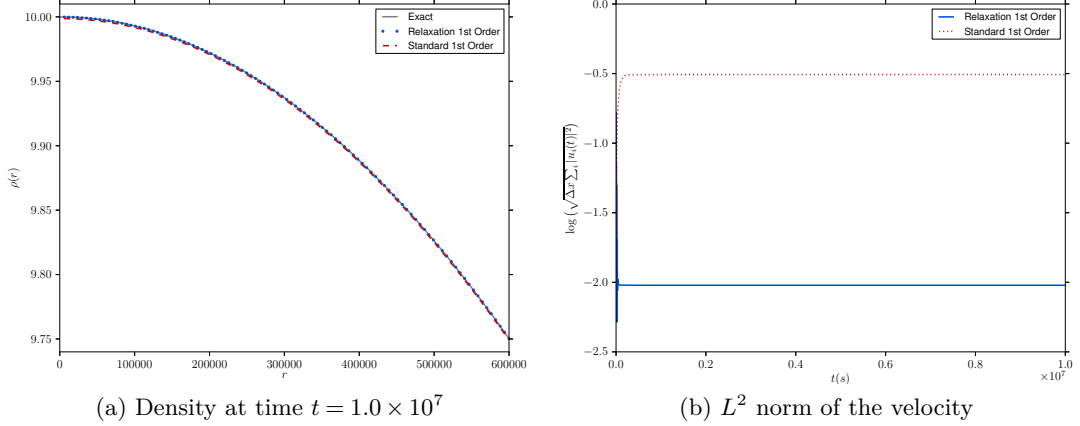
FIGURE 4.9. Comparison of relaxation and standard schemes for the self-gravitational fluid at equilibrium, using $N_r = 100$ cells and $a_0 = 1.05$. The approximate number of time steps for this simulation is 1.065×10^7 steps, for both methods.

shows that the residual velocity is far lower for the relaxation method than for the standard method. Thus, the relaxation scheme enables a good approximation of equilibrium solutions since it generates very low parasitic currents.

4.5 Conclusions

In this chapter, we have detailed the derivation of a one-dimensional relaxation model that ensures adequate coupling of the Poisson and Euler equations and yields an interesting scheme described in the limit as the penalty parameter c_h tends to zero. Although several asymptotically stable methods for the Euler-Poisson system in the quasineutral limit have already been developed [40, 46], they become far too complex in three dimensions or when an implicit formulation is required. We have presented here a simpler numerical scheme based on a Godunov-type solver deduced from a relaxation system to resolve accurately steady equilibrium flows.

Many problems of current interest require not only the preservation of equilibrium states but also robust numerical simulations. With different types of examples, we have established the scheme's robustness and demonstrated its ability to capture and preserve steady and perturbed quasi-steady states when required. Additionally, in view of astrophysical simulations, the last test case shows that the method is able to preserve the stationary regime of self-gravitational equilibrium flows. Future work will be devoted to a well-balanced time implicit formulation of the method and simulations of 3D self-gravitating astrophysical problems.

Finite Volumes in Toroidal Geometry

Introduction

Many problems possess obvious geometric symmetries in coordinate systems for Euclidean space in which several (if not all) coordinate lines and surfaces are curved. Thus, it results more convenient and sometimes simpler to describe them using the formalism of curvilinear coordinates rather than the Cartesian ones. In the context of plasma physics, numerous problems occur in a spatial domain that can be represented by a torus and one example of ongoing research concerns the study of plasma confinement in a tokamak, which is currently the most developed and researched candidate for controlled, thermonuclear fusion power production. Additionally, in the field of astrophysics, several problems are characterized by a central gravitational field, e.g., thin accretion disks [93, 94] or the evolution of protoplanetary nebula leading to the formation of planets around a young star [78].

From a mathematical point of view, even though space and time scales are clearly different, these types of problems can be described by systems of equations having a common structure. Hence, in order to obtain approximate solutions for these problems, similar numerical methods in curvilinear coordinates can be used, to some extent. In particular, the choice of an adequate approximation strategy depends heavily on the toroidal geometry and on the existence of an intense force field governing the physics of the problem. A toroidal geometry (see, for instance, Figure 5.1) is a three-dimensional domain defined as

$$\hat{\Omega}_{3d}^{\mathcal{T}} = \bigcup_{\phi=0}^{2\pi} \hat{\Omega}_{2d}(\phi), \tag{5.1}$$

where, for any toroidal angle ϕ, $\hat{\Omega}_{2d}(\phi)$ is a rotation of angle ϕ (around a given axis) of a fixed surface known as poloidal section; we denote the boundary of the domain $\hat{\Omega}_{3d}^{\mathcal{T}}$ by $\partial\hat{\Omega}_{3d}^{\mathcal{T}}$. In this framework, numerical methods need to take into account all geometrical effects and any strong anisotropy existing in the flows, which in turn are largely dominated by convective phenomena having a preferred direction.

(a) Torus   (b) Toroidal system of coordinates
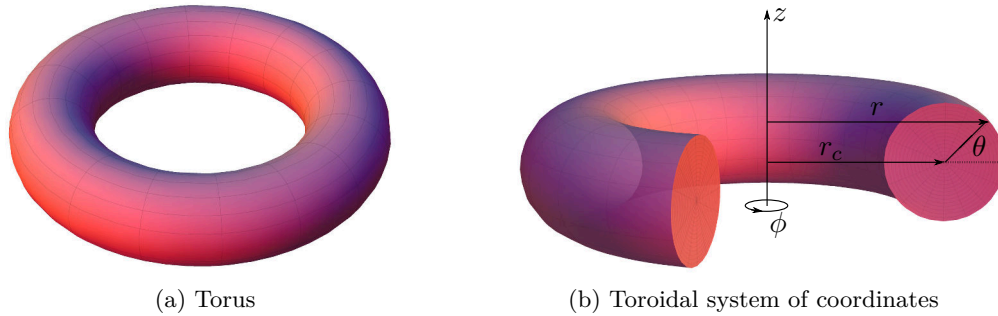
FIGURE 5.1. Example of a toroidal geometry.

The focus of this chapter is to describe a numerical tool that can be adapted to toroidal geometry based on finite volume methods for hyperbolic conservation laws in cylindrical coordinates, whose design is not as straightforward as in the Cartesian case since valuable conservation properties are sometimes lost when discretizing. Moreover, vectors in curvilinear coordinate systems are expressed in terms of bases that are spatially dependent and the projection of a vector onto a local basis introduces geometrical source terms (arising from the variations of this basis with respect to the coordinate variables) to the conservation equations. From a numerical point of view, the challenge then consists in finding a proper approximation of the geometrical terms such that all of the system's conservation properties are kept, avoiding the introduction of possible numerical errors that may affect stability and accuracy.

Bonnement et al.'s approach [22] consists in constructing the finite volume approximation for a hyperbolic system of conservation laws in general curvilinear coordinates without utilizing any preliminary projection when dealing with the vector equations, e.g., those that describe the evolution of the magnetic field in ideal MHD. All averaged quantities are chosen carefully in order to construct a scheme capable of capturing the principal characteristics of the physical models, and in this way, "automatically approximate the non-conservative terms in a consistent manner independently of the curvilinear system used" [22]. In this chapter, we examine their approach in cylindrical coordinates and apply it for the simulation of stable hydrodynamic flows in a three-dimensional rectangular torus. The chapter structure is the following: first, we present all necessary background information on curvilinear coordinates in the subsequent section; next, we describe the finite volume methods in these coordinates, paying particular attention to the geometrical terms; then, the developed strategy is validated through an application to a stationary, multi-dimensional test problem in Section 5.3; and finally, concluding remarks are given in the last section.

5.1   A Review of Curvilinear Coordinates

In order to use finite volume approximations in toroidal geometries, we first consider a system of conservation laws formulated in the Cartesian (or physical) domain $\Omega(\boldsymbol{x}) \subset \mathbb{R}^3$ and then describe it in a curvilinear computational domain $\hat{\Omega}(\boldsymbol{\xi}) \subset \mathbb{R}^3$. Curvilinear coor-

dinates may be derived from the usual Cartesian ones x_i by employing a transformation $\Upsilon : \boldsymbol{x} \to \boldsymbol{\xi}$ (that is locally invertible $\Upsilon^{-1} : \boldsymbol{\xi} \to \boldsymbol{x}$) at each point. For example, one has

$$\left.\begin{array}{l} x_1 = r\cos\phi \\ x_2 = r\sin\phi \\ x_3 = z \end{array}\right\} \quad \overset{\Upsilon}{\underset{\Upsilon^{-1}}{\rightleftarrows}} \quad \left\{\begin{array}{l} r = (x_1^2 + x_2^2)^{1/2} \\ \phi = \tan^{-1}\left(\frac{x_2}{x_1}\right) \\ z = x_3, \end{array}\right. \tag{5.2}$$

for the cylindrical coordinate system $\boldsymbol{\xi} = (r, \phi, z)$, as seen in Figure 5.2. Formally speaking, this one-to-one map Υ is assumed to be at least a $\mathcal{C}^1$-diffeomorphism, meaning that the determinant J of the Jacobian matrix

$$\mathscr{J}_\Upsilon = \begin{pmatrix} \frac{\partial x^1}{\partial z^1} & \frac{\partial x^1}{\partial z^2} & \cdots & \frac{\partial x^1}{\partial z^d} \\ \frac{\partial x^2}{\partial z^1} & \frac{\partial x^2}{\partial z^2} & \cdots & \frac{\partial x^2}{\partial z^d} \\ \vdots & \vdots & \ddots & \vdots \\ \frac{\partial x^d}{\partial z^1} & \frac{\partial x^d}{\partial z^2} & \cdots & \frac{\partial x^d}{\partial z^d} \end{pmatrix} \tag{5.3}$$

is positive [22].
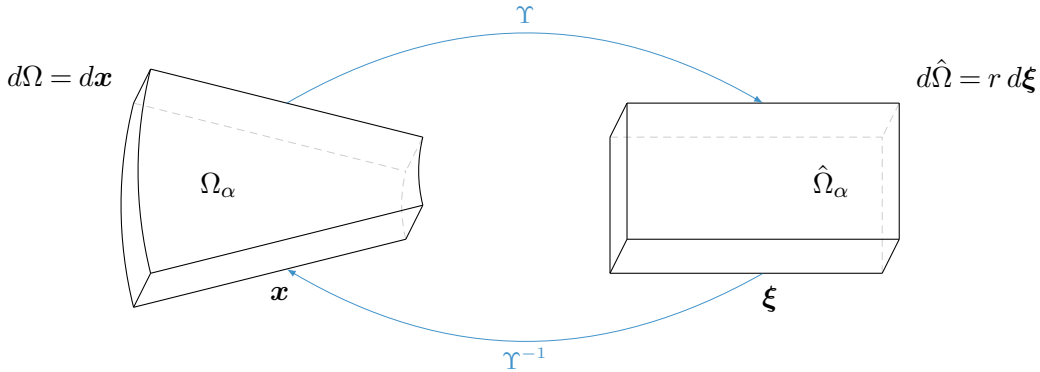
FIGURE 5.2. Transformation of an example control volume from the cylindrical coordinate system to the Cartesian one and back.

Employing the Einstein summation convention, any vector $\boldsymbol{v}$ in a d-dimensional space can be written as

$$\boldsymbol{v} = v_k \boldsymbol{e}^k = v^k \boldsymbol{e}_k, \tag{5.4}$$

where v_k (respectively, v^k) are the vector components with respect to the dual or contravariant basis $\boldsymbol{e}^k$ (respectively, covariant basis $\boldsymbol{e}_k$). These basis vectors have the property of being mutually dual, i.e.,

$$\boldsymbol{e}^k \cdot \boldsymbol{e}_j = \delta_j^k \tag{5.5}$$

with δ_j^k the Kronecker tensor having covariant index j and contravariant index k. Now, restricting ourselves to the three-dimensional case $d = 3$ and to cylindrical or spherical

coordinate systems with coordinates ξ^k ($k = 1, 2, 3$), most commonly used to define a torus, one can make the distinction between natural basis vectors

$$\boldsymbol{e}_k = \frac{\partial \boldsymbol{x}}{\partial \xi^k}, \quad \boldsymbol{x} = x^1 \mathbf{i} + x^2 \mathbf{j} + x^3 \mathbf{k}, \tag{5.6}$$

and the physical or normalized ones

$$\tilde{\boldsymbol{e}}_k = \frac{\boldsymbol{e}_k}{\|\boldsymbol{e}_k\|}, \tag{5.7}$$

which are orthogonal and orthonormal, respectively (being $\mathbf{i}$, $\mathbf{j}$ and $\mathbf{k}$ the standard basis vectors). For clarity of presentation, indices i will henceforth be associated to Cartesian elements, and for the curvilinear coordinate systems, we will use mostly j or k; thus,

$$\boldsymbol{e}_k = \frac{\partial x^i}{\partial \xi^k} \boldsymbol{e}_i \quad \text{and} \quad \boldsymbol{e}^k = \frac{\partial \xi^k}{\partial x^i} \boldsymbol{e}^i. \tag{5.8}$$

5.1.1   Vector and Tensor Calculus: Gradient and Divergence

Now, we go over the mathematical definitions of gradient and divergence in curvilinear coordinates. First, consider a scalar function s and its gradient given by

$$\nabla s = \frac{\partial s}{\partial \boldsymbol{x}} = \frac{\partial s}{\partial \xi^k} \boldsymbol{e}^k, \tag{5.9}$$

usually expressed in terms of physical basis vectors $\boldsymbol{e}^k$ (and not in terms of the normalized ones $\tilde{\boldsymbol{e}}^k$). Additionally, to compute the gradient of a vector or tensor, it is necessary to keep in mind that basis vectors in curvilinear coordinates are functions of position unlike in the Cartesian case and

$$\frac{\partial \boldsymbol{e}_m}{\partial \xi^l} = \frac{\partial^2 x^i}{\partial \xi^l \partial \xi^k} \boldsymbol{e}_i, \tag{5.10}$$

which in the dual space becomes

$$\Gamma^k_{ml} = \boldsymbol{e}^k \cdot \frac{\partial \boldsymbol{e}_m}{\partial \xi^l}, \tag{5.11}$$

where Γ^k_{ml} is a Christoffel symbol (of the second kind), also called a *coefficient of connection* [6]. Then, the gradient of the vector $\boldsymbol{v}(\boldsymbol{\xi})$ is defined in the following way:

$$\nabla \boldsymbol{v} = \frac{\partial \left(v^j \boldsymbol{e}_j \right)}{\partial \boldsymbol{x}} = \left(\frac{\partial v^j}{\partial \xi^l} + v^m \Gamma^j_{ml} \right) \boldsymbol{e}_j \otimes \boldsymbol{e}^l; \tag{5.12}$$

that of a tensor $\boldsymbol{T}$ as

$$\nabla \boldsymbol{T} = \frac{\partial \left(T^{jk} \boldsymbol{e}_j \otimes \boldsymbol{e}_k \right)}{\partial \boldsymbol{x}} = \left(\frac{\partial T^{jk}}{\partial \xi^l} + T^{mk} \Gamma^j_{ml} + T^{jm} \Gamma^k_{ml} \right) \boldsymbol{e}_j \otimes \boldsymbol{e}_k \otimes \boldsymbol{e}^l. \tag{5.13}$$

Essentially, the divergence of a vector $\boldsymbol{v}(\boldsymbol{\xi})$ or tensor $\boldsymbol{T}$ is obtained by contraction of the associated gradient expression such that

$$\nabla \cdot \boldsymbol{v} = \frac{\partial v^k}{\partial \xi^k} + v^k \Gamma^j_{kj}, \quad \nabla \cdot \boldsymbol{T} = \left(\frac{\partial T^{jk}}{\partial \xi^k} + T^{mk} \Gamma^j_{mk} + T^{jm} \Gamma^k_{mk} \right) \boldsymbol{e}_j, \tag{5.14}$$

and by using the identity $\Gamma^j_{kj} = 1/J \, \partial_{\xi^k}(J)$, one gets the two compact relations

$$\nabla \cdot \boldsymbol{v} = \frac{1}{J} \frac{\partial (J\boldsymbol{v} \cdot \boldsymbol{e}^k)}{\partial \xi^k}, \tag{5.15a}$$

$$\nabla \cdot \boldsymbol{T} = \frac{1}{J} \frac{\partial (J\boldsymbol{T} \cdot \boldsymbol{e}^k)}{\partial \xi^k}. \tag{5.15b}$$

5.1.2 Cylindrical Coordinate System

The cylindrical coordinate system can be seen as an extruded three-dimensional version of the known 2D polar coordinate system. The link between the coordinates $\boldsymbol{\xi} = (r, \phi, z)$, with $\boldsymbol{\xi} \in (0, \infty) \times [0, 2\pi) \times (-\infty, \infty)$, and the Cartesian ones is given in (5.2); the determinant of the associated transformation Υ is $J = r$. Covariant basis vectors (5.6) are defined as

$$\boldsymbol{e}_r = \begin{pmatrix} \cos\phi \\ \sin\phi \\ 0 \end{pmatrix}, \quad \boldsymbol{e}_\phi = \begin{pmatrix} -r\sin\phi \\ r\cos\phi \\ 0 \end{pmatrix}, \quad \boldsymbol{e}_z = \begin{pmatrix} 0 \\ 0 \\ 1 \end{pmatrix}, \tag{5.16}$$

and the contravariant ones as $\boldsymbol{e}^r = \boldsymbol{e}_r$, $\boldsymbol{e}^\phi = (-\sin\phi/r, \cos\phi/r, 0)^T$, $\boldsymbol{e}^z = \boldsymbol{e}_z$. Furthermore, the corresponding normalized bases

$$\tilde{\boldsymbol{e}}_r = \boldsymbol{e}_r, \quad \tilde{\boldsymbol{e}}_\phi = \tfrac{1}{r}\boldsymbol{e}_\phi, \quad \tilde{\boldsymbol{e}}_z = \boldsymbol{e}_z, \tag{5.17}$$

constitute the change-of-variable matrix $\boldsymbol{O}_\phi = (\tilde{\boldsymbol{e}}_r \;\; \tilde{\boldsymbol{e}}_\phi \;\; \tilde{\boldsymbol{e}}_z)$, which in turn satisfies the property $\boldsymbol{O}_\phi \boldsymbol{O}_\phi^T = \boldsymbol{I}$. In expanded form, this matrix is

$$\boldsymbol{O}_\phi = \begin{pmatrix} \cos\phi & -\sin\phi & 0 \\ \sin\phi & \cos\phi & 0 \\ 0 & 0 & 1 \end{pmatrix}, \tag{5.18}$$

equally expressed in terms of

$$\tilde{\boldsymbol{e}}^r = \boldsymbol{e}^r, \quad \tilde{\boldsymbol{e}}^\phi = r\boldsymbol{e}^\phi, \quad \tilde{\boldsymbol{e}}^z = \boldsymbol{e}^z. \tag{5.19}$$

Equipped with the above notations, we can write down the formulations of the gradient and divergence operators in cylindrical coordinates. For a scalar s, equation (5.9) leads to

$$\nabla s = \frac{\partial s}{\partial r}\boldsymbol{e}_r + \frac{\partial s}{\partial \phi}\boldsymbol{e}_\phi + \frac{\partial s}{\partial z}\boldsymbol{e}_z = \frac{\partial s}{\partial r}\tilde{\boldsymbol{e}}_r + \frac{1}{r}\frac{\partial s}{\partial \phi}\tilde{\boldsymbol{e}}_\phi + \frac{\partial s}{\partial z}\tilde{\boldsymbol{e}}_z. \tag{5.20}$$

Any vector $\boldsymbol{v}$ in Cartesian coordinates can be defined as a function of the covariant bases in the cylindrical coordinate system, namely

$$
\begin{aligned}
\boldsymbol{v}(\boldsymbol{x}) &= v^x\,\mathbf{i} \;+ v^y\,\mathbf{j} \;+ v^z\,\mathbf{k}, \\
\boldsymbol{v}(\boldsymbol{\xi}) &= v^r\,\boldsymbol{e}_r + v^\phi\,\boldsymbol{e}_\phi + v^z\,\boldsymbol{e}_z = \tilde{v}^r\,\tilde{\boldsymbol{e}}_r + \tilde{v}^\phi\,\tilde{\boldsymbol{e}}_\phi + \tilde{v}^z\,\tilde{\boldsymbol{e}}_z,
\end{aligned}
\tag{5.21}
$$

where $\tilde{v}^r\,\tilde{\boldsymbol{e}}_r + \tilde{v}^\phi\,\tilde{\boldsymbol{e}}_\phi + \tilde{v}^z\,\tilde{\boldsymbol{e}}_z = \boldsymbol{O}_\phi\,(v^r,\,r\,v^\phi,\,v^z)^T$. Equation (5.15a) then yields

$$
\nabla\cdot\boldsymbol{v}(\boldsymbol{\xi}) = \frac{1}{r}\left(\frac{\partial(r\,v^r)}{\partial r} + \frac{\partial(r\,v^\phi)}{\partial\phi} + \frac{\partial(r\,v^z)}{\partial z}\right) = \frac{1}{r}\left(\frac{\partial(r\,\tilde{v}^r)}{\partial r} + \frac{\partial(\tilde{v}^\phi)}{\partial\phi} + \frac{\partial(r\,\tilde{v}^z)}{\partial z}\right).
\tag{5.22}
$$

Finally, for the tensor $\boldsymbol{T}(\boldsymbol{\xi})$ decomposed as

$$
\begin{aligned}
\boldsymbol{T}(\boldsymbol{\xi}) =\ & \tilde{T}^{rr}\tilde{\boldsymbol{e}}_r\otimes\tilde{\boldsymbol{e}}_r + \tilde{T}^{r\phi}\tilde{\boldsymbol{e}}_r\otimes\tilde{\boldsymbol{e}}_\phi + \tilde{T}^{rz}\tilde{\boldsymbol{e}}_r\otimes\tilde{\boldsymbol{e}}_z + \tilde{T}^{\phi r}\tilde{\boldsymbol{e}}_\phi\otimes\tilde{\boldsymbol{e}}_r \\
& + \tilde{T}^{\phi\phi}\tilde{\boldsymbol{e}}_\phi\otimes\tilde{\boldsymbol{e}}_\phi + \tilde{T}^{\phi z}\tilde{\boldsymbol{e}}_\phi\otimes\tilde{\boldsymbol{e}}_z + \tilde{T}^{zr}\tilde{\boldsymbol{e}}_z\otimes\tilde{\boldsymbol{e}}_r + \tilde{T}^{z\phi}\tilde{\boldsymbol{e}}_z\otimes\tilde{\boldsymbol{e}}_\phi + \tilde{T}^{zz}\tilde{\boldsymbol{e}}_z\otimes\tilde{\boldsymbol{e}}_z,
\end{aligned}
\tag{5.23}
$$

its divergence (see equation (5.15b)) reads

$$
\nabla\cdot\boldsymbol{T}(\boldsymbol{\xi}) = \frac{1}{r}\left(\frac{\partial(r\,\boldsymbol{T}\cdot\boldsymbol{e}^r)}{\partial r} + \frac{\partial(r\,\boldsymbol{T}\cdot\boldsymbol{e}^\phi)}{\partial\phi} + \frac{\partial(r\,\boldsymbol{T}\cdot\boldsymbol{e}^z)}{\partial z}\right).
\tag{5.24}
$$

By substituting $\boldsymbol{e}^r, \boldsymbol{e}^\phi, \boldsymbol{e}^z$ from (5.19) into (5.24) and expanding the result, one is able to determine the following expression:

$$
\begin{aligned}
\nabla\cdot\boldsymbol{T}(\boldsymbol{\xi}) =\ & \tfrac{1}{r}\partial_r(r\,\tilde{T}^{rr}\tilde{\boldsymbol{e}}_r + r\,\tilde{T}^{r\phi}\tilde{\boldsymbol{e}}_\phi + r\,\tilde{T}^{rz}\tilde{\boldsymbol{e}}_z) \\
& + \tfrac{1}{r}\partial_\phi(\tilde{T}^{\phi r}\tilde{\boldsymbol{e}}_r + \tilde{T}^{\phi\phi}\tilde{\boldsymbol{e}}_\phi + \tilde{T}^{\phi z}\tilde{\boldsymbol{e}}_z) + \tfrac{1}{r}\partial_z(r\,\tilde{T}^{zr} + r\,\tilde{T}^{z\phi} + r\,\tilde{T}^{zz}),
\end{aligned}
\tag{5.25}
$$

which in the physical or normalized basis comes to be

$$
\tilde{\boldsymbol{e}}^r\cdot(\nabla\cdot\boldsymbol{T}(\boldsymbol{\xi})) = \tfrac{1}{r}[\,\partial_r(r\,\tilde{T}^{rr}) + \partial_\phi(\tilde{T}^{\phi r}) + \partial_z(r\,\tilde{T}^{zr}) - \tilde{T}^{\phi\phi}\,],
\tag{5.26a}
$$

$$
\tilde{\boldsymbol{e}}^\phi\cdot(\nabla\cdot\boldsymbol{T}(\boldsymbol{\xi})) = \tfrac{1}{r}[\,\partial_r(r\,\tilde{T}^{r\phi}) + \partial_\phi(\tilde{T}^{\phi\phi}) + \partial_z(r\,\tilde{T}^{z\phi}) + \tilde{T}^{\phi r}\,],
\tag{5.26b}
$$

$$
\tilde{\boldsymbol{e}}^z\cdot(\nabla\cdot\boldsymbol{T}(\boldsymbol{\xi})) = \tfrac{1}{r}[\,\partial_r(r\,\tilde{T}^{rz}) + \partial_\phi(\tilde{T}^{\phi z}) + \partial_z(r\,\tilde{T}^{zz})\,],
\tag{5.26c}
$$

after having considered $\partial_\phi\tilde{\boldsymbol{e}}^r = \tilde{\boldsymbol{e}}^\phi$ and $\partial_\phi\tilde{\boldsymbol{e}}^\phi = -\tilde{\boldsymbol{e}}^r$.

5.2 Finite Volume Schemes in Cylindrical Coordinates

This section deals with the design of a finite volume approximation for hyperbolic conservation laws in cylindrical coordinates, following the pattern of mathematical developments given in Bonnement et al.'s paper [22, p. 165-170], but with some changes in the presentation style and the addition of a subsection on control volumes and outward normals. Thus, let us start by considering the general system of conservation laws (1.1b), which we rewrite here for convenience:

$$
\partial_t\boldsymbol{w} + \nabla\cdot\boldsymbol{\mathcal{F}}(\boldsymbol{w}) = 0, \quad \text{in } \Omega(\boldsymbol{x})\times(0,T).
\tag{5.27}
$$

Recalling the transformation $\Upsilon : \boldsymbol{x} \to \boldsymbol{\xi}$ (5.2) with Jacobian determinant $\det \mathcal{J}_\Upsilon = J = r$, the above expression becomes

$$\frac{\partial \boldsymbol{w}}{\partial t} + \frac{1}{r} \frac{\partial (r \, \boldsymbol{\mathcal{F}}(\boldsymbol{w}) \cdot \boldsymbol{e}^k)}{\partial \xi^k} = 0, \quad \text{in } \hat{\Omega}(\boldsymbol{\xi}) \times (0, T), \tag{5.28}$$

having used equality (5.15). To proceed with the construction of the finite volume method, it is helpful to study separately the scalar and vector-valued cases for the state variable $\boldsymbol{w}$, for which the flux $\boldsymbol{\mathcal{F}}$ is respectively a vector and tensor. However, before diving into details concerning these cases, we must specify the subdivisions of the computational domain $\hat{\Omega}(\boldsymbol{\xi})$ and the associated elements.

5.2.1 Control Volumes and Outward Normals

The design of the finite volume method (first-order accurate) can be achieved by properly defining the control volumes and their normals. We choose to decompose the computational domain $\hat{\Omega}(\boldsymbol{\xi})$ into N non-overlapping subdomains, i.e.,

$$\hat{\Omega}(\boldsymbol{\xi}) = \bigcup_{\alpha=1}^{N} \hat{\Omega}_\alpha(\boldsymbol{\xi}), \quad \hat{\Omega}_\mu \cap \hat{\Omega}_\nu = \emptyset \quad \text{for } \mu \neq \nu, \quad \mu, \nu = 1, \dots, N, \tag{5.29}$$

being $\hat{\Omega}_\alpha$ a cell with volume $|\hat{\Omega}_\alpha|$ and $\hat{\boldsymbol{n}} = (n_r, n_\phi, n_z)$ the outward pointing unit normal field of its boundary $\partial \hat{\Omega}_\alpha$.

5.2.1.1 Structured Meshes

To find a numerical approximation in a structured mesh, we break the spatial domain into grid cells with centers indexed as i, j, k, where i, j and k refer to the r-, ϕ- and z-coordinate directions, respectively. Notice that these symbols play multiple roles in different contexts and we urge the reader to take particular care so as to avoid any confusion. Moreover, $\Delta r = 1/N_r$, $\Delta \phi = 1/N_\phi$ and $\Delta z = 1/N_z$ are the grid spacings such that $r_i = (i-1)\Delta r$, $\phi_j = (j-1)\Delta \phi$ and $z_k = (k-1)\Delta z$, with $i = 1, \dots, N_r$, $j = 1, \dots, N_\phi$ and $k = 1, \dots, N_z$; as in other chapters, the corresponding cell interfaces are denoted by half integers. We can therefore write the domain decomposition as

$$\hat{\Omega}(\boldsymbol{\xi}) = \bigcup_{\alpha=1}^{N} \hat{\Omega}_\alpha(\boldsymbol{\xi}) = \bigcup_{i,j,k} \hat{\Omega}_{i,j,k}(\boldsymbol{\xi}), \quad N = N_r \times N_\phi \times N_z. \tag{5.30}$$

5.2.1.2 Toroidal Cells

One might choose to decompose the toroidal geometry $\hat{\Omega}_{3d}^{\mathcal{T}}$ in the sense of (5.29) by simply setting $N = N_\phi$ in (5.1) and defining

$$\hat{\Omega}_\alpha(\boldsymbol{\xi}) = \bigcup_{\phi_j}^{\phi_{j+1}} \hat{\Omega}_{2d,j}(\phi), \tag{5.31}$$

where the poloidal section $\hat{\Omega}_{2d,j}$ (see, for instance, Figure 5.3) has a boundary of the form $\partial \hat{\Omega}_{2d,j} = \hat{\Omega}_{2d}(\phi_j) + [\phi_j, \phi_{j+1}] \times \partial \hat{\Omega}_{2d} + \hat{\Omega}_{2d}(\phi_{j+1})$.
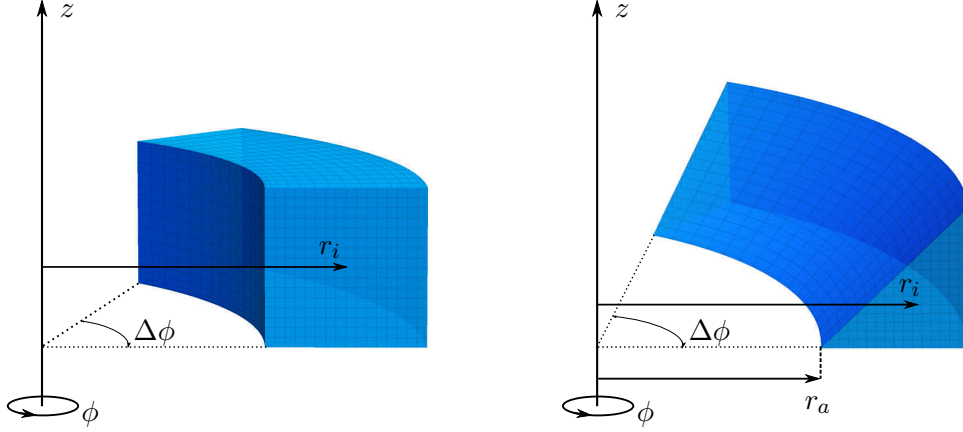
FIGURE 5.3. Control volumes generated by revolving rectangular (left) and triangular (right) sections in a three-dimensional space about the z-axis.

For a control volume $\hat{\Omega}_{2d,j}$, the quantity $|\hat{\Omega}_{2d,j}|$ is directly related to the evaluation of the divergence over the cell and can be found as follows:

$$|\hat{\Omega}_{2d,j}| = \int_{\hat{\Omega}_{2d,j}} \frac{\nabla \cdot \boldsymbol{x}}{3} \, d\boldsymbol{x} = \int_{\phi_j}^{\phi_{j+1}} \int_{\hat{\Omega}_{2d}} \frac{\nabla \cdot \boldsymbol{x}}{3} \, r \, d\boldsymbol{\xi}. \qquad (5.32)$$

By using relation (5.22), we are able to obtain

$$\frac{3\,|\hat{\Omega}_{2d,j}|}{\phi_{j+1} - \phi_j} = \int_{\hat{\Omega}_{2d}} \Big(\partial_r(r^2) + \partial_z(rz)\Big) \, dr \, dz = \int_{\partial\hat{\Omega}_{2d}} \Big(r^2\, n_r + rz\, n_z\Big) \, d\mathcal{S}, \qquad (5.33)$$

being n_r and n_z components of the unit normal vector $\hat{\boldsymbol{n}}$. Now, considering a boundary $\partial\hat{\Omega}_{2d}$ composed only of straight edges $e \in \partial\hat{\Omega}_{2d}$ with unit normal vectors denoted by $\hat{\boldsymbol{n}}_e = (n_{er}, n_{e\phi}, n_{ez})^T$, we write

$$\int_{\partial\hat{\Omega}_{2d}} \Big(r^2\, n_r + rz\, n_z\Big) \, d\mathcal{S} = \sum_{e \in \partial\hat{\Omega}_{2d}} \int_e \Big(r^2\, n_{er} + rz\, n_{ez}\Big) \, d\mathcal{S}_e. \qquad (5.34)$$

Since the edges are assumed to be straight lines of definite length $|e|$, both r and z can be defined in terms of l (the normalized coordinate aligned with e), such that

$$r(l) = (1-l)\, r_{e,a} + l\, r_{e,b}, \quad z(l) = (1-l)\, z_{e,a} + l\, z_{e,b}, \qquad (5.35)$$

and with $\Delta\phi_j = \phi_{j+1} - \phi_j$, equation (5.33) can be rewritten as

$$\frac{3\,|\hat{\Omega}_{2d,j}|}{\Delta\phi_j} = \sum_{e \in \partial\hat{\Omega}_{2d}} |e| \left(n_{er} \int_0^1 r(l)^2 \, dl + n_{ez} \int_0^1 r(l)z(l) \, dl \right). \qquad (5.36)$$

Then, the result derived above is algebraically manipulated to determine the expression

$$|\hat{\Omega}_{2d,j}| = \tfrac{1}{3} \Delta\phi_j \sum_{e \in \partial\hat{\Omega}_{2d}} n_{er} |e| \left[r_{e,a} r_{e,b} + \tfrac{1}{3}(r_{e,a} - r_{e,b})^2 \right] \tag{5.37}$$

$$+ \tfrac{1}{3} \Delta\phi_j \sum_{e \in \partial\hat{\Omega}_{2d}} n_{ez} |e| \left[\tfrac{1}{2}(r_{e,a} z_{e,b} + z_{e,a} r_{e,b}) + \tfrac{1}{3}(r_{e,a} - r_{e,b})(z_{e,a} - z_{e,b}) \right],$$

whose interest is most obvious for general control volumes in unstructured meshes.

Examples $\hat{\Omega}_\alpha$

To exemplify the usage of the previous formulation, let us consider both toroidal cells $\hat{\Omega}_\alpha$ (5.31) displayed in Figure 5.3. If the poloidal section is a rectangle of size $\Delta r \times \Delta z$, by employing equation (5.37) one gets

$$|\hat{\Omega}_{2d,j}| = r_i \Delta\phi_j \Delta r \Delta z, \tag{5.38}$$

for which it was necessary to work with the definitions of the unit normals related to the square's four edges, specifically $(1,0,0)^T$, $(0,0,1)^T$, $(-1,0,0)^T$ and $(0,0,-1)^T$. In the right-hand side of (5.38), r_i is the radius of the poloidal section's centroid.

With regard to the triangle with two sides of length L, we assume the following unit normal vectors for the edges: $(1,0,0)^T$, $1/\sqrt{2}(-1,0,1)^T$ and $(0,0,-1)^T$. Hence,

$$\begin{aligned} |\hat{\Omega}_{2d,j}| &= \tfrac{1}{3}\Delta\phi_j \left[L\,(r_a + L)^2 - \tfrac{1}{3}L\left(3r_a\,(r_a + L) + L^2\right) + \tfrac{1}{6}L\left(3r_a L + 2L^2\right) \right] \\ &= \tfrac{1}{2}\Delta\phi_j\, L^2 \left(r_a + \tfrac{2}{3}L \right), \end{aligned} \tag{5.39}$$

which is a result that can be verified using Pappus-Guildinus theorem. For this, the *elemental volume* is $V_j = 1/2\, r_i \Delta\phi_j\, L^2$, being $L^2/2$ the area of the triangular section; in this context, the radius to its centroid is $r_i = r_a + 2/3L$ and consequently, $V_j = |\hat{\Omega}_{2d,j}|$.

For these examples, the geometries and the corresponding outward normal vectors were designed to make the estimation of the volumes simple and straightforward. However, in the general case, one needs to properly determine all variables $\hat{\boldsymbol{n}}_e$ for a given subdomain $\hat{\Omega}_{2d,j}$ such that the equality

$$0 = \int_{\hat{\Omega}_{2d,j}} \nabla \cdot \mathbf{1}\, d\boldsymbol{x} = \int_{\phi_j}^{\phi_{j+1}} \int_{\hat{\Omega}_{2d}} \nabla \cdot \mathbf{1}\; r\, d\boldsymbol{\xi}, \tag{5.40}$$

is satisfied. Performing steps similar to the ones used at the beginning of the subsection 5.2.1.2, we have

$$0 = \int_{\phi_j}^{\phi_{j+1}} \int_{\partial\hat{\Omega}_{2d,j}} \left((\cos\phi + \sin\phi)\, n_r + n_z \right) r\, dl\, d\phi \tag{5.41}$$

$$+ |\hat{\Omega}_{2d}| \left((\cos\phi_{j+1} - \sin\phi_{j+1})\, n_{\phi_{j+1}} + (\cos\phi_j - \sin\phi_j)\, n_{\phi_j} \right),$$

recalling that $\partial\hat{\Omega}_{2d,j} = \hat{\Omega}_{2d}(\phi_j) + [\phi_j, \phi_{j+1}] \times \partial\hat{\Omega}_{2d} + \hat{\Omega}_{2d}(\phi_{j+1})$. The terms $n_{\phi_{j+1}}$ and n_{ϕ_j} refer to the second components of the outward unit normal vectors to $\hat{\Omega}_{2d}(\phi_{j+1})$ and

$\hat{\Omega}_{2d}(\phi_j)$, respectively. Note that the previous expression can be simplified to produce

$$0 = \sum_{e \in \partial \hat{\Omega}_{2d,j}} \tfrac{1}{2} |e| (r_{e,a} + r_{e,b}) \left[\Big((\sin \phi_{j+1} - \sin \phi_j) - (\cos \phi_{j+1} - \cos \phi_j) \Big) n_{er} + \Delta \phi_j \, n_{ez} \right]$$
$$+ |\hat{\Omega}_{2d}| \left[(\cos \phi_{j+1} - \sin \phi_{j+1}) \, n_{\phi_{j+1}} + (\cos \phi_j - \sin \phi_j) \, n_{\phi_j} \right]. \tag{5.42}$$

5.2.2 Scalar Equation

Taking $\boldsymbol{w} = s$ a scalar and $\boldsymbol{\mathcal{F}}(\boldsymbol{w}) = \boldsymbol{v}$ a vector, equation (5.28) turns into

$$\boxed{\frac{\partial s}{\partial t} + \frac{1}{r} \frac{\partial (r \, \boldsymbol{v} \cdot \boldsymbol{e}^k)}{\partial \xi^k} = 0, \quad \text{in } \hat{\Omega}(\boldsymbol{\xi}) \times (0, T),} \tag{5.43}$$

and integrating it over a control volume $\hat{\Omega}_\alpha$, gives

$$\frac{1}{|\hat{\Omega}_\alpha|} \int_{\hat{\Omega}_\alpha} \frac{\partial s}{\partial t} \, d\hat{\Omega} + \frac{1}{|\hat{\Omega}_\alpha|} \int_{\hat{\Omega}_\alpha} \frac{1}{r} \frac{\partial (r \, \boldsymbol{v} \cdot \boldsymbol{e}^k)}{\partial \xi^k} \, d\hat{\Omega} = 0, \tag{5.44}$$

after having divided the result by the cell's volume. Now, let us introduce the average value of the scalar variable over this cell and denote it by s_α, i.e.,

$$s_\alpha = \frac{1}{|\hat{\Omega}_\alpha|} \int_{\hat{\Omega}_\alpha} rs \, d\boldsymbol{\xi}, \tag{5.45}$$

recalling that $d\hat{\Omega} = r \, d\boldsymbol{\xi}$. Since $\hat{\Omega}_\alpha$ is fixed in time, it is then possible to rewrite (5.44) as

$$\frac{\partial s_\alpha}{\partial t} + \frac{1}{|\hat{\Omega}_\alpha|} \int_{\hat{\Omega}_\alpha} \frac{\partial (r \, \boldsymbol{v} \cdot \boldsymbol{e}^k)}{\partial \xi^k} \, d\boldsymbol{\xi} = 0, \tag{5.46}$$

which is equivalent to

$$\frac{\partial s_\alpha}{\partial t} + \frac{1}{|\hat{\Omega}_\alpha|} \int_{\partial \hat{\Omega}_\alpha} \Big(rv^k (\boldsymbol{e}_k \cdot \hat{\boldsymbol{n}}) \Big) \, d\hat{\sigma}(\boldsymbol{\xi}) = 0, \tag{5.47}$$

by application of the divergence theorem, with $d\hat{\sigma}(\boldsymbol{\xi})$ the Lebesgue measure on the surface $\partial \hat{\Omega}_\alpha$. If we assume the boundary $\partial \hat{\Omega}_\alpha$ to be defined only by straight edges $e \in \partial \hat{\Omega}_\alpha$ with their corresponding outward pointing unit normal vectors $\hat{\boldsymbol{n}}_e$, equation (5.47) becomes

$$\frac{\partial s_\alpha}{\partial t} + \frac{1}{|\hat{\Omega}_\alpha|} \sum_{e \in \partial \hat{\Omega}_\alpha} \int_e \Big(rv^k (\boldsymbol{e}_k \cdot \hat{\boldsymbol{n}}_e) \Big) \, d\hat{\sigma}_e(\boldsymbol{\xi}) = 0, \tag{5.48}$$

where the summation part is estimated from knowledge of numerical fluxes [64, 90, 129].

For the purpose of exemplification, consider first the term $\int_e (\cdot) \, d\hat{\sigma}_e(\boldsymbol{\xi})$ of the above relation in cylindrical coordinates (refer to equation (5.22)) such that

$$\int_e rv^k n_{ek} \, d\hat{\sigma}_e(\boldsymbol{\xi}) = \int_e \Big(r\tilde{v}^r \, n_{er} + \tilde{v}^\phi \, n_{e\phi} + r\tilde{v}^z \, n_{ez} \Big) \, d\hat{\sigma}_e(\boldsymbol{\xi}), \tag{5.49}$$

and then set $s = \rho$ and $\boldsymbol{v} = \rho\boldsymbol{u} = \rho\tilde{u}^r\,\tilde{\boldsymbol{e}}_r + \rho\tilde{u}^\phi\,\tilde{\boldsymbol{e}}_\phi + \rho\tilde{u}^z\,\tilde{\boldsymbol{e}}_z$ in (5.48, 5.49), yielding

$$\frac{\partial\rho_\alpha}{\partial t} + \frac{1}{|\hat{\Omega}_\alpha|}\sum_{e\in\partial\hat{\Omega}_\alpha}\int_e \left(r\rho\tilde{u}^r\,n_{er} + \rho\tilde{u}^\phi\,n_{e\phi} + r\rho\tilde{u}^z\,n_{ez}\right)d\hat{\sigma}_e(\boldsymbol{\xi}) = 0, \qquad (5.50)$$

i.e., the equation of conservation of mass in cylindrical coordinates. Using the notation of Section 5.2.1.1, the discretization of this equation on a structured mesh is

$$\rho_{i,j,k}^{n+1} = \rho_{i,j,k}^n - \frac{1}{r_i}\frac{\Delta t}{\Delta r}\left[r_{i+\frac{1}{2}}(\rho\tilde{u}^r)_{i+\frac{1}{2},j,k} - r_{i-\frac{1}{2}}(\rho\tilde{u}^r)_{i-\frac{1}{2},j,k}\right]$$
$$- \frac{1}{r_i}\frac{\Delta t}{\Delta\phi}\left[(\rho\tilde{u}^\phi)_{i,j+\frac{1}{2},k} - (\rho\tilde{u}^\phi)_{i,j-\frac{1}{2},k}\right] - \frac{\Delta t}{\Delta z}\left[(\rho\tilde{u}^z)_{i,j,k+\frac{1}{2}} - (\rho\tilde{u}^z)_{i,j,k-\frac{1}{2}}\right],$$
$$(5.51)$$

since $|\hat{\Omega}_{i,j,k}| = r_i\Delta r\Delta\phi\Delta z$. We wish to add that a similar expression can be found for the conservation of the energy density in the context of the Euler equations (1.20) for inviscid compressible gas flows.

5.2.3 Vector Equation: Two Approaches for Discretization

Let us now turn our attention to the case where $\boldsymbol{w} = \boldsymbol{v}$ is a vector and $\boldsymbol{\mathcal{F}}(\boldsymbol{w}) = \boldsymbol{T}$ a tensor, so that equation (5.28) can be rewritten as

$$\boxed{\frac{\partial\boldsymbol{v}}{\partial t} + \frac{1}{r}\frac{\partial(r\boldsymbol{T}\cdot\boldsymbol{e}^k)}{\partial\xi^k} = 0, \quad \text{in } \hat{\Omega}(\boldsymbol{\xi})\times(0,T).} \qquad (5.52)$$

By integrating (5.52) over $\hat{\Omega}_\alpha$ and dividing the result by $|\hat{\Omega}_\alpha|$, as was done in Section 5.2.2 (**Scalar Equation**), one gets

$$\frac{1}{|\hat{\Omega}_\alpha|}\int_{\hat{\Omega}_\alpha}\frac{\partial\boldsymbol{v}}{\partial t}\,d\hat{\Omega} + \frac{1}{|\hat{\Omega}_\alpha|}\int_{\hat{\Omega}_\alpha}\frac{1}{r}\frac{\partial(r\boldsymbol{T}\cdot\boldsymbol{e}^k)}{\partial\xi^k}\,d\hat{\Omega} = 0. \qquad (5.53)$$

Given that $\boldsymbol{v}$ is a vector, equation (5.53) needs to be expressed component-by-component in a given basis; thus, the methodology used to obtain the final discretization is not straightforward as in the scalar case. In the following, we will present two methods for this purpose and the associated equivalence relation between them.

Method I: *Projection→Integration*

This classic approach consists in taking the scalar product between equation (5.52) and the normalized covariant basis $\tilde{\boldsymbol{e}}_k$ (respectively, normalized contravariant basis $\tilde{\boldsymbol{e}}^k$) to obtain a scalar equation for the contravariant component $\tilde{v}^k$ (respectively, covariant component $\tilde{v}_k$) of $\boldsymbol{v}$. Then, the resulting equation gets discretized using the approach of Section 5.2.2; hereafter, this method will be referred to as *projection→integration*.

It can be easily verified that the projection of equation (5.52) onto $\tilde{\boldsymbol{e}}^k$ is simply

$$\frac{\partial(\tilde{v}^k)}{\partial t} + \tilde{\boldsymbol{e}}^k\cdot\left[\frac{1}{r}\frac{\partial(r\boldsymbol{T}\cdot\boldsymbol{e}^k)}{\partial\xi^k}\right] = 0, \qquad (5.54)$$

and by employing definition (5.26), one is able to expand it in cylindrical coordinates in order to obtain three relations:

$$\partial_t \tilde{v}^r + \tfrac{1}{r}[\,\partial_r(r\tilde{T}^{rr}) + \partial_\phi(\tilde{T}^{\phi r}) + \partial_z(r\tilde{T}^{zr})\,] = \tfrac{1}{r}\tilde{T}^{\phi\phi}, \qquad (5.55a)$$

$$\partial_t \tilde{v}^\phi + \tfrac{1}{r}[\,\partial_r(r\tilde{T}^{r\phi}) + \partial_\phi(\tilde{T}^{\phi\phi}) + \partial_z(r\tilde{T}^{z\phi})\,] = -\tfrac{1}{r}\tilde{T}^{\phi r}, \qquad (5.55b)$$

$$\partial_t \tilde{v}^z + \tfrac{1}{r}[\,\partial_r(r\tilde{T}^{rz}) + \partial_\phi(\tilde{T}^{\phi z}) + \partial_z(r\tilde{T}^{zz})\,] = 0. \qquad (5.55c)$$

Note that since cylindrical basis vectors are spatially dependent, they do not commute with the differential operators and this is the reason why some geometrical source terms appear in the previous equations. This in turn implies that (5.55) is no longer in conservation form, i.e., the conservative character of system (5.52) is lost when projecting as in (5.54). Moreover, utilizing the methodology detailed in Section 5.2.2, we specify

$$|\hat{\Omega}_\alpha|\frac{\partial \tilde{v}^r_\alpha}{\partial t} + \sum_{e \in \partial\hat{\Omega}_\alpha}\int_e \left(r\tilde{T}^{rr}\,n_{er} + \tilde{T}^{\phi r}\,n_{e\phi} + r\tilde{T}^{zr}\,n_{ez}\right)d\hat{\sigma}_e(\boldsymbol{\xi}) = \int_{\hat{\Omega}_\alpha}\tilde{T}^{\phi\phi}\,d\boldsymbol{\xi}, \qquad (5.56a)$$

$$|\hat{\Omega}_\alpha|\frac{\partial \tilde{v}^\phi_\alpha}{\partial t} + \sum_{e \in \partial\hat{\Omega}_\alpha}\int_e \left(r\tilde{T}^{r\phi}\,n_{er} + \tilde{T}^{\phi\phi}\,n_{e\phi} + r\tilde{T}^{z\phi}\,n_{ez}\right)d\hat{\sigma}_e(\boldsymbol{\xi}) = -\int_{\hat{\Omega}_\alpha}\tilde{T}^{\phi r}\,d\boldsymbol{\xi}, \qquad (5.56b)$$

$$|\hat{\Omega}_\alpha|\frac{\partial \tilde{v}^z_\alpha}{\partial t} + \sum_{e \in \partial\hat{\Omega}_\alpha}\int_e \left(r\tilde{T}^{rz}\,n_{er} + \tilde{T}^{\phi z}\,n_{e\phi} + r\tilde{T}^{zz}\,n_{ez}\right)d\hat{\sigma}_e(\boldsymbol{\xi}) = 0, \qquad (5.56c)$$

which can be discretized in space on a structured mesh, resulting in

ⓡ $|\hat{\Omega}_{i,j,k}|\,\partial_t(\tilde{v}^r_{i,j,k}) + \Delta\phi\Delta z(r_{i+1/2}\tilde{T}^{rr}_{i+1/2,j,k} - r_{i-1/2}\tilde{T}^{rr}_{i-1/2,j,k})$ $\hspace{5cm}(5.57a)$

$\quad + \Delta r\Delta z(\tilde{T}^{\phi r}_{i,j+1/2,k} - \tilde{T}^{\phi r}_{i,j-1/2,k}) + r_i\Delta r\Delta\phi(\tilde{T}^{zr}_{i,j,k+1/2} - \tilde{T}^{zr}_{i,j,k-1/2}) = \int_{\hat{\Omega}_{i,j,k}}\tilde{T}^{\phi\phi}(\boldsymbol{\xi})\,d\boldsymbol{\xi},$

ⓟ $|\hat{\Omega}_{i,j,k}|\,\partial_t(\tilde{v}^\phi_{i,j,k}) + \Delta\phi\Delta z(r_{i+1/2}\tilde{T}^{r\phi}_{i+1/2,j,k} - r_{i-1/2}\tilde{T}^{r\phi}_{i-1/2,j,k})$ $\hspace{5cm}(5.57b)$

$\quad + \Delta r\Delta z(\tilde{T}^{\phi\phi}_{i,j+1/2,k} - \tilde{T}^{\phi\phi}_{i,j-1/2,k}) + r_i\Delta r\Delta\phi(\tilde{T}^{z\phi}_{i,j,k+1/2} - \tilde{T}^{z\phi}_{i,j,k-1/2}) = \int_{\hat{\Omega}_{i,j,k}}-\tilde{T}^{\phi r}(\boldsymbol{\xi})\,d\boldsymbol{\xi},$

ⓩ $|\hat{\Omega}_{i,j,k}|\,\partial_t(\tilde{v}^z_{i,j,k}) + \Delta\phi\Delta z(r_{i+1/2}\tilde{T}^{rz}_{i+1/2,j,k} - r_{i-1/2}\tilde{T}^{rz}_{i-1/2,j,k})$ $\hspace{5cm}(5.57c)$

$\quad + \Delta r\Delta z(\tilde{T}^{\phi z}_{i,j+1/2,k} - \tilde{T}^{\phi z}_{i,j-1/2,k}) + r_i\Delta r\Delta\phi(\tilde{T}^{zz}_{i,j,k+1/2} - \tilde{T}^{zz}_{i,j,k-1/2}) = 0.$

There are various strategies that can be used to compute the "source terms" present on the right-hand side of equation (5.57). Some authors (see [129] for a list of references) have pointed out that their discretization should be associated to the boundary cell values obtained from the Riemann problem solution. How to properly evaluate these terms becomes natural when the integration is performed before the projection of equations.

Method II: *Integration→Projection*

As in the paper of Bonnement et al. [22], we recommend the use of the procedure that follows, which from now will be called *integration→projection* approach. Its simplicity

is not its only advantage; it also accounts for a general (and implicit) discretization of the geometrical source terms.

First, let us define the average basis $\tilde{\boldsymbol{e}}_{k,\alpha}$ in the control volume $\hat{\Omega}_\alpha$ as

$$\tilde{\boldsymbol{e}}_{k,\alpha} = \frac{1}{|\hat{\Omega}_\alpha|} \int_{\hat{\Omega}_\alpha} r\, \tilde{\boldsymbol{e}}_k \, d\boldsymbol{\xi} \quad \text{so that} \quad \frac{1}{|\hat{\Omega}_\alpha|} \int_{\hat{\Omega}_\alpha} r\, \boldsymbol{v} \, d\boldsymbol{\xi} = \tilde{v}_\alpha^k \tilde{\boldsymbol{e}}_{k,\alpha}, \tag{5.58}$$

being $\tilde{v}_\alpha^k$ constant in the cell. Then, after establishing the dual average basis $\tilde{\boldsymbol{e}}_\alpha^k$, the finite volume approximation reads

$$\frac{\partial \tilde{v}_\alpha^k}{\partial t} \tilde{\boldsymbol{e}}_{k,\alpha} + \frac{1}{|\hat{\Omega}_\alpha|} \int_{\hat{\Omega}_\alpha} \frac{\partial (r\boldsymbol{T} \cdot \boldsymbol{e}^k)}{\partial \xi^k} \, d\boldsymbol{\xi} = 0, \tag{5.59}$$

and its projection onto $\tilde{\boldsymbol{e}}_\alpha^k$ as

$$\frac{\partial \tilde{v}_\alpha^k}{\partial t} + \frac{\tilde{\boldsymbol{e}}_\alpha^k}{|\hat{\Omega}_\alpha|} \cdot \int_{\hat{\Omega}_\alpha} \frac{\partial (r\boldsymbol{T} \cdot \boldsymbol{e}^k)}{\partial \xi^k} \, d\boldsymbol{\xi} = 0. \tag{5.60}$$

Switching to the cylindrical coordinate system context, we need to find the explicit expressions for the average values of the normalized basis vectors over a cell, i.e., for

$$\tilde{\boldsymbol{e}}_{r,\alpha} = \frac{1}{|\hat{\Omega}_\alpha|} \int_{\hat{\Omega}_\alpha} r\, \tilde{\boldsymbol{e}}_r \, d\boldsymbol{\xi}, \quad \tilde{\boldsymbol{e}}_{\phi,\alpha} = \frac{1}{|\hat{\Omega}_\alpha|} \int_{\hat{\Omega}_\alpha} r\, \tilde{\boldsymbol{e}}_\phi \, d\boldsymbol{\xi}, \quad \tilde{\boldsymbol{e}}_{z,\alpha} = \frac{1}{|\hat{\Omega}_\alpha|} \int_{\hat{\Omega}_\alpha} r\, \tilde{\boldsymbol{e}}_z \, d\boldsymbol{\xi}. \tag{5.61}$$

Considering once more the notation introduced in Section 5.2.1.1, we are able to deduce

$$\tilde{\boldsymbol{e}}_{r,i,j,k} = \frac{1}{\Delta\phi} \begin{pmatrix} \sin(\phi_{j+1/2}) - \sin(\phi_{j-1/2}) \\ \cos(\phi_{j-1/2}) - \cos(\phi_{j+1/2}) \\ 0 \end{pmatrix}, \quad \tilde{\boldsymbol{e}}_{\phi,i,j,k} = \frac{1}{\Delta\phi} \begin{pmatrix} \cos(\phi_{j+1/2}) - \cos(\phi_{j-1/2}) \\ \sin(\phi_{j+1/2}) - \sin(\phi_{j-1/2}) \\ 0 \end{pmatrix}, \tag{5.62}$$

and $\tilde{\boldsymbol{e}}_{z,i,j,k} = \tilde{\boldsymbol{e}}_z$. In addition, the corresponding dual values are given by

$$\tilde{\boldsymbol{e}}_{i,j,k}^r = \frac{\Delta\phi^2}{2\,(1 - \cos\Delta\phi)} \tilde{\boldsymbol{e}}_{r,i,j,k}, \quad \tilde{\boldsymbol{e}}_{i,j,k}^\phi = \frac{\Delta\phi^2}{2\,(1 - \cos\Delta\phi)} \tilde{\boldsymbol{e}}_{\phi,i,j,k}, \quad \tilde{\boldsymbol{e}}_{i,j,k}^z = \tilde{\boldsymbol{e}}^z. \tag{5.63}$$

We have now all the necessary ingredients to derive the finite volume approximation associated to the *integration→projection* approach in cylindrical coordinates. With the above definitions and recalling the one of divergence for a tensor in (5.25), equation (5.59) is expanded into

$$
\begin{aligned}
|\hat{\Omega}_{i,j,k}| \big[&\partial_t(\tilde{v}_{i,j,k}^r)\tilde{\boldsymbol{e}}_{r,i,j,k} + \partial_t(\tilde{v}_{i,j,k}^\phi)\tilde{\boldsymbol{e}}_{\phi,i,j,k} + \partial_t(\tilde{v}_{i,j,k}^z)\tilde{\boldsymbol{e}}_{z,i,j,k} \big] \\
&+ \Delta\phi[\Delta z(r_{i+1/2}\tilde{T}_{i+1/2,j,k}^{rr} - r_{i-1/2}\tilde{T}_{i-1/2,j,k}^{rr}) + r_i\Delta r(\tilde{T}_{i,j,k+1/2}^{zr} - \tilde{T}_{i,j,k-1/2}^{zr})]\tilde{\boldsymbol{e}}_{r,i,j,k} \\
&+ \Delta\phi[\Delta z(r_{i+1/2}\tilde{T}_{i+1/2,j,k}^{r\phi} - r_{i-1/2}\tilde{T}_{i-1/2,j,k}^{r\phi}) + r_i\Delta r(\tilde{T}_{i,j,k+1/2}^{z\phi} - \tilde{T}_{i,j,k-1/2}^{z\phi})]\tilde{\boldsymbol{e}}_{\phi,i,j,k} \\
&+ \Delta\phi[\Delta z(r_{i+1/2}\tilde{T}_{i+1/2,j,k}^{rz} - r_{i-1/2}\tilde{T}_{i-1/2,j,k}^{rz}) + r_i\Delta r(\tilde{T}_{i,j,k+1/2}^{zz} - \tilde{T}_{i,j,k-1/2}^{zz})]\tilde{\boldsymbol{e}}_{z,i,j,k} \\
&+ \Delta r\Delta z[\tilde{T}_{i,j+1/2,k}^{\phi r}\tilde{\boldsymbol{e}}_{r|\phi_{j+1/2}} - \tilde{T}_{i,j-1/2,k}^{\phi r}\tilde{\boldsymbol{e}}_{r|\phi_{j-1/2}}] \\
&+ \Delta r\Delta z[\tilde{T}_{i,j+1/2,k}^{\phi\phi}\tilde{\boldsymbol{e}}_{\phi|\phi_{j+1/2}} - \tilde{T}_{i,j-1/2,k}^{\phi\phi}\tilde{\boldsymbol{e}}_{\phi|\phi_{j-1/2}}] \\
&+ \Delta r\Delta z[\tilde{T}_{i,j+1/2,k}^{\phi z} - \tilde{T}_{i,j-1/2,k}^{\phi z}]\tilde{\boldsymbol{e}}_{z,i,j,k} \\
&= 0.
\end{aligned}
\tag{5.64}
$$

Furthermore, a projection of this long expression onto $\tilde{\boldsymbol{e}}^{r}_{i,j,k}$, $\tilde{\boldsymbol{e}}^{\phi}_{i,j,k}$, $\tilde{\boldsymbol{e}}^{z}_{i,j,k}$, yields

$$\text{ⓡ } |\hat{\Omega}_{i,j,k}|\, \partial_t(\tilde{v}^r_{i,j,k}) + \Delta\phi\Delta z(r_{i+1/2}\tilde{T}^{rr}_{i+1/2,j,k} - r_{i-1/2}\tilde{T}^{rr}_{i-1/2,j,k})$$
$$+\, r_i\Delta r\Delta\phi(\tilde{T}^{zr}_{i,j,k+1/2} - \tilde{T}^{zr}_{i,j,k-1/2}) - \tfrac{1}{2}\Delta r\Delta\phi\Delta z(\tilde{T}^{\phi\phi}_{i,j+1/2,k} + \tilde{T}^{\phi\phi}_{i,j-1/2,k})$$
$$+\, \tfrac{1}{2}\Delta r\Delta\phi\Delta z\,(\sin\Delta\phi)/(1-\cos\Delta\phi)\,(\tilde{T}^{\phi r}_{i,j+1/2,k} - \tilde{T}^{\phi r}_{i,j-1/2,k}) \qquad = 0, \quad (5.65\text{a})$$

$$\text{ⓟ } |\hat{\Omega}_{i,j,k}|\, \partial_t(\tilde{v}^{\phi}_{i,j,k}) + \Delta\phi\Delta z(r_{i+1/2}\tilde{T}^{r\phi}_{i+1/2,j,k} - r_{i-1/2}\tilde{T}^{r\phi}_{i-1/2,j,k})$$
$$+\, r_i\Delta r\Delta\phi(\tilde{T}^{z\phi}_{i,j,k+1/2} - \tilde{T}^{z\phi}_{i,j,k-1/2}) + \tfrac{1}{2}\Delta r\Delta\phi\Delta z(\tilde{T}^{\phi r}_{i,j+1/2,k} + \tilde{T}^{\phi r}_{i,j-1/2,k})$$
$$+\, \tfrac{1}{2}\Delta r\Delta\phi\Delta z\,(\sin\Delta\phi)/(1-\cos\Delta\phi)\,(\tilde{T}^{\phi\phi}_{i,j+1/2,k} - \tilde{T}^{\phi\phi}_{i,j-1/2,k}) \qquad = 0, \quad (5.65\text{b})$$

$$\text{ⓩ } |\hat{\Omega}_{i,j,k}|\, \partial_t(\tilde{v}^z_{i,j,k}) + \Delta\phi\Delta z(r_{i+1/2}\tilde{T}^{rz}_{i+1/2,j,k} - r_{i-1/2}\tilde{T}^{rz}_{i-1/2,j,k})$$
$$+\, \Delta r\Delta z(\tilde{T}^{\phi z}_{i,j+1/2,k} - \tilde{T}^{\phi z}_{i,j-1/2,k}) + r_i\Delta r\Delta\phi(\tilde{T}^{zz}_{i,j,k+1/2} - \tilde{T}^{zz}_{i,j,k-1/2}) = 0. \quad (5.65\text{c})$$

Equivalence Relation in Cylindrical Coordinates

The full comparison between equations (5.57) (*projection→integration*) and those of the *integration→projection* approach (see above) is summarized in the subsequent result.

Proposition 5.2.1. *The projection→integration and integration→projection procedures applied to a vector equation written in cylindrical coordinates are equivalent if and only if the source terms (of projection→integration) are discretized in the following way:*

$$\int_{\hat{\Omega}_{i,j,k}} \tilde{T}^{\phi\phi}(\boldsymbol{\xi})\, d\boldsymbol{\xi} = \tfrac{1}{2}\Delta r\Delta\phi\Delta z(\tilde{T}^{\phi\phi}_{i,j+1/2,k} + \tilde{T}^{\phi\phi}_{i,j-1/2,k})$$
$$+ \Delta r\Delta z\left(1 - \frac{\Delta\phi}{2}\frac{\sin\Delta\phi}{1-\cos\Delta\phi}\right)(\tilde{T}^{\phi r}_{i,j+1/2,k} + \tilde{T}^{\phi r}_{i,j-1/2,k}) \quad (5.66\text{a})$$

$$\int_{\hat{\Omega}_{i,j,k}} \tilde{T}^{\phi r}(\boldsymbol{\xi})\, d\boldsymbol{\xi} = \tfrac{1}{2}\Delta r\Delta\phi\Delta z(\tilde{T}^{\phi r}_{i,j+1/2,k} + \tilde{T}^{\phi r}_{i,j-1/2,k})$$
$$- \Delta r\Delta z\left(1 - \frac{\Delta\phi}{2}\frac{\sin\Delta\phi}{1-\cos\Delta\phi}\right)(\tilde{T}^{\phi\phi}_{i,j+1/2,k} + \tilde{T}^{\phi\phi}_{i,j-1/2,k}) \quad (5.66\text{b})$$

Moreover, this discretization is consistent on $\boldsymbol{\xi}$.

Let us note that, after dividing by the cell's volume $\hat{\Omega}_{i,j,k} = r_i\Delta\phi_j\Delta r\Delta z$, the two equations in the above proposition can be rewritten in the following way:

$$\frac{r_i}{|\hat{\Omega}_{i,j,k}|}\int_{\hat{\Omega}_{i,j,k}} \tilde{T}^{\phi\phi}(\boldsymbol{\xi})\, d\boldsymbol{\xi} = \tfrac{1}{2}(\tilde{T}^{\phi\phi}_{i,j+1/2,k} + \tilde{T}^{\phi\phi}_{i,j-1/2,k}) + c(\Delta\phi)(\tilde{T}^{\phi r}_{i,j+1/2,k} + \tilde{T}^{\phi r}_{i,j-1/2,k})$$

$$\frac{r_i}{|\hat{\Omega}_{i,j,k}|}\int_{\hat{\Omega}_{i,j,k}} \tilde{T}^{\phi r}(\boldsymbol{\xi})\, d\boldsymbol{\xi} = \tfrac{1}{2}(\tilde{T}^{\phi r}_{i,j+1/2,k} + \tilde{T}^{\phi r}_{i,j-1/2,k}) - c(\Delta\phi)(\tilde{T}^{\phi\phi}_{i,j+1/2,k} + \tilde{T}^{\phi\phi}_{i,j-1/2,k}),$$
$$(5.67)$$

having defined the function

$$c(x) = \left(\frac{1}{x} - \frac{\sin x}{2 - 2\cos x} \right). \tag{5.68}$$

As one refines the underlying mesh, the mean values of $\tilde{T}^{\phi\phi}$ and $\tilde{T}^{\phi\phi}$ should be recovered in equation (5.67). Thus, by looking at the right-hand side of (5.67), it is clear that for this to be the case, the limit of $c(\Delta\phi)$ should be zero as $\Delta\phi \to 0$. To verify this, we write

$$\lim_{x \to 0} c(x) = \frac{1}{2} \left(\lim_{x \to 0} \frac{x\sin x + 2(\cos x - 1)}{x(\cos x - 1)} \right), \tag{5.69}$$

and by applying L'Hôpital's rule three times, we finally obtain

$$\lim_{x \to 0} \frac{x\sin x + 2(\cos x - 1)}{x(\cos x - 1)} = \lim_{x \to 0} \frac{x\cos x + \sin x}{3\cos x - x\sin x} = \frac{\lim_{x \to 0}(\sin x)}{\lim_{x \to 0}(3\cos x - x\sin x)}, \tag{5.70}$$

which is zero since the limit of $\sin(x)$ as $x \to 0$ is zero. Therefore, we can write

$$\lim_{x \to 0} c(x) = 0, \tag{5.71}$$

and conclude that the discretization of Proposition 5.2.1 is indeed consistent on $\boldsymbol{\xi}$.

5.3 Numerical Results

In this section, we present first numerical results for an interesting test problem defined on a three-dimensional rectangular torus, in order to validate the approach detailed in this chapter for cylindrical coordinates; only first-order approximations are considered for the moment.

5.3.1 Three-Dimensional Gresho Vortex

The two-dimensional Gresho vortex problem [70] consists of a stable time-independent vortex, where the pressure gradient is well-balanced with the centrifugal force. It is supposed that the density ρ and the radial velocity $\tilde{u}^r$ are, respectively, one and zero everywhere. In addition, both the angular velocity $\tilde{u}^\phi$ and pressure p depend solely on the radius r, namely

$$\tilde{u}^\phi(r) = \begin{cases} 5r \\ -5r + 2 \\ 0 \end{cases}, \quad p(r) = \begin{cases} \frac{25}{2}r^2 + 5 & \text{if } 0.0 \le r < 0.2, \\ \frac{25}{2}r^2 - 20r + 9 - 4\ln(0.2) + 4\ln(r) & \text{if } 0.2 \le r < 0.4, \\ 3 + 4\ln(2) & \text{if } 0.4 \le r < r_{\max}, \end{cases} \tag{5.72}$$

with $r_{\max}$ being the maximum radius of the domain. The Gresho problem was originally used for incompressible flows in [70] and later applied to the Euler equations in [98]. All initial profiles are shown in Figure 5.4, with $r_{\max} = 1$. We verify that the centrifugal force matches the pressure gradient in the following way:

$$\frac{\tilde{u}_\phi^2}{r} = \frac{\partial p}{\partial r} = \begin{cases} 25r & \text{if } 0.0 \le r < 0.2, \\ 25r - 20 + \frac{4}{r} & \text{if } 0.2 \le r < 0.4, \\ 0 & \text{if } 0.4 \le r < r_{\max}. \end{cases} \tag{5.73}$$

(a) Density ρ (b) Velocity $\tilde{u}^r$ (c) Velocity $\tilde{u}^\phi$ (d) Pressure p
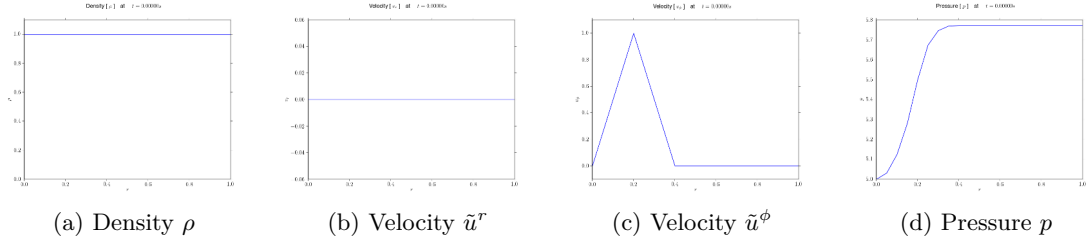
FIGURE 5.4. Exact solution of the 2D Gresho vortex problem [70, 98].

For our purposes, we modify this test and adapt it to a toroidal geometry. Thus, we assume once more that the density $\rho = 1$ and the radial velocity $\tilde{u}^r = 0$, everywhere in the computational domain. Moreover, we define the angular velocity such that its profile matches the one of Figure 5.5c but shifted by one unit in the r-direction, i.e.,

$$\tilde{u}_\phi(r) = \begin{cases} 5(r-1) & \text{if } 1.0 \leq r < 1.2, \\ -5r + 7 & \text{if } 1.2 \leq r < 1.4, \\ 0 & \text{if } 1.4 \leq r < r_{\max}. \end{cases} \tag{5.74}$$

Then, the pressure can be obtained as a solution of the ordinary differential equation $p'(r) = \tilde{u}_\phi^2/r$ such that

$$p(r) = \begin{cases} 25(\frac{1}{2}r^2 - 2r + \ln(r)) + \frac{85}{2} & 1.0 \leq r < 1.2, \\ \frac{25}{2}r^2 - 70r + 49\ln(r) + \frac{133}{2} - 24\ln(1.2) & 1.2 \leq r < 1.4, \\ 49\ln(1.4) - 24\ln(1.2) - 7 & 1.4 \leq r < r_{\max}. \end{cases} \tag{5.75}$$

In Figure 5.5, we have depicted these profiles with $r_{\max} = 2$. As a last step, a simple extension of the previous problem to three dimensions is done by setting $\boldsymbol{w}(r, \phi, z) = \boldsymbol{w}(r)$, for all ϕ and z.

(a) Density ρ (b) Velocity $\tilde{u}^r$ (c) Velocity $\tilde{u}^\phi$ (d) Pressure p
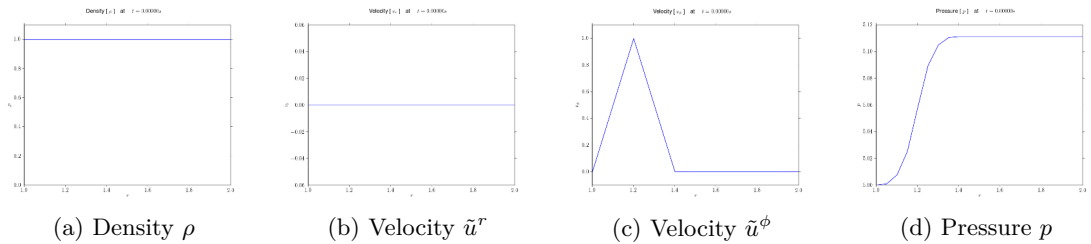
FIGURE 5.5. Exact solution of the modified two-dimensional Gresho vortex problem.

Now, we compute this equilibrium flow for the Euler equations of gas dynamics with an ideal equation of state ($\gamma = 5/3$). The problem is initialized on a cylindrical computational mesh of size $[1, 2] \times [0, 2\pi] \times [-0.5, 0.5]$ consisting of $10 \times 4 \times 10$ uniform

cells and is run a sufficiently long time $T = 500$, using a CFL of 0.9. Periodic boundary conditions are set in ϕ; reflecting ones in z and for the exterior boundary in the r-direction; and the slip BC is applied to the remaining boundary. Despite the coarseness of the mesh, the cylindrical method gives a solution close to the stationary one as can be appreciated in Figure 5.6.

(a) Density at $t = 0.0$ (b) Velocity mag. at $t = 0.0$ (c) Pressure at $t = 0.0$

(d) Density at $t = 50.0$ (e) Velocity mag. at $t = 50.0$ (f) Pressure at $t = 50.0$
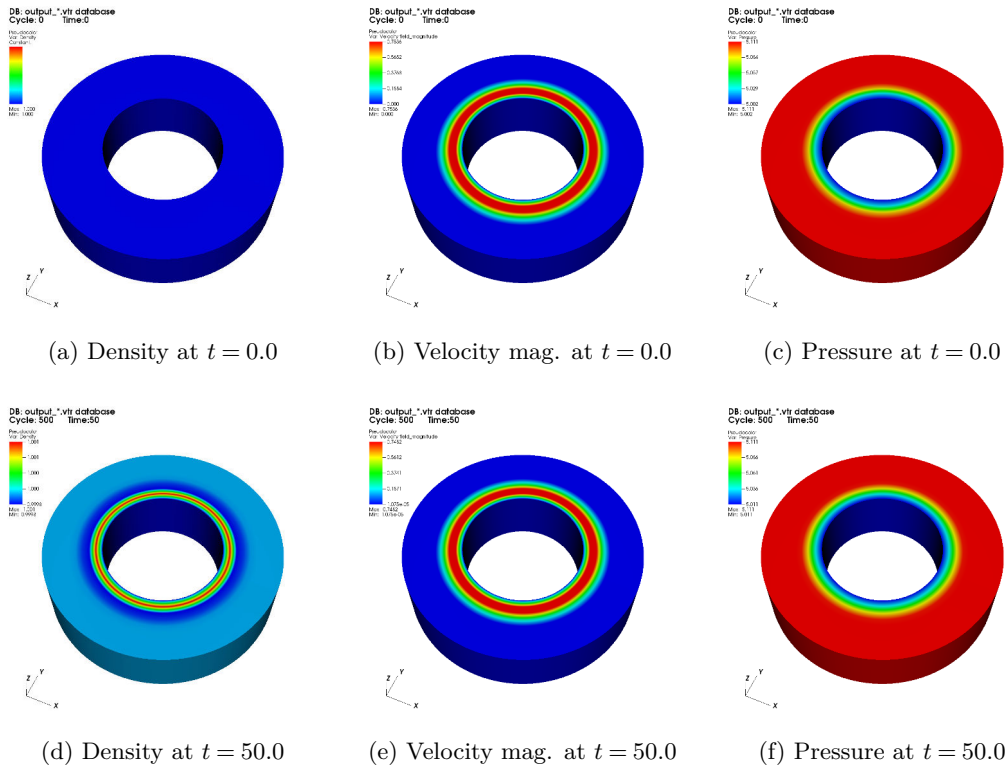
FIGURE 5.6. Density, pressure and velocity magnitude for the three-dimensional Gresho test in a toroidal geometry, with $N = 10 \times 4 \times 10$ and at times $t = 0$ (top) and $t = 50$ (bottom).

Figure 5.7 shows the evolution in time of the L^2 error for the density (left) and the L^2 norm of the velocity (right), in logarithmic scales. The four different lines in each plot correspond to a change in the number of cells in the toroidal direction when performing the simulations. Observe that as this number is increased, the slope of the stabilized line diminishes for the L^2 error, representing more stability in the long run. Note that errors remain small even if N_ϕ is small.

5.4 Conclusions

We have studied the derivation of finite volume methods in cylindrical coordinates for hyperbolic conservation laws. Since vectors in curvilinear coordinate systems are expressed in terms of bases that are spatially dependent, the projection of a vector onto a local basis introduces geometrical source terms that should not be arbitrarily dis-

(a) L^2 error   (b) L^2 norm of the velocity
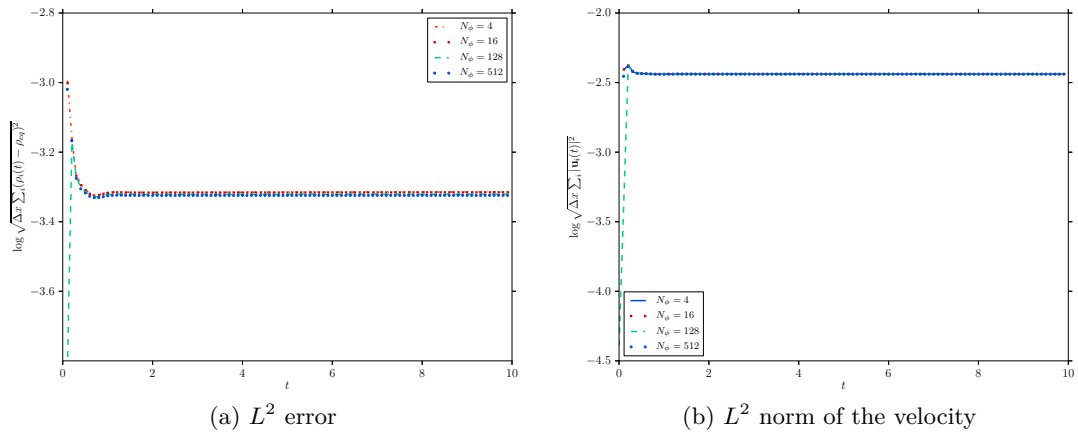
FIGURE 5.7. Results in logarithmic scale for the three-dimensional Gresho vortex with $10 \times N_\phi \times 10$ cells; computations performed on one processor.

cretized. Actually, we have investigated the proper approximation of these geometrical terms such that all of the system's conservation properties are kept. A numerical test has been proposed and the approach has been successfully applied for the simulation of a stable hydrodynamic flow in a three-dimensional rectangular torus. More numerical tests should be performed, especially in the context of MHD equations.

CHAPTER 6

Conclusions and Perspectives

The work presented in this thesis deals with the study and design of Godunov-type finite volume methods for the numerical solution of systems of conservation laws, with particular interest in applications to gas dynamics and magnetohydrodynamics. In general, we believe that simple formulations can be highly effective in practice, as Godunov-type schemes are likely to be implemented and used by individuals who are not algorithm developers themselves as means to simulate real problems in various contexts. With simplicity we do not mean developing simplistic solutions that compromise quality, but rather providing the method's fundamental considerations and resulting expressions in a way that will allow others to reproduce our findings without any unnecessary difficulties.

In the first part, we have described a simple multidimensional Riemann solver for hyperbolic conservation laws that can be regarded as a 2D generalization or extension of the HLL formalism. The associated numerical strategy relies on an approximate description of the two-dimensional Riemann problem consisting of planar waves which separate several constant states. We make use of the consistency with the integral formulation through Rankine-Hugoniot relations (holding across the discontinuities) to derive closed-form expressions for the fluxes, facilitating their implementation. The problem's unknowns are in fact solutions of an overdetermined system that we solve using a least squares approximation. We have also provided a robust assembling approach (based on varying weights) that is useful to estimate the total flux at the cells' faces, which has been validated through several numerical tests applied to subsonic and supersonic flows. In addition to the simplicity, we have also proposed a generalization to unstructured grids with a formulation that is mostly algebraic rather than geometrical. We argue that jump conditions can be improved by designing complex profiles so that the Rankine-Hugoniot relations define an invertible system; extensions of more complex solvers such as the HLLE (linear intermediate state) and HLLC (with a contact discontinuity wave) are also feasible. Moreover, given that the consistency with the integral formulation through these relations holds in three dimensions as well, a genuine 3D solver can be obtained in future work. The application of our solver for the evolution of the MHD equations (and not only for the estimation of the electric field as in Chapter 3) is possible.

Next, our investigation and comparison of two different methods that aim to maintain the divergence-free property of the magnetic field have assured us (and hopefully, the reader as well) that it is a constraint that cannot be ignored without having consequences. In particular, we have investigated the hyperbolic divergence technique proposed by Dedner et al. [45] applied to the ideal MHD equations on a collocated grid and have compared it to the constrained transport approach, originally introduced by Evans and Hawley [52] and which relies on a staggered formulation of the magnetic and electric fields. Our findings show that the advantage of the divergence cleaning technique is its simplicity in terms of implementation and the fact that it is based on the cell-centered formulation favored in the Godunov approach; however, it has the drawback of depending on tunable parameters, which in turn are avoided in the constrained transport methodology. Although this last method, i.e., the CT one, sometimes presents loss of conservation of the total energy density, it has an inherently divergence-free magnetic field given its associated staggered mesh discretization and the 2D Riemann solver can easily be employed to estimate the staggered electric field. Through different numerical test cases, we have been able to reproduce results obtained by other authors and conclude that both methods are robust and efficient (yet, they still permit room for improvement). Although we find that the hyperbolic divergence cleaning generates more diffusive results than the constrained transport, the simplicity of the method makes it an attractive technique for our future work in the design of a high order finite volume approximation for hyperbolic conservation laws in curvilinear unstructured grids.

In Chapter 4, we have shown the derivation of a Suliciu-type relaxation model that ensures adequate coupling of the Poisson and Euler equations, yielding an interesting scheme described in the limit as a penalty parameter tends to zero. In view of astrophysical simulations, the asymptotic regime of self gravitational equilibrium flows must be preserved, and although several asymptotically stable methods for the Euler-Poisson system in the quasineutral limit have already been developed [40, 46], they become far too complex in three dimensions or when an implicit formulation is required. We have proposed a simpler numerical scheme based on a Godunov-type solver deduced from a relaxation system, and with different types of examples, we have established the scheme's robustness and demonstrated its ability to capture and preserve steady (and perturbed quasi-steady) states when required. Moreover, the scheme has been reconsidered in spherical coordinates in order to recover precisely the solution of the Lane-Emden equation. Future work will be devoted to a well-balanced time implicit formulation of the method and simulations of 3D self-gravitating astrophysical problems.

Finally, we have studied the derivation of finite volume methods in cylindrical coordinates for hyperbolic conservation laws. Since vectors in curvilinear coordinate systems are expressed in terms of bases that are spatially dependent, the projection of a vector onto a local basis introduces geometrical source terms that should not be arbitrarily discretized. Actually, we have investigated the proper approximation of these geometrical terms such that all of the system's conservation properties are kept; the approach has been applied for the simulation of a stable hydrodynamic flow in a three-dimensional rectangular torus. Forthcoming works include extending this approach to unstructured

meshes and applying the resulting schemes to real magnetic confinement fusion problems, with the aim of contributing to this exciting field of research.

Most of the numerical results in this thesis have been obtained with the software HERACLES [66], a 3D parallel hydrodynamical code used to simulate astrophysical fluid flows. In the context of high-performance computing (HPC), the code uses the MPI library to distribute large computational domains among many processors and perform the necessary communication among them. Recently, a new cluster named *Poincare* was installed at Maison de la Simulation for development, testing and research, featuring: 92 nodes for calculation, each with 2 processors Sandy Bridge E5-2670, i.e., 16 cores per node; 2 large nodes x3755 M3 with 64 cores each; and 4 GPU nodes. As a matter of fact, all results on more than one core have been computed using Poincare, allowing us to investigate several problems on mesh sizes that were previously beyond reach.

Conclusions et Perspectives

Le travail présenté dans cette thèse traite de l'étude et de la construction des méthodes volumes finis de type Godunov pour résoudre numériquement des systèmes de lois de conservation, avec un intérêt particulier dans les équations de la dynamique des gaz et de la magnétohydrodynamique. En général, nous croyons que les formulations simples sont très efficaces dans la pratique pour simuler de problèmes du monde réel, étant donné que les schémas de type Godunov sont susceptibles d'être mises en œuvre et utilisés par des individus qui ne sont pas des développeurs eux-mêmes. Avec le terme «simple», nous ne parlons pas de développement de solutions simplistes où la qualité est compromise, mais plutôt d'apporter des idées et des expressions fondamentales de l'approche d'une manière qui permette aux autres de reproduire nos résultats sans difficulté.

Dans la première partie, nous avons décrit un solveur de Riemann multidimensionnel simple et peut être considéré comme une généralisation 2D du formalisme HLL pour les lois de conservation hyperboliques. La stratégie numérique associée s'appuie sur un profil approché du problème de Riemann bidimensionnel constitué d'ondes planes séparant des états constants. Nous proposons d'utiliser la consistance avec la formulation intégrale à travers les relations de Rankine-Hugoniot afin d'obtenir des expressions assez simples à mettre en œuvre du flux numérique. Les inconnues du problème de Riemann 2D sont alors les solutions d'un système surdéterminé que nous résolvons par la méthode des moindres carrés. Nous avons également fourni une approche d'assemblage robuste qui s'avère utile pour estimer le flux total aux faces des cellules et qui a été validé par plusieurs cas tests d'écoulements subsoniques et supersoniques. En plus de la simplicité, nous avons également proposé une généralisation de la méthode aux maillages non structurés avec une formulation algébrique. Nous savons que les relations de saut peuvent être améliorées si nous considérons des profils complexes pour lesquels les conditions Rankine-Hugoniot définissent un système inversible ; des extensions de solveurs de Riemann plus complexes comme HLLE (état intermédiaire linéaire) et HLLC (avec un discontinuité de contact) sont également envisageables. En outre, étant donné que la consistance avec la formulation intégrale à travers les relations de saut s'applique aussi en trois dimensions, un solveur 3D peut être obtenu dans les travaux à venir. L'application de notre solveur pour l'évolution des équations MHD (et pas seulement pour l'estimation du champ électrique dans le Chapitre 3) est un des perspectives de ce travail.

Ensuite, notre étude s'est porté sur la comparaison de deux stratégies numériques

visant à préserver, au niveau discret, la contrainte de divergence nulle sur le champ magnétique. Les résultats obtenus montrent que cette contrainte ne peut pas être ignorée numériquement, sas conséquences néfastes sur la fiabilité des résultats. En particulier, nous avons étudié la technique d'épuration de la divergence par une correction hyperbolique («hyperbolic cleaning»), proposée par Dedner et al. [45] et appliquée aux équations de la MHD idéale sur une grille colocalisée. Nous la comparons à l'approche du transport contraint, initialement introduit par Evans et Hawley [52] et qui, utilise une grille décalée (pour les champs magnétiques et électriques) pour maintenir cette propriété. Nos résultats montrent que l'avantage de la technique hyperbolic cleaning est sa simplicité en termes de la mise en œuvre et du fait qu'elle est basée sur la formulation centrée des cellules (cette formulation s'intègre aisément dans l'approche Godunov). Cependant, cette technique a l'inconvénient de dépendre de paramètres ajustables. La méthode CT n'a, quant à elle, pas de paramètres ajustables mais présente parfois une perte de la conservation de l'énergie totale, mais elle a l'avantage d'avoir un champ magnétique avec une divergence parfaitement nulle sur la discrétisation décalée ; le solveur Riemann 2D peut facilement être utilisé pour estimer le champ électrique aux coins du maillage. Grâce à différents tests numériques, nous avons été en mesure de reproduire les résultats obtenus par d'autres auteurs et de conclure que les deux méthodes sont robustes et efficaces (mais, ils permettent toujours place à l'amélioration). Même si nous constatons que l'épuration de la divergence par une correction hyperbolique génère des résultats plus diffusifs que ceux du transport contraint, la simplicité de la méthode est attrayante pour nos travaux futurs sur la construction des schémas volumes finis d'ordre élevés pour les lois de conservation hyperboliques en maillages non structurés et curvilignes.

Dans le chapitre 4, nous avons présenté la dérivation d'un modèle de relaxation de type Suliciu qui assure un couplage adéquat des équations d'Euler et de la équation de Poisson, donnant un schéma intéressant qui est obtenu à la limite quand le paramètre de pénalisation tend vers zéro. Au vu des simulations numériques en astrophysique, le régime asymptotique des équilibres autogravitationnels doit être préservé, et même si plusieurs méthodes asymptotiques et stables pour ce système d'Euler-Poisson à la limite quasi neutre ont déjà été mis en œuvre [40, 46], ils deviennent trop complexes soit en trois dimensions ou lorsque quand une formulation implicite est nécessaire. Nous avons proposé un schéma numérique simple basé sur un solveur de type Godunov construit à partir du modèle de relaxation, et avec différents types d'exemples, nous avons testé la robustesse du schéma et démontré sa capacité de capturer et préserver des états stables (et quasi-stables) lorsque le problème l'exige. En outre, le schéma a été aussi formulé en coordonnées sphériques afin de récupérer avec précision la solution de l'équation de Lane-Emden. Les travaux à venir traiteront de la formulation implicite et bien équilibrée de la méthode et des simulations de problèmes autogravitationnels en trois dimensions.

Enfin, nous avons étudié la dérivation des méthodes volumes finis en coordonnées cylindriques pour les lois de conservation hyperboliques. Puisque les vecteurs dans

systèmes de coordonnées curvilignes sont exprimés en termes de bases qui sont spatialement variables, la projection d'un vecteur sur une base locale introduit des termes sources géométriques qui ne doivent pas être arbitrairement discrétisés. En fait, nous avons étudié la bonne approximation de ces termes géométriques afin que toutes les propriétés de conservation du système soient conservées ; la méthode a été appliquée pour simuler un écoulement hydrodynamique stable dans un tore rectangulaire tridimensionnel. Travaux à venir incluent l'extension de cette approche aux maillages non structurés et l'application des schémas résultants aux problèmes réels de la fusion par confinement magnétique, avec pour objectif de contribuer à ce domaine de recherche.

La plupart des résultats numériques dans cette thèse ont été obtenus avec la plateforme de calcul HERACLES [66], un code hydrodynamique parallèle en trois dimensions utilisé pour simuler des écoulements en astrophysique. Dans le contexte de calcul haute performance, le code utilise la bibliothèque MPI permettant de distribuer des grands domaines de calcul sur plusieurs nœuds et d'effectuer la communication nécessaire entre eux. Récemment, un nouveau cluster, nommé Poincaré, a été installé à la Maison de la Simulation pour faciliter le développement, la recherche et l'expérimentation, avec : 92 nœuds de calcul (chacun avec 2 processeurs Sandy Bridge E5-2670, c'est à dire, 16 cœurs par nœud), 4 nœuds GPU et 2 grands nœuds x3755 M3 avec 64 cores chacun. En fait, tous les résultats sur plusieurs cœurs ont été calculés en utilisant Poincaré et nous permettent d'étudier les différents problèmes sur des maillages très fins.

Invertible Matrix M to Obtain the 2D Fluxes

Here, we are interested in finding the determinant of M, introduced in Section 2.2.2.2, and analyzing the result. We begin by evaluating the matrix product $A^T A$ in order to get

$$M = \begin{pmatrix} \delta_1^{f2} + \delta_2^{f2} + \delta_3^{f2} + \delta_4^{f2} & \delta_1^f \delta_1^g + \delta_2^f \delta_2^g + \delta_3^f \delta_3^g + \delta_4^f \delta_4^g \\ \delta_1^f \delta_1^g + \delta_2^f \delta_2^g + \delta_3^f \delta_3^g + \delta_4^f \delta_4^g & \delta_1^{g2} + \delta_2^{g2} + \delta_3^{g2} + \delta_4^{g2} \end{pmatrix}, \tag{A.1}$$

which is a two-dimensional square matrix with a straightforward determinant

$$\begin{aligned} \det M = \; & \delta_1^{f2}\delta_2^{g2} + \delta_1^{f2}\delta_3^{g2} + \delta_1^{f2}\delta_4^{g2} + \delta_2^{f2}\delta_1^{g2} + \delta_2^{f2}\delta_3^{g2} + \delta_2^{f2}\delta_4^{g2} \\ & + \delta_3^{f2}\delta_1^{g2} + \delta_3^{f2}\delta_2^{g2} + \delta_3^{f2}\delta_4^{g2} + \delta_4^{f2}\delta_1^{g2} + \delta_4^{f2}\delta_2^{g2} + \delta_4^{f2}\delta_3^{g2} \\ & - 2\,\delta_1^f \delta_1^g \delta_2^f \delta_2^g - 2\,\delta_1^f \delta_1^g \delta_3^f \delta_3^g - 2\,\delta_1^f \delta_1^g \delta_4^f \delta_4^g - 2\,\delta_2^f \delta_2^g \delta_3^f \delta_3^g - 2\,\delta_2^f \delta_2^g \delta_4^f \delta_4^g - 2\,\delta_3^f \delta_3^g \delta_4^f \delta_4^g, \end{aligned} \tag{A.2}$$

after expansion and some simplification. It is well-known from basic linear algebra that M is nonsingular if and only if its determinant is nonzero. Thus, we propose to rewrite equation (A.2) as a sum of squared binomials

$$\begin{aligned} \det M = \; & \left(\delta_1^f \delta_2^g - \delta_2^f \delta_1^g \right)^2 + \left(\delta_1^f \delta_3^g - \delta_3^f \delta_1^g \right)^2 + \left(\delta_2^f \delta_4^g - \delta_4^f \delta_2^g \right)^2 \\ & + \left(\delta_3^f \delta_2^g - \delta_2^f \delta_3^g \right)^2 + \left(\delta_4^f \delta_1^g - \delta_1^f \delta_4^g \right)^2 + \left(\delta_4^f \delta_3^g - \delta_3^f \delta_4^g \right)^2, \end{aligned} \tag{A.3}$$

that is obviously greater or equal to zero. It suffices then to find a term that is greater than zero to prove the determinant is strictly positive.

For this, we consider the squared binomial $r_{ne} = \left(\delta_4^f \delta_1^g - \delta_1^f \delta_4^g \right)^2$ and acknowledge the following: $\delta_4^f = s_n^e - s_s^e > 0$, recalling that s_n^e and s_s^e are the distinct maximum and minimum signal velocities (2.11) associated with the one-dimensional Riemann problem on the right of the y-axis, and $\delta_1^g = s_e^n - s_w^n > 0$, using an analogous reasoning. Therefore, we are certain that the product $\delta_4^f \delta_1^g > 0$ and the only way that r_{ne} would become zero is if $\delta_4^f \delta_1^g = |\delta_1^f \delta_4^g|$. Next, we denote by r_{sw} the term $\left(\delta_3^f \delta_2^g - \delta_2^f \delta_3^g \right)^2$ and using an approach similar to the previous one, we find that r_{sw} vanishes only if $\delta_2^f \delta_3^g = |\delta_3^f \delta_2^g|$, given that $\delta_2^f \delta_3^g > 0$ since both $\delta_3^g, \delta_2^f < 0$.

Two simple but useful properties that hold for the absolute value are $|ab| = |a||b|$, for any $a, b \in \mathbb{R}$, and $ab \leq |a||b|$, so that we can obtain $\delta_4^f \delta_1^g - \delta_1^f \delta_4^g \geq 0$ and $\delta_2^f \delta_3^g - \delta_3^f \delta_2^g \geq 0$, or their sum $\bar{s} = \delta_4^f \delta_1^g + \delta_2^f \delta_3^g - \delta_1^f \delta_4^g - \delta_3^f \delta_2^g \geq 0$. By performing some algebra, we find that $\bar{s} = \frac{2}{\Delta t^2} a_{**}$, and, provided the assumption $\Delta t > 0$ is satisfied, we recover $r_{en} + r_{sw} > 0$ as long as $a_{**} \neq 0$. In other words, if $a_{**} \neq 0$, the determinant of $\boldsymbol{M}$ is strictly positive and the matrix is invertible

$$\boldsymbol{M}^{-1} = \frac{1}{\det \boldsymbol{M}} \begin{pmatrix} \delta_1^{g2} + \delta_2^{g2} + \delta_3^{g2} + \delta_4^{g2} & -\delta_1^f \delta_1^g - \delta_2^f \delta_2^g - \delta_3^f \delta_3^g - \delta_4^f \delta_4^g \\ -\delta_1^f \delta_1^g - \delta_2^f \delta_2^g - \delta_3^f \delta_3^g - \delta_4^f \delta_4^g & \delta_1^{f2} + \delta_2^{f2} + \delta_3^{f2} + \delta_4^{f2} \end{pmatrix}. \qquad \text{(A.4)}$$

Implementation Notes

B.1 Einfelt Speeds

Here, we provide the algorithm to compute the pair of wave speeds s_l^α and s_r^α of Section 2.2.4.1 in the case where the spatial domain is multidimensional.

Algorithm 1 Defining s_l^α and s_r^α in the direction of $\boldsymbol{\nu}_\alpha$

1: **function** TOTAL_ENTHALPY(ρ, e, p)
2: $\quad H \leftarrow (\rho e + p)/\rho$
3: $\quad$ **return** H
4:
5: **function** SOUND_SPEED$(\boldsymbol{u}, H, \gamma)$
6: $\quad c \leftarrow \left[(\gamma - 1)(H - \frac{1}{2}\sum_{m=1}^{d} \boldsymbol{u}_m^2)\right]^{1/2}$
7: $\quad$ **return** c
8:
9: **function** AVERAGE$(\rho_l, \rho_r, (\cdot)_l, (\cdot)_r)$
10: $\quad den \leftarrow \sqrt{\rho_l} + \sqrt{\rho_r}$
11: $\quad \overline{(\cdot)} \leftarrow \left[\sqrt{\rho_l}\,(\cdot)_l + \sqrt{\rho_r}\,(\cdot)_r\right]/den$
12: $\quad$ **return** $\overline{(\cdot)}$

13:
14: $H_l \leftarrow$ TOTAL_ENTHALPY(ρ_l, e_l, p_l)
15: $H_r \leftarrow$ TOTAL_ENTHALPY(ρ_r, e_r, p_r)
16:
17: $\overline{\boldsymbol{u}} \leftarrow$ AVERAGE$(\rho_l, \rho_r, \boldsymbol{u}_l, \boldsymbol{u}_r)$
18: $\overline{H} \leftarrow$ AVERAGE$(\rho_l, \rho_r, H_l, H_r)$
19:
20: $c_l \leftarrow$ SOUND_SPEED$(\boldsymbol{u}_l, H_l, \gamma)$
21: $c_r \leftarrow$ SOUND_SPEED$(\boldsymbol{u}_r, H_r, \gamma)$
22: $\overline{c} \leftarrow$ SOUND_SPEED$(\overline{\boldsymbol{u}}, \overline{H}, \gamma)$
23:
24: $s_l^\alpha \leftarrow \min(\overline{\boldsymbol{u}} \cdot \boldsymbol{\nu}_\alpha - \overline{c}, \boldsymbol{u}_l \cdot \boldsymbol{\nu}_\alpha - c_l)$
25: $s_r^\alpha \leftarrow \max(\overline{\boldsymbol{u}} \cdot \boldsymbol{\nu}_\alpha + \overline{c}, \boldsymbol{u}_r \cdot \boldsymbol{\nu}_\alpha + c_r)$

B.2 Pseudocode for *Manual Assembling*

With regard to equation (2.89) and its analogue in the y direction, we present three snippets of pseudocode that will help the reader compute the values for the speeds $\tilde{s}_\alpha$, with $\alpha \in \{n, s, e, w\}$, and for the "*hll2D*" fluxes.

After obtaining the eight approximate signal velocities that determine the vectors (2.21), we propose to restrict in some cases the diagonal crossing of the interaction region corners (2.25), in order to reduce further coding difficulties. Basically, we want to avoid the type of situations where a corner lies in the quadrant diagonal to that where

its subsonic counterpart would be and, at the same time, at least two of the remaining corners are in their respective "subsonic" quadrants. For this, we use:

Algorithm 2 Restricting certain crossings

1: **if** $(s_e^n < 0$ and $s_n^e < 0)$ **then**   ▷ Northeast
2:     **if** $s_n^w > 0$ **then** $s_n^e \leftarrow 0$
3:     **if** $s_e^s > 0$ **then** $s_e^n \leftarrow 0$
4: **if** $(s_w^n > 0$ and $s_n^w < 0)$ **then**   ▷ Northwest
5:     **if** $s_w^s < 0$ **then** $s_w^n \leftarrow 0$
6:     **if** $s_n^e > 0$ **then** $s_n^w \leftarrow 0$

7: **if** $(s_w^s > 0$ and $s_s^w > 0)$ **then**   ▷ Southwest
8:     **if** $s_w^n < 0$ **then** $s_w^s \leftarrow 0$
9:     **if** $s_s^e < 0$ **then** $s_s^w \leftarrow 0$
10: **if** $(s_e^s < 0$ and $s_s^e > 0)$ **then**   ▷ Southeast
11:     **if** $s_e^n > 0$ **then** $s_e^s \leftarrow 0$
12:     **if** $s_s^w < 0$ **then** $s_s^e \leftarrow 0$

We then recover all one- and two-dimensional states and fluxes with equations (2.23), (2.24), (2.38), (2.53), and (2.60). To estimate the values of the speeds and fluxes mentioned in the first paragraph of this section, we suggest considering the following piece of pseudocode:

Algorithm 3 Defining the speeds $\tilde{s}_\alpha$ for $\alpha \in \{n,s,e,w\}$, and the fluxes $\widetilde{\phi}_x^{hll2D}$ and $\widetilde{\phi}_y^{hll2D}$

1: **if** $(s_s^e \geq 0$ and $s_s^w \geq 0)$ **then**
2:     $\tilde{s}_e \leftarrow s_s^e$ ▷ Above x-axis
3:     $\tilde{s}_w \leftarrow s_s^w$
4: **else if** $(s_n^e \leq 0$ and $s_n^w \leq 0)$ **then**
5:     $\tilde{s}_e \leftarrow s_n^e$ ▷ Below x-axis
6:     $\tilde{s}_w \leftarrow s_n^w$
7: **else**
8:     $\tilde{s}_e \leftarrow s_e^{n+} - s_n^{e+}(s_e^{s+} - s_e^{n+})/(s_s^{e-} - s_n^{e+})$
9:     $\tilde{s}_w \leftarrow s_w^{s-} - s_s^{w-}(s_w^{n-} - s_s^{w-})/(s_n^{w+} - s_s^{w-})$
10:
11: **if** $(s_w^n \geq 0$ and $s_w^s \geq 0)$ **then**
12:     $\tilde{s}_n \leftarrow s_n^w$ ▷ Right of y-axis
13:     $\tilde{s}_s \leftarrow s_s^w$
14: **else if** $(s_e^n \leq 0$ and $s_e^s \leq 0)$ **then**
15:     $\tilde{s}_n \leftarrow s_n^e$ ▷ Left of y-axis
16:     $\tilde{s}_s \leftarrow s_s^e$
17: **else**
18:     $\tilde{s}_n \leftarrow s_w^{n+} - s_w^{n-}(s_n^{w+} - s_e^{n+})/(s_n^{n-} - s_e^{n+})$
19:     $\tilde{s}_s \leftarrow s_s^{e-} - s_e^{s+}(s_s^{e-} - s_s^{w-})/(s_e^{s+} - s_w^{s-})$
20:
21: **if** $(\tilde{s}_w \geq 0$ and $\tilde{s}_s \geq 0)$ **then**
22:     $\widetilde{\phi}_x^{hll2D} \leftarrow [(\tilde{s}_n - \tilde{s}_s)\boldsymbol{f}_{*w} + \tilde{s}_s \boldsymbol{f}_{sw}]/\tilde{s}_n$
23:     $\widetilde{\phi}_y^{hll2D} \leftarrow [(\tilde{s}_e - \tilde{s}_w)\boldsymbol{g}_{s*} + \tilde{s}_w \boldsymbol{g}_{sw}]/\tilde{s}_e$
24: **else if** $(\tilde{s}_w \geq 0$ and $\tilde{s}_n \leq 0)$ **then**
25:     $\widetilde{\phi}_x^{hll2D} \leftarrow [(\tilde{s}_s - \tilde{s}_n)\boldsymbol{f}_{*w} + \tilde{s}_n \boldsymbol{f}_{nw}]/\tilde{s}_s$

26:     $\widetilde{\phi}_y^{hll2D} \leftarrow [(\tilde{s}_e - \tilde{s}_w)\boldsymbol{g}_{n*} + \tilde{s}_w \boldsymbol{g}_{nw}]/\tilde{s}_e$
27: **else if** $(\tilde{s}_e \leq 0$ and $\tilde{s}_s \geq 0)$ **then**
28:     $\widetilde{\phi}_x^{hll2D} \leftarrow [(\tilde{s}_n - \tilde{s}_s)\boldsymbol{f}_{*e} + \tilde{s}_s \boldsymbol{f}_{se}]/\tilde{s}_n$
29:     $\widetilde{\phi}_y^{hll2D} \leftarrow [(\tilde{s}_w - \tilde{s}_e)\boldsymbol{g}_{s*} + \tilde{s}_e \boldsymbol{g}_{se}]/\tilde{s}_w$
30: **else if** $(\tilde{s}_e \leq 0$ and $\tilde{s}_n \leq 0)$ **then**
31:     $\widetilde{\phi}_x^{hll2D} \leftarrow [(\tilde{s}_s - \tilde{s}_n)\boldsymbol{f}_{*e} + \tilde{s}_n \boldsymbol{f}_{ne}]/\tilde{s}_s$
32:     $\widetilde{\phi}_y^{hll2D} \leftarrow [(\tilde{s}_w - \tilde{s}_e)\boldsymbol{g}_{n*} + \tilde{s}_e \boldsymbol{g}_{ne}]/\tilde{s}_w$
33: **else if** $\tilde{s}_w \geq 0$ **then**
34:     $\widetilde{\phi}_x^{hll2D} \leftarrow \boldsymbol{f}_{*w}$
35:     $\widetilde{\phi}_y^{hll2D} \leftarrow [(\tilde{s}_e - \tilde{s}_w)\boldsymbol{g}_{**} + \tilde{s}_w \boldsymbol{g}_{*w}]/\tilde{s}_e$
36: **else if** $\tilde{s}_e \leq 0$ **then**
37:     $\widetilde{\phi}_x^{hll2D} \leftarrow \boldsymbol{f}_{*e}$
38:     $\widetilde{\phi}_y^{hll2D} \leftarrow [(\tilde{s}_w - \tilde{s}_e)\boldsymbol{g}_{**} + \tilde{s}_e \boldsymbol{g}_{*e}]/\tilde{s}_w$
39: **else if** $\tilde{s}_s \geq 0$ **then**
40:     $\widetilde{\phi}_x^{hll2D} \leftarrow [(\tilde{s}_n - \tilde{s}_s)\boldsymbol{f}_{**} + \tilde{s}_s \boldsymbol{f}_{s*}]/\tilde{s}_n$
41:     $\widetilde{\phi}_y^{hll2D} \leftarrow \boldsymbol{g}_{s*}$
42: **else if** $\tilde{s}_n \leq 0$ **then**
43:     $\widetilde{\phi}_x^{hll2D} \leftarrow [(\tilde{s}_s - \tilde{s}_n)\boldsymbol{f}_{**} + \tilde{s}_n \boldsymbol{f}_{n*}]/\tilde{s}_s$
44:     $\widetilde{\phi}_y^{hll2D} \leftarrow \boldsymbol{g}_{n*}$
45: **else**
46:     $\widetilde{\phi}_x^{hll2D} \leftarrow \boldsymbol{f}_{**}$
47:     $\widetilde{\phi}_y^{hll2D} \leftarrow \boldsymbol{g}_{**}$

Algorithm 3 serves to understand how the "*hll2D*" fluxes found in equation (2.89) are to be defined. However, we introduce a more general algorithm associated with the *manual assembling* (2.91) that serves to obtain robust first- and second-order approximations. Observing closely, we find that the flux estimation part of Algorithm 3 is somehow contained in what follows:

Algorithm 4 Defining the fluxes $\widetilde{\boldsymbol{\phi}}_{x_n}^{hll2D}$, $\widetilde{\boldsymbol{\phi}}_{x_s}^{hll2D}$, $\widetilde{\boldsymbol{\phi}}_{y_e}^{hll2D}$ and $\widetilde{\boldsymbol{\phi}}_{y_w}^{hll2D}$

1: $\tilde{s}_y = \max(|\tilde{s}_n|, |\tilde{s}_s|)$
2: $\tilde{s}_x = \max(|\tilde{s}_e|, |\tilde{s}_w|)$
3:
4: **if** ($\tilde{s}_w \geq 0$ and $\tilde{s}_s \geq 0$) **then**
5: $\quad \widetilde{\boldsymbol{\phi}}_{x_n}^{hll2D} \leftarrow [(\tilde{s}_n - \tilde{s}_s)\boldsymbol{f}_{*w} + \tilde{s}_s \boldsymbol{f}_{sw}]/\tilde{s}_n$
6: $\quad \widetilde{\boldsymbol{\phi}}_{x_s}^{hll2D} \leftarrow \boldsymbol{f}_{sw}$
7: $\quad \widetilde{\boldsymbol{\phi}}_{y_e}^{hll2D} \leftarrow [(\tilde{s}_e - \tilde{s}_w)\boldsymbol{g}_{s*} + \tilde{s}_w \boldsymbol{g}_{sw}]/\tilde{s}_e$
8: $\quad \widetilde{\boldsymbol{\phi}}_{y_w}^{hll2D} \leftarrow \boldsymbol{g}_{sw}$
9: **else if** ($\tilde{s}_w \geq 0$ and $\tilde{s}_n \leq 0$) **then**
10: $\quad \widetilde{\boldsymbol{\phi}}_{x_n}^{hll2D} \leftarrow \boldsymbol{f}_{nw}$
11: $\quad \widetilde{\boldsymbol{\phi}}_{x_s}^{hll2D} \leftarrow [(\tilde{s}_s - \tilde{s}_n)\boldsymbol{f}_{*w} + \tilde{s}_n \boldsymbol{f}_{nw}]/\tilde{s}_s$
12: $\quad \widetilde{\boldsymbol{\phi}}_{y_e}^{hll2D} \leftarrow [(\tilde{s}_e - \tilde{s}_w)\boldsymbol{g}_{n*} + \tilde{s}_w \boldsymbol{g}_{nw}]/\tilde{s}_e$
13: $\quad \widetilde{\boldsymbol{\phi}}_{y_w}^{hll2D} \leftarrow \boldsymbol{g}_{nw}$
14: **else if** ($\tilde{s}_e \leq 0$ and $\tilde{s}_s \geq 0$) **then**
15: $\quad \widetilde{\boldsymbol{\phi}}_{x_n}^{hll2D} \leftarrow [(\tilde{s}_n - \tilde{s}_s)\boldsymbol{f}_{*e} + \tilde{s}_s \boldsymbol{f}_{se}]/\tilde{s}_n$
16: $\quad \widetilde{\boldsymbol{\phi}}_{x_s}^{hll2D} \leftarrow \boldsymbol{f}_{se}$
17: $\quad \widetilde{\boldsymbol{\phi}}_{y_e}^{hll2D} \leftarrow \boldsymbol{g}_{se}$
18: $\quad \widetilde{\boldsymbol{\phi}}_{y_w}^{hll2D} \leftarrow [(\tilde{s}_w - \tilde{s}_e)\boldsymbol{g}_{s*} + \tilde{s}_e \boldsymbol{g}_{se}]/\tilde{s}_w$
19: **else if** ($\tilde{s}_e \leq 0$ and $\tilde{s}_n \leq 0$) **then**
20: $\quad \widetilde{\boldsymbol{\phi}}_{x_n}^{hll2D} \leftarrow \boldsymbol{f}_{ne}$
21: $\quad \widetilde{\boldsymbol{\phi}}_{x_s}^{hll2D} \leftarrow [(\tilde{s}_s - \tilde{s}_n)\boldsymbol{f}_{*e} + \tilde{s}_n \boldsymbol{f}_{ne}]/\tilde{s}_s$
22: $\quad \widetilde{\boldsymbol{\phi}}_{y_e}^{hll2D} \leftarrow \boldsymbol{g}_{ne}$
23: $\quad \widetilde{\boldsymbol{\phi}}_{y_w}^{hll2D} \leftarrow [(\tilde{s}_w - \tilde{s}_e)\boldsymbol{g}_{n*} + \tilde{s}_e \boldsymbol{g}_{ne}]/\tilde{s}_w$
24: **else if** $\tilde{s}_w \geq 0$ **then**

25: $\quad \widetilde{\boldsymbol{\phi}}_{x_n}^{hll2D} \leftarrow [(\tilde{s}_y - \tilde{s}_n)\boldsymbol{f}_{nw} + \tilde{s}_n \boldsymbol{f}_{*w}]/\tilde{s}_y$
26: $\quad \widetilde{\boldsymbol{\phi}}_{x_s}^{hll2D} \leftarrow [(\tilde{s}_y + \tilde{s}_s)\boldsymbol{f}_{sw} - \tilde{s}_s \boldsymbol{f}_{*w}]/\tilde{s}_y$
27: $\quad \widetilde{\boldsymbol{\phi}}_{y_e}^{hll2D} \leftarrow [(\tilde{s}_e - \tilde{s}_w)\boldsymbol{g}_{**} + \tilde{s}_w \boldsymbol{g}_{*w}]/\tilde{s}_e$
28: $\quad \widetilde{\boldsymbol{\phi}}_{y_w}^{hll2D} \leftarrow \boldsymbol{g}_{*w}$
29: **else if** $\tilde{s}_e \leq 0$ **then**
30: $\quad \widetilde{\boldsymbol{\phi}}_{x_n}^{hll2D} \leftarrow [(\tilde{s}_y - \tilde{s}_n)\boldsymbol{f}_{ne} + \tilde{s}_n \boldsymbol{f}_{*e}]/\tilde{s}_y$
31: $\quad \widetilde{\boldsymbol{\phi}}_{x_s}^{hll2D} \leftarrow [(\tilde{s}_y + \tilde{s}_s)\boldsymbol{f}_{se} - \tilde{s}_s \boldsymbol{f}_{*e}]/\tilde{s}_y$
32: $\quad \widetilde{\boldsymbol{\phi}}_{y_e}^{hll2D} \leftarrow \boldsymbol{g}_{*e}$
33: $\quad \widetilde{\boldsymbol{\phi}}_{y_w}^{hll2D} \leftarrow [(\tilde{s}_w - \tilde{s}_e)\boldsymbol{g}_{**} + \tilde{s}_e \boldsymbol{g}_{*e}]/\tilde{s}_w$
34: **else if** $\tilde{s}_s \geq 0$ **then**
35: $\quad \widetilde{\boldsymbol{\phi}}_{x_n}^{hll2D} \leftarrow [(\tilde{s}_n - \tilde{s}_s)\boldsymbol{f}_{**} + \tilde{s}_s \boldsymbol{f}_{s*}]/\tilde{s}_n$
36: $\quad \widetilde{\boldsymbol{\phi}}_{x_s}^{hll2D} \leftarrow \boldsymbol{f}_{s*}$
37: $\quad \widetilde{\boldsymbol{\phi}}_{y_e}^{hll2D} \leftarrow [(\tilde{s}_x - \tilde{s}_e)\boldsymbol{g}_{se} + \tilde{s}_e \boldsymbol{g}_{s*}]/\tilde{s}_x$
38: $\quad \widetilde{\boldsymbol{\phi}}_{y_w}^{hll2D} \leftarrow [(\tilde{s}_x + \tilde{s}_w)\boldsymbol{g}_{sw} - \tilde{s}_w \boldsymbol{g}_{s*}]/\tilde{s}_x$
39: **else if** $\tilde{s}_n \leq 0$ **then**
40: $\quad \widetilde{\boldsymbol{\phi}}_{x_n}^{hll2D} \leftarrow \boldsymbol{f}_{n*}$
41: $\quad \widetilde{\boldsymbol{\phi}}_{x_s}^{hll2D} \leftarrow [(\tilde{s}_s - \tilde{s}_n)\boldsymbol{f}_{**} + \tilde{s}_n \boldsymbol{f}_{n*}]/\tilde{s}_s$
42: $\quad \widetilde{\boldsymbol{\phi}}_{y_e}^{hll2D} \leftarrow [(\tilde{s}_x - \tilde{s}_e)\boldsymbol{g}_{ne} + \tilde{s}_e \boldsymbol{g}_{n*}]/\tilde{s}_x$
43: $\quad \widetilde{\boldsymbol{\phi}}_{y_w}^{hll2D} \leftarrow [(\tilde{s}_x + \tilde{s}_w)\boldsymbol{g}_{nw} - \tilde{s}_w \boldsymbol{g}_{n*}]/\tilde{s}_x$
44: **else**
45: $\quad \widetilde{\boldsymbol{\phi}}_{x_n}^{hll2D} \leftarrow [(\tilde{s}_y - \tilde{s}_n)\boldsymbol{f}_{n*} + \tilde{s}_n \boldsymbol{f}_{**}]/\tilde{s}_y$
46: $\quad \widetilde{\boldsymbol{\phi}}_{x_s}^{hll2D} \leftarrow [(\tilde{s}_y + \tilde{s}_s)\boldsymbol{f}_{s*} - \tilde{s}_s \boldsymbol{f}_{**}]/\tilde{s}_y$
47: $\quad \widetilde{\boldsymbol{\phi}}_{y_e}^{hll2D} \leftarrow [(\tilde{s}_x - \tilde{s}_e)\boldsymbol{g}_{*e} + \tilde{s}_e \boldsymbol{g}_{**}]/\tilde{s}_x$
48: $\quad \widetilde{\boldsymbol{\phi}}_{y_w}^{hll2D} \leftarrow [(\tilde{s}_x + \tilde{s}_w)\boldsymbol{g}_{*w} - \tilde{s}_w \boldsymbol{g}_{**}]7/\tilde{s}_x$

B.3 Cases I-IV of the Solution $\boldsymbol{\mathcal{W}}_\delta$

We provide the following pieces of pseudocode to aid in the numerical implementation of the four distinct cases associated with the solution $\boldsymbol{\mathcal{W}}_\delta$ obtained in Section 4.2:

Algorithm 5 Defining the jumps and wave speeds, followed by the cases

---

1: $[\![\psi]\!] \leftarrow \psi_r - \psi_l$
2: $[\![\pi]\!] \leftarrow (\pi_r - \pi_l) + a^2 (\tau_r - \tau_l)$

3: $\sigma \quad \leftarrow \frac{1}{2}\left(u_l + u_r - [\![\tilde{\pi}]\!]/a\right)$

4:

5: $s_0 \leftarrow 0$

6: $s_l \leftarrow u_l - a\,\tau_l$

7: $s_r \leftarrow u_r + a\,\tau_r$

8:

9: **if** $(s_l > 0)$ **then**

10:     go to **Algorithm 6**

11: **else if** $(s_l < 0$ and $\sigma \geq 0)$ **then**

12:     go to **Algorithm 7**

13: **else if** $(s_r > 0$ and $\sigma \leq 0)$ **then**

14:     go to **Algorithm 8**

15: **else**

16:     go to **Algorithm 9**

Algorithm 6 Case I: $s_l > 0$

1: **if** $(2[\![\psi]\!] > (u_l^2 - a^2\tau_l^2))$ **then**

2:     **print** "Automatic adjustment of a."

3:     ADJUST_A$(1.01\,a)$

4:     go to **Algorithm 5**

5:

6: $\text{var} \leftarrow \sqrt{1 - 2[\![\psi]\!]/(u_l^2 - a^2\tau_l^2)}$

7:

8: **if** $(\,|[\![\tilde{\pi}]\!]| \geq a(s_r - s_l\,\text{var}))$ **then**   ▷ Degenerate

9:     **print** "Degenerate case"

10:     eps $\leftarrow$ 1.0e-12

11:

12:     **if** $(\,|u_l| < \text{eps})$ **then**

13:         go to **Case II**

14:     **else**

15:         ADJUST_A$(1.01\,u_l/\tau_l)$

16:         go to **Algorithm 5**

17:

18: $\tau_l^* \quad\leftarrow \tau_l\,\text{var}$ ▷ Density

19: $\tau_l^{**} \leftarrow (s_r - [\![\tilde{\pi}]\!]/a - s_l\,\text{var})/(2a)$

20: $\tau_r^* \quad\leftarrow \tau_l^{**} + [\![\tilde{\pi}]\!]/a^2$

21:

22: $\rho_l^* \quad\leftarrow 1/\tau_l^*$

23: $\rho_l^{**} \leftarrow 1/\tau_l^{**}$

24: $\rho_r^* \quad\leftarrow 1/\tau_r^*$

25:

26: $u_l^* \quad\leftarrow u_l\,\tau_l^*/\tau_l$ ▷ Velocity

27: $u_l^{**} \leftarrow u_l^* + a(\tau_l^{**} - \tau_l^*)$

28: $u_r^* \quad\leftarrow u_l^{**}$

29: $s_m \quad\leftarrow u_l^{**}$

30:

31: $\boldsymbol{u}_l^* \quad\leftarrow (u_l^* - u_l)\boldsymbol{e} + \boldsymbol{u}_l$

32: $\boldsymbol{u}_l^{**} \leftarrow (u_l^{**} - u_l)\boldsymbol{e} + \boldsymbol{u}_l$

33: $\boldsymbol{u}_r^* \quad\leftarrow (u_r^* - u_r)\boldsymbol{e} + \boldsymbol{u}_r$

34:

35: $\pi_l^* \quad\leftarrow \pi_l + a^2(\tau_l - \tau_l^*)$ ▷ Pressure

36: $\pi_l^{**} \leftarrow \pi_l + a^2(\tau_l - \tau_l^{**})$

37: $\pi_r^* \quad\leftarrow \pi_l^{**}$

38:

39: **if** (not isothermal) **then**   ▷ Energy

40:     $\epsilon_l^* \quad\leftarrow \epsilon_l + ((\pi_l^*)^2 - \pi_l^2)/(2a^2)$

41:     $\epsilon_l^{**} \leftarrow \epsilon_l + ((\pi_l^{**})^2 - \pi_l^2)/(2a^2)$

42:     $\epsilon_r^* \quad\leftarrow \epsilon_r + ((\pi_r^*)^2 - \pi_r^2/(2a^2)$

43:

44:     $(\rho e)_l^* \quad\leftarrow \rho_l^* \ (\epsilon_l^* + |\boldsymbol{u}_l^*|^2/2)$

45:     $(\rho e)_l^{**} \leftarrow \rho_l^{**}(\epsilon_l^{**} + |\boldsymbol{u}_l^{**}|^2/2)$

46:     $(\rho e)_r^* \quad\leftarrow \rho_r^* \ (\epsilon_r^* + |\boldsymbol{u}_r^*|^2/2)$

47:

48: $\boldsymbol{s} \leftarrow (s_0, s_l, s_m, s_r)^T$ ▷ Wave speeds

49:

50: $\boldsymbol{M}_s(1,3) \leftarrow \rho_l^{**}$ ▷ Solution

51: $\boldsymbol{M}_s(2:\vartheta-1,3) \leftarrow \rho_l^{**}\boldsymbol{u}_l^{**}$

52:

53: **if** (not isothermal) **then**

54:     $\boldsymbol{M}_s(\vartheta,3) \leftarrow (\rho e)_l^{**}$

55:

56: $\rho_{sol} \leftarrow \rho_l^*$

57: $\boldsymbol{u}_{sol} \leftarrow \boldsymbol{u}_l^*$

58: $\pi_{sol} \leftarrow \pi_l^*$

Algorithm 7 Case II: $s_l < 0 < s_r$, $\sigma > 0$

1: $\alpha \leftarrow s_r - [\![\tilde{\pi}]\!]/a$
2: $\text{sgn} \leftarrow \alpha/|\alpha|$
3:
4: $\text{var} \leftarrow \sqrt{([\![\psi]\!]/s_l)^2 + \alpha^2}$
5:
6: $\tau_l^* \;\leftarrow (-s_l + [\![\psi]\!]/s_l + \text{sgn} \, \text{var})/(2a)$ ▷ Density
7: $\tau_l^{**} \leftarrow (\alpha + [\![\psi]\!]/\alpha + \sqrt{([\![\psi]\!]/\alpha)^2 + s_l^2})/(2a)$
8: $\tau_r^* \;\leftarrow \tau_l^{**} + [\![\tilde{\pi}]\!]/a^2$
9:
10: $\rho_l^* \;\leftarrow 1/\tau_l^*$
11: $\rho_l^{**} \leftarrow 1/\tau_l^{**}$
12: $\rho_r^* \;\leftarrow 1/\tau_r^*$
13:
14: $u_l^* \;\leftarrow s_l + a\tau_l^*$ ▷ Velocity
15: $u_l^{**} \leftarrow u_l^*(\tau_l^{**}/\tau_l^*)$
16: $u_r^* \;\leftarrow u_l^{**}$
17: $s_m \leftarrow u_l^{**}$
18:
19: $\boldsymbol{u}_l^* \;\leftarrow (u_l^* - u_l)\boldsymbol{e} + \boldsymbol{u}_l$
20: $\boldsymbol{u}_l^{**} \leftarrow (u_l^{**} - u_l)\boldsymbol{e} + \boldsymbol{u}_l$
21: $\boldsymbol{u}_r^* \;\leftarrow (u_r^* - u_r)\boldsymbol{e} + \boldsymbol{u}_r$

22:
23: $\pi_l^* \;\leftarrow \pi_l + a^2(\tau_l - \tau_l^*)$ ▷ Pressure
24: $\pi_l^{**} \leftarrow \pi_l + a^2(\tau_l - \tau_l^{**})$
25: $\pi_r^* \;\leftarrow \pi_l^{**}$
26:
27: **if** (not isothermal) **then** ▷ Energy
28: $\quad \epsilon_l^* \;\leftarrow \epsilon_l + ((\pi_l^*)^2 - \pi_l^2)/(2a^2)$
29: $\quad \epsilon_l^{**} \leftarrow \epsilon_l + ((\pi_l^{**})^2 - \pi_l^2)/(2a^2)$
30: $\quad \epsilon_r^* \;\leftarrow \epsilon_r + ((\pi_r^*)^2 - \pi_r^2/(2a^2)$
31:
32: $\quad (\rho e)_l^* \;\leftarrow \rho_l^* \;(\epsilon_l^* + |\boldsymbol{u}_l^*|^2/2)$
33: $\quad (\rho e)_l^{**} \leftarrow \rho_l^{**}(\epsilon_l^{**} + |\boldsymbol{u}_l^{**}|^2/2)$
34: $\quad (\rho e)_r^* \;\leftarrow \rho_r^* \;(\epsilon_r^* + |\boldsymbol{u}_r^*|^2/2)$
35:
36: $\boldsymbol{s} \leftarrow (s_l, s_0, s_m, s_r)^T$ ▷ Wave speeds
37:
38: $\boldsymbol{M}_s(1,3) \leftarrow \rho_l^{**}$ ▷ Solution
39: $\boldsymbol{M}_s(2:\vartheta-1,3) \leftarrow \rho_l^{**}\boldsymbol{u}_l^{**}$
40: **if** (not isothermal) **then** $\boldsymbol{M}_s(\vartheta,3) \leftarrow (\rho e)_l^{**}$
41:
42: $\rho_{sol}, \boldsymbol{u}_{sol}, \pi_{sol} \leftarrow \rho_l^{**}, \boldsymbol{u}_l^{**}, \pi_l^{**}$

Algorithm 8 Case III: $s_l < 0 < s_r$, $\sigma < 0$

1: $\beta \leftarrow s_l - [\![\tilde{\pi}]\!]/a$
2: $\text{sgn} \leftarrow \beta/|\beta|$
3:
4: $\text{var} \leftarrow \sqrt{([\![\psi]\!]/s_r)^2 + \beta^2}$
5:
6: $\tau_r^* \;\leftarrow (s_r + [\![\psi]\!]/s_r - \text{sgn} \, \text{var})/(2a)$ ▷ Density
7: $\tau_r^{**} \leftarrow (-\beta + [\![\psi]\!]/\beta + \sqrt{([\![\psi]\!]/\beta)^2 + s_r^2})/(2a)$
8: $\tau_l^* \;\leftarrow \tau_r^{**} - [\![\tilde{\pi}]\!]/a^2$
9:
10: $\rho_r^* \;\leftarrow 1/\tau_r^*$
11: $\rho_r^{**} \leftarrow 1/\tau_r^{**}$
12: $\rho_l^* \;\leftarrow 1/\tau_l^*$
13:
14: $u_r^* \;\leftarrow s_r - a\tau_r^*$ ▷ Velocity
15: $u_r^{**} \leftarrow u_r^*(\tau_r^{**}/\tau_r^*)$
16: $u_l^* \;\leftarrow u_r^{**}$
17: $s_m \leftarrow u_r^{**}$
18:
19: $\boldsymbol{u}_r^* \;\leftarrow (u_r^* - u_r)\boldsymbol{e} + \boldsymbol{u}_r$
20: $\boldsymbol{u}_r^{**} \leftarrow (u_r^{**} - u_r)\boldsymbol{e} + \boldsymbol{u}_r$
21: $\boldsymbol{u}_l^* \;\leftarrow (u_l^* - u_l)\boldsymbol{e} + \boldsymbol{u}_l$

22:
23: $\pi_r^* \;\leftarrow \pi_r + a^2(\tau_r - \tau_r^*)$ ▷ Pressure
24: $\pi_r^{**} \leftarrow \pi_r + a^2(\tau_r - \tau_r^{**})$
25: $\pi_l^* \;\leftarrow \pi_r^{**}$
26:
27: **if** (not isothermal) **then** ▷ Energy
28: $\quad \epsilon_r^* \;\leftarrow \epsilon_r + ((\pi_r^*)^2 - \pi_r^2)/(2a^2)$
29: $\quad \epsilon_r^{**} \leftarrow \epsilon_r + ((\pi_r^{**})^2 - \pi_r^2)/(2a^2)$
30: $\quad \epsilon_l^* \;\leftarrow \epsilon_l + ((\pi_l^*)^2 - \pi_l^2/(2a^2)$
31:
32: $\quad (\rho e)_r^* \;\leftarrow \rho_r^* \;(\epsilon_r^* + |\boldsymbol{u}_r^*|^2/2)$
33: $\quad (\rho e)_r^{**} \leftarrow \rho_r^{**}(\epsilon_r^{**} + |\boldsymbol{u}_r^{**}|^2/2)$
34: $\quad (\rho e)_l^* \;\leftarrow \rho_l^* \;(\epsilon_l^* + |\boldsymbol{u}_l^*|^2/2)$
35:
36: $\boldsymbol{s} \leftarrow (s_l, s_m, s_0, s_r)^T$ ▷ Wave speeds
37:
38: $\boldsymbol{M}_s(1,3) \leftarrow \rho_r^{**}$ ▷ Solution
39: $\boldsymbol{M}_s(2:\vartheta-1,3) \leftarrow \rho_r^{**}\boldsymbol{u}_r^{**}$
40: **if** (not isothermal) **then** $\boldsymbol{M}_s(\vartheta,3) \leftarrow (\rho e)_r^{**}$
41:
42: $\rho_{sol}, \boldsymbol{u}_{sol}, \pi_{sol} \leftarrow \rho_r^{**}, \boldsymbol{u}_r^{**}, \pi_r^{**}$

Algorithm 9 Case IV: $s_r < 0$

1: **if** $(2[\![\psi]\!] < -(u_r^2 - a^2\tau_r^2))$ **then**
2:     **print** "Automatic adjustment of a."
3:     ADJUST_A$(1.01\,a)$
4:     go to **Algorithm 5**
5:
6: var $\leftarrow \sqrt{1 + 2[\![\psi]\!]/(u_r^2 - a^2\tau_r^2)}$
7:
8: **if** $(|[\![\tilde\pi]\!]| \geq a(-s_l + s_r\,\text{var}))$ **then** ▷ Degenerate
9:     **print** "Degenerate case"
10:     eps $\leftarrow$1.0e-12
11:
12:     **if** $(|u_r| < \text{eps})$ **then**
13:         go to **Case III**
14:     **else**
15:         ADJUST_A$(-1.01\,u_r/\tau_r)$
16:         go to **Algorithm 5**
17:
18: $\tau_r^* \leftarrow \tau_r\,\text{var}$ ▷ Density
19: $\tau_r^{**} \leftarrow (-s_l + [\![\tilde\pi]\!]/a + s_r\,\text{var})/(2a)$
20: $\tau_l^* \leftarrow \tau_r^{**} - [\![\tilde\pi]\!]/a^2$
21:
22: $\rho_r^* \leftarrow 1/\tau_r^*$
23: $\rho_r^{**} \leftarrow 1/\tau_r^{**}$
24: $\rho_l^* \leftarrow 1/\tau_l^*$
25:
26: $u_r^* \leftarrow u_r\,\tau_r^*/\tau_r$ ▷ Velocity
27: $u_r^{**} \leftarrow u_r^* + a(\tau_r^* - \tau_r^{**})$
28: $u_l^* \leftarrow u_r^{**}$
29: $s_m \leftarrow u_r^{**}$

30:
31: $\boldsymbol{u}_r^* \leftarrow (u_r^* - u_r)\boldsymbol{e} + \boldsymbol{u}_r$
32: $\boldsymbol{u}_r^{**} \leftarrow (u_r^{**} - u_r)\boldsymbol{e} + \boldsymbol{u}_r$
33: $\boldsymbol{u}_l^* \leftarrow (u_l^* - u_l)\boldsymbol{e} + \boldsymbol{u}_l$
34:
35: $\pi_r^* \leftarrow \pi_r + a^2(\tau_r - \tau_r^*)$ ▷ Pressure
36: $\pi_r^{**} \leftarrow \pi_r + a^2(\tau_r - \tau_r^{**})$
37: $\pi_l^* \leftarrow \pi_r^{**}$
38:
39: **if** (not isothermal) **then**   ▷ Energy
40:     $\epsilon_r^* \leftarrow \epsilon_r + ((\pi_r^*)^2 - \pi_r^2)/(2a^2)$
41:     $\epsilon_r^{**} \leftarrow \epsilon_r + ((\pi_r^{**})^2 - \pi_r^2)/(2a^2)$
42:     $\epsilon_l^* \leftarrow \epsilon_l + ((\pi_l^*)^2 - \pi_l^2/(2a^2)$
43:
44:     $(\rho e)_r^* \leftarrow \rho_r^*\,(\epsilon_r^* + |\boldsymbol{u}_r^*|^2/2)$
45:     $(\rho e)_r^{**} \leftarrow \rho_r^{**}(\epsilon_r^{**} + |\boldsymbol{u}_r^{**}|^2/2)$
46:     $(\rho e)_l^* \leftarrow \rho_l^*\,(\epsilon_l^* + |\boldsymbol{u}_l^*|^2/2)$
47:
48: $\boldsymbol{s} \leftarrow (s_l, s_m, s_r, s_0)^T$ ▷ Wave speeds
49:
50: $\boldsymbol{M}_s(1,3) \leftarrow \rho_r^{**}$ ▷ Solution
51: $\boldsymbol{M}_s(2:\vartheta-1,3) \leftarrow \rho_r^{**}\boldsymbol{u}_r^{**}$
52:
53: **if** (not isothermal) **then**
54:     $\boldsymbol{M}_s(\vartheta,3) \leftarrow (\rho e)_r^{**}$
55:
56: $\rho_{sol} \leftarrow \rho_r^*$
57: $\boldsymbol{u}_{sol} \leftarrow \boldsymbol{u}_r^*$
58: $\pi_{sol} \leftarrow \pi_r^*$

Algorithm 10 Final solution

1: $\boldsymbol{M}_s(1,1) \leftarrow \rho_l$
2: $\boldsymbol{M}_s(1,2) \leftarrow \rho_l^*$
3: $\boldsymbol{M}_s(1,4) \leftarrow \rho_r^*$
4: $\boldsymbol{M}_s(1,5) \leftarrow \rho_r$
5:
6: $\boldsymbol{M}_s(2:\vartheta-1,1) \leftarrow \rho_l\boldsymbol{u}_l$
7: $\boldsymbol{M}_s(2:\vartheta-1,2) \leftarrow \rho_l^*\boldsymbol{u}_l^*$
8: $\boldsymbol{M}_s(2:\vartheta-1,4) \leftarrow \rho_r^*\boldsymbol{u}_r^*$
9: $\boldsymbol{M}_s(2:\vartheta-1,5) \leftarrow \rho_r\boldsymbol{u}_r$

10:
11: **if** (not isothermal) **then**
12:     $\boldsymbol{M}_s(\vartheta,1) \leftarrow (\rho e)_l$
13:     $\boldsymbol{M}_s(\vartheta,2) \leftarrow (\rho e)_l^*$
14:     $\boldsymbol{M}_s(\vartheta,4) \leftarrow (\rho e)_r^*$
15:     $\boldsymbol{M}_s(\vartheta,5) \leftarrow (\rho e)_r$
16:
17: $\boldsymbol{\phi}^l, \boldsymbol{\phi}^r \leftarrow$ GET_FLUX$(\boldsymbol{s}, \boldsymbol{M}_s)$

List of Figures

List of Tables

Bibliography

[1] ITER: The project. http://www.iter.org/proj. Accessed: 2014-08-25.

[2] R. Abgrall. Approximation du problème de Riemann vraiment multidimensionnel des équations d'Euler par une méthode de type Roe (I): La linéarisation. *Comptes Rendus de l'Académie des Sciences. Série 1, Mathématique*, 319(5):499–504, 1994.

[3] R. Abgrall. Approximation du problème de Riemann vraiment multidimensionnel des équations d'Euler par une méthode de type Roe (II): Solution du problème de Riemann approché. *Comptes Rendus de l'Académie des Sciences. Série 1, Mathématique*, 319(6):625–629, 1994.

[4] R. Abgrall and S. Karni. A relaxation scheme for the two-layer shallow water system. In *Hyperbolic Problems: Theory, Numerics, Applications*, pages 135–144. Springer Berlin Heidelberg, 2008.

[5] D. Aregba-Driollet and C. Berthon. Numerical approximation of Kerr-Debye equations. Preprint hal-00293728, 2008.

[6] G. Arfken. *Mathematical Methods for Physicists*. Academic Press, 3rd edition, 1985.

[7] S. A. Balbus and J. C. Papaloizou. On the dynamical foundations of α disks. *The Astrophysical Journal*, 521:650–658, 1999.

[8] D. S. Balsara. Linearized formulation of the Riemann problem for adiabatic and isothermal magnetohydrodynamics. *The Astrophysical Journal Supplement Series*, 116(1):119, 1998.

[9] D. S. Balsara. Multidimensional HLLE Riemann solver: Application to Euler and magnetohydrodynamic flows. *Journal of Computational Physics*, 229(6):1970–1993, 2010.

[10] D. S. Balsara. A two-dimensional HLLC Riemann solver for conservation laws: Application to Euler and magnetohydrodynamic flows. *Journal of Computational Physics*, 231(22):7476–7503, 2012.

[11] D. S. Balsara, M. Dumbser, and R. Abgrall. Multidimensional HLLC Riemann solver for unstructured meshes - With application to Euler and MHD flows. *Journal of Computational Physics*, 261(0):172–208, 2014.

[12] D. S. Balsara and D. S. Spicer. A staggered mesh algorithm using high order Godunov fluxes to ensure solenoidal magnetic fields in magnetohydrodynamic simulations. *Journal of Computational Physics*, 149(2):270–292, 1999.

[13] T. Barth. On the role of involutions in the discontinuous Galerkin discretization of Maxwell and magnetohydrodynamic systems. In *Compatible Spatial Discretizations*, volume 142 of *The IMA Volumes in Mathematics and its Applications*, pages 69–88. Springer New York, 2006.

[14] M. Baudin, C. Berthon, F. Coquel, R. Masson, and Q. H. Tran. A relaxation method for two-phase flow models with hydrodynamic closure law. *Numerische Mathematik*, 99(3):411–440, 2005.

[15] C. Berthon. Stability of the MUSCL schemes for the Euler equations. *Communications in Mathematical Sciences*, 3(2):133–157, 2005.

[16] C. Berthon. Numerical approximations of the 10-moment Gaussian closure. *Mathematics of Computation*, 75(256):1809–1831, 2006.

[17] C. Berthon, B. Braconnier, and B. Nkonga. Numerical approximation of a degenerated non-conservative multifluid model: Relaxation scheme. *International Journal for Numerical Methods in Fluids*, 48(1):85–90, 2005.

[18] C. Berthon, M. Breuß, and M.-O. Titeux. A relaxation scheme for the approximation of the pressureless Euler equations. *Numerical Methods for Partial Differential Equations*, 22(2):484–505, 2006.

[19] C. Berthon, P. Charrier, and B. Dubroca. An HLLC scheme to solve the M1 model of radiative transfer in two space dimensions. *Journal of Scientific Computing*, 31(3):347–389, 2007.

[20] C. Berthon and F. Marche. A positive preserving high order VFRoe scheme for shallow water equations: A class of relaxation schemes. *SIAM Journal on Scientific Computing*, 30(5):2587–2612, 2008.

[21] S. J. Billett and E. F. Toro. Unsplit WAF-type schemes for three dimensional hyperbolic conservation laws. In E. F. Toro and J. F. Clarke, editors, *Numerical Methods for Wave Propagation*, volume 47 of *Fluid Mechanics and Its Applications*, pages 75–124. Springer Netherlands, 1998.

[22] A. Bonnement, T. Fajraoui, H. Guillard, M. Martin, A. Mouton, B. Nkonga, and A. Sangam. Finite volume method in curvilinear coordinates for hyperbolic conservation laws. In *ESAIM: Proc.*, volume 32, pages 163–176, 2011.

[23] F. Bouchut. *Nonlinear stability of finite volume methods for hyperbolic conservation laws, and well-balanced schemes for sources*. Frontiers in Mathematics. Birkhäuser, 2004.

[24] J. U. Brackbill and D. C. Barnes. The effect of nonzero $\nabla \cdot \mathbf{B}$ on the numerical solution of the magnetohydrodynamic equations. *Journal of Computational Physics*, 35(3):426–430, 1980.

[25] M. Brio and C. C. Wu. An upwind differencing scheme for the equations of ideal magnetohydrodynamics. *Journal of Computational Physics*, 75:400–422, 1988.

[26] M. Brio, A. R. Zakharian, and G. M. Webb. Two-dimensional Riemann solver for Euler equations of gas dynamics. *Journal of Computational Physics*, 167(1):177–195, 2001.

[27] P. Cargo and G. Gallice. Roe matrices for ideal MHD and systematic construction of Roe matrices for systems of conservation laws. *Journal of Computational Physics*, 136(2):446 – 466, 1997.

[28] C. Chalons and F. Coquel. Navier-Stokes equations with several independent pressure laws and explicit predictor-corrector schemes. *Numerische Mathematik*, 101(3):451–478, 2005.

[29] C. Chalons and J.-F. Coulombel. Relaxation approximation of the Euler equations. *Journal of Mathematical Analysis and Applications*, 348(2):872–893, 2008.

[30] T. Chang, G.-Q. Chen, and S. Yang. On the 2-D Riemann problem for the compressible Euler equations. I. Interaction of shocks and rarefaction waves. *Discrete and Continuous Dynamical Systems*, 1:555–584, 1995.

[31] F. F. Chen. *Introduction to Plasma Physics and Controlled Fusion*. Number v. 1 in Introduction to Plasma Physics and Controlled Fusion. Springer, 1984.

[32] G.-Q. Chen, C. D. Levermore, and T.-P. Liu. Hyperbolic conservation laws with stiff relaxation terms and entropy. *Communications on Pure and Applied Mathematics*, 47(6):787–830, 1994.

[33] J.-P. Chièze. Elements of hydrodynamics applied to the interstellar medium. In *Starbursts Triggers, Nature, and Evolution*, volume 9 of *Centre de Physique des Houches*, pages 77–100. Springer Berlin Heidelberg, 1998.

[34] C. Chiosi. Hertzsprung-Russell Diagram. In P. Murdin, editor, *Encyclopedia of Astronomy and Astrophysics*. 2000.

[35] A. J. Chorin. Random choice solution of hyperbolic systems. *Journal of Computational Physics*, 22(4):517–533, 1976.

[36] F. Coquel and B. Perthame. Relaxation of energy and approximate Riemann solvers for general pressure laws in fluid dynamics. *SIAM Journal on Numerical Analysis*, 35(6):2223–2249, 1998.

[37] R. Courant and K. Friedrichs. *Supersonic flow and shock waves*. Interscience Publishers, New York, 1948.

[38] R. Courant, K. Friedrichs, and H. Lewy. Über die partiellen differenzengleichungen der mathematischen physik. *Mathematische Annalen*, 100(1):32–74, 1928.

[39] P. Crispel, P. Degond, and M.-H. Vignal. An asymptotically stable discretization for the Euler-Poisson system in the quasi-neutral limit. *Comptes Rendus Mathematique*, 341(5):323–328, 2005.

[40] P. Crispel, P. Degond, and M.-H. Vignal. An asymptotic preserving scheme for the two-fluid Euler-Poisson model in the quasineutral limit. *Journal of Computational Physics*, 223(1):208–234, 2007.

[41] W. Dai and P. R. Woodward. On the divergence-free condition and conservation laws in numerical simulations for supersonic magnetohydrodynamical flows. *The Astrophysical Journal*, 494(1):317, 1998.

[42] P. A. Davidson. *An Introduction to Magnetohydrodynamics*. Cambridge Texts in Applied Mathematics. Cambridge University Press, 2001.

[43] H. Deconinck and R. Abgrall. Introduction to residual distribution methods. *Lecture Series-Von Karman Institute for Fluid Dynamics*, 1:4, 2006.

[44] H. Deconinck, K. Sermeus, and R. Abgrall. Status of multidimensional upwind residual distribution schemes and applications in aeronautics. In *Proceedings of the AIAA Fluids 2000 Conference, Denver, 2000, paper 2000-2328, 19 pp*, 2000.

[45] A. Dedner, F. Kemm, D. Kröner, C.-D. Munz, T. Schnitzer, and M. Wesenberg. Hyperbolic divergence cleaning for the MHD equations. *Journal of Computational Physics*, 175(2):645–673, 2002.

[46] P. Degond, F. Deluzet, A. Sangam, and M.-H. Vignal. An asymptotic preserving scheme for the Euler equations in a strong magnetic field. *Journal of Computational Physics*, 228(10):3540–3558, 2009.

[47] P. Degond, S. Jin, and J.-G. Liu. Mach-number uniform asymptotic-preserving gauge schemes for compressible flows. *Bulletin of the Institute of Mathematics, Academia Sinica, New Series*, 2(4):851–892, 2007.

[48] P. Degond, J.-G. Liu, and M.-H. Vignal. Analysis of an asymptotic preserving scheme for the Euler-Poisson system in the quasineutral limit. *SIAM Journal on Numerical Analysis*, 46(3):1298–1322, 2008.

[49] B. Després and C. Mazeran. Lagrangian gas dynamics in two dimensions and Lagrangian systems. *Archive for Rational Mechanics and Analysis*, 178(3):327–372, 2005.

[50] B. Einfeldt. On Godunov-type methods for gas dynamics. *SIAM Journal on Numerical Analysis*, 25(2):294–318, 1988.

[51] B. Einfeldt, P. L. Roe, C. D. Munz, and B. Sjogreen. On Godunov-type methods near low densities. *Journal of Computational Physics*, 92:273–295, 1991.

[52] C. R. Evans and J. F. Hawley. Simulation of magnetohydrodynamic flows: A constrained transport method. *Astrophysical Journal, Part 1*, 332:659–677, 1988.

[53] L. C. Evans. *Partial Differential Equations.* Graduate studies in mathematics. American Mathematical Society, 2010.

[54] R. Eymard, T. Gallouët, and R. Herbin. Finite volume methods. *Handbook of Numerical Analysis*, 7:713–1018, 2000.

[55] S. Fabre. Stability analysis of the Euler-Poisson equations. *Journal of Computational Physics*, 101(2):445–451, 1992.

[56] M. Fey and M. Torrilhon. A constrained transport upwind scheme for divergence-free advection. In T. Y. Hou and E. Tadmor, editors, *Hyperbolic Problems: Theory, Numerics, Applications*, pages 529–538. Springer Berlin Heidelberg, 2003.

[57] A. Frank, T. W. Jones, D. Ryu, and J. B. Gaalaas. The Magnetohydrodynamic Kelvin-Helmholtz Instability: A Two-dimensional Numerical Study. *The Astrophysical Journal*, 460:777, 1996.

[58] S. Fromang, P. Hennebelle, and R. Teyssier. A high order Godunov scheme with constrained transport and adaptive mesh refinement for astrophysical MHD. *Astronomy & Astrophysics*, 457:371–384, 2006.

[59] J. M. Gallardo, C. Parés, and M. Castro. On a well-balanced high-order finite volume scheme for shallow water equations with topography and dry areas. *Journal of Computational Physics*, 227(1):574–601, 2007.

[60] T. Gallouët, J.-M. Hérard, and N. Seguin. Some approximate Godunov schemes to compute shallow-water equations with topography. *Computers & Fluids*, 32(4):479–513, 2003.

[61] T. A. Gardiner and J. M. Stone. An unsplit Godunov method for ideal MHD via constrained transport in three dimensions. *Journal of Computational Physics*, 227(8):4123–4141, 2008.

[62] J. Glimm. Solutions in the large for nonlinear hyperbolic systems of equations. *Communications on Pure and Applied Mathematics*, 18(4):697–715, 1965.

[63] J. Glimm and P. D. Lax. Decay of solutions of systems of hyperbolic conservation laws. *Bulletin of the American Mathematical Society*, 73(1):105–105, 1967.

[64] E. Godlewski and P.-A. Raviart. *Numerical approximation of hyperbolic systems of conservation laws*, volume 118. Springer, 1996.

[65] S. K. Godunov. A finite difference method for the numerical computation of discontinuous solutions of the equations of fluid dynamics. *Matematicheskii Sbornik*, 47:271–306, 1959.

[66] M. González, E. Audit, and P. Huynh. HERACLES: A three-dimensional radiation hydrodynamics code. *Astronomy & Astrophysics*, 464(2):429–435, 2007.

[67] J. J. Gottlieb and C. P. T. Groth. Assessment of Riemann solvers for unsteady one-dimensional inviscid flows of perfect gases. *Journal of Computational Physics*, 78(2):437–458, 1988.

[68] J. Greenberg, A. LeRoux, R. Baraille, and A. Noussair. Analysis and approximation of conservation laws with source terms. *SIAM Journal on Numerical Analysis*, 34(5):1980–2007, 1997.

[69] J. M. Greenberg and A. Y. Leroux. A well-balanced scheme for the numerical processing of source terms in hyperbolic equations. *SIAM Journal on Numerical Analysis*, 33(1):1–16, 1996.

[70] P. M. Gresho and S. T. Chan. On the theory of semi-implicit projection methods for viscous incompressible flow and its implementation via a finite element method that also introduces a nearly consistent mass matrix. Part 2: Implementation. *International Journal for Numerical Methods in Fluids*, 11(5):621–659, 1990.

[71] H. Guillard and E. Daniel. A well balanced scheme for gas flows in protoplanetary nebulae. In *Finite Volumes for Complex Applications IV*, pages 355–364. Hermes Science Publisher, 2005.

[72] K. Gurski. An HLLC-type approximate Riemann solver for ideal magnetohydrodynamics. *SIAM Journal on Scientific Computing*, 25(6):2165–2187, 2004.

[73] A. Harten and P. Lax. A random choice finite difference scheme for hyperbolic conservation laws. *SIAM Journal on Numerical Analysis*, 18(2):289–315, 1981.

[74] A. Harten, P. Lax, and B. van Leer. On upstream differencing and Godunov-type schemes for hyperbolic conservation laws. *SIAM Review*, 25(1):35–61, 1983.

[75] C. Helzel, J. A. Rossmanith, and B. Taetz. An unstaggered constrained transport method for the 3D ideal magnetohydrodynamic equations. *Journal of Computational Physics*, 230(10):3803–3829, 2011.

[76] T. Y. Hou and P. G. LeFloch. Why nonconservative schemes converge to wrong solutions: Error analysis. *Mathematics of Computation*, 62(206):497–530, 1994.

[77] T. J. Hughes, L. Mazzei, and K. E. Jansen. Large eddy simulation and the variational multiscale method. *Computing and Visualization in Science*, 3(1-2):47–59, 2000.

[78] S. Inaba, P. Barge, E. Daniel, and H. Guillard. A two-phase code for protoplanetary disks. *Astronomy & Astrophysics*, 431(1):365–379, 2005.

[79] R. A. James. The solution of Poisson's equation for isolated source distributions. *Journal of Computational Physics*, 25(2):71–93, 1977.

[80] P. Janhunen. A positive conservative method for magnetohydrodynamics based on HLL and Roe methods. *Journal of Computational Physics*, 160(2):649–661, 2000.

[81] G.-S. Jiang and C.-W. Shu. Efficient implementation of weighted ENO schemes. *Journal of Computational Physics*, 126(1):202–228, 1996.

[82] S. Jin. A steady-state capturing method for hyperbolic systems with geometrical source terms. *ESAIM: Mathematical Modelling and Numerical Analysis*, 35:631–645, 7 2001.

[83] S. Jin and Z. P. Xin. The relaxation schemes for systems of conservation laws in arbitrary space dimensions. *Communications on Pure and Applied Mathematics*, 48(3):235–276, 1995.

[84] R. Kippenhahn and A. Weigert. *Stellar structure and evolution*. Astronomy and Astrophysics Library. Springer, 1990.

[85] A. Kurganov, S. Noelle, and G. Petrova. Semi-discrete central-upwind schemes for hyperbolic conservation laws and Hamilton-Jacobi equations. *SIAM Journal on Scientific Computing*, 23:707–740, 2000.

[86] A. Kurganov and E. Tadmor. Solution of two-dimensional Riemann problems for gas dynamics without Riemann problem solvers. *Numerical Methods for Partial Differential Equations*, 18(5):584–608, 2002.

[87] P. Lax and X. Liu. Solution of two-dimensional Riemann problems of gas dynamics by positive schemes. *SIAM Journal on Scientific Computing*, 19(2):319–340, 1998.

[88] P. Lax and B. Wendroff. Systems of conservation laws. *Communications on Pure and Applied Mathematics*, 13(2):217–237, 1960.

[89] R. J. LeVeque. Balancing source terms and flux gradients in high-resolution Godunov methods: The quasi-steady wave-propagation algorithm. *Journal of Computational Physics*, 146(1):346–365, 1998.

[90] R. J. LeVeque. *Finite volume methods for hyperbolic problems*, volume 31. Cambridge University Press, 2002.

[91] R. J. LeVeque and D. S. Bale. Wave propagation methods for conservation laws with source terms. In *Proceedings of the 7th International Conference on Hyperbolic Problems*, pages 609–618, 1998.

[92] R. J. LeVeque and M. Pelanti. A class of approximate Riemann solvers and their relation to relaxation schemes. *Journal of Computational Physics*, 172(2):572–591, 2001.

[93] H. Li, S. A. Colgate, B. Wendroff, and R. Liska. Rossby wave instability of thin accretion disks. III. Nonlinear simulations. *The Astrophysical Journal*, 551(2):874, 2001.

[94] H. Li, J. M. Finn, R. V. E. Lovelace, and S. A. Colgate. Rossby wave instability of thin accretion disks. II. Detailed linear theory. *The Astrophysical Journal*, 533(2):1023, 2000.

[95] J. Li, Z. Yang, and Y. Zheng. Characteristic decompositions and interactions of rarefaction waves of 2-D Euler equations. *Journal of Differential Equations*, 250(2):782–798, 2011.

[96] Y. Li. Convergence of the nonisentropic Euler-Poisson equations to incompressible type Euler equations. *Journal of Mathematical Analysis and Applications*, 342(2):1107–1125, 2008.

[97] T. Linde. A practical, general-purpose, two-state HLL Riemann solver for hyperbolic conservation laws. *International Journal for Numerical Methods in Fluids*, 40(3-4):391–402, 2002.

[98] R. Liska and B. Wendroff. Comparison of several difference schemes on 1D and 2D test problems for the Euler equations. *SIAM Journal on Scientific Computing*, 25(3):995–1017, 2003.

[99] T.-P. Liu and T. Yang. Well-posedness theory for hyperbolic conservation laws. *Communications on Pure and Applied Mathematics*, 52(12):1553–1586, 1999.

[100] P. Londrillo and L. Del Zanna. High-order upwind schemes for multidimensional magnetohydrodynamics. *The Astrophysical Journal*, 530(1):508, 2000.

[101] P. Londrillo and L. Del Zanna. On the divergence-free condition in Godunov-type schemes for ideal magnetohydrodynamics: The upwind constrained transport method. *Journal of Computational Physics*, 195(1):17–48, 2004.

[102] J. Luo, K. Xu, and N. Liu. A well-balanced symplecticity-preserving gas-kinetic scheme for hydrodynamic equations under gravitational field. *SIAM Journal on Scientific Computing*, 33(5):2356–2381, 2011.

[103] P.-H. Maire, R. Abgrall, J. Breil, and J. Ovadia. A cell-centered Lagrangian scheme for two-dimensional compressible flow problems. *SIAM Journal on Scientific Computing*, 29(4):1781–1824, 2007.

[104] P.-H. Maire and B. Nkonga. Multi-scale Godunov-type method for cell-centered discrete Lagrangian hydrodynamics. *Journal of Computational Physics*, 228(3):799–821, 2009.

[105] A. Malagoli, G. Bodo, and R. Rosner. On the Nonlinear Evolution of Magneto-hydrodynamic Kelvin-Helmholtz Instabilities. *The Astrophysical Journal*, 456:708, 1996.

[106] A. Mignone, P. Tzeferacos, and G. Bodo. High-order conservative finite difference GLM-MHD schemes for cell-centered MHD. *Journal of Computational Physics*, 229(17):5896–5920, 2010.

[107] T. Miyoshi and K. Kusano. A multi-state HLL approximate Riemann solver for ideal magnetohydrodynamics. *Journal of Computational Physics*, 208(1):315–344, 2005.

[108] C.-D. Munz, P. Omnes, R. Schneider, E. Sonnendrücker, and U. Voß. Divergence correction techniques for Maxwell solvers based on a hyperbolic model. *Journal of Computational Physics*, 161(2):484–511, 2000.

[109] C.-D. Munz, R. Schneider, E. Sonnendrücker, and U. Voss. Maxwell's equations when the charge conservation is not satisfied. *Comptes Rendus de l'Académie des Sciences - Series I - Mathematics*, 328(5):431–436, 1999.

[110] R. Natalini and F. Rousset. Convergence of a singular Euler-Poisson approximation of the incompressible Navier-Stokes equations. *Proceedings of the American Mathematical Society*, 134:2251–2258, 2006.

[111] S. Noelle, N. Pankratz, G. Puppo, and J. R. Natvig. Well-balanced finite volume schemes of arbitrary order of accuracy for shallow water flows. *Journal of Computational Physics*, 213(2):474–499, 2006.

[112] K. G. Powell. An approximate Riemann solver for magnetohydrodynamics (that works in more than one dimension). Technical Report 94-24, ICASE, Langley, VA, 1994.

[113] D. J. Price and J. J. Monaghan. Smoothed particle magnetohydrodynamics: III. Multidimensional tests and the $\nabla \cdot \mathbf{B}$ constraint. *Monthly Notices of the Royal Astronomical Society*, 364(2):384–406, 2005.

[114] J. J. Quirk. A contribution to the great Riemann solver debate. *International Journal for Numerical Methods in Fluids*, 18(6):555–574, 1994.

[115] J. J. Quirk. Godunov-type schemes applied to detonation flows. In J. Buckmaster, T. L. Jackson, and A. Kumar, editors, *Combustion in High-Speed Flows*, volume 1 of *ICASE/LaRC Interdisciplinary Series in Science and Engineering*, pages 575–596. Springer Netherlands, 1994.

[116] R. D. Richtmyer and K. W. Morton. *Difference methods for initial-value problems*. Number 4. Interscience Publishers, Wiley, New York-London-Sydney, 1967.

[117] P. L. Roe. Approximate Riemann solvers, parameter vectors, and difference schemes. *Journal of Computational Physics*, 43(2):357–372, 1981.

[118] P. L. Roe. Characteristic-based schemes for the Euler equations. *Annual Review of Fluid Mechanics*, 18(1):337–365, 1986.

[119] J. Rossmanith. An unstaggered, high-resolution constrained transport method for magnetohydrodynamic flows. *SIAM Journal on Scientific Computing*, 28(5):1766–1797, 2006.

[120] R. Saurel, M. Larini, and J. C. Loraud. Exact and approximate Riemann solvers for real gases. *Journal of Computational Physics*, 112(1):126–137, 1994.

[121] M. Schleicher. Eine einfaches und effizientes verfahren zur lösung des Riemannproblems. *Zeitschrift für Flugwissenschaften und Weltraumforschung*, 17(4):265–269, 1993.

[122] C. W. Schulz-Rinne, J. P. Collins, and H. M. Glaz. Numerical solution of the Riemann problem for two-dimensional gas dynamics. *SIAM Journal on Scientific Computing*, 14(6):1394–1414, 1993.

[123] L. I. Sedov. Propagation of strong blast waves. *Prikl. Mat. Mekh*, 10(2):241–250, 1946.

[124] J. M. Stone and T. Gardiner. A simple unsplit Godunov method for multidimensional MHD. *New Astronomy*, 14(2):139–148, 2009.

[125] I. Suliciu. On modelling phase transitions by means of rate-type constitutive equations. Shock wave structure. *International Journal of Engineering Science*, 28(8):829–841, 1990.

[126] I. Suliciu. Some stability-instability problems in phase transitions modelled by piecewise linear elastic or viscoelastic constitutive equations. *International Journal of Engineering Science*, 30(4):483–494, 1992.

[127] A. Suresh. Positivity-preserving schemes in multidimensions. *SIAM Journal on Scientific Computing*, 22(4):1184–1198, 2000.

[128] R. Teyssier, S. Fromang, and E. Dormy. Kinematic dynamos using constrained transport with high order Godunov schemes and adaptive mesh refinement. *Journal of Computational Physics*, 218(1):44–67, 2006.

[129] E. F. Toro. *Riemann solvers and numerical methods for fluid dynamics: A practical introduction.* Springer, 3rd edition, 2009.

[130] G. Tóth. The $\nabla \cdot \mathbf{B} = 0$ constraint in shock-capturing magnetohydrodynamics codes. *Journal of Computational Physics*, 161(2):605–652, 2000.

[131] P. Váchal, R. Liska, and B. Wendroff. Fully two-dimensional HLLEC Riemann solver and associated difference schemes. In *Numerical Mathematics and Advanced Applications ENUMATH 2003*, pages 815–824. Springer-Verlag, 2004.

[132] S. Van Criekingen, E. Audit, J. Vides, and B. Braconnier. Time-implicit hydrodyanmics for Euler flows. In *ESAIM Proc. of the SMAI 2013 Congress, Seignosse, France*, forthcoming 2014.

[133] B. van Leer. Towards the ultimate conservative difference scheme. I. The quest of monotonicity. In H. Cabannes and R. Temam, editors, *Proceedings of the Third International Conference on Numerical Methods in Fluid Mechanics*, volume 18 of *Lecture Notes in Physics*, pages 163–168. Springer Berlin Heidelberg, 1973.

[134] B. van Leer. Towards the ultimate conservative difference scheme. II. Monotonicity and conservation combined in a second-order scheme. *Journal of Computational Physics*, 14(4):361–370, 1974.

[135] B. van Leer. Towards the ultimate conservative difference scheme. III. Upstream-centered finite-difference schemes for ideal compressible flow. *Journal of Computational Physics*, 23(3):263–275, 1977.

[136] B. van Leer. Towards the ultimate conservative difference scheme. IV. A new approach to numerical convection. *Journal of Computational Physics*, 23(3):276–299, 1977.

[137] B. van Leer. Towards the ultimate conservative difference scheme. V. A second-order sequel to Godunov's method. *Journal of Computational Physics*, 32(1):101–136, 1979.

[138] J. Vides, E. Audit, H. Guillard, and B. Nkonga. Divergence-free MHD simulations with the HERACLES code. In *ESAIM: Proc.*, volume 43, pages 180–194, 2013.

[139] J. Vides, E. Audit, and B. Nkonga. A relaxation scheme for inviscid flows under gravitational influence. In *ESAIM Proc. of the SMAI 2013 Congress, Seignosse, France*, forthcoming 2014.

[140] J. Vides, B. Braconnier, E. Audit, C. Berthon, and B. Nkonga. A Godunov-type solver for the numerical approximation of gravitational flows. *Communications in Computational Physics*, 15(1):46–75, 2014.

[141] J. Vides, B. Nkonga, and E. Audit. A simple two-dimensional extension of the HLL Riemann solver for gas dynamics. INRIA Research Report No. 8540, 2014.

[142] J. Vides, B. Nkonga, and E. Audit. A simple two-dimensional extension of the HLL Riemann solver for hyperbolic systems of conservation laws. *Journal of Computational Physics*, forthcoming 2014.

[143] J. Vides, S. Van Criekingen, M. Szydlarski, and E. Audit. A Godunov-type solver for gravitational flows: Towards a time-implicit version in the HERACLES code. In *8th International Conference of Numerical Modeling of Space Plasma Flows (ASTRONUM 2013)*, volume 488, pages 279–284, 2014.

[144] J. VonNeumann and R. D. Richtmyer. A method for the numerical calculation of hydrodynamic shocks. *Journal of Applied Physics*, 21(3):232–237, 1950.

[145] B. Wendroff. A two-dimensional HLLE Riemann solver and associated Godunov-type difference scheme for gas dynamics. *Computers & Mathematics with Applications*, 38(11-12):175–185, 1999.

[146] H. Weyl. Shock waves in arbitrary fluids. *Communications on Pure and Applied Mathematics*, 2(2-3):103–122, 1949.

[147] G. B. Whitham. *Linear and nonlinear waves.* John Wiley & Sons, 1974.

[148] P. Woodward and P. Colella. The numerical simulation of two-dimensional fluid flow with strong shocks. *Journal of Computational Physics*, 54(1):115–173, 1984.

[149] Y. Xing and C.-W. Shu. High order well-balanced WENO scheme for the gas dynamics equations under gravitational fields. *Journal of Scientific Computing*, 54(2-3):645–662, 2013.

[150] K. S. Yee. Numerical solution of initial boundary value problems involving Maxwell's equations in isotropic media. *IEEE Trans. Antennas and Propagation*, pages 302–307, 1966.

[151] T. Zhang and Y. Zheng. Conjecture on the structure of solutions of the Riemann problem for two-dimensional gas dynamics systems. *SIAM Journal on Mathematical Analysis*, 21(3):593–630, 1990.

[152] Y. Zheng. *Systems of conservation laws: Two-dimensional Riemann problems.* Progress in nonlinear differential equations and their applications. Birkhäuser, 2001.

Schémas de type Godunov pour la
modélisation hydrodynamique et magnétohydrodynamique

Résumé : L'objectif principal de cette thèse concerne l'étude, la conception et la mise en œuvre numérique de schémas volumes finis associés aux solveurs de type Godounov. On s'intéresse à des systèmes hyperboliques de lois de conservation non linéaires, avec une attention particulière sur les équations d'Euler et les équations MHD idéale. Tout d'abord, nous dérivons un solveur de Riemann simple et véritablement multidimensionnelle, pouvant s'appliquer à tout système de lois de conservation. Ce solveur peut être considéré comme une généralisation 2D de l'approche HLL. Les ingrédients de base de la dérivation sont : la consistance avec la formulation intégrale et une utilisation adéquate des relations de Rankine-Hugoniot. Au final nous obtenons des expressions assez simples et applicables dans les contextes des maillages structurés et non structurés. Dans un second temps, nous nous intéressons à la préservation, au niveau discret, de la contrainte de divergence nulle du champ magnétique pour les équations de la MHD idéale. Deux stratégies sont évaluées et nous montrons comment le solveur de Riemann multidimensionnelle peut être utilisé pour obtenir des simulations robustes à divergence numérique nulle. Deux autres points sont abordés dans cette thèse : la méthode de relaxation pour un système Euler-Poisson pour des écoulements gravitationnels en astrophysique, la formulation volumes finis en coordonnées curvilignes. Tout au long de la thèse, les choix numériques sont validés à travers de nombreux résultats numériques.

Mots-clés : Schéma de type Godunov, solveur de Riemann multidimensionnel, solveur de Riemann approché, méthode de relaxation, lois de conservation, dynamique des gaz, magnétohydrodynamique, effets gravitationnels

Godunov-type schemes for
hydrodynamic and magnetohydrodynamic modeling

Abstract: The main objective of this thesis concerns the study, design and numerical implementation of finite volume schemes based on the so-called Godunov-type solvers for hyperbolic systems of nonlinear conservation laws, with special attention given to the Euler equations and ideal MHD equations. First, we derive a simple and genuinely two-dimensional Riemann solver for general conservation laws that can be regarded as an actual 2D generalization of the HLL approach, relying heavily on the consistency with the integral formulation and on the proper use of Rankine-Hugoniot relations to yield expressions that are simple enough to be applied in the structured and unstructured contexts. Then, a comparison between two methods aiming to numerically maintain the divergence constraint of the magnetic field for the ideal MHD equations is performed and we show how the 2D Riemann solver can be employed to obtain robust divergence-free simulations. Next, we derive a relaxation scheme that incorporates gravity source terms derived from a potential into the hydrodynamic equations, an important problem in astrophysics, and finally, we review the design of finite volume approximations in curvilinear coordinates, providing a fresher view on an alternative discretization approach. Throughout this thesis, numerous numerical results are shown.

Key-words: Godunov-type scheme, multidimensional Riemann solver, approximate Riemann solver, relaxation method, conservation laws, gas dynamics, magnetohydrodynamics, gravitational effects